Dissertation
submitted to the
Combined Faculties for the Natural Sciences and for Mathematics
of the Ruperto Carola University of Heidelberg, Germany
for the degree of
Doctor of Natural Sciences

presented by
Diplom-Physicist: Hartmut Bösch
born in: Metzingen

Oral examination: 14.02.2002

Studies of the Stratospheric Nitrogen and Iodine Chemistry by Balloon-Borne DOAS Measurements and Model Calculations

Referees: Prof. Dr. Ulrich Platt
Prof. Dr. Konrad Mauersberger

Untersuchungen der Stickstoff- und Jodchemie der Stratosphäre mittels ballongetragener DOAS-Messungen und Modellrechnungen

Neben den Halogenverbindungen haben vor allem die Stickstoffverbindungen einen entscheidenden Einfluß auf den stratosphärischen Ozonabbau. Trotz intensiver Forschung konnte ein quantitatives Verständnis des Ozonverlusts aufgrund der komplexen Wechselwirkungsmechanismen zwischen chemischen und dynamischen Prozessen bisher nicht erreicht werden.

Im Rahmen dieser Doktorarbeit wurden Messungen stratosphärischer Spurenstoffprofile mittels ballongestützter Differentieller Optischer Absorptions Spektroskopie (DOAS) durchgeführt und interpretiert. Das Hauptaugenmerk galt dabei der genauen Bestimmung des Gehalts und der Verteilung von O_3, NO_2, IO und OIO unter unterschiedlichen geophysikalische Bedingungen.

Durch die Kombination der DOAS Messungen mit den Resultaten eines ebenfalls auf der Gondel installierten Fourier Transform Interferometers und der Einbeziehung dreidimensionaler Modellrechungen, konnte der stratospärische Stickstoffhaushalts detailliert untersucht werden. Es konnte gezeigt werden, daß die Modelle erhebliche Unsicherheiten bei der Beschreibung der atmosphärischen Transportprozesse aufweisen und daß die chemischen Mechanismen, die das Verhältnis der verschiedenen Stickstoffverbindungen regulieren, nur unvollständig verstanden sind.

Die gleichzeitige Bestimmung der Obergrenzen des stratosphärischen IO und OIO Gehalts zusammen mit photochemischen Modellrechungen ermöglichte eine Abschätzung der Obergrenze des gesamten gasförmigen Jods der unteren Stratosphäre mit bisher nicht erreichter Genauigkeit. Die Photolyse von OIO stellt dabei eine wesentliche Unsicherheit dar. Es konnte gezeigt werden, daß selbst im Rahmen der abgeschätzten Obergrenzen von 0.1 ppt oder 0.065 ppt (je nachdem ob OIO Phtotolyse zugelassen wird oder nicht) die Jodchemie einen signifikanten Beitrag zum Ozonverlust in mitteren Breiten leisten kann.

Studies of the Stratospheric Nitrogen and Iodine Chemistry by Balloon-Borne DOAS Measurements and Model Calculations

It is well known, that the stratospheric ozone depletion is controlled mainly by halogen and nitrogen compounds. As a result of the complex interaction between chemical and dynamical processes, a quantitative understanding of the ozone loss has not been achieved till now, although it was subject of several years of intensive scientific research.

This thesis reports and discusses balloon-borne Differential Optical Absorption Spectroscopy (DOAS) measurements of stratospheric trace gas profiles. The focus of this study was to measure the vertical distribution of O_3, NO_2, IO, and OIO during different geophysical conditions.

In combination with the results of a Fourier Transform Interferometer, sharing the gondola with the DOAS instrument, and with 3-D chemistry model calculations it was possible to investigate the nitrogen chemistry in detail. Large deficits in the model's treatment of the atmospheric transport processes as well as in the understanding of the processes that control the partitioning of the nitrogen species have been found.

Upper limits of the stratospheric amounts of IO and OIO were simultaneously inferred. The combination of these observations with photochemical model calculations allowed to precisely infer the upper limit of total gaseous iodine in the lower stratosphere. It is noteworthy, that even within the inferred upper limits of total iodine of 0.1 ppt or 0.065 ppt (allowing or omitting OIO photolysis), iodine still has the potential to significantly reduce the mid-latitudinal stratospheric ozone level.

Contents

Chapter 1

Introduction

The unique role of ozone in absorbing most of the biologically damaging ultraviolet radiation (UV) of the incoming solar radiation was already recognized in the 19th century by *Cornu* [1879] and *Hartley* [1880]. Stratospheric ozone[1] converts the UV radiation into heat, which determines the thermal structure of the stratosphere.

Although it was realized in the early 1970s, that anthropogenic emissions of nitrogen and halogen compounds influence the stratospheric ozone budget [*Crutzen* 1970; *Molina and Rowland* 1974], the discovery of a dramatic ozone loss over Antarctica was surprising [*Farman et al.* 1985]. It was found, that this phenomena of an almost 100% ozone reduction at altitudes between 12 km and 20 km, referred to as the Antarctic ozone hole, occurs regularly every spring. The anthropogenic emissions of chlorofluorcarbons (CFCs) were soon identified as the likely cause and the future production of CFCs and of other ozone depleting substances such as halons was reduced stepwise and finally stopped by the Montreal Protocol in 1987 and its amendments (London, 1990; Copenhagen, 1992; Montreal, 1997).

The mechanisms, responsible for the formation of the Antarctic ozone hole, are believed to be quantitatively understood now. The dynamical prerequisite is the formation of a strong winterly cyclone over the pole, called the polar vortex. Inside this 'chemical containment vessel' the temperatures can drop below 196 K and so-called polar stratospheric clouds (PSCs) can form [*Toon et al.* 1986; *Crutzen and Arnold* 1986]. Stable inorganic halogen compounds such as HCl, $ClONO_2$ or $BrONO_2$ then react on the surface of these PSCs and form more reactive and ozone destroying species Cl_2, HOCl, and BrCl [*Solomon et al.* 1986]. As soon as the sunlight returns, latter species photodissociate and destroy ozone through catalytic cycles.

The discovery of the Antarctic ozone hole raised the question whether a chemical induced ozone depletion is also occurring in other regions. During the Arctic winter, the similar meteorological conditions lead to the formation of a polar vortex in the stratosphere just like over Antarctica. However, strong dynamical disturbances, caused by the large-scale weather system, make the Arctic vortex less stable and prevent the temperatures from being as low as in Antarctica. Therefore, the potential for PSC formation and ozone depletion is much reduced. Nevertheless, chemical active bromine and chlorine compounds are also formed over the Arctic and the observed ozone loss can be as large as 70% around 20 km[*EORCU* 2000]. Besides the

---

[1] About 90% of the atmospheric ozone resides in the stratosphere, a layer that begins between 8 and 18 km and extents to 50 km.

stratospheric ozone depletion over the poles, a statistically significant, negative trend in ozone is observed also in both hemispheres at mid and high latitudes during all seasons. It is believed, that the increased bromine and chlorine loading of the stratosphere has primarily contributes to the mid-latitudinal ozone loss, as same heterogenous reactions that occur in the polar regions can take place on background aerosol in the tropopause[2] region [*WMO* 1998].

Although most of the key processes involved in the ozone depletion are well understood, discernible discrepancies are observed when comparing the predictions of chemical model calculations with atmospheric measurements. For instance, neither the ozone destruction observed during the Arctic winter nor the mid-latitudinal trend can be quantitatively explained by models [*EC-Report* 2001].

The differential optical absorption spectroscopy (DOAS) is a well established technique for the sensitive detection and quantification of atmospheric trace gases. Within the scope of this Ph. D. thesis, a balloon-borne DOAS instrument, installed on the LPMA[3]/DOAS balloon gondola, was used to measure the vertical distributions of O_3, NO_2, IO and OIO during a series of eight flights in different latitudes and seasons.

The main objective of this thesis is the detailed investigation of the stratospheric nitrogen chemistry. An accurate knowledge of the processes controlling the abundances and the partitioning of nitrogen species is crucial for the ozone chemistry as nitrogen oxides are directly involved in the ozone depletion[4] and as they modulate the strength and the length of the ozone depletion during the polar winter/spring through the deactivation of chlorine and bromine[5]. The combination of the DOAS measurements with the results obtained with an Fourier Transform Interferometer sharing the gondola with the DOAS instrument, provides the ability to study the budget and partitioning of the nitrogen species in detailed and to identify and explore the current deficits of so-called Chemical Transport Models (CTMs).

Another objective is to sensitively estimate the amount of total stratospheric iodine. As first proposed by *Solomon et al.* [1994], iodine can significantly contribute to the observed mid-latitudinal trend in ozone. Past measurements of stratospheric IO, however, yielded negative results [*Pundt et al.* 1998; *Wennberg et al.* 1997], but recent laboratory as well as field studies have revitalized the importance of stratospheric iodine [e.g. *Alicke et al.* 1999; *Cox et al.* 1999; *Cronhite et al.* 1999; *Allan et al.* 2000; *Frieß et al.* 2001; *Wittrock et al.* 2000]. The balloon-borne DOAS measurements provide a unique tool to sensitively search for the spectroscopic signatures of stratospheric IO and, for the first time, of OIO. In combination with photochemical model calculations, these measurements allow to quantify the potential amount of gaseous iodine in the lower stratosphere.

This thesis is organized as follows. The second chapter gives a brief overview of the most important radiative processes in the earth's atmosphere. The third chapter presents the current knowledge of the stratospheric chemistry and especially highlights the nitrogen and iodine chemistry. Also included is a discussion of the relevant dynamical processes. The methodology

---

[2] Lower boundary of the stratosphere

[3] LPMA=Laboratoire de Physique Moléculaire et Application

[4] In the altitude range between 25 km and 40 km the dominant contribution to the ozone depletion is through nitrogen chemistry [e.g. *Brasseur and Solomon* 1986].

[5] The denoxification (the transformation of active nitrogen oxides to stable nitrogen species) and denitrification (the irreversible removal nitrogen through uptake and sedimentation of large particles) are essential prerequisites for a strong and long-lasting ozone depletion [e.g. *Fahey et al.* 1990].

is subject of the the fourth chapter. There the used instrumentation, the measurement technique and the methods used to retrieve vertical trace gas distributions is described. The fifth chapter gives an overview of the results of the NO_2 and O_3 measurements, including extensive comparisons with other measurements and model calculations. A detailed investigation of the partitioning and the budget of nitrogen species is presented in the sixth chapter. The seventh chapter present the results of the IO and OIO measurements. Finally a summary and outlook are provided in the eighth chapter.

Chapter 2

Basics of the Atmospheric Radiative Transfer

A photon, traversing the earth's atmosphere can undergo a large number of processes. It can be Rayleigh or Raman scattered on air molecules, Mie scattered on aerosols, cloud droplets or ice particles or it can be absorbed by them. Since the absorption by aerosols and cloud droplets can be neglected in the UV/vis/NIR[1] wavelength range (~300-800 nm), only the gaseous absorption of molecules will be considered here. The following sections describe the different scattering processes and the molecular absorption in more detail beginning with the definitions of the basic quantities for the radiative transfer.

2.1 Definitions

The incident radiant energy per time dW_λ at wavelegth λ on an arbitrary orientated area element dA is given by the *irradiance* E_λ

$$E_\lambda = \frac{dW_\lambda}{dA} \tag{2.1}$$

Taking into account the orientation of the area element and the solid angle Ω of the incident radiation we obtain the *radiance* L_λ often simply called intensity I_λ:

$$L_\lambda = \frac{dW_\lambda}{dA_\perp \, d\Omega} \tag{2.2}$$

with $dA_\perp = dA \cos\vartheta$ and ϑ being between the direction of the incident beam and the normal of the element of area. By integrating L_λ over the half sphere considering the factor $\cos\vartheta$ the irradiance can be calculated:

$$E_\lambda = \int_{2\pi} L_\lambda \cos\vartheta \, d\Omega \tag{2.3}$$

For isotropic radiation, i.e. $L_\lambda = L_{0,\lambda}$, the integration is trivial and yields $E_\lambda = \pi L_{0,\lambda}$. A quantity of major importance for the photochemistry is the *actinic flux* F_λ, obtained by integrating L_λ

---

[1] UV: ultraviolet; vis: visible; NIR: near infrared

over the whole sphere

$$F_\lambda = \int_{4\pi} L_\lambda \, d\Omega \tag{2.4}$$

2.2 Scattering

2.2.1 Rayleigh Scattering

Rayleigh scattering occurs if the dimension of the scatterers is small compared to the wavelength of the incident radiation (e.g., air molecules). The scattered light can be treated as radiation emitted by an oscillating dipole, excited by the oscillating field of the incident electromagnetic wave. The scattering cross section can be calculated and shows a λ^{-4} dependency for light frequencies smaller than the natural frequency of the oscillator (see , e.g. [*Feynman et al.* 1965]). An accurate empirical formula for the total cross section taking into account the polarizability and the anisotropy of air molecules is given by [*Brasseur and Solomon* 1986]

$$\sigma_{Rayl} = \frac{4.0 \cdot 10^{-28}}{\lambda^{3.916+0.074\lambda+\frac{0.05}{\lambda}}} \ \mathrm{cm}^2 \tag{2.5}$$

with λ given in μm. The phase function for Rayleigh scattering for unpolarized light is given by

$$p(\theta) = \frac{3}{4}\ (1 + \cos^2\theta) \tag{2.6}$$

or when taking into account the anisotropy of the molecules by [*Penndorf* 1957]

$$p(\theta) = 0.7629\ (1 + 0.932 \cos^2\theta). \tag{2.7}$$

2.2.2 Mie Scattering

If the dimension of the scattering particle is comparable or larger than the wavelength of the incident light then Mie scattering occurs. In this case, the emission of a large number of excited dipoles in the particles has to be considered. The resulting interference effects lead to a strong emphasis of the forward direction of the scattered light. This scattering characteristic can be well approximated by the Henyey Greenstein phase function:

$$p(\theta) = \frac{1 - g^2}{(1 + g^2 - 2g\cos\theta)^{3/2}}, \tag{2.8}$$

with the asymmetry factor

$$g = <\cos\theta> = \frac{1}{2} \int_{-1}^{+1} p(\theta) \cdot \cos\theta \ d(\cos\theta). \tag{2.9}$$

For atmospheric aerosols an asymmetry factor in the range between 0.6 and 0.7 is usually assumed. Since a mixture of aerosols of different size is found in the atmosphere the macroscopic extinction coefficient is used instead of the scattering cross section. This macroscopic extinction coefficient is defined as the integral of the particle size distribution times the scattering cross section and the particle surface [*Van De Hulst* 1957]. The size distribution of atmospheric aerosols is well described by the Junge distribution ($\sim r^{-s-1}$) with $s = 3.5 \pm 1$ [*Junge* 1961]. This leads to a λ^{3-s} dependence of the macroscopic extinction coefficient.

2.2.3 Raman Scattering

Inelastic scattering of light on molecules, called Raman scattering, occurs, if during the scattering process the rotational or rotational-vibrational state of the molecule and thus the energy of the scattered photon changes. Consequently, the molecular scattered light consists of the Rayleigh line (due to the elastic scattering) accompanied by several closely spaced vibrational Raman bands, each consisting of several rotational Raman lines. However, the total cross section for Raman scattering is only in the range of a few percent of the Rayleigh cross section with the same phase function as for Rayleigh scattering. Detailed calculations of the Raman cross section for air molecules (O_2 and N_2) can be found in *Bussemer* [1993], *Haug* [1996], and *Funk* [2000].

For measurements of scattered sun light, the implication of Raman scattering lies in the 'filling in' of Fraunhofer lines. This effect is referred to as *Ring effect* [*Grainger and Ring* 1962]. Strong atmospheric absorption lines can also be affected by the Ring effect [*Fish and Jones* 1995].

2.3 Absorption

An atom or molecule can change its internal state to a higher state by absorption of a photon from an electromagnetic radiation field if the energy difference of the two states equals the energy of the absorbed photon. The transition probability shows a linear dependency on the energy density of the radiation field with a proportionality factor called *Einstein coefficient* for absorption[2]. The strength of the absorption is thus given by the Einstein coefficient which can be obtained by quantum mechanical calculations[3]. Besides the energy conservation some *selection rules* for the transitions have to be obeyed. The selection rules can be inferred by considering the symmetry properties of the wave functions of the atomic or molecular states. The atomic or molecular specific absorption characteristics are expressed in terms of an absorption cross section, which is a measure for the probability of absorption at a certain wavelength.

While for atoms only electronic transitions are possible, for molecules electronic, rotational and vibrational transitions occur. Molecular absorption spectra in the UV/vis wavelength range ($\sim$ 300-700 nm) consist of rotational-vibrational spectra of different electronic transitions. However, the rotational-vibrational spectrum of an electronic transition is often superimposed by lines of other transitions and thus identification of individual lines is not possible. The absorption cross sections of the most important species in the visible wavelength range are displayed in Figure 2.1. In the microwave and infrared region the absorption is due to rotational transitions and rotational-vibrational transitions, respectively. In this wavelength range, it is often possible to identify single absorption lines.

The spectral lines of the (originally monochromatic) transitions are broadened by Doppler

---

[2] Atoms or molecules can change their internal state by absorption and stimulated or spontaneous emission. An Einstein coefficient is assigned to each of the three processes. Close relationships between the three coefficients can be found by steady state assumptions [*Schwabl* 1993].

[3] Time dependent perturbation theory show that the Einstein coefficients depend on the square of the dipole matrix element of the transition. The dipole matrix element is defined as the expectation value of the position vector of the electron taking into consideration the wave function of both states of the transition.

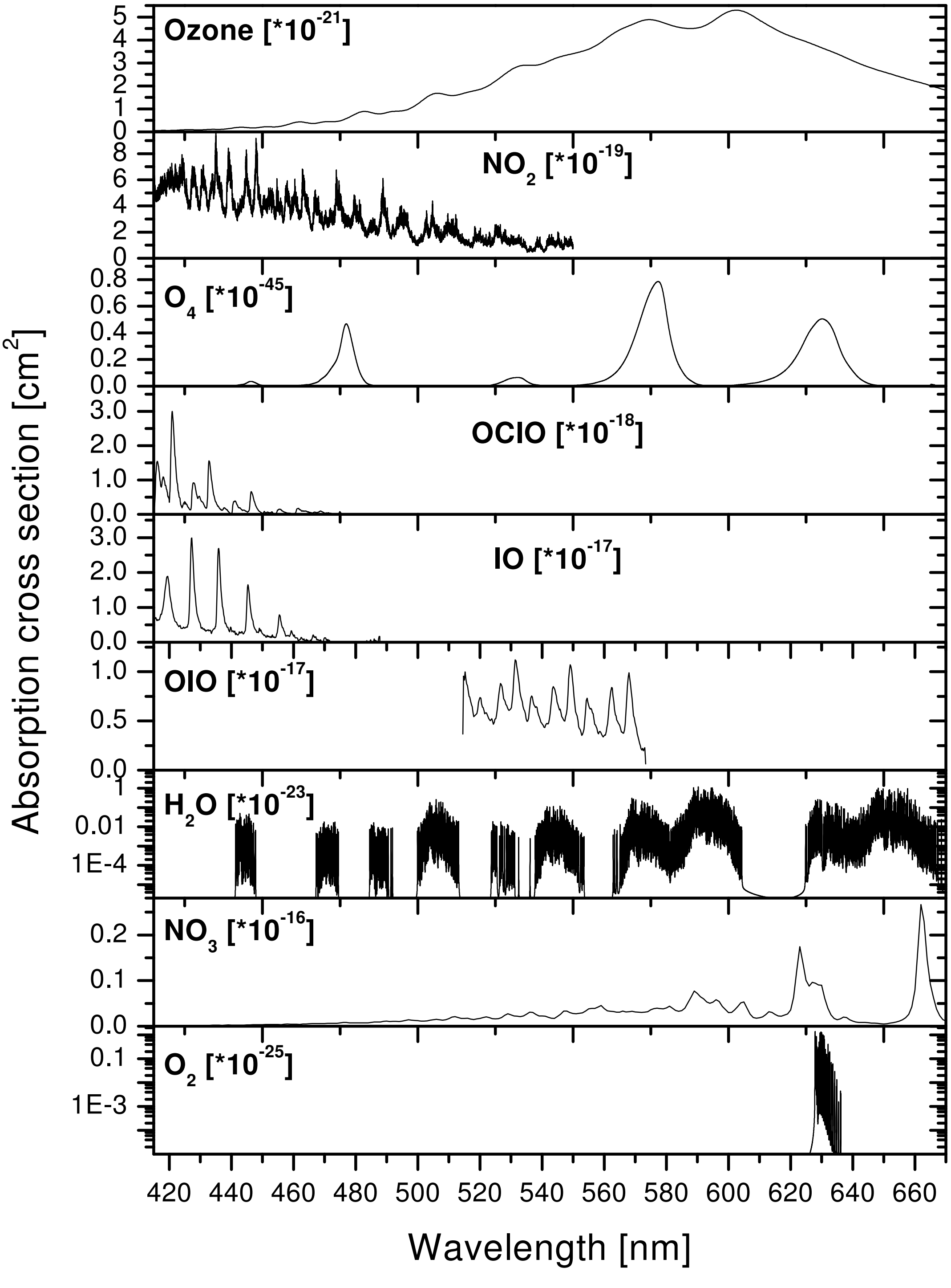

Figure 2.1: *Absorption cross sections in the visible wavelength range. Shown is -from the top to the bottom- ozone [Burrows et al. 1999],* NO_2 *[Harder et al. 1997],* O_4 *[Greenblatt et al. 1990], OClO [Wahner et al. 1987], IO [Harwood et al. 1997], OIO [Cox et al. 1999] ,* H_2O *[Rothman et al. 1996],* NO_3 *[Sander 1986], and* O_2 *[Rothman et al. 1996]. For* O_4*, the collisional pair absorption cross section is shown (see chapter 4.1.4).*

and pressure broadening. Under atmospheric conditions, the natural line width, associated with the radiative lifetime of the excited state, is negligible compared to the Doppler and pressure broadening. The absorbing atoms or molecules are in thermal motion. Thus the statistically distributed Doppler shift of the absorption frequency leads to a broadening of the spectral line with a Gaussian line shape. The interaction of the absorbing atom or molecule with neighboring atoms or molecules (e.g, during collisions) causes a shift of the energy levels. This energy shift depends on the level itself and the distance between the collision partners. For statistically distributed distances this results in a broadening of the line and a Lorentzian line shape. In general the line shape of atmospheric absorption lines is clearly dominated by pressure broadening, only for low pressures (in the higher atmosphere) the Doppler broadening becomes important. Both broadening effects can be taken into account by using a Voigt profile, given by the convolution of both line shapes.

2.4 Photochemical Effects

Absorption of ultraviolet and visible photons by atmospheric molecules can induce transitions into electronical states which may then photodissociate. The photodissociation rate of a molecule A is given by

$$\frac{dn(A)}{dt} = -j_A \cdot n(A) \tag{2.10}$$

where $n(A)$ represents the concentration of the molecule and j_A the photodissociation probability or coefficient. The photodissociation coefficient can be calculated by integration of the product of the absorption cross section σ, the quantum yields[4] ϵ and the actinic flux F

$$J_A = \int \epsilon(\lambda)\,\sigma(\lambda)\,F(\lambda)\,d\lambda \tag{2.11}$$

The spectral distribution of the absorption cross section and the quantum yield is determined in the laboratory and can vary with temperature (and pressure). In most cases, the quantum yield is near unity but may be less, especially near the dissociation limit. This limit corresponds to the minimum energy required to dissociate the molecule[5].

---

[4] The quantum yields describes the probability for photodissociation after absorption of a photon

[5] The wavelength given for photolytical reactions in chapter 3 indicate this dissociation limit

Chapter 3

Stratospheric Chemistry and Dynamics

The earth's atmosphere can be described as a series of layers defined by their thermal characteristics (Figure 3.1). Each layer (called sphere) is a region where the temperature gradient with respect to the altitude has a constant sign and the boundaries (called pause) are given by the zeros of the temperature gradient. The lowest layer beginning at the earth's surface is called *troposphere*. Here the temperature decreases with altitude down to values of 220 - 200 K at the upper boundary of the troposphere (tropopause). The layer next is the *stratosphere*. In this layer the temperature increases again to values around 270 K at the upper boundary (stratopause). While the lower boundary is dependent on the geographical latitude with elevations about 18 km at the equator and roughly 8 km at the poles, the upper boundary is uniformly around 50 km. The temperature at any location of the stratosphere is determined by diabatic and radiative processes involving ozone as a UV/vis heating agent, CO_2 as an IR coolant and superimposed local fluxes of heat. As a result of the positive temperature gradient, the transport and mixing is less efficient than in the troposphere. Moreover, the mass exchange between both layers of the atmosphere is slow and only long-lived tropospheric species such as H_2O, N_2O, CH_4 and CFC's can survive long enough to enter the stratosphere. The most important stratospheric species is ozone. Although ozone is present in the atmosphere in all layers, the bulk of ozone resides in the lower stratosphere with a maximum concentration at $\sim$ 25 km, referred to as the *stratospheric ozone layer*. Beside it's role for the stratospheric heating, ozone has two further important effects. Its most outstanding feature is the relationship between its UV absorption spectrum and the protection of living organism from the short wavelength solar UV radiation. All solar radiation between 200-300 nm is intercepted in the mid and lower stratosphere due to the presence of ozone. Furthermore, ozone is a so-called greenhouse gas. It is infrared active and contributes to the radiative transfer in the long wavelength regime of the terrestrial radiation.

In the present chapter we will focus on the chemical processes which are responsible for the current distribution of stratospheric trace gases, in particular ozone, nitrogen and halogen compounds. Afterwards the basics of stratospheric dynamics will be described briefly. Finally, the processes leading to the so-called *stratospheric ozone hole* will be discussed.

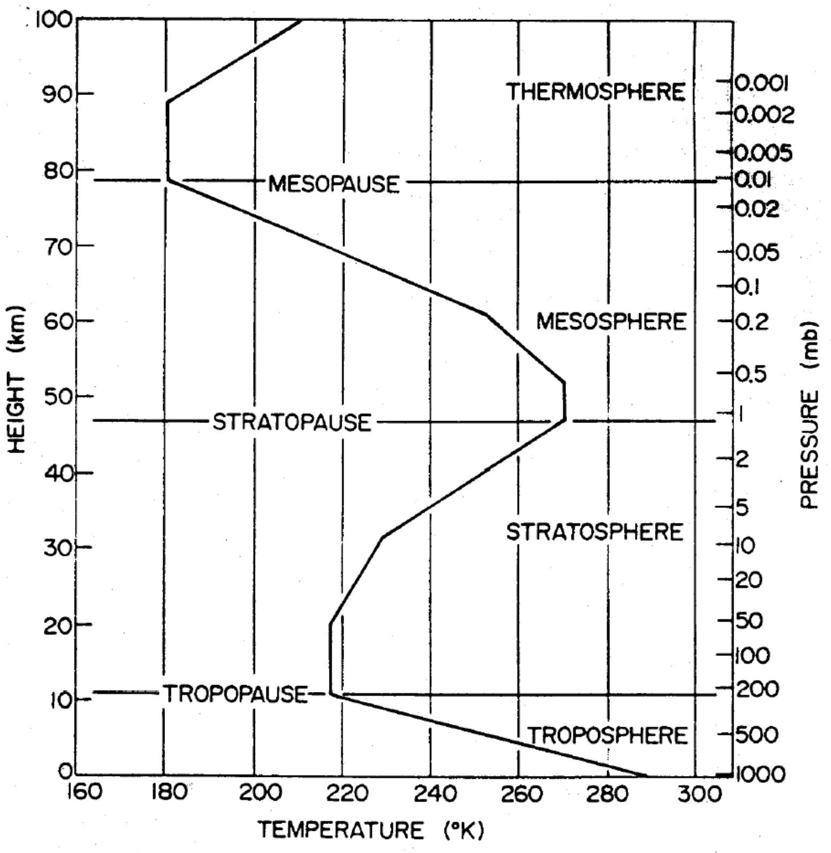

Figure 3.1: *Vertical structure of the earth 's atmosphere. The temperature profile is an idealized profile based on the US Standard Atmosphere [NOAA-S/T76-1562 1976]. The transitions of the different atmospheric layers are given by the maxima and minima of the temperature profile (denoted as pause).*

3.1 Stratospheric Ozone

A chemical scheme for the formation and destruction of ozone in the stratosphere involving only oxygen species was first proposed by *Chapman* [1930]. The photodissociation of molecular oxygen by ultraviolet radiation produces atomic oxygen, which can react to ozone with molecular oxygen via a three-body reaction:

$$\mathrm{O_2} \xrightarrow{h\nu} \mathrm{O + O} \qquad (\lambda \leq 242\,\mathrm{nm}) \tag{3.1}$$

$$\mathrm{O + O_2} \xrightarrow{M} \mathrm{O_3} \tag{3.2}$$

The photodissociation of ozone followed by the reaction of atomic oxygen with either another oxygen atom or with ozone represents the ozone loss processes.

$$\mathrm{O_3} \xrightarrow{h\nu} \mathrm{O_2 + O(^1D)} \qquad (\lambda \leq 310\,\mathrm{nm}) \tag{3.3}$$

$$O(^1D) \xrightarrow{M} O \tag{3.4}$$

$$O_3 \xrightarrow{h\nu} O_2 + O \qquad (\lambda \leq 1180\,\mathrm{nm}) \tag{3.5}$$

$$O + O \xrightarrow{M} O_2 \tag{3.6}$$

$$O + O_3 \longrightarrow 2\,O_2 \tag{3.7}$$

Due to the strong attenuation of the short wavelength radiation, the photolysis of O_2 (reaction 3.1) and thus the production of ozone occurs mainly in the upper stratosphere. The photolysis of ozone (reactions 3.3 and 3.5)below 50 km represents a gross but not net loss process over timescales of the order of minutes, since almost all the atomic oxygen produced reforms ozone within a few seconds or less (reaction 3.2).

An important aspect of atmospheric chemistry is the family concept. If we define the O_x family as the sum of the odd-oxygen such as ozone, O, and $O(^1D)$[1] then a number of reactions only convert one species of the O_x family into another without changing the total O_x concentration. One important consequence is the difference in lifetime. While the lifetime of the individual species is short (e.g. $\sim 10^{-8}$ s for $O(^1D)$ at 30 km) the lifetime of the family as a whole is several weeks. The use of chemical families allows a clearer distinction to be drawn between reactions which represent net and gross production and loss terms over the time scales considered.

According to the photochemical model of ozone production, the rate of O_2 photodissociation and hence the O_3 production shows a maximum for overhead sun. As a consequence the largest ozone production is found in the equatorial region, but even at 60° latitude the production rate is still effective. However, as a result of transport and mixing processes, the average global distribution of ozone deviates substantially from the pure photochemical predictions. Hence, the global distribution strongly depends on latitude and season with the highest concentrations found in each hemisphere at high latitudes during spring.

The stratospheric ozone profile can qualitatively be well explained with the Chapman theory, based on pure oxygen chemistry. Even the existence of the concentration maximum in the lower stratosphere is predicted correctly. But a quantitative comparison with the measured ozone profile shows that the concentrations are largely overestimated. It soon became clear, that stratospheric ozone was chemically destroyed not solely by reactions with atomic oxygen but also by catalytic reactions, involving OH (HO_x-cycle [*Bates and Nicolet* 1950]), NO (NO_x-cycle [*Crutzen* 1970; *Johnston* 1971]), Cl (ClO_x-cycle [*Molina and Rowland* 1974]), and Br (BrO_x-cycle [*Wofsy et al.* 1975]):

$$X + O_3 \longrightarrow XO + O_2 \tag{3.8}$$

$$XO + O \longrightarrow X + O_2 \tag{3.9}$$

$$\text{net:} \qquad O_3 + O \longrightarrow 2\,O_2 \tag{3.10}$$

where X denotes one of the radicals OH, NO, Cl, or Br. The radical X is regenerated by reaction 3.9 and is once more available for another ozone destruction cycle until removed by a sink process. Thus, already a small concentration of the catalyst X can have a large impact on the ozone concentration. In addition to this cycle, there is a second, important cycle of ozone destruction which does not involve oxygen atoms:

$$OH + O_3 \longrightarrow HO_2 + O_2 \tag{3.11}$$

---

[1] In a similar manner, the HO_x, ClO_x, BrO_x, and NO_x families can be defined

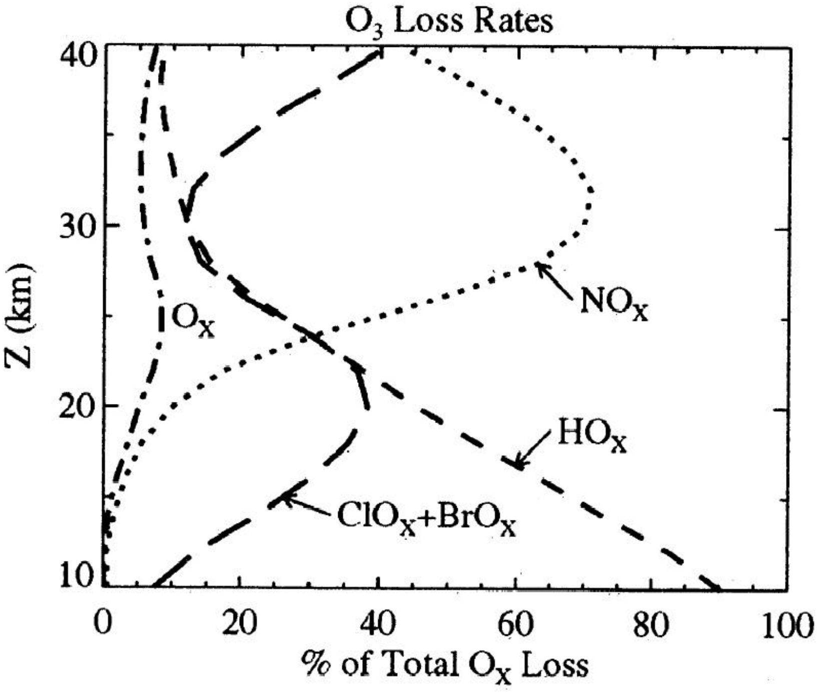

Figure 3.2: *The O_3 loss rates due to the catalytic cycles involving NO_x, HO_x, ClO_x+BrO_x, and O_x reactive families as a percentage of total O_3 loss rates for 60° N in October computed for the 1990s using JPL-97 [DeMore et al. 1997] values. Adapted from Portmann et al. [1999].*

$$HO_2 + O_3 \longrightarrow OH + 2\,O_2 \tag{3.12}$$
$$\text{net:} \quad 2\,O_3 \longrightarrow 3\,O_2 \tag{3.13}$$

This cycle works only for HO_x. As a consequence of the non-participation of oxygen atoms, this cycle is also important for lower altitudes.

Another type of catalytic cycles involving the species of different families is given by the following scheme:

$$X + O_3 \longrightarrow XO + O_2 \tag{3.14}$$
$$Y + O_3 \longrightarrow YO + O_2 \tag{3.15}$$
$$XO + YO \longrightarrow X + Y + O_2 \tag{3.16}$$
$$\text{net:} \quad 2\,O_3 \longrightarrow 3\,O_2 \tag{3.17}$$

with X=OH and Y=Cl, X=OH and Y=Br or X=Br and Y=Cl. Here, the recycling of the catalysts does not involve atomic oxygen, thus the cycle is of importance in the lower stratosphere where the catalytic ozone destruction cycles involving only species of one family is suppressed. The relative contributions of the various cycles to the ozone destruction is shown in Figure 3.2, calculated for mid-latitudinal conditions (60°N) in October. The relative contributions strongly vary with altitude. While in the lower stratosphere, the HO_x cycle dominates the ozone loss with a smaller contribution of the ClO_x+BrO_x cycle, the O_3 loss between 25 and 40 km is almost solely caused by the NO_x cycle and above 40 km, the catalytic cycles involving halogens play the dominant role. The relative contributions for other latitudes or seasons will differ from the calculations shown in the figure. It should be mentioned, that this holds true only outside the so-called polar vortex (see section 3.9). As discussed in section 3.5, the (dramatic) ozone loss during polar spring is clearly caused by cycles involving chlorine (and bromine).

These catalytic cycles together with the Chapman cycle describe well the observed ozone profile (for non-ozone hole conditions). As mentioned at the beginning of this section, the ozone concentration is strongly dependent on stratospheric transport and mixing processes. However, it became clear that anthropogenic emissions of long-lived trace gases such as N_2O, CH_4, chlorofluorcarbons (CFCs) or halons has a crucial impact on the stratospheric ozone concentration, since these gases can react to species serving as catalysts in the ozone destruction cycles. In addition, the emission of manmade CFCs was identified as the major source of the ozone-destroying chlorine responsible for the so-called stratospheric ozone hole in polar regions (discussed in more detail in section 3.5).

Besides the striking effect of the polar ozone hole, there is a slight global decrease of the total ozone column. This trend is globally not uniform, but does depend on season and geographical latitude. If the global trend is corrected for natural variations such as the 11-year solar cycle, a linear regression yields a decrease by ~ 3% per decade [e.g. *WMO* 1998]. The vertical distribution of this ozone trend is shown in Figure 3.3. Two maxima can clearly be observed, one around 40

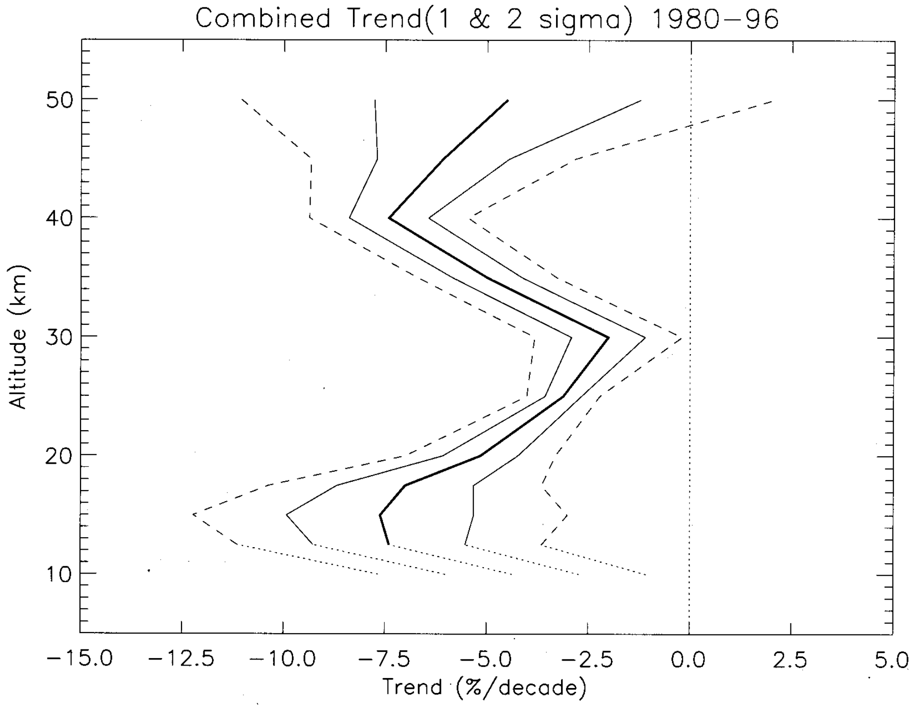

Figure 3.3: *Mean, annually averaged trend in the vertical distribution of ozone that occurred over northern mid-latitudes from 1980 - 1996. Additionally, the combined uncertainties for 67 % confidence limits and 95 % confidence limits are shown. Adapted from Pyle et al. [1999].*

km and one around 15 km, while in between the ozone loss is rather small. It is evident, that the increased chlorine and bromine loading has contributed to the observed mid-altitude ozone loss, which is also consistent with the vertical dependence of the ozone depletion (compare Figure 3.2 and Figure 3.3). However, the magnitude of the trend in ozone can not solely be explained by the known gas-phase chemistry combined with the increase in the stratospheric bromine and chlorine loading. Several dynamical as well as new chemical mechanisms have been proposed to contribute to the ozone trend. As shown by *Solomon et al.* [1998], a changing aerosol surface area significantly modulates the effect that the gradually increasing halogen loading has on stratospheric ozone. Responsible for this modulation are chemical reactions taking place on the surface of sulfate aerosols like hydrolysis of N_2O_5 which indirectly enhances active chlorine and direct chlorine activation at cold temperatures. Further it is discussed if the mid-latitudinal ozone loss can partly be explained by polar effects (transport of polar air to mid-latitudes) or circulation changes such as changes in the tropopause height. However, there are still deficits in understanding the mid-latitude ozone loss (Figure 3.4), e.g. it is not clear up to now if iodine catalyzed ozone destruction contributes significantly to this ozone loss as proposed by *Solomon et al.* [1994] (see also section 3.3.3 and chapter 7).

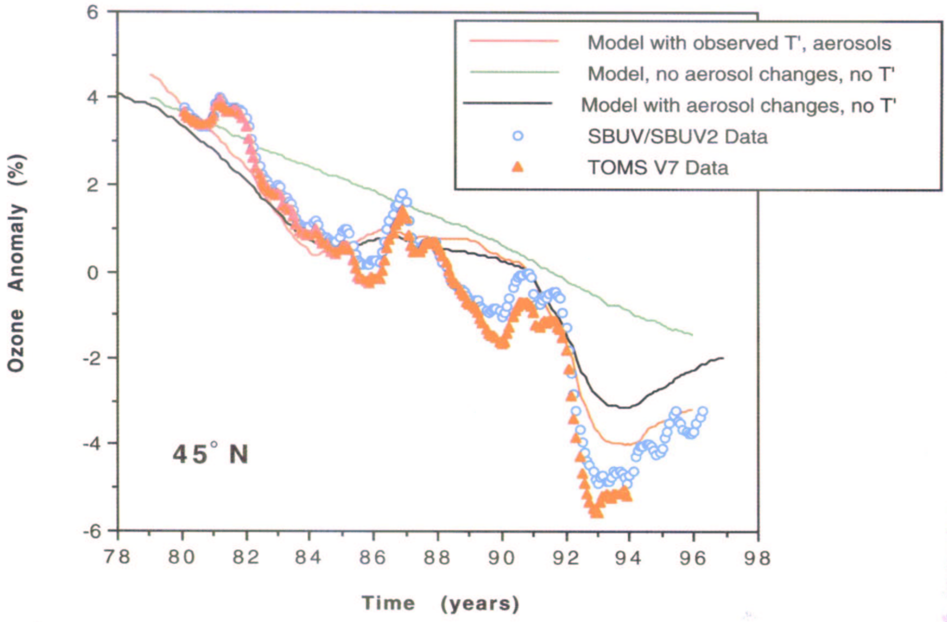

Figure 3.4: *Observed and calculated total ozone anomalies from 1979 to 1997 at 45 °N. The observations are zonally averaged TOMS and combined SBUV/SBUV2 data. Three different model calculations are shown, all including chlorine and bromine increase. The green line uses constant aerosol loading, the black line includes the observed aerosol variation and the red line additionally includes zonal mean temperature and planetary wave temperature amplitudes. Adapted from WMO [1998].*

3.2 Nitrogen Chemistry

The dominant net source of stratospheric NO_x (=NO+NO_2) is the reaction of $O(^1D)$ atoms with N_2O:

$$\begin{aligned} O(^1D) + N_2O &\longrightarrow 2\,NO && (3.18) \\ &\longrightarrow N_2 + O_2 && (3.19) \end{aligned}$$

This reaction is very fast and produces NO with a fractional yield of 58 %. N_2O has natural and anthropogenic sources with a ratio of 2:1. The major contributions to the total source strength come from oceans and tropical forests and hence are of natural origin. As a consequence of biomass burning and the use of artificial fertilizers, the N_2O level has increased from the pre-industrial level of approx. 260 - 285 ppb to 311 ppb today with a mean growth rate of 0.25 % per year during the 1980s. More recently the growth rate decreased from about 1 ppb per year in 1991 to 0.5 ppb per year in 1993. The cause for this decrease is unknown, but several mechanisms have been suggested, like reduction the of the use of fertilizers or stratospheric circulation changes induced by the Mt. Pinatubo eruption. Further, the growth rate increased again in 1995 to 0.6 ppb per year [*WMO* 1998]. N_2O is an inert gas with a lifetime of 120±30 years for which no destruction processes in the lower stratosphere are known. The only concurring loss process to reaction 3.18 is the photolysis of N_2O

$$N_2O \xrightarrow{h\nu} N_2 + O(^1D) \qquad (\lambda \leq 398 \text{ nm}) \qquad (3.20)$$

In fact, the N_2O oxidation (reaction 3.18) is only a secondary loss process for N_2O, accounting for 10% of the removal.

There is another significant, but highly variable source of NO_y[2] in the mesosphere and lower thermosphere due to solar proton events (SPEs), galactic cosmic rays (GCRs) and energetic electron precipitations (EEP), which produce atomic nitrogen through dissociations, predissociations or dissociative ionizations in collisions with N_2. The SPEs are the result of high-energy solar protons (up to 500 MeV) originating from solar flares bombarding the mesosphere and even the stratosphere. These events are sporadic and vary greatly in the energy spectrum [*Jackman et al.* 2000; *Jackman et al.* 2001; *Palmer et al.* 2001; *Randall et al.* 2001]. The GCRs are very high energy particles (up to a few GeV) originating from outside the solar system and are modulated by the 11-year solar cycle [*Nicolet* 1975]. The EEP from the outer trapping regions of the magnetosphere occurs essentially continuously modulated with the 27-day solar rotation period and the 11-year solar cycle with energies that range from 1 keV to 10-20 MeV [*Randall et al.* 1998; *Siskind et al.* 2000; *Callis* 2001]. The observed NO_x formed in the mesosphere and thermosphere flows, in part, into the stratosphere during winter and early spring, when there is downward atmospheric transport at mid- to high latitudes, descending to 20-25 km depending on the strength of the downward motion. For large descent rates of the air masses and in the absence of sunlight and horizontal mixing, an anomalous enhancement of NO_x in the middle stratosphere can be observed. In recent years, satellite observations have shown, that this is a fairly regular occurrence in the southern hemisphere polar stratospheric vortex during late winter and spring [*Randall et al.* 1998; *Randall et al.* 2001]. Still unclear is the importance of these

---

[2] NO_y is the sum of the reactive nitrogen species, i. e. $NO_y = NO + NO_2 + NO_3 + 2\,N_2O_5 + HNO_3 + ClONO_2 + HO_2NO_2 + BrONO_2 +$ aerosol nitrate

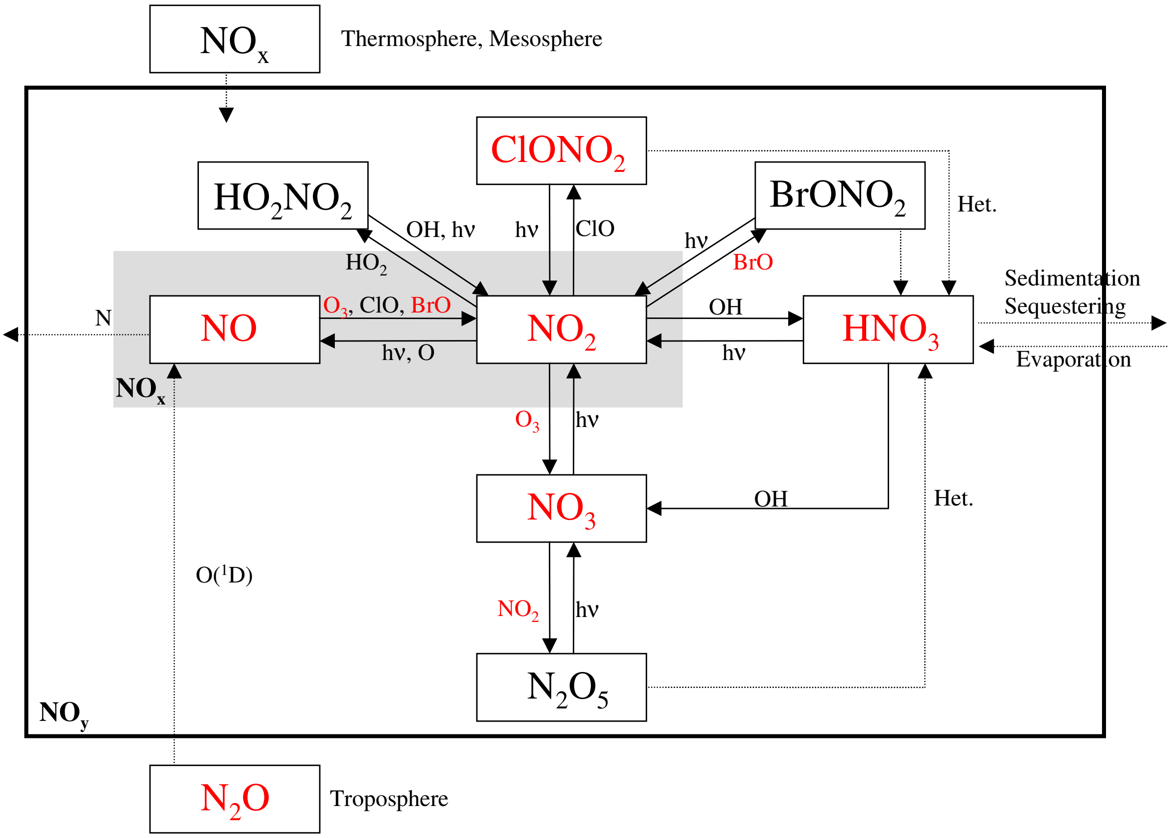

Figure 3.5: *Principle components, sources, sinks, and pathways of the NO_y family. The dotted lines indicate heterogenous pathways. The red marked species can be measured with the instruments onboard the LPMA/DOAS balloon gondola.*

NO_x enhancements to the overall stratospheric NO_x budget. Estimations of *Vitt and Jackman* [1996] and *Siskind et al.* [2000] suggest, that the peak values for the southern hemisphere of the EEP source are about 3-5% of the N_2O oxidations source, 11-18% of the peak SPE source and $25-30\%$ of the GCR source. These values are probably not representative for the northern hemisphere where NO_x enhancements are less apparent and have not been observed yet [*Siskind et al.* 1997; *Rinsland et al.* 1999].

During daytime, NO and NO_2 are in photochemical steady-state mostly via the reactions

$$NO + O_3 \longrightarrow NO_2 + O_2 \qquad (3.21)$$
$$NO_2 + O \longrightarrow NO + O_2 \qquad (3.22)$$

and the NO_2 photodissociation

$$NO_2 \xrightarrow{h\nu} NO + O \qquad (\lambda \leq 405 \text{ nm}) \qquad (3.23)$$

In addition, primary NO to NO_2 conversion can also proceed with oxidants other than O_3

$$NO + HO_2 \longrightarrow NO_2 + OH \qquad (3.24)$$

$$NO + RO_2 \longrightarrow NO_2 + RO \tag{3.25}$$

$$NO + ClO \longrightarrow NO_2 + Cl \tag{3.26}$$

In the stratosphere, the only relevant organic peroxy radical RO is CH_3O_2 which is formed in the oxidation of CH_4. This reaction scheme yields the following expression for the ratio of NO and NO_2

$$\frac{[NO]}{[NO_2]} = \frac{j_{NO_2} + k_{3.22}[O]}{k_{3.21}[O_3] + k_{3.24}[HO_2] + k_{3.25}[CH_3O_2] + k_{3.26}[ClO]} \tag{3.27}$$

with the photodissociation coefficient j_{NO_2} and the rate constants k for the various reactions. This ratio is close to one over most of the stratosphere during daytime, but increases rapidly above 40 km because of the increasing atomic oxygen densities.

With the beginning of the night, NO is rapidly converted to NO_2 as a result of diminishing photolysis of NO_2. NO_2 will react with ozone to build-up NO_3, an important nighttime nitrogen species,

$$NO_2 + O_3 \longrightarrow NO_3 + O_2 \tag{3.28}$$

During daytime NO_3 is rapidly destroyed by photolysis:

$$NO_3 \xrightarrow{h\nu} NO_2 + O \qquad (\lambda \leq 587\,\text{nm}) \tag{3.29}$$

$$\xrightarrow{h\nu} NO + O_2 \qquad (\lambda \leq 11080\,\text{nm}) \tag{3.30}$$

In a next step, NO_3 can react with NO_2 to form the reservoir species[3] N_2O_5

$$NO_3 + NO_2 \longrightarrow N_2O_5 \tag{3.31}$$

N_2O_5 is destroyed through collisional decomposition

$$N_2O_5 \xrightarrow{M} NO_3 + NO_2 \tag{3.32}$$

or through photolysis during the day

$$N_2O_5 \xrightarrow{h\nu} NO_3 + NO_2 \qquad (\lambda \leq 1252\,\text{nm}) \tag{3.33}$$

The fast photolysis of NO_2 together with the slow photolysis of N_2O_5 is responsible for the typical diurnal variation of NO_2. As a result of the beginning photolysis after sunrise, a strong decreases of the NO_2 concentrations is observed. In the course of the day, the NO_2 concentration is slowly increasing due to the N_2O_5 photolysis and finally in the evening the decreasing NO_2 photolysis causes a fast increase of the concentration. All in all, the NO_2 concentration shows a tilt 'tub shaped' diurnal variation (e.g. [*Otten* 1997]).

The latitudinal distribution of odd nitrogen shows increasing concentrations with increasing latitude in summer, while in winter the abundance decreases polewards of 40°N - 50°N [*Noxon* 1979; *Coffey et al.* 1981]. The tendency for NO_x to increase at high latitudes in summer can be understood in terms of atmospheric transport in a similar manner like for ozone. The observed

---

[3] so called, because these species do not destroy odd oxygen

decrease in the winter season at high latitude is the result of the combined effects of dynamics and chemistry. As a consequence of the reduced solar radiation during the polar winter, most of the nitrogen has formed reservoir species and the NO_x concentrations are smallest (*denoxification*). In addition, the formation of the so-called polar vortex (see section 3.9) prevents the poleward transport of NO_x-rich mid-latitudinal air.

The part NO_2 plays in the stratospheric ozone chemistry is ambiguous. On one hand, NO_2 participates in the ozone destroying NO_x cycle, on the other hand, it is involved in a number of reactions forming reservoir species.

$$NO_2 + OH \xrightarrow{M} HNO_3 \tag{3.34}$$

$$NO_2 + ClO \xrightarrow{M} ClONO_2 \tag{3.35}$$

$$NO_2 + BrO \xrightarrow{M} BrONO_2 \tag{3.36}$$

The catalysts can be released by photolysis

$$HNO_3 \xrightarrow{h\nu} OH + NO_2 \qquad (\lambda \leq 604 \text{ nm}) \tag{3.37}$$

$$ClONO_2 \xrightarrow{h\nu} Cl + NO_3 \qquad (\lambda \leq 735 \text{ nm}) \tag{3.38}$$

$$\xrightarrow{h\nu} ClO + NO_2 \qquad (\lambda \leq 1065 \text{ nm} \tag{3.39}$$

$$BrONO_2 \xrightarrow{h\nu} Br + NO_3 \qquad (\lambda \leq 861 \text{ nm}) \tag{3.40}$$

$$\xrightarrow{h\nu} BrO + NO_2 \qquad (\lambda \leq 1129 \text{ nm}) \tag{3.41}$$

or by reactions with OH

$$HNO_3 + OH \longrightarrow NO_3 + H_2O \tag{3.42}$$

Both, the formation and the decline of HNO_3 are slow processes, thus HNO_3 only has a small impact on the diurnal variation of NO_x. As a result of the long lifetime, HNO_3 builds up in large concentrations generally exceeding that of total NO_x. Another important production channel of HNO_3 is the heterogeneous hydrolysis of N_2O_5 occurring on the surfaces of stratospheric aerosols such as aqueous sulfate aerosol or ice

$$N_2O_5(g) + H_2O(s) \longrightarrow 2\,HNO_3(s) \tag{3.43}$$

It could be shown, that during polar winter HNO_3 becomes by far the dominant NO_y species. This could be explained by the participation of heterogeneous processes (reaction 3.43) which continuously converted N_2O_5 into HNO_3 and the inefficiency of the HNO_3 destruction processes (reactions 3.37 and 3.42). [e.g., *Wetzel et al.* 1995; *Toumi et al.* 1993]. This is an important prerequisite for the formation of the stratospheric ozone hole during polar spring, an issue being discussed in section 3.5.

Total reactive nitrogen, NO_y, has a very long photochemical lifetime in the middle and lower stratosphere. In the upper stratosphere NO_y is removed via the following reaction and the lifetime decreases

$$NO + N \longrightarrow N_2 + O \tag{3.44}$$

with N being produced by photolysis of NO. As N_2O is the major source of stratospheric NO_y, the distributions of NO_y and N_2O in the stratosphere are photochemically linked. Below 30 km, the mixing ratio of NO_y has been found to be almost linearly anti-correlated with N_2O [*Loewenstein et al.* 1993; *Kondo et al.* 1994; *Kondo et al.* 1996; *Keim et al.* 1997]. The slope of this lower stratospheric correlation is controlled by a combination of photochemistry and dynamics. At higher altitudes (30-70 km) the shape of the correlation curve is overwhelmingly influenced by the rapid loss of NO_y via reaction 3.44. At these altitudes the correlation becomes nonlinear as it approaches a maximum. Above $\sim$ 70 km, NO_y increases rapidly with altitude and is predominately composed of NO [*Michelson et al.* 1998]. NO is produced in the upper mesosphere and thermosphere by reactions of O_2 with $N(^2D)$, being generated by N_2 photolysis or dissociation through charged particles bombardment.

Conversely, deviations from the known correlation can be used to quantify the degree of irreversible NO_y removal through denitrification, the sedimentation of HNO_3 bearing PSC particles inside the winterly polar vortex (see section 3.5) [*Fahey et al.* 1990; *Sugita et al.* 1998; *Rinsland et al.* 1999; *Waibel et al.* 1999; *Popp et al.* 2001]. Horizontal mixing of subsided innervortex air with extravortex air masses can also lead to substantial changes in the NO_y/N_2O relationship, which might then be mistaken for denitrification [*Waugh et al.* 1997; *Kondo et al.* 1999; *Rex et al.* 1999]. The horizontal mixing of two distinct air masses at the same potential temperature level will lead to a mixture that will not lie on the original correlation. The correlation will now show distinct mixing lines on individual isentropic surfaces. Such a deviation from the initial correlation can only result from the descent and mixing, if the the correlation is nonlinear. Its occurrence is particulary likely if the correlation has a maximum in the middle stratosphere [*Plumb and Ko* 1992; *Waugh et al.* 1997]. The effect of descent and mixing can be distinguished from denitrification by taking into account additional compact and non-linear tracer-tracer correlations such as CH_4/N_2O [*Kondo et al.* 1999; *Rex et al.* 1999] or CO_2/N_2O [*Waugh et al.* 1997]. The departures from the compact O_3/N_2O or O_3/CH_4 relationship can even be used to quantify chemical ozone depletion [*Proffitt et al.* 1990; *Mueller et al.* 1996]. Recently *Plumb et al.* [2000] pointed out, that a single mixing line with unique endpoints is characteristic for the very special case of a single mixing event between two, and only two, air masses. In the presence of continuous mixing the tracer relationship can not be regarded as mixing lines between uniquely defined endpoints and the mixing line approach is likely to fail.

3.3 Halogen Chemistry

3.3.1 Chlorine Chemistry

Stratospheric ClO_x[4] has a variety of sources, all of which are associated with the release of Cl atoms from chlorinated organics by direct photolysis or OH (or $O(^1D)$) initiated oxidations chains. Among them, methyl chloride (CH_3Cl) is the only important source species which is produced by natural and artificial processes. The most prominent artificial sources are the chlorofluorcarbons (CFCs). CFCs are chemically inert gases which are photostable and have a low solubility in water. Thus the lifetime of CFCs in the troposphere is very large, varying from years to centuries and resulting in an almost uniform distribution in the troposphere. Accordingly, the

---

[4] $ClO_x=Cl+ClO+2\cdot Cl_2O_2$

CFCs reach the stratosphere, where they are converted to ClO_x. After the Montreal protocol (1987) and the amendments of Copenhagen (1989), and London (1992) the industrial production of CFCs was limited and finally stopped. The CFCs were replaced by partly halogenated substitutes (the so-called HCFCs), which are less stable and hence have a shorter tropospheric lifetime (for lifetimes and tropospheric concentrations of CFCs as well as HCFCs see *WMO* [1998]). The present tropospheric chlorine loading has already reached its maximum, with a present value of 3.6 ppb. It increased by $\sim$ 3%/year during the 1980's and is presently decreasing at a rate of $\sim$ 1%/year. The same does not hold true for the stratosphere, since the mean transport time between the troposphere and the mid-latitudinal, lower stratosphere is 3-4 years. A peak in the stratospheric chlorine burden is expected to occur between 1999 and 2001 depending on the altitude [*Engel et al.* 2000] and a decrease with the beginning of the 21st century. It should be emphasized that due to the declining temperatures in the stratosphere and due to changes in the bromine loading (section 3.3.2) of the stratosphere, this will not necessarily mean that stratospheric ozone values will recover by that time to pre ozone hole levels [*Shindell et al.* 1998; *Waibel et al.* 1999].

Once chlorine is released from the halocarbons, it undergoes a variety of reactions. Similar to NO_x, ClO_x is dominated by the rapid cyclic transformation between Cl and ClO, namely by the reactions

$$\begin{aligned} \mathrm{Cl + O_3} &\longrightarrow \mathrm{ClO + O_2} && (3.45)\\ \mathrm{ClO + NO} &\longrightarrow \mathrm{Cl + NO_2} && (3.46)\\ \mathrm{ClO + OH} &\longrightarrow \mathrm{Cl + HO_2} && (3.47)\\ \mathrm{ClO + O} &\longrightarrow \mathrm{Cl + O_2} && (3.48) \end{aligned}$$

and the photolysis of ClO

$$\mathrm{ClO} \xrightarrow{h\nu} \mathrm{Cl + O} \qquad (3.49)$$

The main temporary reservoir species for ClO_x are formed through the reactions with NO_2, HO_2 and CH_4

$$\begin{aligned} \mathrm{ClO + NO_2} &\xrightarrow{M} \mathrm{ClONO_2} && (3.50)\\ \mathrm{ClO + HO_2} &\longrightarrow \mathrm{HOCl + O_2} && (3.51)\\ \mathrm{Cl + HO_2} &\longrightarrow \mathrm{HCl + O_2} && (3.52)\\ \mathrm{Cl + CH_4} &\longrightarrow \mathrm{HCl + CH_3} && (3.53) \end{aligned}$$

The active forms are again regenerated from $ClONO_2$ and HOCl by photolysis,

$$\begin{aligned} \mathrm{ClONO_2} &\xrightarrow{h\nu} \mathrm{Cl + NO_3} && (\lambda \leq 735\,\mathrm{nm}) && (3.54)\\ &\xrightarrow{h\nu} \mathrm{ClO + NO_2} && (\lambda \leq 1065\,\mathrm{nm}) && (3.55)\\ \mathrm{HOCl} &\xrightarrow{h\nu} \mathrm{Cl + OH} && (\lambda \leq 500\,\mathrm{nm}) && (3.56) \end{aligned}$$

or from HCl[5] by reaction with OH

$$\mathrm{HCl + OH} \longrightarrow \mathrm{Cl + H_2O} \qquad (3.57)$$

---

[5] The absorption of HCl is limited to $\lambda \leq 205$ nm and hence its photolysis is extremely inefficient

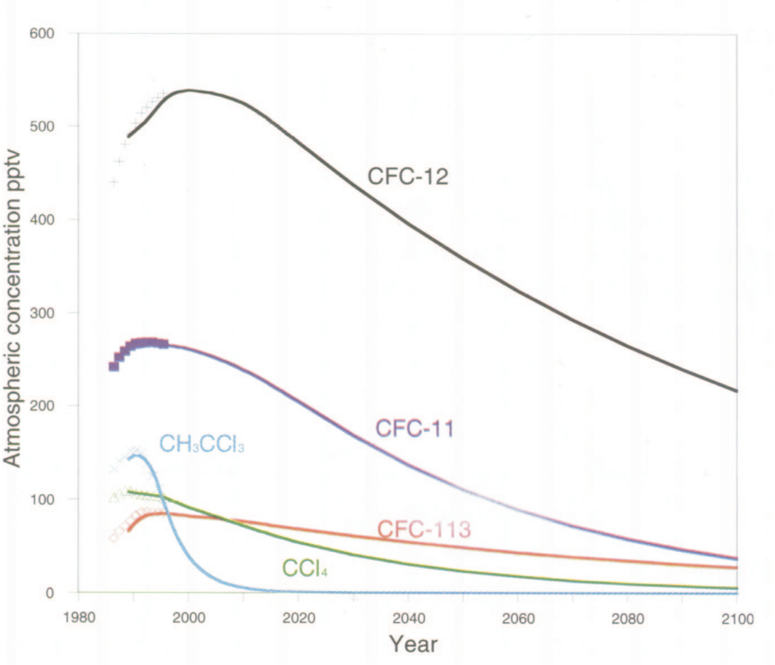

Figure 3.6: *Atmospheric concentrations of chlorofluorcarbons (CFCs) and chlorocarbons. The points show concentrations determined in background air at Mace Head, Ireland and the lines are projections of global average concentrations. Also shown are the predicted future concentrations extrapolated from the measurements using scenarios described in WMO [1998]. Adapted from Pyle et al. [1999].*

Among them, only the photolysis of HOCl is efficient. As a consequence, most of the chlorine is present in its inactive forms HCl and $ClONO_2$. A significant re-conversion to ClO_x occurs only between 30 km and 45 km, while for altitudes around 50 km nearly all chlorine resides as HCl [*Solomon* 1999]. As a result, the impact of chlorine on the stratospheric ozone content is restricted to the upper stratosphere (see Figure 3.2). For so-called ozone-hole conditions, heterogenous processes lead to an efficient release of active ClO_x and a subsequent ozone destruction (see section 3.5). For low temperatures, the activation of chlorine can also occur on liquid sulfate aerosols in mid-latitudes as well as in polar regions [*Webster et al.* 1998; *Solomon et al.* 1998].

3.3.2 Bromine Chemistry

As for ClO_x, the source of BrO_x[6] in the stratosphere is the decomposition of brominated organics (halons and methylbromide CH_3Br) by photolysis or reactions with OH and $O(^1D)$. Although, halons photodissociate more readily, but their tropospheric lifetime is still large [*WMO* 1998].

---

[6] BrO_x=Br+BrO

The dominant source is CH_3Br which provides more than 50% of the total bromine content [*Wamsley et al.* 1998]. CH_3Br is released by natural (biomass burning, oceans) and anthropogenic (agriculture, gasoline additive, etc.) processes and has a lifetime of 0.4 to 0.9 years [*WMO* 1998]. It is believed that the natural processes account for approximately 60-80% of the total CH_3Br burden. Measurements in air extracted from deep firn at two Antarctic locations indicate a steady trend by about 2 ppt from the midtwentieth century to present [*Sturges et al.* 2001]. Another important source of bromine are the manmade halons. Their production was discontinued as a result of the Montreal protocol. In contrast to CFCS the tropospheric concentrations are expected to continue to rise during the next years [*Fraser et al.* 1999] (see Figure 3.7). Less of the halons are emitted promptly as compared to CFCs, since they are almost exclusively used as fire extinguishing agents, but their tropospheric trend already decreases. Additional minor source gases are CH_2Br_2 and CH_2BrCl with atmospheric lifetimes of years and tropospheric mixing ratios of 1.1 and 0.14 ppt, respectively.

No stability has occurred yet for the stratospheric bromine levels and significant vertical gradients exists. The total stratospheric bromine content is currently assessed to 18-20 ppt and is the second most important halogen known to destroy stratospheric ozone. The impact of short-lived organic bromine species [*Dvortsov et al.* 1999] and the influx of inorganic bromine compounds from the troposphere to the stratosphere [*Ko et al.* 1997] is still an unsolved issue. Recent studies of *Fitzenberger et al.* [2000] and *Pfeilsticker et al.* [2000] suggest an inorganic Br influx of (3.1 ± 3.5) ppt from the free troposphere to the stratosphere.

The fast BrO/Br conversion is promoted by a number of reactions

$$\begin{aligned}
\mathrm{Br + O_3} &\longrightarrow \mathrm{BrO + O_2} && (3.58)\\
\mathrm{BrO + NO} &\longrightarrow \mathrm{Br + NO_2} && (3.59)\\
\mathrm{BrO + ClO} &\longrightarrow \mathrm{BrCl + O_2} && (3.60)\\
&\longrightarrow \mathrm{Br + OClO} && (3.61)\\
&\longrightarrow \mathrm{Br + ClOO} && (3.62)\\
\mathrm{BrO + O} &\longrightarrow \mathrm{Br + O_2} && (3.63)\\
\mathrm{BrO} &\xrightarrow{h\nu} \mathrm{Br + O} \qquad (\lambda \leq 515 \text{ nm}) && (3.64)
\end{aligned}$$

The main reservoir species are formed in reactions with NO_2, HO_2, ClO and CH_2O

$$\begin{aligned}
\mathrm{Br + NO_2} &\xrightarrow{M} \mathrm{BrONO_2} && (3.65)\\
\mathrm{BrO + HO_2} &\longrightarrow \mathrm{HOBr + O_2} && (3.66)\\
\mathrm{BrO + ClO} &\longrightarrow \mathrm{BrCl + O_2} && (3.67)\\
\mathrm{Br + HO_2} &\longrightarrow \mathrm{HBr + O_2} && (3.68)\\
\mathrm{Br + CH_2O} &\longrightarrow \mathrm{HBr + CHO} && (3.69)
\end{aligned}$$

The active species Br and BrO are again released by photolysis

$$\begin{aligned}
\mathrm{BrONO_2} &\xrightarrow{h\nu} \mathrm{Br + NO_3} \qquad (\lambda \leq 861\,\text{nm}) && (3.70)\\
&\xrightarrow{h\nu} \mathrm{BrO + NO_2} \qquad (\lambda \leq 1129\,\text{nm}) && (3.71)\\
\mathrm{HOBr} &\xrightarrow{h\nu} \mathrm{Br + OH} \qquad (\lambda \leq 578\,\text{nm}) && (3.72)\\
\mathrm{BrCl} &\xrightarrow{h\nu} \mathrm{Br + Cl} \qquad (\lambda \leq 546\,\text{nm}) && (3.73)
\end{aligned}$$

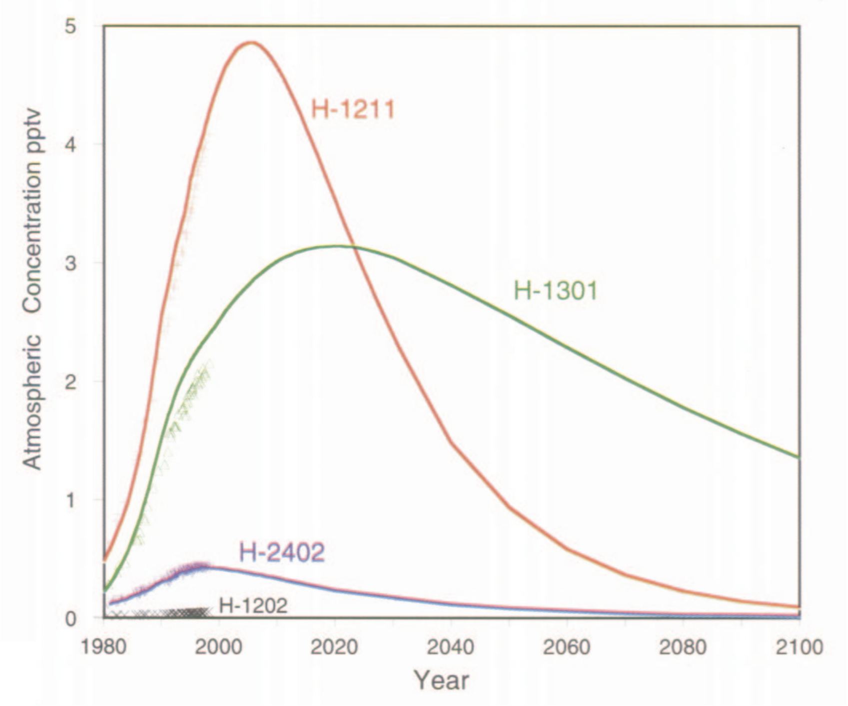

Figure 3.7: *Atmospheric concentrations of halons. The points show concentrations determined in background air at Cape Grim, Tasmania and the lines are projections of global average concentrations. Also shown are the predicted future concentrations extrapolated from the measurements using scenarios described in WMO [1998]. Adapted from Pyle et al. [1999].*

Because of the relatively long wavelength absorption of these reservoir species, their photodissociation is very efficient throughout the whole stratosphere. Moreover, Br atoms are rapidly regenerated from HBr via

$$\mathrm{HBr} + \mathrm{OH} \quad \longrightarrow \quad \mathrm{Br} + \mathrm{H_2O} \qquad (3.74)$$

As a result the partitioning of the total bromine content between active and inactive species is shifted more towards the active forms as compared to chlorine. Thus, bromine is more efficient in destroying ozone than chlorine.

Reaction 3.61 is the only relevant production channel of OClO in the lower stratosphere. However, the fast photolysis of OClO

$$\mathrm{OClO} \quad \xrightarrow{h\nu} \quad \mathrm{ClO} + \mathrm{O} \qquad (\lambda \leq 470 \text{ nm}) \qquad (3.75)$$

prevents the build-up of large concentrations during daytime. Nevertheless, OClO is an important indicator of chlorine activation and ozone depletion [e.g., *Solomon et al.* 1987; *Erle* 1999; *Fitzenberger* 2000; *Wagner et al.* 2001].

An important loss reaction of $\mathrm{BrONO_2}$ is the hydrolysis on the surface of polar stratospheric clouds or liquid sulphate aerosols. The hydrolysis together with other heterogenous reactions can lead to substantial chlorine activation on sulphate aerosols outside the polar vortex [*Erle et al.* 1998].

3.3.3 Iodine Chemistry

The source of atmospheric iodine is thought to be the fast photolysis of alkyl iodides such as CH_3I, CH_2I_2, C_2H_5I, CH_2ClI, CH_2IBr etc., with lifetimes ranging from 4 days (for methyl iodide, CH_3I) to only 5 minutes (for diiodomethane, CH_2I_2) [*WMO* 1998; *Carpenter et al.* 1999]. These species are released into the troposphere from supersaturated oceanic surface waters, where they are formed as metabolic byproducts of many marine algae species and phytoplankton [*Schall and Heumann* 1993; *Davis et al.* 1996]. Furthermore, biomass burning may emit some methyl iodide into the atmosphere [*Andreae et al.* 1996]. Significant anthropogenic sources are not known[7]. The main source for atmospheric iodine is thought to be methyl iodide. In the marine boundary layer mixing ratios in the range of 0.5 to 1 ppt were observed [*Blake et al.* 1997; *Carpenter et al.* 1999]. However, marine hot spots could exceed 1 ppt [e.g. *Yokouchi et al.* 1996]. Atmospheric data are scarce for iodocarbons other than CH_3I. In general, their mixing ratios are found to be in the range of 0.1 ppt or even smaller [*Schall and Heumann* 1993; *Yokouchi et al.* 1997; *Carpenter et al.* 1999], only for diiodomethane (CH_2I_2) mixing ratios of a few tenths of a ppt were found [*Schall and Heumann* 1993]. Changes in the ocean temperature or other factors could potentially trigger trends in the emissions of theses compounds, although not observed in measurements of CH_3I in polar firn air [*Sturges et al.* 2001].

Atmospheric iodine has received considerable attention through the detection of iodine oxide in the mid latitude marine boundary layer with mixing rations of up to 6 to 8 ppt [*Alicke et al.* 1999; *Allan et al.* 2000; *Hebestreit* 2001]. Observations of tropospheric IO in the polar regions have also been reported recently [*Wittrock et al.* 2000; *Frieß et al.* 2001]. In contrast, the situation for the stratosphere is still unclear. Ground based Fourier Transform measurements during solar occultation at Kitt Peak (40°N) [*Wennberg et al.* 1997] and balloon-borne DOAS solar occultation observations at mid and high latitudes [*Pundt et al.* 1998] yielded negative results for stratospheric iodine, with upper limits of $0.2(+0.3-0.2)$ ppt for the total column of iodine and 0.2 ± 0.1 ppt for lower stratospheric IO, respectively. However, more recently *Wittrock et al.* [2000] revealed large total atmospheric columns of IO from DOAS zenith sky measurements at Spitsbergen (79°N). Accounting for the observation geometry of the measurement and adopting a photochemical scheme for stratospheric iodine, they interpreted the observed variation of the IO column with solar zenith angle as an indication for the presence of stratospheric IO. Besides tropospheric IO contributing to their total atmospheric column, they concluded that stratospheric IO could occasionally be as large as $0.65-0.8\,(\pm0.2)$ ppt.

The short tropospheric lifetimes of the iodocarbons will generally preclude significant transport of these gases to the stratosphere. However, convective clouds can transport insoluble material very rapidly from low altitudes to the upper troposphere and even lower stratosphere, particularly in the tropics. A recent study of *Davis et al.* [1996] reports methyl iodide mixing ratios of some 0.1 ppt in the middle and upper free troposphere of the tropics and subtropics. Also *Murphy et al.* [1997; 1998; 2000] could detect some iodine tied to upper tropospheric aerosols with mixing ratios being as large as 1 ppt. Also, in analogy to recent findings on the budget

---

[7] One man-made iodocarbon, CF_3I, has been developed as a potential halon replacement, but there are no reports of its occurrence in the atmosphere

and chemistry of atmospheric bromine [*Fitzenberger et al.* 2000; *Pfeilsticker et al.* 2000], it can be speculated that at stratospheric entry level some iodine may already be present in gaseous inorganic rather than organic form. The sparse information, that is available until now, does not allow to draw a conclusive picture, it is likely that some iodine may enter the stratosphere.

The impact of iodine on the chemistry of stratospheric ozone has first been investigated by *Solomon et al.* [1994]. Based on the limited information available by then, they concluded that already 1 ppt of total reactive gaseous iodine would possibly dominate the ozone destruction in the lowermost stratosphere at mid- and high latitudes in winter. They suggested that interhalogen reactions can lead to rapid ozone loss:

$$\begin{aligned} X + O_3 &\longrightarrow XO + O_2 && (3.76)\\ I + O_3 &\longrightarrow IO + O_2 && (3.77)\\ XO + IO &\longrightarrow X + I + O_2 && (3.78)\\ &\longrightarrow XOO + I && (3.79)\\ &\longrightarrow IX + O_2 && (3.80) \end{aligned}$$

with X = Br or Cl.

The I/IO ratio determined by the above reactions is further influenced by the photolysis of IO

$$IO \xrightarrow{h\nu} I + O \qquad (\lambda \leq 500 \text{ nm}) \qquad (3.81)$$

and the reaction of IO with NO and possibly with OH

$$\begin{aligned} IO + NO &\longrightarrow I + NO_2 && (3.82)\\ IO + OH &\longrightarrow I + HO_2 && (3.83) \end{aligned}$$

The reservoir species HI, HOI and $IONO_2$ are formed through reactions with HO_2 and NO_2

$$\begin{aligned} IO + HO_2 &\longrightarrow HOI + O_2 && (3.84)\\ I + HO_2 &\longrightarrow HI + O_2 && (3.85)\\ IO + NO_2 &\xrightarrow{M} IONO_2 && (3.86) \end{aligned}$$

The active forms (I and IO) are reconverted by photolysis

$$\begin{aligned} HI &\xrightarrow{h\nu} I + H && (\lambda \leq 401 \text{ nm}) && (3.87)\\ HOI &\xrightarrow{h\nu} I + OH && (\lambda \leq 554 \text{ nm}) && (3.88)\\ IONO_2 &\xrightarrow{h\nu} IO + NO_2 && && (3.89)\\ &\xrightarrow{h\nu} I + NO_3 && && (3.90) \end{aligned}$$

The photolysis of HOI and $IONO_2$ is very fast and hence their daytime concentrations are small. The absorption of HI appears mainly in the short UV wavelength range, thus the photodissociation is inefficient and HI is mainly destroyed by reacting with OH

$$HI + OH \longrightarrow I + H_2O \qquad (3.91)$$

The reservoir species INO and INO_2 can be neglected primarily with the arguments given by *Solomon et al.* [1994]. The formation of both molecules is far to slow to compensate for the rapid photodissociation necessary for a significant accumulation in the stratosphere [e.g. *McFiggins et al.* 2000]. This chemical scheme suggests that IO is by far the dominant iodine species in the lower stratosphere during daytime [*Wennberg et al.* 1997; *Pundt et al.* 1998]. Therefore the efficiency in destroying ozone is much larger per molecule than that of Cl or Br.

A large difference of the iodine chemistry to those of chlorine and bromine is the formation and stability of the halogen dioxides OClO, OBrO, and OIO. The ab initio calculations of *Misra and Marshall* [1998] suggested a threshold for the photodissociation of OIO of 418 nm, while the visible absorption spectrum of OIO covers the wavelength range 480 - 660 nm [*Himmelmann et al.* 1996; *Cox et al.* 1999; *Ingham et al.* 2000]. The absorption of OIO below 480 nm is weak if occurring at all. Therefore rapid photolysis of OIO will not occur as it does for OClO or OBrO. However, the recent study of [*Allan et al.* 2001] found that OIO must largely predissociate to I + O_2 following the absorption. They computed extremely fast troposheric photolysis rates for 40°N mid-summer midday of $j=0.36\ s^{-1}$ or $2.2\ s^{-1}$ depending on the OIO cross section used. From laboratory studies it is known that OIO is formed either by the reactions of IO with ClO or BrO, or the self-reaction of IO

$$\begin{aligned} IO + ClO &\longrightarrow OIO + Cl && (3.92)\\ &\longrightarrow \text{products} && (3.93)\\ IO + BrO &\longrightarrow OIO + Br && (3.94)\\ &\longrightarrow \text{products} && (3.95)\\ IO + IO &\longrightarrow OIO + I && (3.96)\\ &\longrightarrow 2\,I + O_2 && (3.97)\\ &\longrightarrow I_2 + O_2 && (3.98)\\ &\longrightarrow I_2O_2 && (3.99) \end{aligned}$$

The reactive forms IO and I are possibly re-converted by reactions of OIO with NO and OH

$$\begin{aligned} OIO + NO &\longrightarrow IO + NO_2 && (3.100)\\ OIO + OH &\longrightarrow HOI + O_2 && (3.101) \end{aligned}$$

First observations of OIO in the marine boundary with mixing ratios up to 8 ppt have been reported [*Hebestreit* 2001; *Allan et al.* 2001]. *Hebestreit* [2001] found, that the major loss process during moderate pollution is the reaction with NO and estimated a lifetime of OIO of approx. 20 min, which is in reasonable agreement with the recent rate constant measurements for the reaction OIO + NO by *Allan et al.* [2001]. It's evident, that OIO may form a major gaseous species in the winter polar stratosphere, since the photolysis is weak and the NO concentrations are low as well, but ClO and BrO concentrations are high.

Finally, recent studies indicate that iodine oxides (IO and OIO) eventually self react and subsequently polymerize into larger and stable chains of iodine oxides [*Vogt et al.* 1999; *Hoffmann et al.* 2001]. Unfortunately, this is still subject of laboratory and field investigations and is not well understood yet. The complete photochemical scheme of the iodine chemistry can be found in Figure 3.8 and the table in Appendix A.

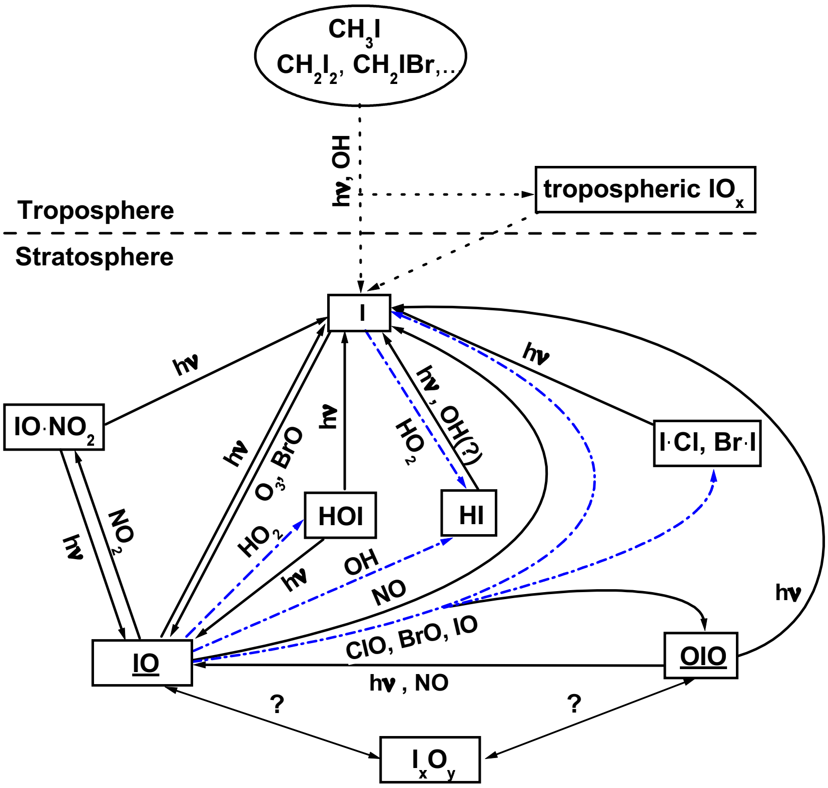

Figure 3.8: *Adopted photochemistry of stratospheric iodine. The dashed arrows indicate major stratospheric odd oxygen loss processes. For the discussion of the question marks see text.*

3.4 Basics of the Stratospheric Dynamics

The temperature field in the stratosphere arises from a balance between radiative and dynamical heating (or cooling). The major sources of radiative heating are provided by absorption of ultraviolet radiation mainly by ozone and to a lesser extend by molecular oxygen. Radiative cooling occurs through infrared emissions of CO_2, H_2O and O_3. Dynamical heating is caused by vertical (diabatic) motion, which occurs partly in response to the annual varying distribution of solar radiation. A substantial part of the vertical motion occurs in response to forces arising from the breaking and dissipation of so-called Rossby waves, planetary waves with a typical wavelength of the earth's diameter [*Andrews et al.* 1987].

The dominant features of the global stratospheric wind system are the strong mean zonal winds. They can be qualitatively understood as thermal winds. The tropical lower stratosphere and the equatorial tropopause region are cold in comparison to the summer polar stratosphere, which is subject to strong radiative heating. As a consequence of the temperature difference, a geostrophic wind forms, flowing in westerly direction. For the winter hemisphere, the situation is contradictory. Due to the low solar radiation, the winter polar stratosphere cools down and a westerly flow regime develops, a feature which is referred to as polar vortex. These strong zonal winds represent a barrier for the meridional mixing of polar with mid-latitudinal or tropical air masses. In contrast to the steady summerly zonal circulation, the winterly winds show irregular structures with waves, instabilities and significant meridional components. The reason for these disturbances is the propagation of tropospheric Rossby-waves into the stratosphere, an effect that is strongly suppressed by the easterly winds in the summer hemisphere [e.g. *Roedel* 2000]

Interhemispheric differences in the intensity, variability and persistence of the polar vortex occur. Due to the differences in the distribution of land and water surfaces on both hemispheres, the Rossby waves are more distinct in the northern hemisphere. Therefore, the northern winter is characterized by strong planetary-scale variability, large interannual variability and frequent occurrence of stratospheric sudden warmings. Sudden warmings are an important feature of the stratospheric meteorology of the northern hemisphere and several types can be distinguished. Major, midwinter warmings are strong warmings in January/February, resulting in a break-down of the polar vortex and a change of the circulation pattern. Minor warmings are warmings which can be very intense, too, but do not result in a change of the circulation. Minor warmings can also occur on the southern hemisphere. Canadian warmings occur in early winter. They are caused by a strengthening and a poleward shift of the Alëuten anticyclone. The final break-down of the polar vortex in spring and the change from winter to summer circulation is called final warming. The vortex is split up followed by a transport of the fragments to mid-latitudes [*Labitzke* 1999].

The gross feature of the annual mean stratospheric meridional circulation is well described by the Brewer-Dobson circulation. Based on global water vapor and ozone observations they suggested a circulation exhibiting rising motion only in the tropics, and descending motion at extra-tropical latitudes (sometimes referred to as 'Hadley cell') [*Brewer* 1949; *Dobson* 1956]. This classical picture of the Brewer-Dobson circulation has been significantly refined in recent years [*WMO* 1998]. The phenomenology of stratospheric transport and mixing reveals a number of distinct regions, depicted in Figure 3.9.

On the winter hemisphere, one has to distinguish between the 'surf zone' of mid-latitudes, which is largely stirred by Rossby wave breaking and the polar vortex being relatively undisturbed. The wave breaking process is associated with erosion of the vortex through detrainment of air from the vortex edge. This air is typically stretched out into filaments. The surf zone also possesses a subtropical edge, isolating the tropics from the surf zone. Erosion processes similar to those seen at the vortex edge are evident.

The summer hemisphere is generally characterized as a region of very weak meridional transport. The residual circulation field in the summer hemisphere has large uncertainties. Diabatic heating rates calculated from UKMO[8] analysis show during July atmospheric cooling (sinking air) poleward of 50° N below 20 km and atmospheric heating (rising air) poleward of 60° N between 25 km and 30 km in altitude. The altitude and latitude of the boundaries between heating and cooling differs for different analysis [*Cordero and Kawa* 2001]. The rising motion of air masses in summer at high latitudes leads to a summer to winter pole flow in the upper stratosphere and mesosphere.

In contrast to the region above, the region referred to as 'lowermost stratosphere' is bounded on its equatorward side by the tropopause rather than by the tropical stratosphere and it seems that the distinction between surf zone and vortex does not exist. The isentropic surfaces of the lowermost stratosphere intersect the mid-latitude tropopause and hence rapid isentropic exchange is possible.

It should be emphasized that a combination of radiative, chemical and dynamical processes

---

[8] United Kingdom Meteorological Office

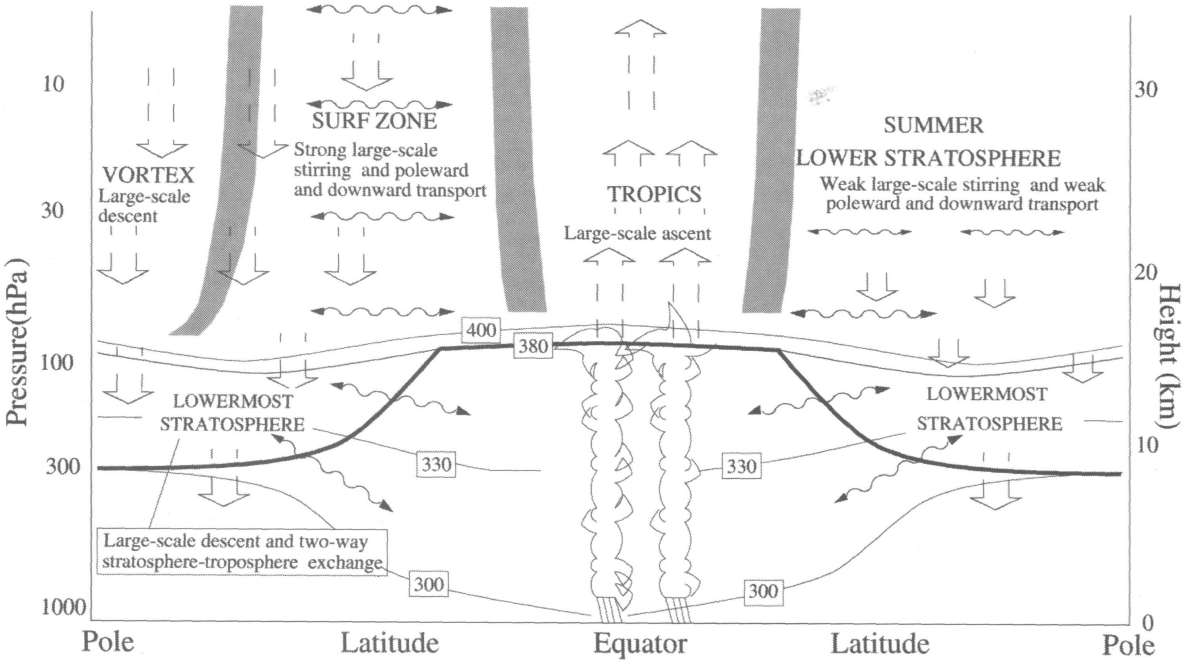

Figure 3.9: *Schematic of the principal regions of the lower stratosphere with distinct transport characteristics. Broad arrows denote the diabatic circulation, wavy arrows denote stirring along isentropic surfaces. The thick solid line is the tropopause. Isentropic surfaces are drawn as thin solid lines. Adapted from WMO [1998]*

maintains the global distribution of ozone and other species. Their distribution is a result of a balance between these processes. The nature of the balance may be different depending on location and season. It appears therefore that in addition to examining the chemistry, transport effects also need to be considered [*Rosenlof* 1999; *Cordero and Kawa* 2001]. Since species such as CH_4 or N_2O are relatively long lived in the (lower) stratosphere their variations can be used to examine transport processes.

3.5 'Ozone Hole' Chemistry

Since the discovery of the ozone hole over Antarctica in the early 1985 [*Farman et al.* 1985], the importance of chemical conversion of ozone related species in the presence of stratospheric particles has become increasingly obvious. These conversions ultimately result in the rapid build-up of active ClO_x (and BrO_x) catalysts which subsequently lead to ozone destruction. The dynamical prerequisite for polar ozone loss is the 'isolation' of radiatively cooled air in the lower stratosphere from exchange with the warmer air from lower latitudes to form a 'chemical containment vessel'. This isolation results from the formation of the winterly polar vortex. As described in section 3.9 the polar vortex is very strong and cold over the Antarctica, while it is generally warmer and more variable over the Arctic. Temperature, size and persistence of

Type	Backscatter signal	Depolarization	Shape	Composition
PSC 1a	weak	negligible	non-spheres	possibly NAT
PSC 1b	very weak	significant	spheres	possibly STS
PSC 2	large	strong	non-spheres	ice

Table 3.1: *PSC classification with respect to their optical properties [e.g., David et al. 1998].*

the polar vortex determine the rate of formation of particles referred to as Polar Stratospheric Clouds (PSCs).

Polar stratospheric clouds have been observed inside the polar vortex already for more than a century, at first without assigning a special meaning to them. Water, nitric acid, and sulfuric acid are expected to be the main constituents of PSCs. Further, these compounds can appear with various concentrations in the PSCs and finally PSCs can be liquid or solid. PSCs were often measured with LIDAR[9] instruments and thus were classified with respect to their optical properties of backscatter and depolarization (see table 3.1).

Type 1 PSCs were observed for temperatures above the freezing point of ice of 188 K [e.g. *McCormick et al.* 1982]. *Crutzen and Arnold* [1986] and *Toon et al.* [1986] supposed that these particles are formed by solid nitric acid trihydrate (NAT)[10], a theory that was supported by measurements of the vapor pressure over crystalline NAT surface [*Hansen and Mauersberger* 1988]. These particles, referred to as type 1a PSCs, can exist a few Kelvin above the freezing point of ice but below the NAT threshold of 196 K. Nitric acid dihydrate (NAD) could also form stable particles up to 2.5 K below the NAT threshold. Typical size distributions of type 1a particles show diameters in the range of 2 to 5 μm and concentrations below 0.1 cm^{-3} [*WMO* 1998]. However, HNO_3 containing particles with diameters around 15 μm were observed in the 1999/2000 Arctic winter stratosphere, believed to be NAT (or NAD) particles ('NAT-rocks') [*Fahey et al.* 2000]. An additional sub-group was identified by *Tsias et al.* [1999], labelled type 1a-enh (enhanced). These particles have a similar diameter as type 1a particles but higher concentrations.

Beside the solid NAT particles, liquid particles can appear for temperatures above the ice freezing point of ice [*Browell et al.* 1990]. These particles are called type 1b PSCs. They are typically found with diameters smaller than 1 μm and a concentration of 10 cm^{-3} [*WMO* 1998], where the particle volume is strongly increasing for temperatures of 3 to 4 K below the NAT threshold. These liquid particles are interpreted as supercooled ternary ($HNO_3/H_2SO_4/H_2O$) solutions (STS) with large H_2O:HNO_3 mole rates of 10 or above [*Schreiner et al.* 1999]. Sulfate aerosols may supercool before freezing and may take up large amounts of water and nitric acid from the gas phase forming STS.

Below the freezing point of ice, type 2 PSCs are formed. They were observed with concentrations between 10^{-4} and 10 cm^{-3} with diameters ranging from 2 to 25 μm [*WMO* 1998]. It is assumed that these particles mainly consist of ice, and hence may lead to dehydration[11] of the middle stratosphere and rehydration at the lower stratosphere [*Fahey et al.* 1990].

---

[9] LIDAR=Light Detection And Ranging

[10] NAT = $HNO_3 \cdot 3H_2O$

[11] Irreversible removal of water vapor from the gas phase by uptake of water by the particles and sedimentation to lower altitudes with subsequent evaporation.

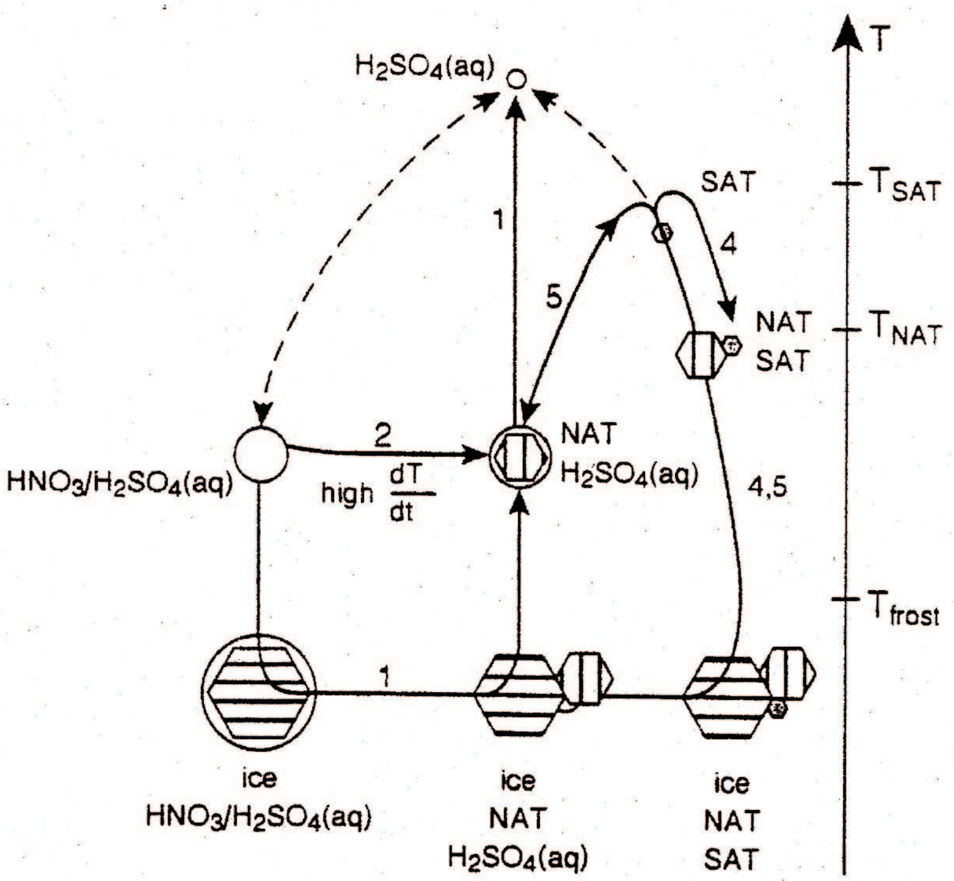

Figure 3.10: *Simplified scheme of the NAT formation. Liquid particles are indicated as circles, whereas solid particles are marked by hexagonals. Adapted from Carslaw et al. [1999]*

The different particle types do not necessarily occur in distinct PSCs. Liquid and solid particles can coexist in the same cloud [e.g. *Tsias et al.* 1999]. This was confirmed by balloon-borne in situ measurements of PSCs by *Voigt et al.* [2000]. They could also measure a H_2O:HNO_3 mole rate in a PSC layer with a stoichiometry of 3:1, which is the first direct evidence for the existence of NAT particles. However, the mechanisms for the formation of these solid type 1 PSCs is still under debate. A simplified scheme of the possible pathways is given in Figure 3.10.

The temperatures in the polar vortex on the southern hemisphere are usually very low and are often below the freezing point of ice for months. Thus, over Antarctica synoptic scale type 2 PSCs are often observed. However, the northern hemisphere polar vortex is warmer and less stable, with temperatures being below the freezing point of ice only for a few days or weeks. Nevertheless, mesoscale processes such as mountain-induced gravity waves can generate vertical air motions that are large enough to adiabatically cool the air parcels below the frost point of ice, leading to the formation of PSCs (lee-wave PSCs) [*Carslaw et al.* 1998; *Rivière et al.* 2000].

Two important prerequisites for a strong and long lasting ozone depletion leading to the formation of a ozone hole are the denoxificiation and the denitrification (see section 3.2). In the absence of sunlight, NO_x is converted to N_2O_5 and via hydrolysis to HNO_3 (denoxification), thus the conversion of active chlorine, ClO_x, to $ClONO_2$ through reaction 3.50 is suppressed. The sedimentation to lower altitudes of large PSC particles containing HNO_3 leads to an irreversible removal of NO_y at higher altitudes (denitrification) and to an extended ozone depletion during polar spring.

Once formed, the PSCs provide the surface for a number of heterogenous reactions converting the chlorine reservoir species HCl and $ClONO_2$ to the more reactive species Cl_2 and HOCl (*chlorine activation*):

$$\begin{align}
\mathrm{ClONO_2(g) + HCl(s)} &\longrightarrow \mathrm{Cl_2(g) + HNO_3(s)} \tag{3.102}\\
\mathrm{ClONO_2(g) + H_2O(s)} &\longrightarrow \mathrm{HOCl(g) + HNO_3(s)} \tag{3.103}\\
\mathrm{HOCl(g) + HCl(s)} &\longrightarrow \mathrm{Cl_2(g) + H_2O(s)} \tag{3.104}
\end{align}$$

Other important reactions additionally involving bromine are

$$\begin{align}
\mathrm{BrONO_2(g) + HCl(s)} &\longrightarrow \mathrm{BrCl(g) + HNO_3(s)} \tag{3.105}\\
\mathrm{BrONO_2(g) + H_2O(s)} &\longrightarrow \mathrm{HOBr(g) + HNO_3(s)} \tag{3.106}\\
\mathrm{HOBr(g) + HCl(s)} &\longrightarrow \mathrm{BrCl(g) + H_2O(s)} \tag{3.107}
\end{align}$$

As soon as the sunlight returns at the beginning of the polar spring, the photochemically unstable compounds Cl_2 and HOCl rapidly photodissociate

$$\begin{align}
\mathrm{Cl_2} &\xrightarrow{h\nu} \mathrm{2Cl} && (\lambda \leq 495\ \mathrm{nm}) \tag{3.108}\\
\mathrm{HOCl} &\xrightarrow{h\nu} \mathrm{Cl + OH} && (\lambda \leq 500\ \mathrm{nm}) \tag{3.109}\\
& \tag{3.110}
\end{align}$$

These processes and the absence of NO_x (preventing the $ClONO_2$ formation) causes a strong enhancement of the active catalysts ClO_x (and BrO_x) in the range of up to 100 times the concentration that is usually observed. The major contribution to ozone loss under these conditions has been shown to be the ClO-dimer cycle [*Molina and Molina* 1987]

$$\begin{align}
\mathrm{ClO + ClO} &\xrightarrow{M} \mathrm{Cl_2O_2} \tag{3.111}\\
\mathrm{Cl_2O_2} &\xrightarrow{h\nu} \mathrm{Cl + ClO_2} \tag{3.112}\\
\mathrm{ClO_2} &\xrightarrow{M} \mathrm{Cl + O_2} \tag{3.113}\\
2 \times (\mathrm{Cl + O_3} &\longrightarrow \mathrm{ClO + O_2}) \tag{3.114}\\
\text{net:} \quad \mathrm{2\,O_3} &\longrightarrow \mathrm{3\,O_2} \tag{3.115}
\end{align}$$

The dimer Cl_2O_2 is thermally unstable and the photodissociation of the dimer requires sunlight. Consequently, this cycle is most effective under cold, sunlit conditions. This cycle is thought to be responsible for most of the ozone loss in Antarctica. In the warmer Arctic a larger portion of the ozone loss may be driven by the ClO_x/BrO_x cycle [*McElroy et al.* 1986]:

$$\begin{align}
\mathrm{ClO + BrO} &\longrightarrow \mathrm{Cl + Br + O_2} \tag{3.116}\\
&\longrightarrow \mathrm{BrCl + O_2} \tag{3.117}
\end{align}$$

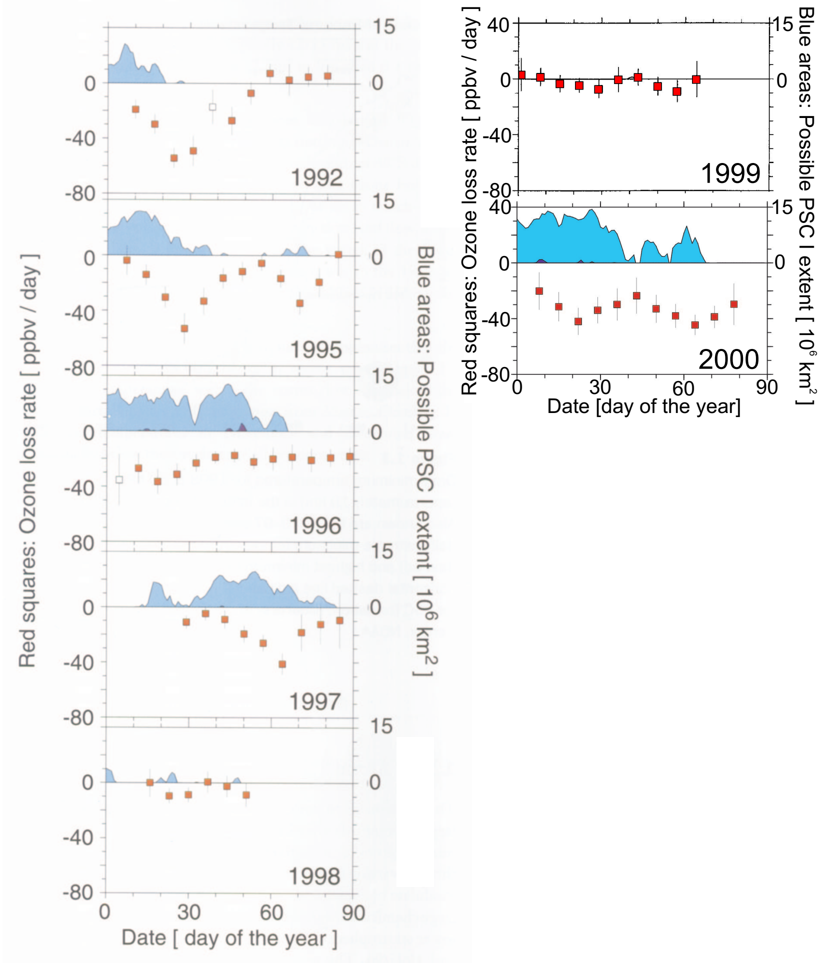

Figure 3.11: *Ozone loss rates at altitudes of about 18-20 km (475 K level) deduced for the winters 1992 to 2000. Also shown is the area of the northern hemisphere below the PSC existence temperature. Adapted from Pyle et al. [1999], EORCU [2000], and Schulz et al. [2001].*

$$\mathrm{BrCl} \xrightarrow{h\nu} \mathrm{Br} + \mathrm{Cl} \qquad (\lambda \leq 546\ \mathrm{nm}) \qquad (3.118)$$

$$\mathrm{Cl} + \mathrm{O_3} \longrightarrow \mathrm{ClO} + \mathrm{O_2} \qquad (3.119)$$

$$\mathrm{Br} + \mathrm{O_3} \longrightarrow \mathrm{BrO} + \mathrm{O_2} \qquad (3.120)$$

$$\text{net:} \quad 2\,\mathrm{O_3} \longrightarrow 3\,\mathrm{O_2} \qquad (3.121)$$

This cycle is also effective at higher temperatures and even in darkness.

With the beginning of the renoxification in early polar spring, i.e. the conversion of nitrogen reservoir species to NO_x, the ozone depletion slows down and finally ends. If denitrification occurs, the ozone depletion continues until the break-down of the polar vortex and the subsequent mixing with ozone-rich mid-latitudinal air. As already mentioned earlier, the Antarctic polar vortex is strong and cold and persists very long, resulting in a strong and horizontally large extended ozone depletion. The vertical distribution of the ozone loss is extremely non-uniform. While between 13 and 20 km ozone is often totally destroyed, it remains essentially unaffected in the lower and upper stratosphere [e.g. *Hoffmann et al.* 1997]. The Arctic polar vortex is on average 10 K warmer than in Antarctica, hence reducing the potential for PSC formation strongly In addition, the Arctic vortex is characterized by a large year to year variability. While for some Arctic winters, the chemical ozone depletion is close to zero, there are also winters with an ozone depletion (Figure 3.11) comparable to the Antarctic ozone hole.

Further, the late-winter/springtime ozone levels show a clear decreasing trend for both poles over the past decade [*Newman et al.* 1997]. For Antarctica, with its stable winterly conditions and cold temperatures (below the 195 K threshold for PSC formation), the ozone level is directly linked to the halogen loading in the stratosphere. The same processes that lead to the ozone loss in Antarctica certainly occur in the Arctic, but the meteorology of the northern hemisphere is more variable, with large interannual differences in the strength of the vortex and the extent of low temperatures. Thus, the evolution of the ozone level in the Arctic not only depends on the future trend of the halogen loading but also on the climate change.

Chapter 4

Methodology

4.1 Absorption Spectroscopy

Absorption Spectroscopy is based on the identification and quantization of atmospheric trace gases by the specific absorption features and strength of each absorber. Most common for the spectroscopic detection of stratospheric trace gases is the use of extraterrestrial light sourcessuch as the sun, the moon, or even stars, while for tropospheric measurements mainly artificial light sources such as lamps or lasers are used. For the stratospheric trace gas measurements presented here, the well established differential optical absorption spectroscopy (DOAS) technique was used with the sun as light source. The following sections briefly discuss the main characteristics of the solar spectrum and the principles of absorption spectroscopy. In subsection 4.1.3 the DOAS technique will be introduced and at the end of this chapter an overview of various effects arising from the shortcomings of the measurement technique will be given.

4.1.1 Solar Spectrum

The spectrum of the solar radiation ranges from the X-rays over UV radiation far into the range of radio waves. On the earth's surface only radiation with wavelengths larger than 300 nm can be observed. Below 300 nm the earth's atmosphere is impervious for radiation due to the strong absorptions of ozone (Hartley band) and the subsequent O_2, N_2 and O absorption. In the infrared wavelength region (μm up to some mm) the solar spectrum is disturbed by strong absorption bands of H_2O and CO_2 (Figure 4.1).

Nearly all of the solar radiation is emitted from the so called *photosphere*, a thin layer of a few hundred kilometers with strong gradients of temperature and pressure (increasing towards the inner layers). Thus the emission of layers with different temperatures superpose. The strong continuous absorption by the outer layers of the radiation emitted by the inner layers and the strong decrease of the temperature, results in a thin layer only contributing to the emission spectrum. This continuous spectrum is overlaid by a large number of absorption lines (*Fraunhofer lines*) originating from higher layers of the photosphere. The analysis of the Fraunhofer lines gives information about the chemical composition and the physical conditions such as pressure and temperature of the solar atmosphere. It could be shown that at least 63 elements occur in

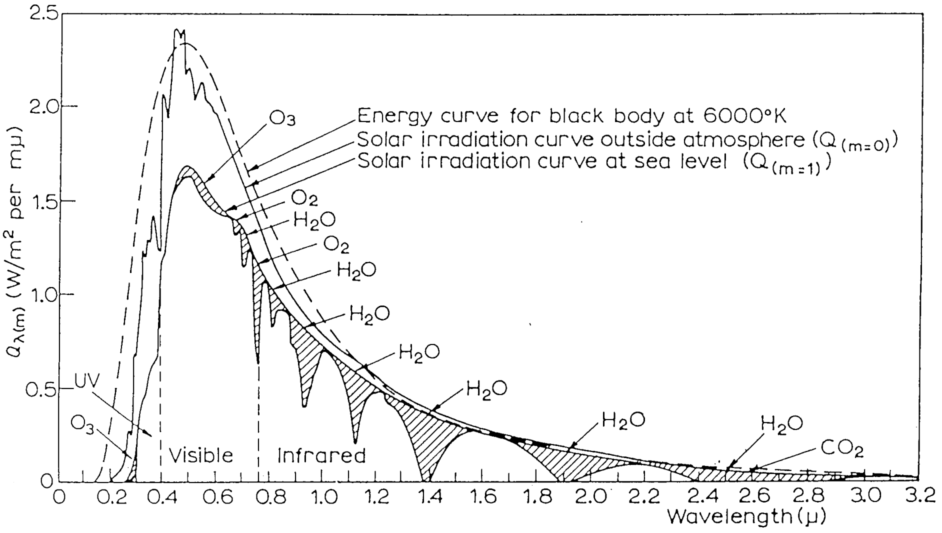

Figure 4.1: *Solar spectrum outside the earth's atmosphere and at sea level. The dashed line indicates the spectrum of a black body for $T = 6000$ K. The grey shaded areas mark the absorptions of O_3, H_2O, CO_2, and O_2. Adapted from Steinegger [1999].*

the solar photosphere, with H and He being the most frequent.

An important characteristic of the sun is the decrease of the observed intensity from the center towards the edge of the solar disk, referred to as *solar center to limb darkening*. This effect is due to the fact, that the observed radiation emitted from the disk center (hence emitted perpendicular to the surface of the sun) originates from geometrically deeper and thus hotter layers than radiation emitted from the edge (emitted under an angle θ to the normal of the surface) (see Figure 4.2). The relative intensity variation as a function of the emission angle θ can be approximated by a linear approach [*Scheffler and Elsässer* 1974]:

$$I_\lambda(\theta)/I_\lambda(0) = (1 + \beta_\lambda \cos\theta)/(1 + \beta_\lambda) \tag{4.1}$$

with the limb darkening coefficient β_λ. For the wavelength range 370 nm to 1000 nm, β_λ varies between 5 and 0.6, respectively (see Figure 4.3). The emission angle θ is directly connected to the distance r from the disk center:

$$r/R = \rho = \sin\theta \tag{4.2}$$

where R is the radius of the solar disk.

The intensity $I_\lambda(\theta)$ can be estimated by the *Eddington-Barbier approximation*:

$$I_\lambda(\theta) \simeq S_\lambda(\tau_\lambda = \cos\theta) \tag{4.3}$$

This means, that the intensity emitted under an angle θ can be approximated by the so-called source function S for the optical depth $\tau_\lambda = \cos\theta^1$. Assuming a so-called local thermodynamical

---

[1] For a given geometrical depth t (relative to an arbitrary zero) the optical depth τ can be calculated by $\tau_\lambda(t) = \int_{-\infty}^{t} \alpha_\lambda \, dt$. The absorption coefficient α_λ can include continuous as well as line absorption.

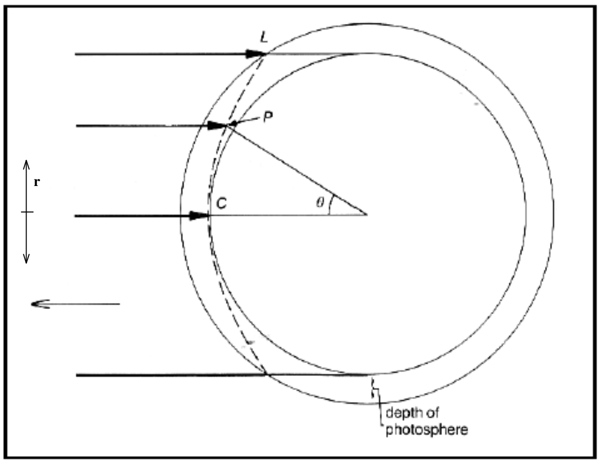

Figure 4.2: *Schematic drawing of the intensity variation along the solar disk. Radiation emitted from the disk center (C) originates from deeper layers of the photosphere than radiation emitted from a point a distance r away from the disk center (e.g. point P or L).*

steady state, the source function is given by the Kirchhoff-Planck function for the local temperature at the optical depth τ_λ. Integration of equation 4.3 over the half sphere yields the irradiance of the whole sun

$$E_\lambda \simeq \pi S_\lambda(\tau_\lambda = 2/3) \tag{4.4}$$

The Eddington-Barbier approximation is valid for all wavelengths and hence it can also be used for wavelengths where strong line absorption occur. The depression of an absorption line is given by

$$r(\theta) = \frac{I(\theta) - I_l(\theta)}{I(\theta)} \tag{4.5}$$

where $I_l(\theta)$ and $I(\theta)$ are the intensities measured at the line center and outside the line, respectively[2]. With the Eddington-Barbier approximation, and neglecting the small differences between the wavelengths of the line center and the surrounding continuum, equation 4.5 can be written as

$$r(\theta) = \frac{S_\lambda(\tau = \cos\theta) - S_\lambda(\tau_l = \cos\theta)}{S_\lambda(\tau = \cos\theta)} \tag{4.6}$$

The optical depth τ_l in the line center includes the continuous and the additional line absorption. Thus, the radiation at wavelengths with line absorption originates from higher layers compared to the continuous radiation. For very strong line absorptions, $S_\lambda(\tau_l = \cos\theta)$ is given by the Kirchhoff-Planck function for the temperature of the sun's surface and , hence, cannot get zero. The effect of solar center to limb darkening also occurs at wavelengths with line absorption, but with a different dependency on θ compared to the continuum. The consequence is a variation of the depression of the absorption lines across the solar disk, e.g. for metals the depression increases with r while for hydrogen lines a decrease is observed.

---

[2] The high density of absorption lines in the solar spectrum makes the definition of the continuum difficult

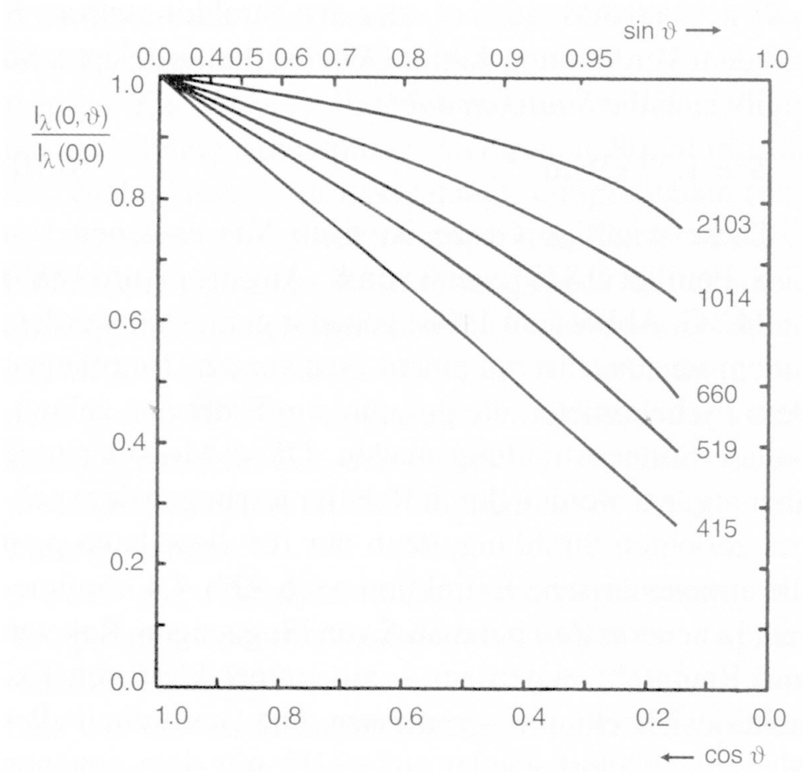

Figure 4.3: *Center to limb darkening as a function of* $\cos\theta$ *for different wavelength (numbers at the end of the lines). Adapted from Unsöld and Baschek [1999]*

The total solar irradiance E is obtained by integrating the spectral intensity over the half sphere and all wavelengths, taking into account the solar center to limb darkening and the Fraunhofer lines. The irradiance at the mean distance d_{earth} (= 1 AU[3] of the earth from the sun) is given by the *solar constant* S:

$$S = ER^2_{sun}/d^2_{earth} = 1.37\,\mathrm{kWm}^{-2} \tag{4.7}$$

with the solar radius $R_{sun} = 696000$ km. Interpreting the solar irradiance in the sense of Stefan-Boltzmann's law, an effective temperature T_{eff} of 5780 K can be assigned to the sun.

The solar irradiance is modulated by the *sun spot cycle* (also referred to as cycle of solar activity) with a period of 11 years. Sun spots are dark areas with an effective temperature of about 3500 K and a diameter of $\sim 10^4$ km. The occurrence of the sun spots is accompanied by several other phenomena such as flares, prominences, and plages , which overcompensate the reduced radiation of the sun spots. The net effect on the irradiance is a slight increase of about 0.1 - 0.2%[4]. The observation of sun spots also allows to determine the duration of the

---

[3] Astronomical unit (AU) = 149598000 km

[4] For certain wavelength ranges the effect is much larger, e.g. between 140 nm and 150 nm the variation is in the order of 100%.

sun's rotation, a cycle of approximately 27 days which determines the periodicity of several geophysical phenomena.

The mean energy per time and area available on the upper side of the earth's atmosphere is given by the solar radiance S times the disk area of the earth divided by the surface of the earth:

$$S_0 = S\,\frac{\pi R_{earth}^2}{4\pi R_{earth}^2} = S/4 \tag{4.8}$$

This mean radiance S_0 in combination with the conversion of energy in the system earth-atmosphere drives most of the relevant atmospheric processes. S_0 shows a significant temporal variation as a result of quasi-periodical changes of certain parameters controlling the trajectory of the earth [*Milankovitch* 1920].

4.1.2 Beer-Lambert Law

The extinction of light with an intensity $I(\lambda)$ passing through an infinitesimally thin layer dl given by[5]

$$dI(\lambda) = -I(\lambda)\,(\alpha_s(\lambda) + \alpha_a(\lambda))\,dl \tag{4.9}$$

where $\alpha_s(\lambda)$ and $\alpha_a(\lambda)$ are the scattering and absorption coefficients, respectively. The sum of $\alpha_s(\lambda)$ and $\alpha_a(\lambda)$ is called extinction coefficient. Neglecting inelastic Raman scattering, the coefficient $\alpha_s(\lambda)$ includes Mie scattering on aerosols and droplets and molecular Rayleigh scattering:

$$\alpha_s(\lambda) = \sigma_{Rayl}(\lambda)\cdot n_{Rayl} + \sigma_{Mie}(\lambda)\cdot n_{Mie} \tag{4.10}$$

with σ is the scattering cross section and the density of the scatterers n . Taking into account all absorbers i with a non-zero absorption cross section σ_i at wavelength λ and their density n_i, the absorption coefficient $\alpha_a(\lambda)$ can be written as

$$\alpha_a(\lambda) = \sum_i \sigma_i(\lambda)\cdot n_i \tag{4.11}$$

Integration of equation 4.9 along the light path L then yields the *Beer-Lambert law*

$$I(\lambda) = I_0(\lambda)\,\exp\left\{-\int_L (\alpha_s(\lambda) + \alpha_a(\lambda))\,dl\right\} \tag{4.12}$$

Introducing the optical density (or depth) τ

$$\tau(\lambda) = -\ln\,\left\{I(\lambda)/I_0(\lambda)\right\} \tag{4.13}$$

equation 4.12 can be expressed as

$$I(\lambda) = I_0(\lambda)\,\exp\left\{-\tau(\lambda)\right\} \tag{4.14}$$

---

[5] The emission of light and the scattering of light from an arbitrary direction in the direction of the considered light beam is neglected.

4.1.3 Differential Optical Absorption Spectroscopy (DOAS)

Applying the Beer-Lambert law directly to a measured intensity I at a certain wavelength, the determination of the absorption of a species requires exact knowledge of the extraterrestrial intensity I_0[6] and the extinction due to Rayleigh and Mie scattering. Also the absorptions of other species at this wavelength have to be separated.

However, if a whole spectrum is measured instead of only a single wavelength, the *Differential Optical Absorption Spectroscopy (DOAS)* technique can be applied and the above limitations can be avoided [*Platt et al.* 1979; *Platt* 1994]. The DOAS technique is based on the fact, that Rayleigh and Mie scattering only weakly vary with wavelength, while the molecular absorption cross sections usually consist of narrow absorption bands (often overlaid by a broad continuum). The absorption cross section σ of a certain species is now split into a low and a high frequency component σ_b and σ'[7], respectively (for illustration see Figure 4.4):

$$\sigma = \sigma_b + \sigma' \tag{4.15}$$

Accordingly, the same can be done for the absorption coefficient α_a. Equation 4.12 can then be rewritten as:

$$I(\lambda) = I_0(\lambda)\, \exp\left\{ - \int_L (\alpha_s(\lambda) + \alpha'_a(\lambda) + \alpha_{a,b})\, dl \right\} = I'_0(\lambda)\, \exp\left\{ - \int_L \alpha'_a(\lambda)\, dl \right\} \tag{4.16}$$

According to equation 4.13 the *differential optical density* τ' can be defined as

$$\tau'(\lambda) = - \ln \left\{ I(\lambda)/I'_0(\lambda) \right\} = \int_L \alpha'_a(\lambda)\, dl = \sum_i \tau'_i(\lambda) \tag{4.17}$$

By a very simple approach, broad band structures can be removed by high pass filtering. In practice, a measured, so-called *Fraunhofer reference spectrum* $I_0(\lambda)$[8] is used and the broad band components $\int_L (\alpha_s(\lambda) + \alpha_{a,b}(\lambda))dl$ are approximated by a polynomial.

Assuming constant pressure and temperature along the light path, the differential absorption cross section $\sigma'_{i,a}(\lambda)$ for species i is independent of the light path and the differential optical density τ'_i can be expressed as

$$\tau'_i(\lambda) = \int_L \alpha'_a(\lambda)\, dl = \sigma'_{i,a}(\lambda) \cdot \int_L n_i\, dl = \sigma'_{i,a}(\lambda) \cdot SCD_i \tag{4.18}$$

with the *slant column density* SCD. This is the quantity that can be obtained from the technique described here.

The above assumption of constant pressure and temperature is usually not fulfilled, a serious shortcoming of this technique (to be discussed in more detail in section 4.1.4).

---

[6] In fact, few measurements of the extraterrestrial solar spectrum exists (e.g., the quasi-extraterrestrial measurement of Kurucz[1984]), but the adaption of these measurements to the used instrument (instrumental resolution, wavelength scale etc.) introduces large errors.

[7] σ' is often called differential absorption cross section

[8] For I_0 the measurement with the smallest absorptions is used. The absorber amounts in the Fraunhofer reference spectrum have to be determined with other methods.

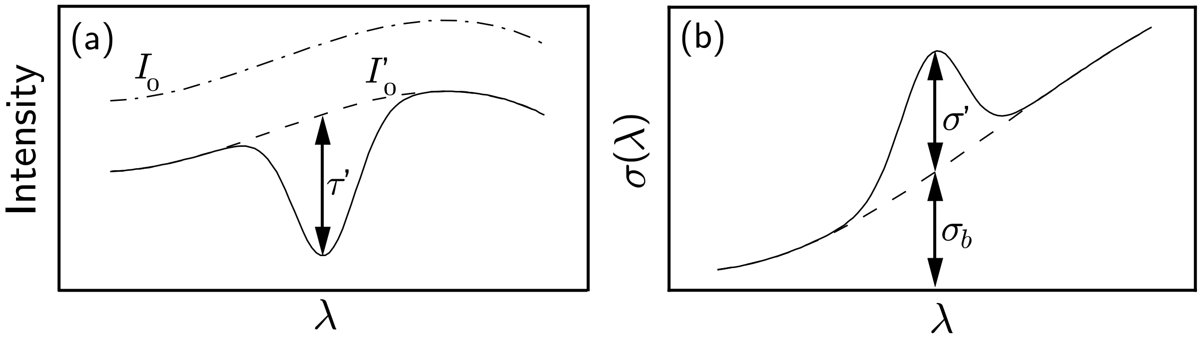

Figure 4.4: *Illustration of the DOAS principle. The absorption cross section σ can be split into a broad band σ_b and a narrow band component σ'.*

Spectral Retrieval

The incoming solar light is spectrally analyzed by a spectrograph and recorded by a detector (here a photodiode array). Thus, the instrumental properties of the spectrograph have to be accounted for. The limited resolution of the spectrograph can be described by a convolution of $I(\lambda)$ with the instrument function H[9]

$$I^*(\lambda) = I(\lambda) \circ H = \int I(\lambda - \lambda') \cdot H(\lambda')\, d\lambda' \tag{4.19}$$

The instrument function combines the effects of the width of the entrance slit and the properties of the grating. Usually the instrument function is measured with narrow emission lines from low pressure lamps (e.g. from mercury). During the recording by the detector, the wavelength range is mapped to N discrete pixels i, each integrating the light in a wavelength interval $\Delta\lambda(i)$ with center wavelength $\lambda(i)$

$$I(i) = \int_{\lambda(i)-\Delta\lambda(i)/2}^{\lambda(i)+\Delta\lambda(i)/2} I^*(\lambda')\, d\lambda' \tag{4.20}$$

For simplification, the symbol I is used again, mistakes are avoided by using the different arguments i and λ.

The logarithm of the intensity $I(i)$ can now be written as

$$\ln I(i) = \ln I_0(i) - \left(\sum_{j=1}^{m} SCD_j \cdot \sigma_j(i) + R(i) + N(i) + A(i) \right) \tag{4.21}$$

The molecular absorptions of the m species are described by their convoluted cross section $\sigma_j(i)$ The broad band components of the extinction like Mie and Rayleigh scattering are represented by $R(i)$. The noise of the detector and the photon noise are described by $N(i)$ and any structures caused by the spectrograph or the detector are summarized by $A(i)$.

The goal of the spectral retrieval is the determination of the slant column densities SCD_j. Therefore, an appropriate model function $F(i)$ is used for the approximation of $\ln I(i)$.

$$F(i) = \ln I_0(i, d_{0,0}, d_{1,0}...) - \left(\sum_{j=1}^{m} a_j \cdot \sigma_j(i, d_{0,j}, d_{1,j}...) + P_r(i) \right) \tag{4.22}$$

---

[9] Usually, the instrument function H depends on the wavelength

The cross sections $\sigma_j(i)$ and $I_0(\lambda)$ are input data to the fitting procedure. The m scaling factors a_j and the additional parameters $d_{x,j}$ are the output. The resulting a_j then correspond to the slant column densities of the different species. The broad band structures are approximated by a polynomial $P_r(i)$ of degree r

$$P_r(i) = \sum_{h=0}^{r} c_h (i - i_c)^h \tag{4.23}$$

with the center pixel i_c of the considered spectral range i_c. To account for possible differences in the wavelength-pixel mapping of $I_0(i)$ and $\sigma_j(i)$ compared to $I(i)$, the reference spectra $I_0(i)$ and $\sigma_j(i)$ can be shifted and squeezed, expressed by the spectral alignment parameters $d_{j,k}$. The parameter $d_{j,0}$ describes a shift of the wavelength-pixel mapping by $d_{j,k}$ pixels. If $d_{j,1} \neq 0$ the spectrum is additionally linearly squeezed, i.e., pixel i is shifted by $d_{j,1}(i - i_c)$ pixels. For $k > 1$ the parameter $d_{j,k}$ describes a squeeze of higher order, usually not used. The misalignment of the different spectra is a result of different measurement conditions (e.g., temperature, pressure), an effect that cannot completely be avoided.

The spectral analysis consists of a *linear least square fit* to derive the parameters a_j and c_h and a *non-linear Levenberg-Marquardt fit* to determine the $d_{j,k}$'s in a sense that

$$\chi^2 = \sum_{i=0}^{n} \left(\frac{\ln I(i) - F(i)}{\epsilon_i} \right)^2 \tag{4.24}$$

is minimized, where n is the number of pixels of the spectral range used for the retrieval and ϵ_i is the measurement error of the i'th diode resulting from the noise of the diodes and the photon noise. Usually, a constant measurement error is assumed for all diodes, i. e. $\epsilon_i = \epsilon = const.$

The fitting procedure starts with a linear least-square fit with initial values for $d_{j,k}$. The retrieved values for a_j and c_h are then input parameters for a Levenberg-Marquardt fit. Only one iterative step is performed and new values for $d_{j,k}$ are obtained, which in turn are used for a new call of the linear fit. The result of the linear fit is again used for a new call of the non-linear fit etc.. If one of several stopping conditions for the Levenberg-Marquardt fit is fulfilled (e.g., convergence of the fit, represented by very small changes of χ^2 from one step to another) the whole procedure is aborted.

The least-square solution for the linear fit can be found analytically either given by a normal equation [*Albritton et al.* 1976; *Stutz* 1996] or by the singular value decomposition [*Press et al.* 1986]. However, the fitting procedure will only give the best possible results including correct errors if the model function is well suited to describe the measurement intensities. If the model lacks relevant processes or if processes are inaccurately described the fit results will be inaccurate. Further prerequisites for the validity of this fitting procedure are independence of the measurement errors ϵ_i, linear independence of the σ_j, and measurement errors with a mean of zero and a finite variance.

The linear least-square procedure also gives an estimate of the measurement error $\hat{\sigma}$ per pixel. If ϵ_i is not explicitly given, $\hat{\sigma}$ is used as measurement error instead. A significant overestimation of the real measurement errors ϵ_i (estimated by considering the different noise contributions) is an indication of an inadequate model function or of systematical errors. Further, it can be shown, that $\hat{\sigma}$ is equal to the root-mean-square (rms) of the remaining residual $Res(i) = \ln I(i) - F(i)$, if the number of pixels n contained in the spectral fitting range is clearly larger than the number of linear parameters of the fitting procedure (sum of the number of cross sections and the degree of the polynomial).

The statistical errors of the parameters a_j and c_h are given by the diagonal elements of the *covariance matrix* Θ. Further, the covariance matrix allows to derive the so-called *correlation coefficients* C_{vw}:

$$C_{vw} = \frac{\Theta_{vw}}{\sqrt{\Theta_{vv}\Theta_{ww}}} \tag{4.25}$$

The correlation matrix is normalized in a way that all diagonal elements have a value of one, with all other elements between ±1. The correlation coefficients C_{vw} are a measure of the correlation of the v'th parameter with the w'th, whereas a value near $\|1\|$ indicates a large correlation of two parameters.

In contrast to the linear least-square fit the Levenberg-Marquardt method is an iterative numerical procedure. The reference spectra $\sigma_j(i)$ and $\ln I_0(i)$ are aligned to $\ln I(i)$ by varying d_{jk} in order to minimize χ^2. Therefore $\sigma_j(i)$ and $\ln I_0(i)$ have to be recalculated for the new wavelength-pixel mapping. This is achieved by cubic spline interpolation. The Levenberg-Marquardt method also gives an estimate of the errors Δd_{jk} of the alignment parameters. As the alignment parameters are input data for the linear fit, the errors Δd_{jk} will influence the results of the linear fit. To investigate this dependence, a numerical method is used. A spectrum is calculated consisting of the various reference spectra scaled, shifted and squeezed according to the results of the linear fit. In addition, the spectrum is shifted and squeezed as given by the errors Δd_{jk}. The results of the linear fit performed with the original spectrum and the spectra additionally shifted and squeezed allows to infer the errors of the linear parameters caused by the errors of the alignment. Assuming an independence of this error and the statistical error of the linear fit, the total error is obtained by Gaussian error propagation.

Commonly, the remaining residual structure $Res(i) = \ln I(i) - F(i)$ of the procedure doesn't consist of pure noise. A pure noise spectrum is characterized by completely independent pixel intensities (equivalent to structures with a width of one pixel), which is a necessary prerequisite for the validity of the linear fit. A real residuum, however, often shows groups of neighboring pixels, which change their intensities simultaneously in a random way, an indication of interdependencies of the pixels. In general, the dependencies of the measurement errors are described by the variance-covariance matrix. If this matrix is known, the linear fit procedure can be extended in a way that the calculation of the fit results also considers the error interdependencies [*Albritton et al.* 1976]. If the variance-covariance matrix is not known, a numerical method can be used to examine the influence of these residual structures on the fit results [*Stutz and Platt* 1996]. Smoothing of a pure noise spectrum with a running mean results in a spectrum similar to the residual that is normally found. The variance-covariance matrix can then easily be calculated by varying the width of the smoothing filter until the the width of the generated structures are of the same order as the width of the residual structures. However, this variance-covariance matrix has to be recalculated for every measured spectrum, a very time-consuming and uncomfortable procedure. Therefore, empirical correction factors for errors given by the fitting procedure were inferred based on Monte Carlo simulations[10]. Smoothed noise spectra with a running mean of different width were added to absorption lines with different half-widths. For all combinations of filter widths and half widths of the absorption lines a linear fit was performed. The resulting variations of the fit parameters allow to derive correction factors, which can be found in *Stutz and Platt* [1996]. Instead of smoothed noise spectra, this analysis can be performed with residual

---

[10] It can be shown that only the fit errors need to be corrected, the changes of the scaling factors are small

spectra calculated by cyclic displacement of the channels of the residual of the fitting procedure [*Hausmann et al.* 1997].

The occurrence of stable residual structures is not captured by this method. Systematical errors can bias the fitting procedure in two ways. First, these residual structures can be misinterpreted as molecular absorptions and second, the fitting errors are mis-estimated. A method to investigate the impact of spectral artifacts on the DOAS evaluation can be found in *Hausmann et al.* [1999]. However, this method is restricted to irregular, non-reproducible structures generated within the optical setup, while it is not valid in the presence of reproducible structures.

An important quantity for the characterization of the quality of trace gas measurements is the theoretical *detection limit*. The detection limit can be defined as the lowest measurable value for a fit parameter a_j or as the smallest detectable average optical density $\overline{D}_{limit}$. For the latter, an average optical density $\overline{D_j}$ of a reference spectrum is defined. $\overline{D_j}$ is given by three times the standard deviation of the reference spectrum $\sigma_j(i)$:

$$\overline{D_j} = 3 \cdot \left[\frac{1}{n-1} \sum_{i=1}^{m} \left(\sigma_j(i) - \overline{\sigma}_j \right)^2 \right]^{1/2} \tag{4.26}$$

As the estimation of the detection limit requires time-consuming Monte-Carlo calculations, only the linear problem is considered (neglecting the uncertainties of the wavelength-pixel mapping) allowing to simplify the derivation of the detection limit. Defining the detection limit $\overline{a}_j$ as the value of a_j with a relative error of 0.5 yields

$$\overline{a}_j = 2 \cdot \sqrt{\Theta_{jj}} \tag{4.27}$$

This still requires the calculation of the covariance matrix Θ (i.e. the evaluation has to be performed). Simplification of the expression for Θ allows to derive an expression for the smallest detectable average optical density $\overline{D}_{limit}$ [*Stutz* 1996]:

$$\overline{D}_{limit} \approx \widehat{\sigma} \frac{6}{\sqrt{n-1}} \tag{4.28}$$

with the mean noise of the measurement $\widehat{\sigma}$ and the number of pixels n. Thus for a given noise level (which has to be estimated) and number of pixels used for the evaluation, the theoretical detection limit can be obtained. However, if an evaluation is performed, equation 4.27 can be used instead for the calculation of the detection limit.

In this Ph. D. thesis the software packages *WinDOAS* [*Van Roozendael and Fayt* 2000] and *MFC* [*Gomer et al.* 1995] were used for the spectral evaluation, both providing the described fitting procedure. An additional feature of *WinDOAS* is the correction of instrumental stray light[11] by additionally including an intensity offset $O(i)$. On the left side of equation 4.21, $\ln I(i)$ is then replaced by $\ln(I(i) - O(i))$, with the intensity offset $O(i)$ described by a polynomial of a degree of up to two. The coefficients of this polynomial are additional parameters of the non-linear fit. Another important feature of *WinDOAS* is that it allows to fix single scaling parameters a_j in the model function $F(i)$. The Fraunhofer reference spectrum $I_0(i)$ is also scaled with a fitting parameter that is determined by the linear fit. It is obvious, that the scaling parameter for the Fraunhofer reference spectrum hat to be set to one. A shortcoming of *WinDOAS* is,

---

[11] Instrumental stray light is caused by reflections inside the spectrograph ,e.g, by light of higher orders or the zero order of the grating

that it does not consider the error propagation of the uncertainties of the non-linear parameters for the estimation of the errors of the linear parameters, as the program package *MFC* does. Another advantage of *MFC* is the existence of a script language, but neither fixing of certain scaling factors nor the utilization of an intensity offset is included. Both programs do not correct the calculated errors for interdependencies of the measurement errors.

4.1.4 Sources of Errors

The precision of the results is determined by the statistical fluctuations (due to noise) of the measured intensities. If the described procedure works well and the prerequisites are fulfilled, the precision is given by the estimated errors of the scaling parameters. However, there exists several effects, that are inaccurately treated by the above described model function. Thes effects result in systematical errors which contribute to the accuracy of the measurement. Also, the estimation of the fitting error will be distorted. For some effects, it is possible to derive a correction term which can be included in the model function. In this subsection a brief but not complete overview will be given of the various effects arising from instrumental shortcomings as well as from physical deficits of the model function.

Noise

The instrument noise is an important parameter for the fitting procedure. The statistical errors of the fitted parameters (and the theoretical detection limit) are determined by the noise of the measurement. The total noise is given by the root-mean-square sum of the individual noise contributions.

The *photoelectron noise* σ_{ph} is due to the statistical distribution of the number of electrons generated by the photons illuminating the detector pixel. Since the number of photoelectrons is distributed according to Poisson statistics, the noise is given by

$$\sigma_{ph} = \sqrt{\alpha \cdot N_{e,total}} \tag{4.29}$$

with the maximum number of photo electrons $N_{e,total}$[12] and the degree of saturation α.

The *dark-current noise* σ_d of a single detector photodiode is due to the statistical variance of the dark current across the junction. The dark current electrons are Poisson distributed and thus for an integration time t and a mean number of dark current electrons per time[13] n the noise is obtained by

$$\sigma_d = \sqrt{n \cdot t} \tag{4.30}$$

In addition, there are 3 constant contributions to the total noise. The *preamplifier noise* σ_{pr} is determined by the current and voltage noise of the preamplifier. The *readout noise* σ_r of a diode pixel results from switching electronic capacities and finally there is the *analog-to-digital converter noise* σ_{adc}.

These noise contributions sum up quadratically to the total noise σ_{tot}:

$$\sigma_{tot} = \sqrt{\sigma_{ph}^2 + \sigma_d^2 + \sigma_{pr}^2 + \sigma_r^2 + \sigma_{adc}^2} \tag{4.31}$$

---

[12] $N_{e,total}$ can be calculated from the semiconductor capacity and the charge voltage

[13] The mean number of dark current electrons depends strongly on the temperature of the photodiode.

For short integration times, the photoelectron noise can usually be neglected. Accordingly, the total noise consists of a constant contribution depending on the number of readouts and the signal dependant photoelectron noise. For large α's the total noise is dominated by the photoelectron noise, thus the (theoretical) signal-to-noise ratio can only be increased by co-adding subsequently recorded spectra.

Solar I_0 Effect and Saturation

The DOAS technique assumes, that the a measured spectrum can be well approximated by a model function F given by the following expression:

$$F(\lambda) = \ln\left\{I_0(\lambda) \circ H\right\} - \left(\sum_{j=1}^{m} a_j \cdot (\sigma_j(\lambda) \circ H) + P_r(\lambda)\right) \tag{4.32}$$

with the I_0 is the Fraunhofer reference spectrum, σ_j is the cross sections of species j, a_j is the scaling factor for species j, P_r is a polynomial and H is the instrument function. The intensity $I^*(\lambda)$ measured with a spectrograph with a certain resolution is given by

$$I^*(\lambda) = I(\lambda) \circ H = \int I_0(\lambda) \cdot e^{\sum_{j=1}^{m} SCD_j \cdot \sigma_j(\lambda) + R(\lambda)} H(\lambda - \lambda')\, d\lambda' \tag{4.33}$$

where R represents the broad band components. For simplification, only one species will be considered and the broad band components will not be taken into account so that the above formula can be rewritten as:

$$\ln I^*(\lambda) = \ln\left\{\int I_0(\lambda) \cdot e^{SCD \cdot \sigma_j(\lambda)} H(\lambda - \lambda')\, d\lambda'\right\} \tag{4.34}$$

It is obvious, that this cannot be transformed easily to an expression similar to equation 4.32. Only in the case of $I_0(\lambda)$=const and $SCD \cdot \sigma_j(\lambda) \ll 1$ the model function is able to properly describe equation 4.34. For atmospheric applications, the second assumption is usually fulfilled and as shown by [*Huppert* 2000] with numerical tests for the example of a BrO DOAS evaluation, the impact of a non-constant $I_0(\lambda)$[14] can be assumed to be small. Nevertheless, this can lead to disturbing residual structures. For some absorbers or for very long light pathes, however, the assumption of a small optical density is not valid and equation 4.34 can not be linearized. This is often called *saturation*

The above restrictions can be avoided and, when using a so-called I_0 *corrected cross section* $\sigma_{I_0}(\lambda)$ instead of $\sigma(\lambda) \circ H$ [*Johnston* 1997]. The I_0 corrected cross section is defined straightforward as

$$\sigma_{I_0}(\lambda) = \frac{1}{S} \frac{\left(I_0(\lambda) e^{S \cdot \sigma(\lambda)}\right) \circ H}{I_0(\lambda) \circ H} \tag{4.35}$$

with a given initial slant column density S. I_0 corrected cross section can be obtained directly with the programm *WinDOAS*, if a high-resolution cross section of the absorber and of the solar spectrum is available. However, as shown by *Huppert* [2000], the use of convoluted cross section results in larger residual structures compared to cross sections recorded with the instrument itself. Thus, for this Ph. D. thesis, mainly cross sections (especially for strong absorbers) recorded

---

[14] The Fraunhofer reference spectrum $I_0(\lambda)$ has large structures and is highly non-constant.

with the same instrument in the laboratory were used for the spectral retrieval. To account for the I_0 *effect*, in same cases, a I_0 correction was calculated and added to the measured cross section[15]. This I_0 correction is obtained by the difference of a I_0 corrected cross section and a conventionally convoluted cross section.

Temperature Dependence of the Absorption Cross Sections

Most of the UV/vis absorption cross sections show a strong dependence on the temperature, i.e. the absolute value and the shape of the cross section change with varying temperature. This effect will certainly influence the results of the spectral evaluation. On the one hand the temperature dependence can directly affect the retrieval of the fit parameters a_j's due to the change of the absolute value, on the other hand the variation of the shape can result in large residual structures. Hence, if the temperature dependence of the cross section of a strong absorber is not taken into account, the detection of an underlying weak absorbers may be impossible. In this Ph. D. thesis, the cross sections of NO_2, O_3, O_4, H_2O, OClO, IO, and OIO were used. Therefore their temperature (and pressure) characteristics will be briefly discussed.

The temperature dependence of the NO_2 cross section in the visible wavelength range is subject of a number of studies [e.g., *Davidson et al.* 1988; *Amoruso et al.* 1993; *Harwood and Jones* 1994; *Harder et al.* 1997; *Kirmse et al.* 1997; *Pfeilsticker et al.* 1999]. The NO_2 cross section can be described as a bell-shaped envelope with a superimposed differential structure. The temperature effect on the cross section is a slight broadening of the envelope with increasing temperature while the amplitude of the superimposed fluctuations decrease. The effect of the broadening of the envelope is largest for the red tail of the cross section, while for the UV the envelope does not change significantly with temperature. Thus, no (or only a very small) dependence of the integrated cross section on the temperature is found. The differential cross section shows an asymmetric increase with decreasing temperatures. The differential cross section has a smaller negative temperature coefficient in the neighborhood of the peaks and a larger positive coefficient in the region in between. The magnitude of this temperature variation depends on the wavelength and the spectral resolution of the instrument used. For a resolution of 0.54 nm (FWHM) the differential cross section at 448 nm increases almost linearly with decreasing temperature by almost 40% from 298 K to 200 K [*Pfeilsticker et al.* 1999]. In addition, at very high spectral resolution the differential cross section shows large change with changing pressure. For the low spectral resolution used in this work, this effect is not of importance.

A detailed study of the temperature dependence of the ozone absorption in the Chappuis band (410 nm - 760 nm) can be found in *Burkholder and Talukdar* [1994] or more recently for the wavelength range 230 - 850 nm by *Voigt et al.* [2001]. Near the peak of the Chappuis band (550 nm - 650 nm) the cross section varies slightly ($< 1\%$), while at wavelengths outside the peak it decreases with decreasing temperature. For example, at 420 nm the absorption cross section decreases by 40% when the temperature decrease from 298 K to 220 K. A pressure dependence is not observed.

The temperature (and pressure) dependence of the O_4 absorption was investigated by *Osterkamp* [1997] and *Pfeilsticker et al.* [2000]. They found that the shape of the O_4 collisional pair

---

[15] The measured cross section has then to be calibrated with the convoluted cross section taken from the literature

absorption cross section[16] does not depend on pressure or temperature, while the magnitude of the cross section decreases by about 11% when increasing the temperature by 50 K.

The H_2O absorption shows large variations for changing temperatures and pressures. For H_2O most of the individual rotational-vibrational lines of the electronic transitions are identified and the absorption line properties are known [*Rothman et al.* 1996]. Accordingly, the H_2O cross section can be calculated for different pressures and temperatures. Since the stratospheric absorption of H_2O is rather small this pressure and temperature effect is of secondary importance here.

The cross section of OClO consists of a series of absorption band overlaid with a broad continuum. The continuum is decreases when the temperature is lowered, while the individual bands get sharper and the peak cross sections increases [*Wahner et al.* 1987; *Komminga et al.* 1999].

The studies of *Laszlo et al.* [1995], *Harwood et al.* [1997], *Hoelscher and Zellner* [2000], *Bloss et al.* [2001] showed that the IO absorption cross section consists of a broad continuum with a superimposed vibronic band structure. The temperature dependence of the cross section has been investigated for the (4-0) band (at 427.7 nm) by *Harwood et al.* [1997] and *Hoelscher and Zellner* [2000]. They found that the differential cross section is independent of temperature for temperatures between 200 K and 300 K. As the continuum cross section is believed to be temperature-independent, an overall independence of the cross section on temperature is assumed. In contrast, the more recent study of *Bloss et al.* [2001] showed, that the differential cross section exhibits a negative temperature dependence.

Measurements of the OIO absorption cross section can be found in *Himmelmann et al.* [1996], *Cox et al.* [1999], *Ingham et al.* [2000] and *Allan et al.* [2001]. Unfortunately, no studies concerning the temperature dependence are available till now.

Since the light measured by the spectrograph has traversed several atmospheric layers with different temperatures, the absorption seen in the spectrum is a composition of absorptions taking place at different temperatures. Accordingly, the residual of the fitting procedure can be decreased by using several cross sections (in general two or three cross sections were used) recorded at different temperatures for the same species [*Sanders* 1996]. The temperatures used should cover the atmospheric temperature range crossed by the measured light. To reduce the linear dependencies of the various cross sections for one species it can be useful to orthogonalize them. Nevertheless, the determination of the SCDs for species with temperature dependent absorption is problematic. The cross section for a certain temperature can only be inadequately approximated by a linear combination of two (or three) cross sections at different temperatures. As shown by *Frieß* [2000] this can lead to significant violations of the conservation of the norm. In this Ph. D. thesis, the SCDs were evaluated by using only one cross-section for this specific species. This cross section should be recorded for a temperature similar to the mean stratospheric temperature. However, to account for the temperature dependence of the absorptions of other species, two or more cross sections for different temperatures were used.

---

[16] The concentration of the collisional complex $O_2{\cdot}O_2$ ($=O_4$) can not independently be measured, thus preventing to derive the equilibrium constant of the complex. As a consequence, the collisional pair absorption cross section (given by the product of the absorption cross section and the equilibrium constant) is used instead an absorption cross section.

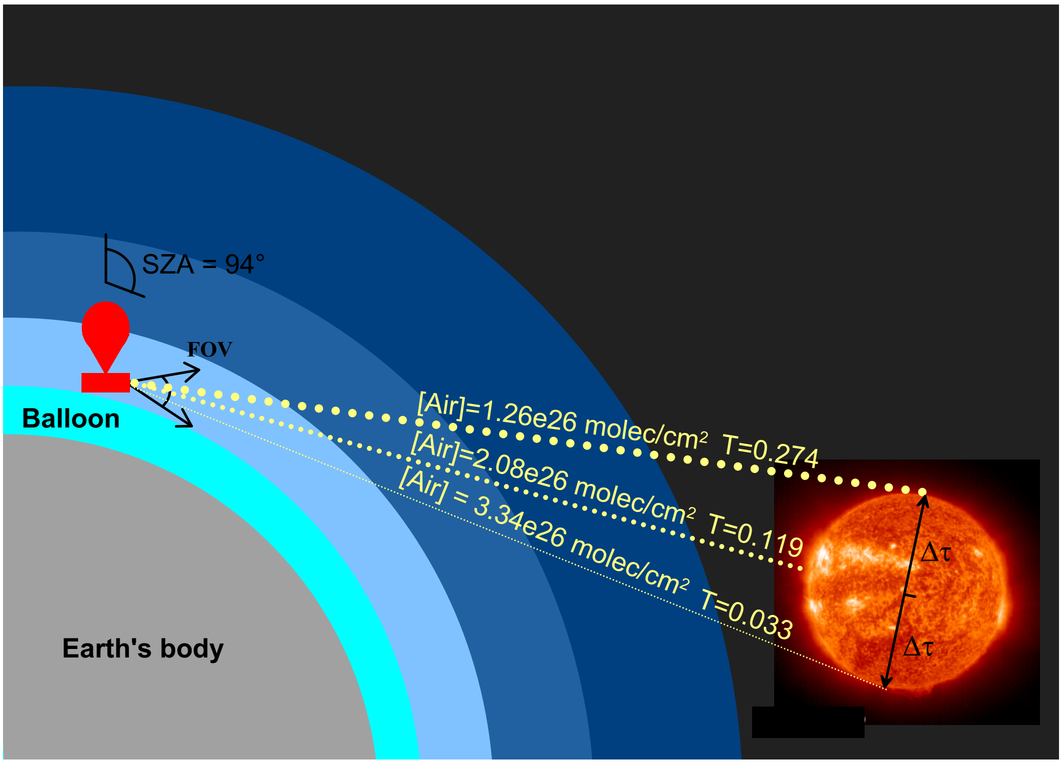

Figure 4.5: *Observation geometry for solar occultation measurements. The number above the line-of-sight, taken from the sun's upper edge, center, and lower edge indicate the air masses and the transmissions with respect to Rayleigh scattering at 434 nm.*

Center-Limb Darkening Correction

The DOAS technique is based on the assumption that the structures of the Fraunhofer spectrum I_0 remain constant for all measurements. In this case, the strong solar lines, with optical densities being 100-1000 times larger than the atmospheric absorption structures, can be removed properly from the measured spectrum and the trace gas absorptions can be evaluated. However for measurements of direct sun light during sunrise or sunset this assumption is not valid. As the solar disk has a diameter of 0.55° when seen from the earth without refraction, the zenith angles and hence the atmospheric air masses are different for rays leaving the upper edge, center or lower edge of the sun, an effect with dramatically increasing importance with increasing solar zenith angle. Thus, the transmission with respect to Rayleigh scattering is a function of the disk location (see Figure 4.5) and the radiance weighted average of the sun shifts from the solar disk center to its upper edge with increasing SZA. That in combination with the variation of the optical densities of the solar Fraunhofer lines across the solar disk (see section 4.1.1), causes a change of the optical densities of the Fraunhofer lines over the course of the occultation measurements (sunrise or sunset). Unfortunately, the relative change of the different solar lines is non-uniform and therefore an exact consideration of this effect is difficult.

Figure 4.6 shows how this process affects our measurements (in the visible wavelength range).

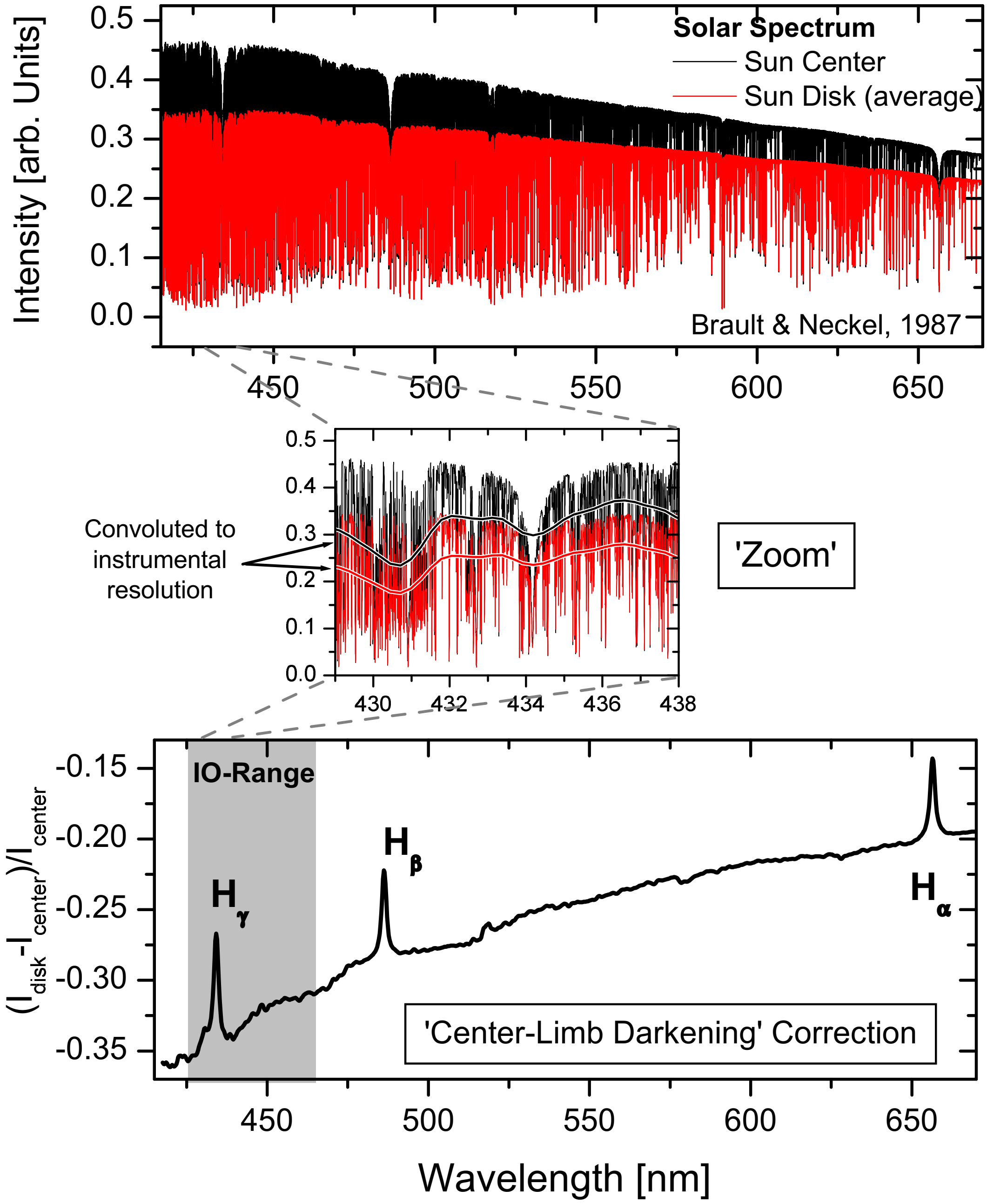

Figure 4.6: *Center to Limb Darkening (CLD) correction. Upper panel: High resolution spectra averaged over the solar disk (red) and from the sun's center (black). The spectra are from Brault and Neckel [1987]. Middle panel: Zoom (429-438 nm) of the spectra shown in the upper panel together with the respective spectra convoluted to the DOAS visible spectrometer's spectral resolution. Lower panel: Calculated CLD correction for the wavelength range covered by the DOAS visible spectrometer.*

In the upper panel, two high resolution solar spectra taken from the solar center and averaged over the whole solar disk are compared[17] [*Brault and Neckel* 1987]. The completely saturated, broad hydrogen lines H_α, H_β and H_γ at 656.3 nm, 486.1 nm, and 434.0 nm respectively can clearly be seen in the spectra. The wavelength interval 429 - 438 nm zoom in the middle panel indicates how the optical density of the H_γ-line and some other non-hydrogen lines differ at our instrument's spectral resolution (FWHM of the instrument function $\sim$ 1.2 nm for the vis-spectrograph) in both spectra. It is noticeable, that after convolution with the instrument function the spectrum shows a strong absorption feature around 431 nm caused by the high density of relatively weak and narrow lines and a weaker line caused by the strong H_γ-line. To correct the changing optical densities of the Fraunhofer lines, it is assumed, that this change can be described by the difference of the disk averaged spectrum I_0 and the center measurement I_c:

$$I_0 \longrightarrow I_0 + a(I_0 - I_c) \tag{4.36}$$

This means that the Fraunhofer reference spectrum I_0[18] has to be replaced by the sum of I_0 and a correction term $I_0 - I_c$ scaled with a factor a. To include this correction in the fitting procedure (see eq. 4.21) the logarithm has to be taken:

$$\begin{aligned}
\ln\{I_0 + a(I_0 - I_c)\} &= \ln\{I_0(1 + a(I_0 - I_c)/I_0)\} && (4.37)\\
&= \ln\{I_0\} + \ln\{1 + a(I_0 - I_c)/I_0)\} && (4.38)\\
&\simeq \ln\{I_0\} + a(I_0 - I_c)/I_0 && (4.39)
\end{aligned}$$

Accordingly, the term $(I_0 - I_c)/I_0$ is used for the correction from now on called *center to limb darkening correction* (CLD correction). The scaling factor a is an additional parameter which has to be determined by the fitting procedure. In the lower panel of Figure 4.6 the center to limb darkening correction is displayed. The correction shows a nearly smooth trend (i.e. the change of the optical densities of the narrow lines is almost negligible at our resolution) with three large peaks at the wavelengths of the hydrogen lines. This correction is firstly applied to solar occultation measurements within this Ph. D. thesis. A detailed investigation of this effect can be found in chapter 7. This correction is also applied to the NO_2 evaluation in chapter 5.2, without further comment.

The effect of the CLD correction for the UV wavelength range is shown in Figure 4.7. The correction consists of several large peaks for wavelengths larger than 370 nm, while for wavelengths below the correction shows a rather smooth shape. Thus, the BrO DOAS retrieval[19] (wavelength intervall: 346 - 360 nm) should not be affected by the CLD correction. However, in the case of OClO, there is some overlap between the wavelength interval of the DOAS evaluation (362 - 390 nm) and that range of the CLD correction containing narrow band structures and hence the center to limb darkening possibly effects the retrieval. Thus, the CLD correction should be included in the OClO fitting procedure.

---

[17] No high resolution solar spectrum from the solar limb is available.

[18] The Fraunhofer spectrum is generally measured for small solar zenith angles, thus it is equal to the convoluted high resolution spectrum of the disk averaged measurement

[19] For details of the BrO DOAS retrieval see *Fitzenberger* [2000]

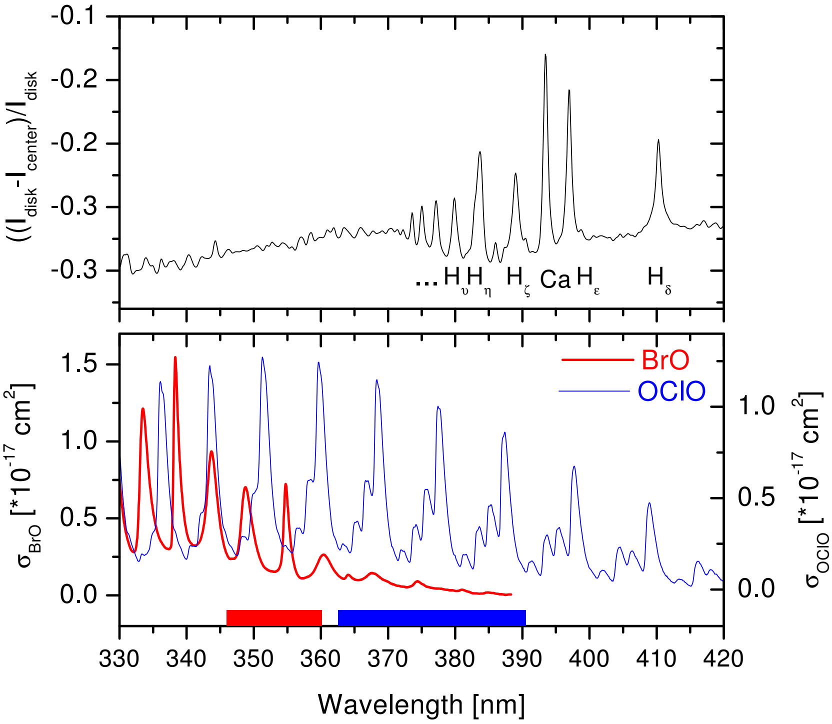

Figure 4.7: *Center to Limb Darkening (CLD) correction for the UV spectrograph. Upper panel: Calculated CLD correction convoluted to the resolution of the UV spectrograph with a denotation of the Fraunhofer lines contributing to the CLD correction (Hydrogen and calcium lines). Lower panel: Absorption cross section of BrO and OClO. The bars at the bottom of this panel indicate the wavelength intervals commonly used for the DOAS evaluation [Fitzenberger 2000].*

Ring Spectrum

For scattered light measurements the depth of the Fraunhofer lines changes with solar zenith angle caused by the filling in effect of Raman scattering (see section 2.2.3). Usually, this is corrected by including a further spectrum into the fitting process [*Solomon et al.* 1987]. This so-called Ring spectrum can be obtained by polarization measurements[20] or by model calculations [*Bussemer* 1993; *Funk* 2000]. For measurements of direct sun light, it is in general assumed that the Ring effect is negligible [*Bauer* 1997; *Pundt et al.* 1998] and no Ring correction is applied. Nevertheless, taking into account the large field of view of the instrument used here (see section 4.2.2), for very low sun some Raman scattered photons are likely to contribute to the measured spectrum. The inclusion of a Ring spectrum in the fitting procedure may thus improve the evaluation of weak absorbers. This is tested for the IO evaluation described in chapter 7.

---

[20] Compared to Rayleigh scattered light, the Raman scattered light shows a weak polarization, thus it is possible to distinguish between both effects by measurements using polarization filters.

Further Effects

As described in subsection 4.1.3, changes in the wavelength-pixel mapping of the measured spectra are compensated by shifts and squeezes of the molecular cross sections (or the measured spectra). As the cross sections (or the spectra) are given on a discrete grid, the shifted and squeezed spectra are obtained by (spline) interpolation. The interpolation results in an approximation of the 'real' value. The approximations is the better the higher the sampling ratio[21]. *Roscoe et al.* [1996] pointed out, that for sampling ratios larger than 4.5 the interpolation errors get small. For the instrument used here, this criteria is fulfilled and thus the interpolation errors should be small. A detailed investigation of this effect (so-called *undersampling effect*) for the UV spectrograph can be found in *Vradelis* [1998] and *Ferlemann et al.* [2000].

In addition, systematical structures can be caused by changes of the instrumental resolution. Due to pressure and temperature variations, the distances between the optical components of the spectrograph and thus the instrumental resolution can slightly change. Each Fraunhofer line and to a smaller degree each absorption band, will cause a positive (negative) large peak at the center of the band and smaller negative (positive) dips at the wings in the residual of the fitting procedure. Also a misalignment of one of the absorption cross sections results in systematical structures. In this case, for each absorption band an almost symmetrical structure with a large positive and negative peak at the wings of the band occur in the residual. Both effects impact the scaling factors a_j as well as the estimated errors [*Ferlemann* 1998]

The fitting procedure requires absorption cross sections with the resolution given by the instrument function. Therefore, a mathematical convolution of high resolved cross sections (e.g. measured with an Fourier Transform Interferometer) with the measured instrument function is performed. However, as the instrument function is only known on the discrete grid, a spline interpolation is used to estimate a high resolution instrument function with the same resolution as the literature cross section. In addition, as the instrument function is usually measured with emission lines of e.g. a mercury lamp, it is only known for certain wavelengths. If the instrument function shows a dependence on the wavelength (an effect often observed), then the shape has to be interpolated for wavelengths between the emission lines [*Vradelis* 1998]. However, the wavelength dependence of the instrument function is often neglected and simply a constant instrument function is used. Both effects cause systematical residual structures and can be avoided by using cross sections measured with the same instrument in the laboratory[22].

There are several instrumental shortcomings which can result in additional residual structures if not corrected for. Differences of the sensitivity of the detector diodes introduce errors if a shift and squeeze is applied in the fitting procedure. Measuring the broadband emission spectrum of a halogen lamp, the sensitivity of the diodes can be obtained. The differences of the diode sensitivity can be corrected by division of the measured spectra with the broadband emission spectrum. Further structures can be cause by the used grating itself. These structures depend on the wavelength an cannot easily be removed. Spectrometer stray light is caused by internal reflections of light from higher orders of the grating or from wavelengths not detected by the diode array. The stray light also occurs as an offset added to the measured intensity, an effect

---

[21] The sampling ratio is given by the number of grid points per full width at half maximum (FWHM) of the instrument function

[22] For the spectral retrieval, absolute cross sections are needed and therefore it is necessary to calibrate the measured cross sections with convoluted absolute cross sections from the literature.

which changes the optical densities of the Fraunhofer lines and of the molecular absorption lines significantly. The stray light can be reduced but not totally suppressed by using filters and light traps for the higher orders of the grating. By including an additional intensity offset possible with the evaluation software *WinDOAS*, the instrumental stray light can be considered within the fitting procedure. The influence of the Memory-effect (Structures of an exposed spectrum can partly be found in the following, not exposed spectrum) and the Etalon effect (caused by multiple reflections on thin parallel surfaces) were investigated by *Bauer* [1997] and were found to be small for the used instrument. When using glass fibres to conduct the light into the spectrograph, structures can be caused by slight variations of the exposure of the fibre entrance and thus the stimulation of different modes. Due to inhomogeneities of the fibre the transmissions of the modes differ. By using e.g. a diffuser plate in front of the fibre a steady exposure is achieved and this effect is avoided.

4.2 Instrumentation

The measurements were presented in this Ph. D. thesis, were performed during a series of eight balloon flights with a DOAS UV/vis spectrograph installed on the LPMA/DOAS[23] balloon gondola. The DOAS spectrograph together with an infrared Fourier Transform Interferometer (FTIR) and two filter actinometers (during two flights only) form an instrumental package. Both, the DOAS spectrograph and the FTIR perform direct sun light measurements during balloon ascent and solar occultation. Thus the measurements of the UV/vis and the infrared instrument can be combined and a large number of trace gases can be detected simultaneously. In this section the DOAS spectrograph, the FTIR, and the actinometers will be briefly described, but first a short technical presentation of the gondola itself will be given.

4.2.1 LPMA/DOAS Balloon Gondola

The LPMA/DOAS balloon gondola is based on a gondola developed for astronomical observations by the Observatoire de Genève and was further optimized for atmospheric measurements by *Camy-Peyret et al.* [1995] (Figure 4.8). The gondola can be stabilized in azimuthal direction with an accuracy of about 0.5 - 0.1° and 1' or better in the lower stratosphere and at the balloon float altitude, respectively. Therefore the gondola is aligned to the magnetic field of the earth with a gyroscope. The gondola can be rotated with respect to the much larger balloon. The rotational energy is converted to frictional heat through the torque of a special joint of the gondola and the balloon. The fine-pointing is performed by a suntracker [*Hawat et al.* 1995], which provides the infrared Fourier Transform Interferometer and the DOAS UV/vis spectrograph with a parallel solar beam. Further the gondola equipment includes pressure and temperature sensors and GPS antennas. Since 1998 the instrumental package has been completed with an on-board ozone sonde.

---

[23] LPMA=Laboratoire de Physique Moléculaire et Applications

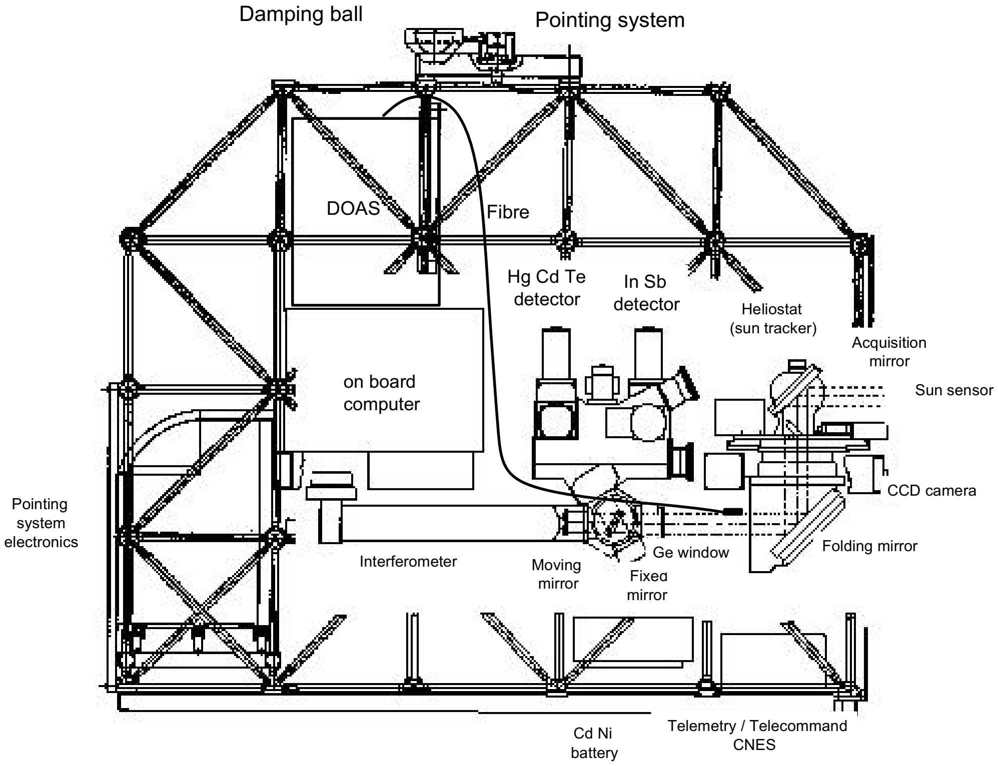

Figure 4.8: *Schematic drawing of the LPMA/DOAS balloon gondola. Direct sun light is directed into the gondola by the suntracker, which is subsequently analyzed by the FTIR and the DOAS instrument.*

4.2.2 The DOAS Spectrograph

For the installation on the LPMA/DOAS balloon gondola, a new DOAS instrument optimized for airborne applications was designed[*Ferlemann* 1998; *Harder* 1999; *Ferlemann et al.* 2000]. The basic features of the instrument are low weight, low power consumption, stability of the spectral imaging and insignificant thermal drift of the spectroscopic system. The instrument consists of two spectrographs in one housing, which analyze the UV and the visible part of the sun light separately (see Figure 4.10). The light enters the spectrograph via two quartz fibres bundles, forming a rectangular entrance slit for each spectrograph on one fibre end. On the other end of the fibres i a telescope optic is mounted intended to average the light received from the sun, to limit the spectral transmission range of the incoming light and to match the f-number of each spectrometer. Coming from the entrance slit, the light reaches a holographic grating, which disperses the light of the respective wavelength range (UV: 320.6 - 422.6 nm; visible: 417.6 - 670.7 nm) onto Peltier cooled photodiode arrays. The width of the entrance slit was chosen to fulfill the sampling criteria given by *Roscoe et al.* [1996], i.e. the FWHM of the instrument function should be sampled with more than 4.5 detector pixels. The instrumental resolution is found to be 0.45 nm (= 4.5 detector pixels) and 1.48 nm (= 5.7 detector pixels) for the UV and

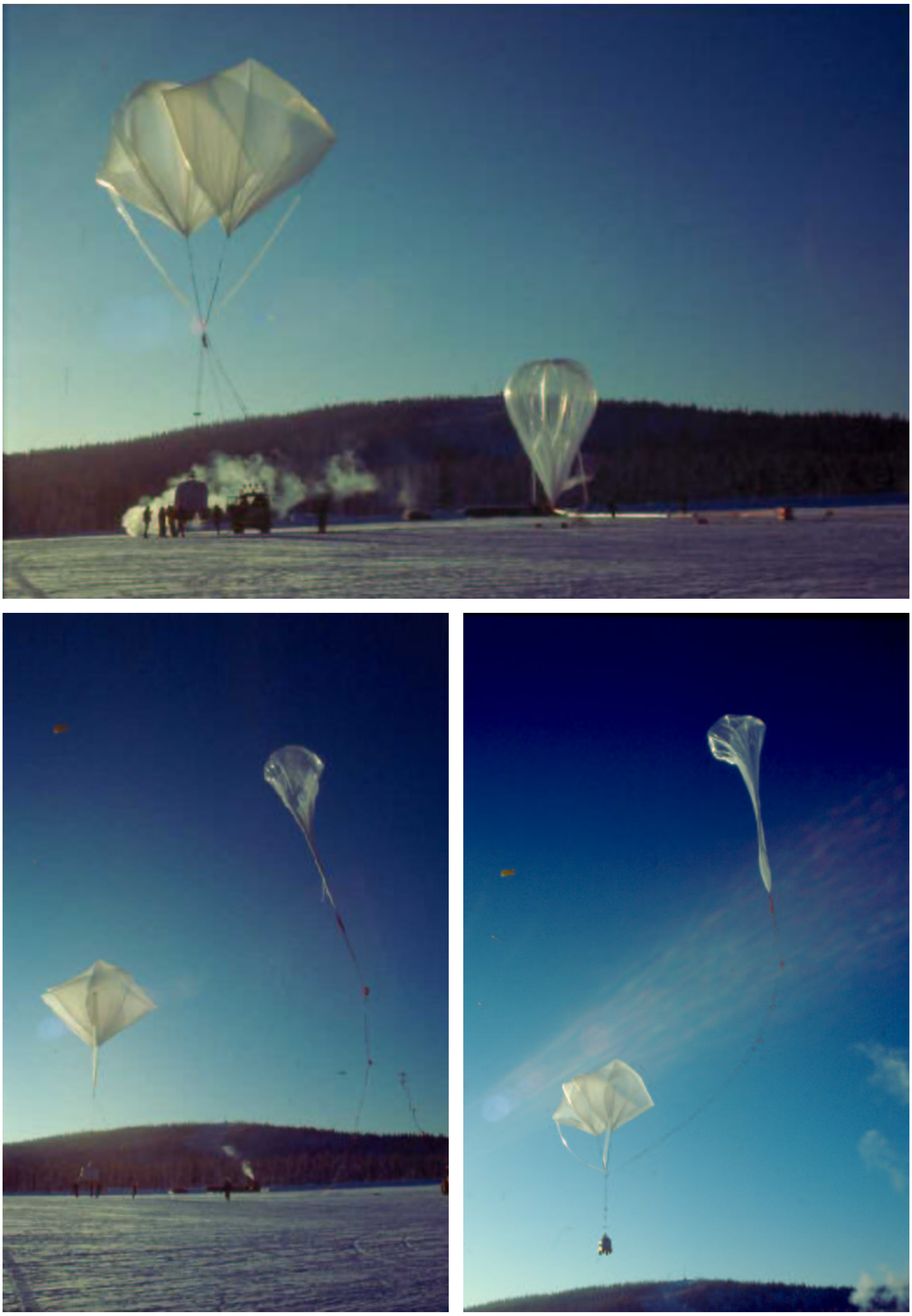

Figure 4.9: *Launch of the LPMA/DOAS balloon gondola at Esrange near Kiruna/northern Sweden on February, 10, 1999. The two small balloons are helium filled auxiliary balloons to keep the gondola in abeyance during the launch.*

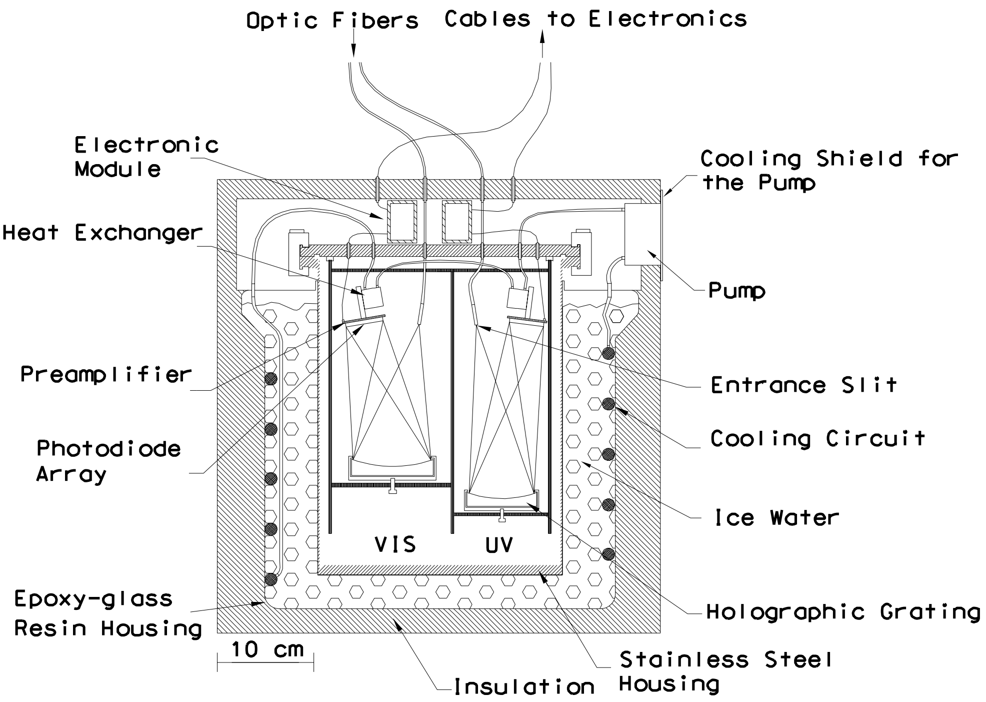

Figure 4.10: *Schematic drawing of the DOAS instrument. Two holographic grating spectrographs (UV and visible) are integrated into a vacuum-sealed stainless-steel container. The light enters the spectrographs through two quartz fibre bundles which form an apparent rectangular slit at their end. Light detection is performed with two photodiode array detectors. The whole container is thermostated by a liquid-water-ice-filled vessel surrounding it. In addition, a refrigerant is circulated in a cooling circuit to regulate the temperature of the optical components and to cool the warm side of the Peltier elements.*

the vis spectrometer, respectively. The whole spectrometer housing is evacuated and thermally stabilized by a surrounding vessel filled with a water-ice mixture. In addition, a refrigerant circulates in a cooling circuit to regulate the temperature of the optical components and to cool the warm side of the photodiode Peltier elements. Low spectrometer stray light is achieved by suppressing the higher-order and zero-order grating reflections by using light traps and, for some flights, by including a dispersive prism preananalyzer for the UV spectrograph[*Vradelis* 1998]. A detailed characterization of the DOAS spectrograph can be found in *Bauer* [1997]. In the wavelength range covered by the combination of the UV and vis spectrograph, absorption features of several species can be found, e.g. O_3, BrO, NO_2, OClO, SO_2, HNO_2, HCHO, O_4 etc. in the UV range and O_3, NO_2, H_2O, O_4, NO_3, OClO, IO, OIO etc.in the vis range. This Ph. D. thesis will focus on results obtained by the visible spectrograph only. For results obtained by evaluation of the UV measurements see *Ferlemann et al.* [1998], *Harder et al.* [1998], *Harder et al.* [2000], *Fitzenberger et al.* [2000], *Fitzenberger* [2000], and *Pfeilsticker et al.* [2000].

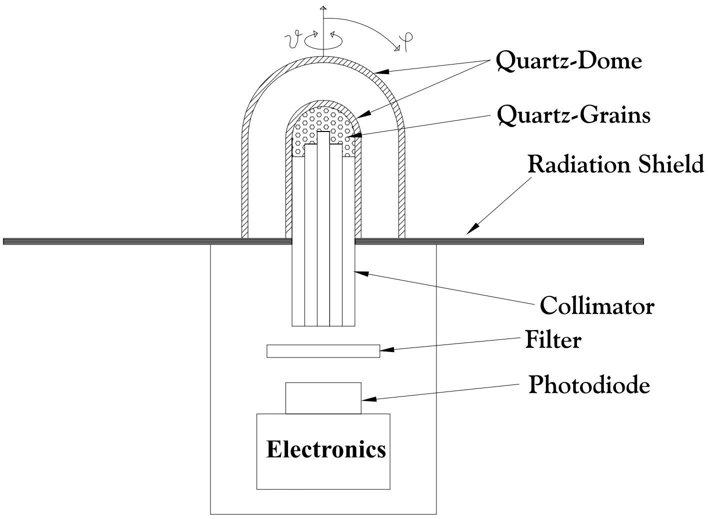

Figure 4.11: *Schematic drawing of the j_{NO_2} sensor. For a detailed description see Schneider [1997].*

4.2.3 The LPMA Fourier Transform Interferometer

The infrared Fourier Transform Interferometer (FTIR) operated by the french LPMA team is based on a DA2 Michelson type interferometer manufactured by BOMEM but customized for balloon operations. The interferometer is equipped with a two channel output optics and is capable to sample simultaneously the interferograms produced by two infrared detectors with an apodised resolution of 0.020 cm^{-1}. The spectral signatures of $ClONO_2$, HNO_3, O_3, CH_4, N_2O, NO, and H_2O are covered by a HgCdTe detector (mid-IR) and those of HCl, NO_2, CH_4, and HF by an InSb detector (near-IR) [*Camy-Peyret et al.* 1995; *Payan et al.* 1998; *Payan et al.* 1999]. The instrument has also been used to measure H_2O and O_2 in the 920 nm and 760 nm region, respectively, to retrieve CCl_2F_2 in the lower stratosphere, and to obtain CO_2 in the 13 μm region [*Camy-Peyret et al.* 1999]. A global fit method [*Carlotti* 1988] associated to an efficient minimization of the Levenberg-Marquardt type is used for the retrieval of vertical mixing ratio profiles from ascent and occultation data. The algorithm allows to combine the information contained in several micro-windows. The molecular parameters used in the forward model are extracted from the HITRAN96 database [*Rothman et al.* 1996].

4.2.4 Actinometer

Filter actinometers measure the actinic flux independent of direction with a characteristic wavelength dependent sensitivity. If the spectral sensitivity is chosen in order to approximate the product of absorption cross section and quantum yield of a certain molecule (here NO_2), then the measurements reproduce the corresponding photolysis frequency j. The filter actinometers (see Figure 4.11) used here were technically similar to those described by *Junkermann et al.* [1989] but with improvements as given in *Schiller et al.* [1994]. The actinometers contain a

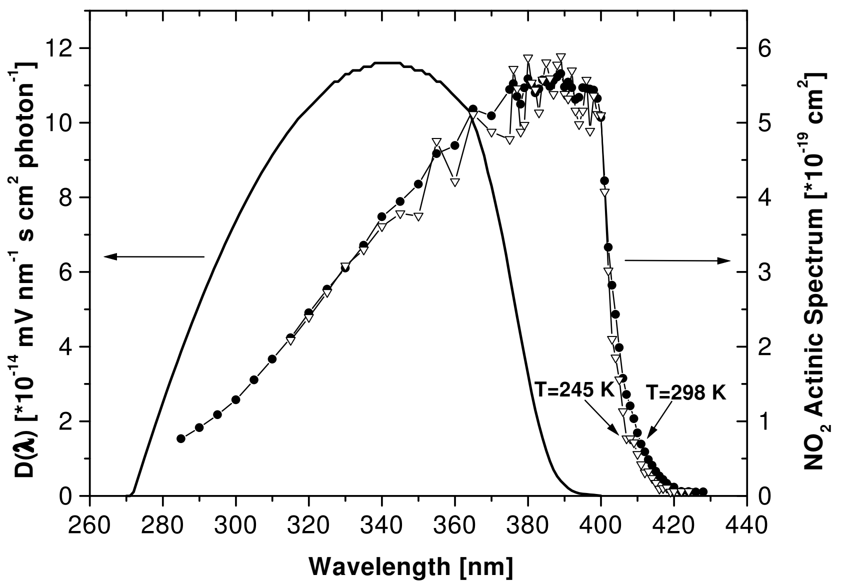

Figure 4.12: *Comparison of the actinic spectrum of NO_2 and the spectral response of the actinometers. For the calculation of the actinic spectrum of NO_2, the quantum yield of Roehl et al. [1994] and the NO_2 absorption cross section of Davidson et al. [1988] is used. The actinic spectrum of NO_2 is calculated for T=245 K and 298 K indicated by open triangles and filled circles, respectively.*

special 2π viewing inlet device collecting the solar radiation from one hemisphere almost independent of the incident angle. Two actinometers were mounted in a way that the symmetry axis of the inlet dome points to the horizon, with one actinometer pointing directly into the sun's azimuthal direction gathering the direct solar radiation and the diffuse radiation from that part of the hemisphere and the second actinometer directing to the opposite hemisphere thus only detecting diffuse radiation. The actinometer's spectral characteristics were fixed to the broad band transmission given by the spectral transmission of Schott UG-11 glasses and the phototube's spectral sensitivity. The spectral sensitivity was measured using a monochromator and a light source. The absolute sensitivity was determined with a calibrated tungsten halogen lamp [*Schneider* 1997]. A comparison of the actinometer's spectral sensitivity and the actinic spectrum of NO_2 is shown in Figure 4.12. As can be seen from the figure, the spectral sensitivity of the actinometer does not perfectly match the actinic spectrum. Therefore, to obtain j_{NO_2} values, the measurement has to be calibrated (depending on height and solar zenith angle) with radiative transfer calculations. For more details see section 5.3.1.

4.3 Profile Retrieval

A balloon flight can be divided in three different phases. The balloon ascent, the balloon float and the solar occultation. During the balloon ascent (see Figure 4.13), the balloon climbs vertically

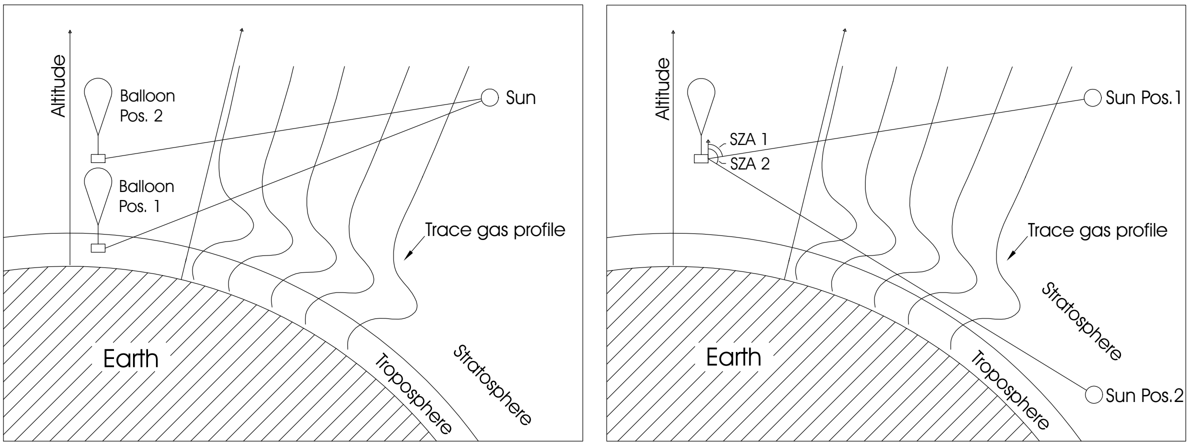

Figure 4.13: *Observation geometry of the measurements for balloon ascent (left panel) and solar occultation (right panel).*

through the trace gas profile (for solar zenith angles well below 90°). Thus, the decrease of the measured slant column densities can be attributed to the concentration of the crossed height segment. During the balloon float, the balloon remains on a constant altitude, while the solar zenith angle increases towards 90°. The first measurement after reaching the maximum altitude (i.e. with the smallest solar zenith angle) is commonly used as the Fraunhofer reference spectrum for the spectral fitting procedure. Further, these measurements can be used to estimate the amount of trace gas absorptions contained in the Fraunhofer reference spectrum with a so-called Langley-plot (see chapter 5.2). During the solar occultation, the balloon altitude remains constant, while the light of the rising or setting sun is measured. Accordingly, the light path of the measurement crosses the trace gas profile beneath the balloon altitude twice for each layer above the so-called tangent point, given by that point of the light path with the smallest distance to the earth's surface[24]. In the course of the solar occultation measurements the tangent height decreases (due to the increasing solar zenith angle) and the light path crosses an increasing part of the trace gas profile. For solar zenith angles larger than 90°, the concentrations of most species (which are of interest in this Ph. D. thesis) are subject to substantial photochemical changes. Therefore, the obtained profiles also include some photochemical changes (especially for solar occultation). There exist several retrieval techniques to derive a trace gas profile from slant column densities measurements [e.g. *Rodgers* 1976; *Delbrück* 1992]. Three different techniques will be presented, here.

4.3.1 Inversions Technique

The atmosphere is divided into N layers, each with constant pressure, temperature and trace gas concentration. The measured slant column density SCD can then be written as the sum of

---

[24] At the tangent point the light path is perpendicular to the earth's surface, resulting in a very long light path at this altitude. Most of the absorption will take place here (also depending on the shape of the profile) and, hence, the measurement can be attributed to this altitude.

the contributions of the individual layers:

$$SCD = \sum_{i=1}^{N} SCD_i = \sum_{i=1}^{N} AMF_i \cdot VCD_i \tag{4.40}$$

The vertical column density VCD_i of layer i is given by the concentration times the height of the layer. The VCD_i is connected to the SCD_i of layer i by the (box-)air mass factor AMF_i, that is given for direct light measurements by the ratio of the length of the light path through the layer to the vertical height of the layer[25]. Extending this concept to the entirety of all M ascent or occultation measurements, a system of linear equations is obtained:

$$\begin{bmatrix} SCD_1 \\ SCD_2 \\ \vdots \\ SCD_M \end{bmatrix} = \begin{bmatrix} AMF_{1,1} & AMF_{1,2} & \dots & AMF_{1,N} \\ AMF_{2,1} & AMF_{2,2} & \dots & AMF_{2,N} \\ \vdots & \vdots & \ddots & \vdots \\ AMF_{M,1} & AMF_{M,2} & \dots & AMF_{M,N} \end{bmatrix} \cdot \begin{bmatrix} VCD_1 \\ VCD_2 \\ \vdots \\ VCD_N \end{bmatrix} \tag{4.41}$$

Introducing the *air mass factor matrix* **AMF**, this can be simplified to

$$\overrightarrow{SCD} = \mathbf{AMF} \cdot \overrightarrow{VCD} \tag{4.42}$$

The matrix **AMF** can be calculated with the raytracing (and profile retrieval) programm *DAMF* [*Schulte* 1996]. The raytracing is based on a Runge-Kutta algorithm [*Press et al.* 1986] taking into account the spherical geometry and the pressure and temperature dependent refraction. To take into account the extent of the solar disk, with a diameter of up to 5 km at the tangent point, the air mass factor matrix is calculated for four rays. Each ray represents one of four equally sized areas, obtained by horizontal splitting of the solar disk. The air mass factor matrix is then obtained by averaging the air mass factor matrixes of the four individual rays.

The desired profile $\overrightarrow{VCD}$ is obtained by inversion of the air mass factor matrix:

$$\overrightarrow{VCD} = \mathbf{AMF}^{-1} \cdot \overrightarrow{SCD} \tag{4.43}$$

The inversion is carried out by the *Singular-Value-Decompostion* (SVD) method [*Press et al.* 1986]. The SVD method makes use of a theorem of linear algebra, that a $M \times N$ matrix, with $M \geq N$, can be written as a product of a $M \times N$ orthogonal matrix $\mathbf{U}$, a $N \times N$ diagonal matrix $\mathbf{W}$ and the transpose of a $N \times N$ orthogonal matrix $\mathbf{V}$. The positive or zero diagonal elements of $\mathbf{W}$ are called singular values. Thus the inverse matrix $\mathbf{AMF}^{-1}$ can easily be calculated:

$$\mathbf{AMF}^{-1} = \mathbf{V}\,[diag(1/w_j)]\,\mathbf{U^T} \tag{4.44}$$

Usually the number of measurements M is much larger than the number of height segments N, thus the inversion problem is overdetermined. The SVD method then gives the best solution for $\overrightarrow{VCD}$ in the least-square sense.

In contrast to iterative profile retrieval techniques (e.g. simulated annealing) the SVD method offers no stopping criteria to avoid over-interpretation of the measured SCD's. Stochastical variations of the SCD's in the range of the measurement errors are interpretated as profile

---

[25] The concept of box-air mass factors is a simple extension of the air mass factor concept for ground based measurements (see e.g. *Perlinski and Solomon* [1993]).

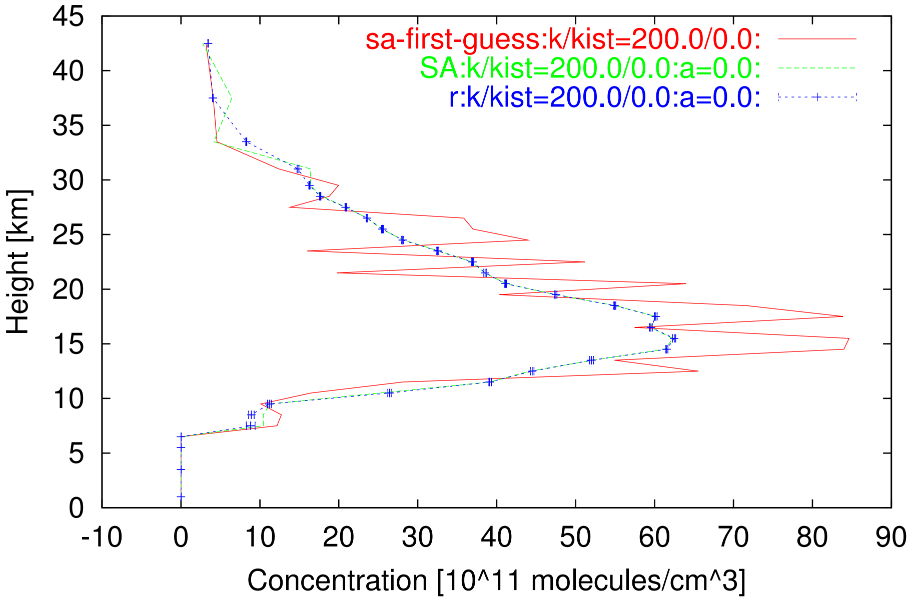

Figure 4.14: *Comparison of O_3 profiles retrieved with the the simulated annealing and the inversion technique. The green dashed line is the simulated annealing profile, the blue dotted line the inversion profile and the red line the first-guess profile for the simulated annealing retrieval.*

information. This becomes apparent by the occurrence of negative entries in the retrieved $\overrightarrow{VCD}$. The equations for very small singular values map large variations in $\overrightarrow{VCD}$ on small variations in $\overrightarrow{SCD}$ and, analogously, equations with very large $1/w_j$ map small variations in $\overrightarrow{SCD}$ on large in $\overrightarrow{VCD}$. Consequently, for a measured $\overrightarrow{SCD}$ with statistical errors it is necessary to set the smallest singular values and their reciprocals to zero. This is achieved by reducing the *condition number* of the air mass factor matrix, defined as the ratio of the largest to the smallest singular value. Setting to zero one or several small singular values only slightly reduces the vertical resolution, while the propagation of the measurement errors is largely suppressed. In this Ph. D. thesis, this method is used as the standard technique. If one of the other techniques is used it is explicitly stated.

4.3.2 Simulated Annealing

Simulated annealing is an iterative method to retrieve the best estimate for the $\overrightarrow{VCD}$. Starting from a given first-guess, a Monte-Carlo technique is used to vary the estimated $\overrightarrow{VCD}_{est}$ until the corresponding $\overrightarrow{SCD}_{est}$ reproduces the measured $\overrightarrow{SCD}_{meas}$ with a certain precision. As a measure of the quality of the estimate, the so-called *cost function* CF is introduced. It can be chosen between several expressions for the cost function, but in general the norm of the difference of the estimated and measured $\overrightarrow{SCD}$ is used. If a new estimate of the $\overrightarrow{VCD}_{est}$ is accepted by the algorithm is decided on the basis of a Boltzmann distributed random number. The probability

P is given by

$$P(\text{'accept new estimate'}) = \min\left(1, \exp\left\{\frac{CF_{new} - CF_{old}}{T}\right\}\right) \tag{4.45}$$

with the *annealing temperature* T, a monotone decreasing parameter (regulated by the cooling rate). First, for large annealing temperatures, the algorithm searches spaciously for the global minimum in the parameter space. With increasing T the algorithm tends to accept only estimates with smaller cost functions. Unfortunately, there are several parameters (annealing temperature, cooling rate ...) which are crucial for the result of the algorithm. These parameters have to be adjusted individually for each measurement. The iteration stops if one of several stopping criteria is fulfilled, e.g. if the cost function of a new estimate is smaller than the cost function of the measurement errors or if the number of iteration steps exceeds a given limit etc. For more details of the implementation of the simulated annealing algorithm in the programm package $DAMF$ see *Luderer* [2001].

This technique is not used in this Ph. D. thesis, but one example will be given. Figure 4.14 shows an ozone profile retrieved with the simulated annealing and the inversion technique. For this study, statistical noise (2%) was added to an initial profile (O_3 profile measured during solar occultation in Kiruna on Feb. 18, 2000) and SCDs were calculated. Then the profiles were calculated with these SCDs. As first-guess profile for the simulated annealing, the initial profile with 40% noise was used. This example shows, that reasonable results are obtained with simulated annealing technique and that this technique can be used alternatively to the inversion technique.

4.3.3 Onion Peeling

The Onion Peeling method attributes the decrease of the measured SCD's directly to the crossed height layers. Accordingly, this method can only be used for balloon ascent (or descent) measurements. For each SCD the corresponding VCD is calculated by

$$VCD = SCD \cdot 1/AMF \simeq SCD \cdot \cos(SZA) \tag{4.46}$$

The approximation for the air mass factor is valid for SZA's well below 90°. Due to the curvature of the earth's surface for $SZA \simeq 90°$ the approximation largely overestimates the air mass factor. The concentration n at a certain height h can be calculated by

$$n(h) = \frac{\delta VCD(h)}{\delta h} = \frac{\Delta VCD(h)}{\Delta h} \tag{4.47}$$

To suppress high frequent oscillations caused by the statistical noise of the measurement, the calculated VCD's can be smoothed by a Gaussian filter.

4.3.4 Averaging Kernel

To introduce the averaging kernels, first another formulation of the retrieval problem will be given [*Rodgers* 1976]. Let $\overrightarrow{VCD}_{true}$ be a true trace gas profile, $\overrightarrow{SCD}$ the measured SCD's and

$\overrightarrow{VCD}_{est}$ the profile estimated by the retrieval algorithm. The retrieval problem can then be formally written as

$$\begin{aligned}
\overrightarrow{SCD} &= F(\overrightarrow{VCD}_{true}, \overrightarrow{b}) && (4.48)\\
\overrightarrow{VCD}_{est} &= I(\overrightarrow{SCD}, \overrightarrow{b}, \overrightarrow{c}) && (4.49)\\
\overrightarrow{VCD}_{est} &= I(F(\overrightarrow{VCD}_{true}, \overrightarrow{b}), \overrightarrow{b}, \overrightarrow{c}) && (4.50)\\
\overrightarrow{VCD}_{est} &= T(\overrightarrow{VCD}_{true}, \overrightarrow{b}, \overrightarrow{c}) && (4.51)
\end{aligned}$$

$\overrightarrow{b}$ and $\overrightarrow{c}$ describe additional parameters of the inversion or forward model (e.g. air mass factor matrix, annealing temperature). F is the *forward model function*, I the *inversion model function* and T is the so-called *transfer function*. The transfer function describes the relation between the real and the estimated profile. For further interpretation, equation 4.51 is linearly expanded around a reference profile $\overrightarrow{VCD}_{ref}$

$$\overrightarrow{VCD}_{est} = T(\overrightarrow{VCD}_{ref}, \overrightarrow{b}, \overrightarrow{c}) + \frac{\delta T}{\delta \overrightarrow{VCD}_{true}} \cdot (\overrightarrow{VCD}_{true} - \overrightarrow{VCD}_{ref}) \qquad (4.52)$$

The matrix of the derivations $\delta T/\delta \overrightarrow{VCD}_{true}$ is called *averaging kernel matrix* **A**. Every $VCD_{est,i}$ is a linear combination of the $VCD_{true,j}$ weighted with the entries of the corresponding row of the averaging kernel matrix (called averaging kernel for the i-th measurement). For an ideal case, the averaging kernel matrix is represented by the unit matrix, i. e. the averaging kernels are given by δ-functions. Deviations of **A** from the unit matrix indicate that neighbored layers also contribute to $VDC_{est,i}$. The width of the averaging kernels can be used to estimate the vertical resolution of the measured profile. The worst case is given by nearly constant averaging kernels or by averaging kernels with two or more maxima. The programm *DAMF* allows the calculations of the averaging kernels with the method presented by *Delbrück* [1992][26].

The averaging kernels for the O_3 profile measured in Kiruna on Feb. 18, 2000 are shown in Figure 4.15. For this calculation a constant error of 2% was assumed. It is evident, that the averaging kernels show a distinct peak with only smaller contributions from other height layers. For balloon ascent (upper panel) relatively broad averaging kernels are found indicating a low vertical resolution of the measurement. However, as the true (fit-) errors are clearly smaller than 2% (in the case of ozone), this has to be considered as an upper limit. A more realistic investigation of the averaging kernels would imply that the true, measured SCD errors are used, but this is not possible yet.

4.3.5 Discussion of Errors

The dominant source of errors for the profile retrieval is given by the errors of the SCDs, which are estimated in the case of the inversion technique. Gaussian error propagation yields:

$$\Delta VCD_i = \sqrt{\sum_j \Big(\sum_i V_{ik} \frac{1}{w_k} U^T_{jk}\Big)^2 \Big(\Delta SCD_j\Big)^2} \qquad (4.53)$$

Commonly, it is assumed that the errors of the SCDs are statistical and thus can be reduced by averaging a certain number of SCDs. Unfortunately, this assumption is only partly valid, as will

---

[26] Only the calculation of the averaging kernels for the simulated annealing technique is implemented.

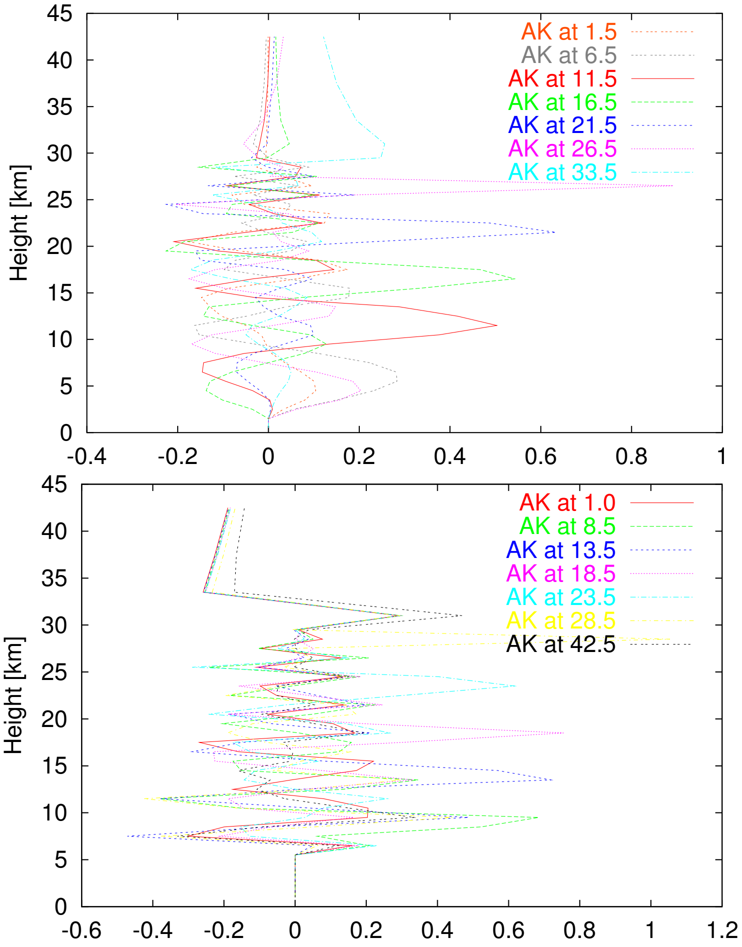

Figure 4.15: *Averaging kernels calculated with the simulated annealing technique for the* O_3 *profile measured in Kiruna on Feb, 18, 2000 during balloon ascent (upper panel) and solar occultation (lower panel). A constant* SCD*-error of 2% was assumed. The numbers in the legend denote the height corresponding to the averaging kernel.The* **AMF** *matrix was calculated taking into account the extension of the solar disk. For clarification, not all averaging kernels are shown.*

be shown later. In the case of the onion peeling technique, only few SCD values are considered for the calculation of the concentration at a certain altitude. Thus the error propagation results in very large errors for retrieved concentrations, which can reduced by smoothing the SCDs before the retrieval is performed. This seems to be necessary to reduce the vertical resolution to a reasonable range (as the technique itself provides no tool to reduce the vertical resolution, e.g. by using a certain height segmentation). In the case of the simulated annealing technique, the calculation of the errors of the retrieved profile is not implemented in the programm package software$DAMF$ yet.

Further important input parameters necessary for the profile retrieval are the atmospheric temperature and pressure profile, the balloon altitude and the solar zenith angle. The uncertainties of this quantities were not considered for the calculation of the profile errors. Temperature and pressure is measured with a Vaisala radiosonde and additional pressure and temperature sensors on-board the gondola for altitudes up to 25-30 km and the balloon float altitude, respectively. The uncertainty of these measurements is 0.5 hPa for the pressure (between 1060 and 3 hPa) and 0.2 K for the temperature. Above the balloon float altitude, the US Standard Atmosphere [*NOAA-S/T76-1562* 1976] (scaled to our conditions) is used, which is only an approximation of the real atmospheric conditions. The altitude of the balloon is measured with onboard GPS which has a vertical uncertainty of approx. 180 m. The solar zenith angle is calculated for a given time and location (measured by the GPS) by the software package *DAMF*, based on a fit for the declination of the sun [*Kubo* 1980]. The more accurate ARI[27] routine calculates the SZA using the ephemerides given by JPL[28] [Gernot Burkhardt, private communication]. The comparison of both calculations for the Kiruna balloon flight in 1999 together with the calculations by *MFC*, the sun-moon routine (both using a similar algorithm as *DAMF*), and by the LPMA team is shown in Figure 4.16. All calculations agree within a reasonable range, however small but significant differences of up to $0.1 - 0.15°$ were found. For large SZAs this will have a significant impact on the profile retrieval, e.g. the altitude of the tangent point can change up to 1-2 km and the total air mass of the measurement up to 5%. Accordingly, all SZAs used within this study were calculated with the ARI routine.

4.4 Chemical Transport Models

Chemical Transport Models (CTMs) are three dimensional simulations of chemical processes in the atmosphere (here stratosphere) using input data of meteorological analysis. In this Ph. D. thesis the model calculations of the CTM's SLIMCAT, KASIMA and REPROBUS were used, which will be briefly described.

4.4.1 SLIMCAT

SLIMCAT is an off-line CTM which is forced by the UK Meteorological Office (UKMO) analysis for the horizontal winds and temperatures [*Chipperfield and Pyle* 1998; *Chipperfield* 1999]. The vertical (diabatic) motion is calculated from the MIDRAD radiation scheme [*Shine* 1987] within the model. The model contains a detailed stratospheric chemistry scheme of the species of the O_x, NO_y, Cl_y, Br_y and HO_x families [*DeMore et al.* 1997] and long-lived tracers such as N_2O, CH_4, CO etc. The long-lived species are integrated using a simple forward Euler integration scheme which is far cheaper in computational cost than the semi implicit scheme used for the short lived species and families. The photolysis rates are calculated using a scheme based on *Lary and Pyle* [1991]. The scheme uses a four-dimensional look-up table (with the coordinates pressure altitude, temperature, O_3 column, and solar zenith angle) to interpolate the j-values to a particular location and time. The standard CTM includes a description of heterogenous chemistry occurring on liquid/solid polar stratospheric clouds (PSCs) and mid-latitude sulphate aerosols. The standard simulations were performed on 12 isentropic levels from 335 K to 2700 K

---

[27] Astronomisches Recheninstitut, University of Heidelberg

[28] Jet Propulsion Laboratory / Development Ephemeris

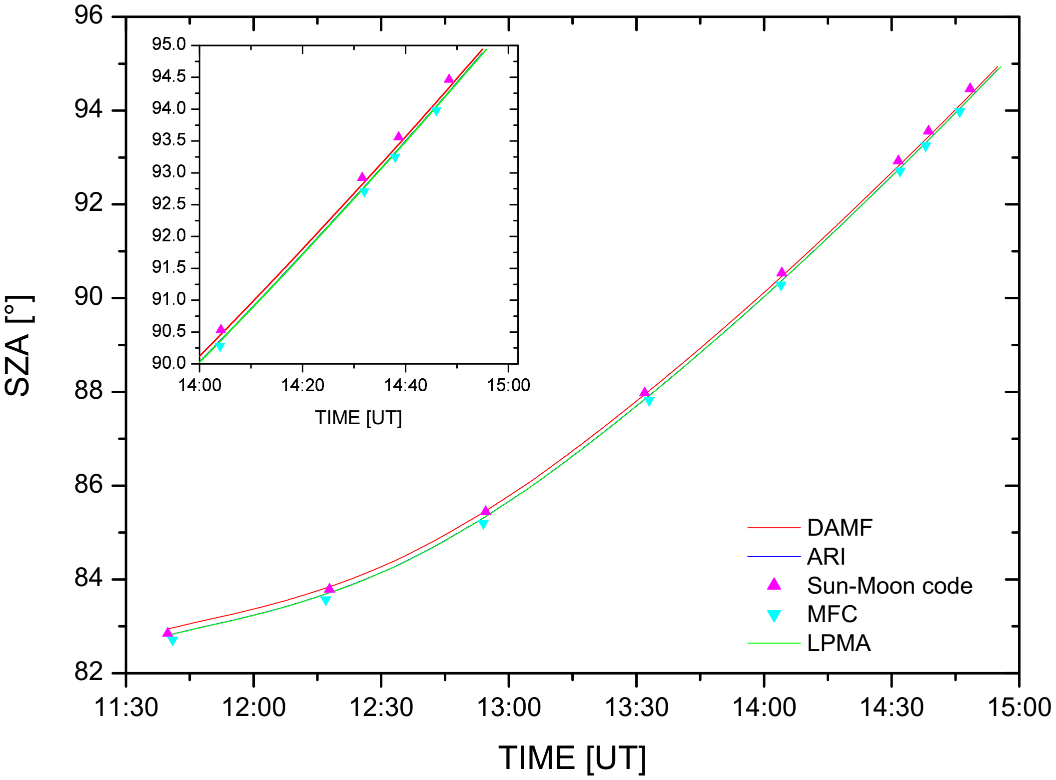

Figure 4.16: *Comparison of the solar zenith angles as calculated by the programm package* $DAMF$ *and with the ARI code for the Kiruna balloon flight in 1999. Additionally, the SZAs calculated by* MFC*, the sun-moon code [Klaus Pfeilsticker, private communication] and the LPMA team were shown. The routine used by* MFC *and* $DAMF$ *is based on the sun-moon code. The SZAs calculated by LPMA and the ARI code agree well, however, all other calculations yielded SZAs scattering around the ARI calculation with deviations up to 0.15°.*

using a horizontal resolution of $7.5° \times 7.5°$. A new release of SLIMCAT uses the recent update of photochemical data given by *Sander et al.* [2000] and an increased number of levels (18 levels).

4.4.2 KASIMA

The Karlsruhe Simulation Model of the Middle Atmosphere (KASIMA) is a mechanistic model of the middle atmosphere. It is coupled to specific meteorological situations by using the analysis from the European Centre for Medium-Range Weather Forecast (ECMWF) in the lower part of the model at pressures above 10 hPa [*Ruhnke et al.* 1999]. At pressures below 10 hPa (up to 120 km pressure altitude) the corresponding prognostic model is used [*Kouker* 1995]. Solar heating rates are calculated within the model. The chemical scheme is using the family concept which groups related chemical species with short photochemical lifetimes. If the photochemical lifetime of a species is large compared to the characteristic time constant for transport, the species is transported separately. The concentrations of the transported (long lived) species are calculated by an iterative Euler backward approximation. The scheme uses 58 chemical species and families. The rate constants of the gas phase reactions and the surface reaction probabilities are taken from *DeMore et al.* [1997] with the update given by *Sander et al.* [2000]. The photodissociation coefficients are interpolated from values in a look-up table calculated using the photonflux model of [*Röth* 1992] and depend on altitude, zenith angle and ozone column. The heterogenous scheme on sulfuric acid aerosols included in KASIMA assumes that sulfuric acid aerosols remain liquid above the freezing point of ice and that they are able to take up species from the gas phase. The heterogenous processes on NAT and ice are calculated by using a conventional polar stratospheric cloud scheme. The standard model uses 32 latitudinal and 64 longitudinal grid points and 63 equidistant levels between 10 and 120 km pressure level.

4.4.3 REPROBUS

REPROBUS is a three-dimensional CTM that extends from the ground up to 10 hPa with a vertical resolution varying from less than 1 km near the tropopause level to 2.2 km in the upper part of the stratosphere [*Lefèvre et al.* 1994; *Lefèvre et al.* 1998]. The densities of 55 chemical species or families are computed, among them 40 species are explicitly transported: these include long-lived species in the lower stratosphere such as N_2O or HCl but also more unstable constituents which have rather long lifetimes in the darkness. Winds and temperatures analyzed by the European Centre for Medium-Range Weather Forecast (ECMWF) were used to drive the transport of the species and to compute their production and loss rates, respectively. Chemical species are advected using a semi-Lagrangian transport code. The photochemical module includes 102 gas phase reactions based on the compilation of *DeMore et al.* [1997] and *Sander et al.* [2000]. The photodissociation frequencies are pre-calculated in a four-dimensional look-up table expressed as a function of altitude, solar zenith angle, ozone column and albedo. Heterogenous processes are taken into account using a relatively detailed scheme that describes the condensation, sedimentation, and evaporation of PSC material. The standard model uses a horizontal resolution of 2° latitude by 2° longitude and 31 height levels.

Chapter 5

NO_2 and O_3 Measurements

In this chapter, the results of the O_3 and NO_2 measurements obtained with the DOAS instrument onboard the LPMA/DOAS balloon gondola during a series of balloon flights will be presented.

Date	**Location**	**Campaign**	**Condition**
Nov. 23, 1996	León/Spain 42.6°N, 5.7°W	CHORUS	mid-lat. fall, sunset
Feb. 14, 1997	Kiruna/Sweden 67.9°N, 21.1°E	ADEOS	high lat. winter, vortex edge, sunset
Jun. 20, 1997	Gap/France 44.0°N, 6.1°E	CHELSOBA	mid.-lat summer, sunrise
Mar. 19, 1998	León/Spain 42.6°N, 5.7°W	CHELOSBA	mid-lat. spring, sunset
Aug. 19, 1998	Kiruna/Sweden 67.9°N, 21.1°E	SABINE/ CHELOSBA	high lat. summer, sunset/sunrise
Feb. 10, 1999	Kiruna/Sweden 67.9°N, 21.1°E	HALOMAX/ THESEO	high lat. winter, vortex core, sunset
Jun. 25, 1999	Gap/France 44.0°N, 6.1°E	HALOMAX/ THESEO	mid-lat. summer, sunrise
Feb. 18, 2000	Kiruna/Sweden 67.9°N, 21.1°E	EUROSOLVE/ THESEO2000	high lat. winter, vortex, sunset

Table 5.1: *Compendium of LPMA/DOAS balloon flights.*

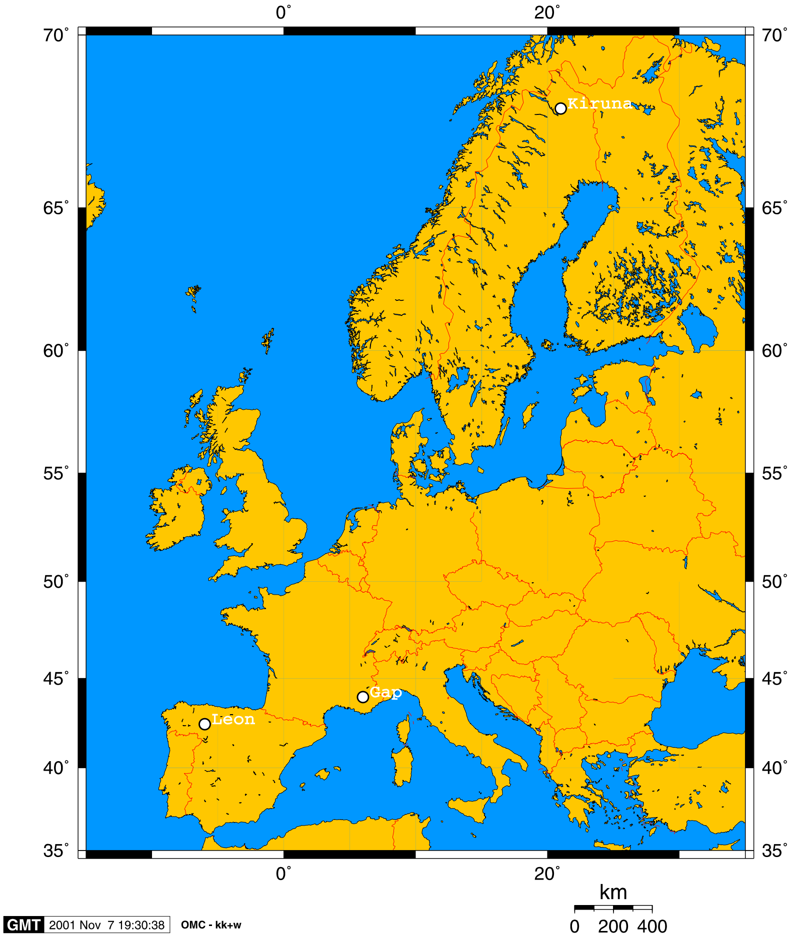

Figure 5.1: *Overview of the locations of the balloon launching sites Kiruna/Sweden, León/Spain, and Gap/France.*

In the first section, a brief discussion of the meteorological conditions during the balloon flights will be given, particular for the flights conducted within the polar vortex. In section 5.2 the DOAS evaluation of NO$_2$ and O$_3$ will be described in detail. The discussion of the results of the O$_3$ and NO$_2$ evaluation as well as of the $j_N O_2$ measurements is subject of section 5.3.

5.1 The LPMA/DOAS Balloon Flights

The LPMA/DOAS balloon flights took place in the framework of the EU-sponsored projects CHORUS, CHELOSBA, THESEO and THESEO2000 and the ADEOS/ILAS satellite validation campaign (see Table 5.1). The balloon was launched at three different sites: at Kiruna in northern Sweden, León in Spain and Gap in France (Figure 5.1). Three of the campaigns were performed during in Arctic winter and one during Arctic summer. Four mid-latitudes campaigns were carried out during spring, summer and autumn. A more detailed description will be given in the following sections.

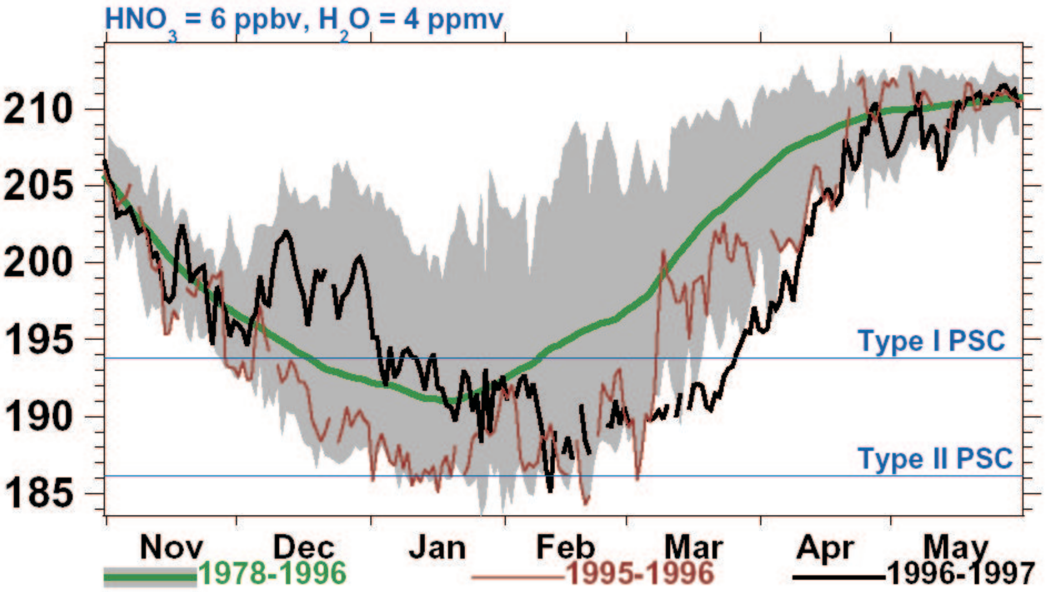

Figure 5.2: *Minimum temperature on the 475 K isentropic surface. The shaded region is the climatological range of 1979-1996 and the green line is the climatological mean. The red line indicates the year 1995/96 and the black line the year 1996/97. The blue lines mark the threshold temperatures for PSC type 1 and type 2 formation. Adapted from Coy et al. [1997].*

5.1.1 Arctic Winter Flights

Kiruna, Feb. 14, 1997

The polar vortex in the winter 1996/1997 was very cold and undisturbed until the end of April. However, the cooling started not before January and persisted until the end of March. The early winter was very warm, due the occurrence of a a Canadian warming, [*Naujokat et al.* 1999; *Pawson and Naujokat* 1999]. Until December the temperature on the 475 K isentropic surface was near the long-term average followed by warmer values through January. The vortex throughout March and April was colder by a significant amount than any vortex observed in the last 18 years during these month (see Figure 5.2). The minimum temperature remained below type 1 PSC formation temperature from the middle of January through most of March [*Coy et al.* 1997]. The formation of a strong polar vortex occurred in late December and was still intact in late April without any major midwinter warmings. The final warming occurred in mid-May. The winter 96/97 was characterized by small heat fluxes into the stratosphere and reduced wave breaking in the lower stratosphere, thus reducing the mixing across the lower vortex. The vortex itself was symmetrically, located above the pole and very large. The boundary region was very wide, indicating a strong but small vortex core at the pole. Measurements show a clear indication for denitrification at 18-23 km during mid-late February [*Kondo et al.* 2000] and to a smaller degree during April [*Rex et al.* 1999]. Significant chemical ozone loss was observed between mid-February and mid-March. In April unusually low ozone values were observed resulting from

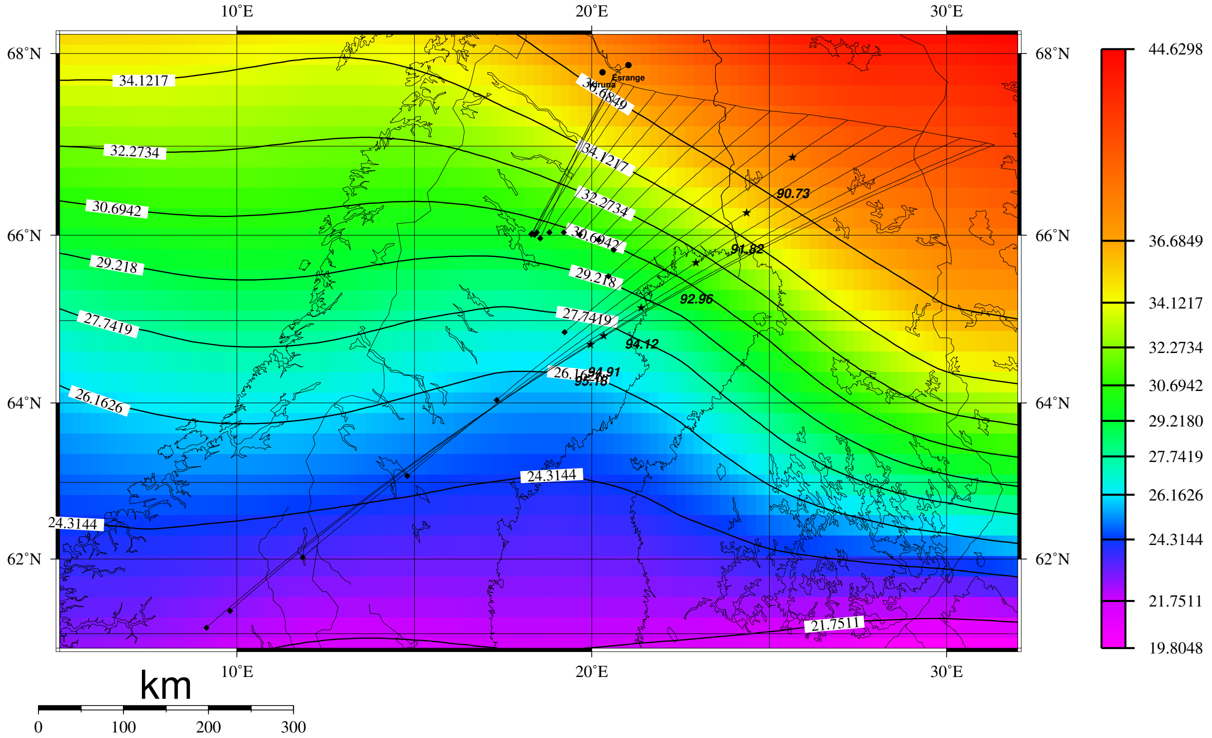

Figure 5.3: *Map of the polar vortex for the balloon flight in Kiruna on Feb. 14, 1997. The color code gives the potential vorticity in PV Units* [10^{-6} *K* m^2 $kg^{-1}s^{-1}$] *on the 475 K isentropic level. The balloon trajectory is the curved line from Kiruna in easterly direction. The straight lines indicate the line of sight of the measurements ending here at an altitude of 40 km.*

dynamical effects rather than chemical. The vertical extend and the maximum local ozone loss was very large but filled out the vortex less completely, thus the vortex averaged ozone loss was lower than in previous years. [*Manney et al.* 1997; *Schulz et al.* 2000].

The balloon was launched on February 14, 1997 at Esrange station near Kiruna/northern Sweden at 12:15 UT at a solar zenith angle of 82 °. The balloon float altitude of 30.2 km was reached at 14:11 UT at SZA=89.6°. At 14:15 UT the solar occultation started (SZA=90°) and ended at 14:55 UT at SZA=94.8° referring to a height of the tangent point of 11.9 km. Due to the winterly polar wind circulation, the balloon moved in easterly direction while measuring the sun in south/south-west direction. The balloon itself was located clearly inside the polar vortex, but close to the vortex boundary[1], during the whole flight. Accordingly, while probing air masses from inside the polar vortex during the balloon ascent, air masses from the boundary region and even from outside the vortex were probed during the course of the solar occultation measurements (see Figure 5.3).

---

[1] The vortex boundary is given by the region of the maximum gradient of the potential vorticity (PV) [*Nash et al.* 1996], but often simple certain values of the PV are used to define the boundary, e.g. 30-36 PV units for the boundary on the 475 K surface

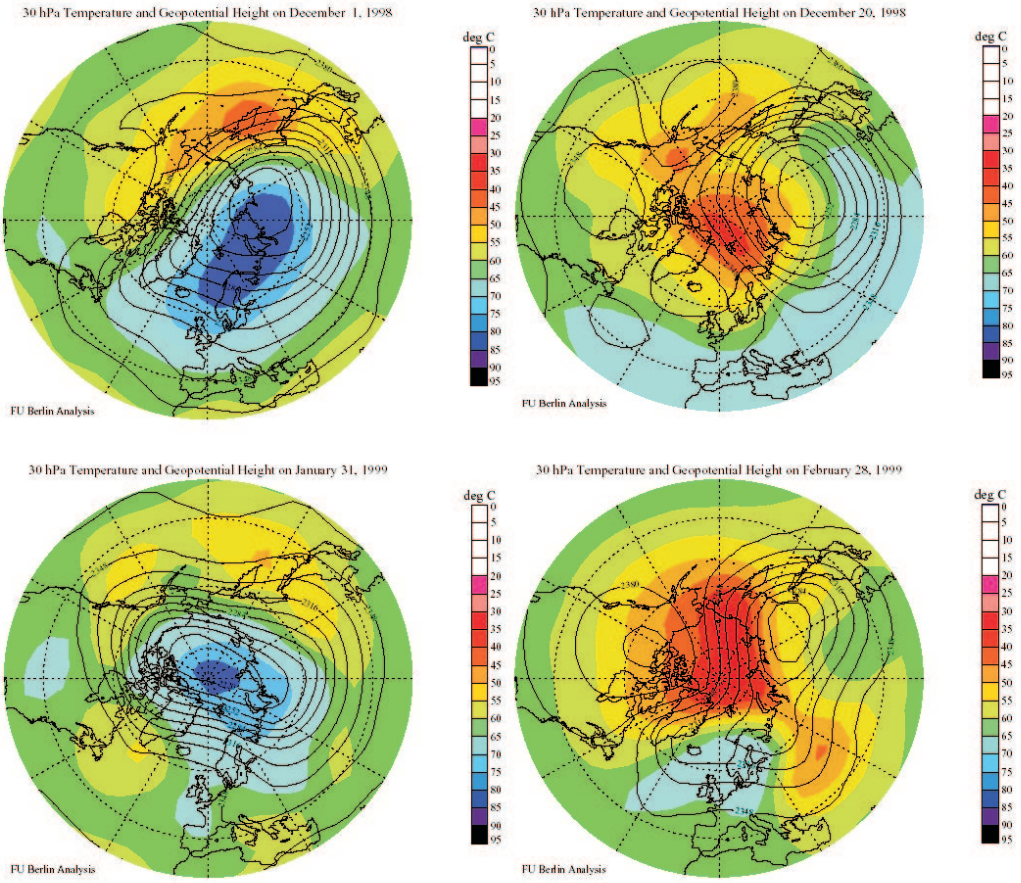

Figure 5.4: *Temperature and geopotential height at 30 hPa level on Dec. 1, 1998, Dec. 12, 1998, Jan. 31, 1999, and 28. Feb, 1999. Adapted from EORCU [1999].*

Kiruna, Feb. 10, 1999

The stratospheric winter 1998/1999 was a dynamic active winter with a disturbed and relatively weak vortex. The winter started cold with a strong polar vortex well established in November. The temperatures were low enough for the formation of PSCs by end of November. However, further PSC formation was prevented by a strong major warming in mid-December. Warm air covered the polar region throughout the stratosphere and the cold air was displaced far to mid-latitudes. This was just the second major warming event occurring in early December within the last 41-years. Temperatures slowly decreased in the stratosphere during January, but the circulation pattern and the temperatures remained disturbed for a long time. It was not before the end of January when a cold vortex was re-established over the polar region (see Figure 5.4). This was the beginning of the second period of this winter with minimum temperatures close or slightly below the threshold for PSC formation. A second major warming occurred around mid-February and the polar regions were covered with warm air and the rest of the cold air was displaced to northern Europe. The final springtime warming started rather early at the

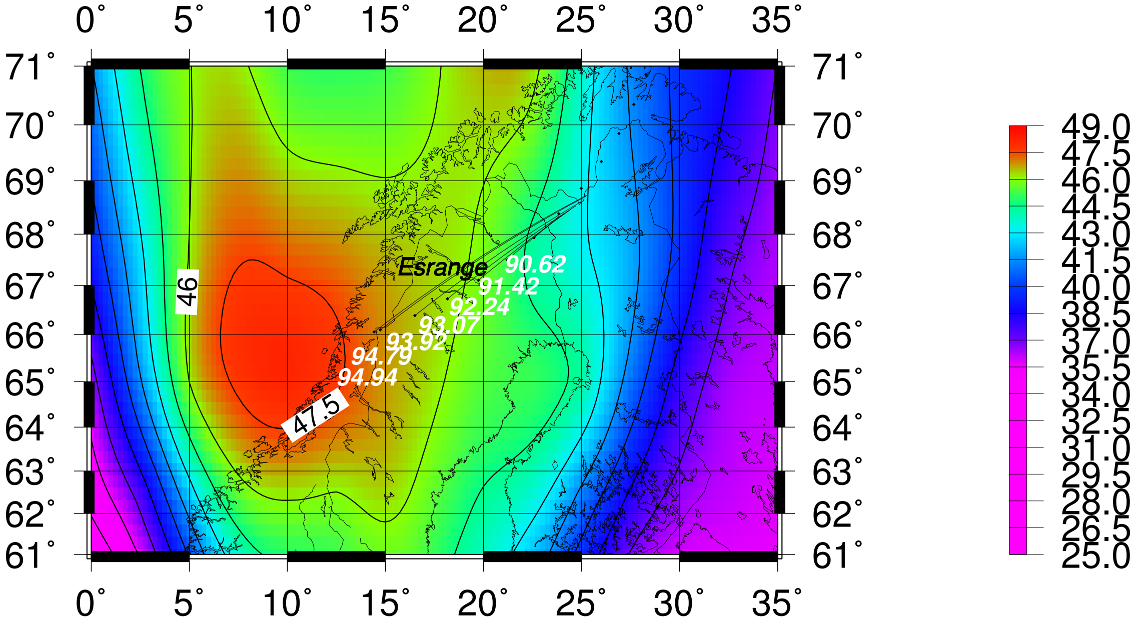

Figure 5.5: *Same as Figure 5.3, but for the balloon flight at Kiruna on Feb. 10, 1999.*

end of February, continuing into March, although a weak cyclonic circulation was re-established at the end of March. This had been the warmest winter in the stratosphere since 1984/1985 [*Naujokat et al.* 1999; *EORCU* 1999]. Only for the first period of possible PSC formation, PSCs were indeed observed over northern Scandinavia. No PSCs were reported for the second period in the first half of February. This might be due to the rare number of observations. Consistently, with the high average temperatures in the stratosphere, being approximately 10 K higher than in previous years, no significant ozone loss was observed on the 465-485 K isentropic surface, apart from some small negative values at the end of December and the beginning of January [*Schulz et al.* 2001]. The loss of the total column of ozone was estimated to be ~ 5% [*Goutail et al.* 2000].

The flight of the LPMA/DOAS gondola was carried out on February 10, 1999, when the polar vortex was located over Kiruna. The balloon was launched at 11:35 UT (SZA=82.5°). The trajectory of the gondola pointed to the easterly direction towards the boundary of the vortex with the line-of-sight of the measurements towards the core of the vortex (see Figure 5.5). The balloon float altitude of 28.5 km was reached at 13:07 UT for a SZA of 86.1°. SZA=90° was reached at 13:59 UT and the solar occultation ended at 14:55 UT (SZA= 94.9° and tangent height = 9.8 km).

Kiruna, Feb. 18, 2000

The arctic winter 1999/2000 was one of the coldest winters in the lower stratosphere since 1964/65. The polar region cooled rapidly in the first half of November, with the polar vortex becoming stronger throughout the stratosphere. The temperatures fell below the PSC threshold in the middle stratosphere by mid-November and in the lower stratosphere by end of the month.

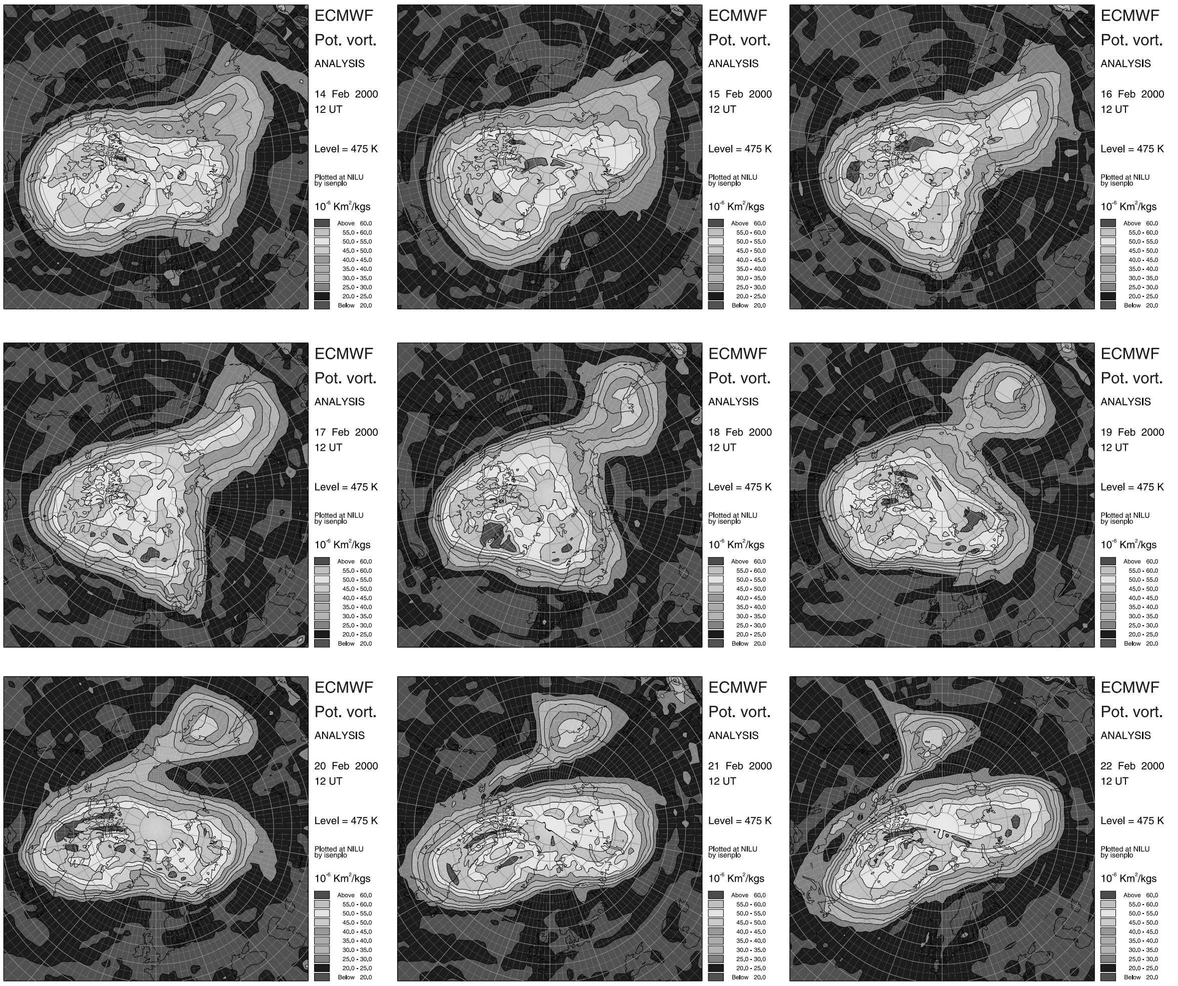

Figure 5.6: *Potential vorticity on the 475 K level for the Arctic region between Feb. 14, 2000 and Feb. 22, 2000.*

During the first half of December the vortex intensified and was cold and mostly undisturbed during the second half. The center of the strong vortex lay between Scandinavia and the Pole with minimum temperatures around and below 188 K (threshold for PSC type 2 formation). Throughout January, the vortex was cold and strong and the minimum temperatures were low enough for PSC formation. In February, an upper stratospheric warming affected the lower stratospheric circulation. However, during the first week of February minimum temperatures temporarily reached the PSC type 2 threshold. The stratosphere above Europe was warm, with Scandinavia outside the polar vortex except for a few days around the eighteenth of February. During March, minimum temperatures were continuously below the PSC threshold in the lower stratosphere. In mid-March, the temperatures rose above the PSC threshold. The vortex split and the two parts were drifting to Canada and to eastern Europe, respectively. The weakened vortex was moving back to the Pole by end of March [*Naujokat et al.* 1999; *EORCU* 2000]. Low temperatures and PSCs occurred as a result of both synoptic and mesoscale (lee-wave) processes.

During this winter PSCs were extensively seen in the vortex with two main periods from mid-December to early February and from late February to mid-March. Very large solid nitric acid trihydrate particles have been measured for the first time in the Arctic stratosphere during this winter [*Fahey et al.* 2000]. The vortex was strongly activated and extensively denitrified to a degree previously observed only in the Antarctica [*Santee et al.* 2000; *Popp et al.* 2001]. Accordingly, the largest local ozone loss yet seen in the Arctic of over 70% was observed in the altitude range of 18-20 km. Most of the ozone loss occurred in March, but losses in January and February were also significant. The loss of the total column of ozone was about 20-25 %, less than in previous years partly as a result of the narrower vertical extend of the PSCs [*EORCU* 2000; *Sinnhuber et al.* 2000].

On February, 18 the gondola was launched at 12:21 UT (SZA = 81.5°), when the polar vortex was located above Kiruna. As shown in Figure 5.7 the balloon gondola moved to the east with the line of sight of the measurements pointing to the south/south-west towards the boundary of the vortex, but still inside the vortex. At 14:11 UT and a SZA of 88.5° the balloon float altitude of 30.0 km was reached. The solar occultation measurements began at 14:25 UT and ended at a SZA of 95.0° at 15:11 UT (tangent height = 9.5 km).

5.1.2 Arctic Summer Flight

The main features of the summer circulation system has been described in section 3.9. A strong and steady zonal wind surrounds the Pole and suppresses the mixing of polar with mid-latitudinal air. At the end of the summer (mid- to end of August), the circulation pattern breaks down and after a period of transition, the formation of the winter circulation begins.

The launch of the balloon gondola took place in Kiruna on August 19, 1998 at 15:52 UT (SZA=73.9°). The break-down of the strong summer circulation already occurred and the predominant stratospheric winds were weak. Hence, flights with very long durations can be performed with the gondola remaining near the launch site. This allows to perform sunset and sunrise measurements during one flight. The gondola reached the float altitude of 39 km at 18:17 UT (SZA = 87.9°). The occultation measurements started at 18:54 UT. The last measurement was at 20:25 UT with a SZA of 95.9° (tangent height of 9.1 km km). After a short nighttime period and a descent of the gondola to 33.2 km, the sunrise measurements began at 1:13 UT (SZA = 94.9°, tangent height of 11.5 km). A SZA of 90° was reached at 2:29 UT and the descent of the balloon started. The descent measurements ended at an altitude of 23.2 km at 4:02 UT (SZA = 82.4°). During the whole flight, the gondola remained in fact close to Kiruna performing sunset measurements in north-westerly and the subsequent sunrise measurements in north-easterly direction.

5.1.3 Mid-Latitude Flights

León, Nov. 23, 1996

In 1996, the polar vortex developed already in October and the westerly zonal wind pattern reached south to a latitude of 30°N. A strong warming in mid-November caused an elongation of the vortex and a split into two parts. One fragment above Island intensified and developed to the main vortex. The vortex boundary came near to northern Spain by mid- to end of November

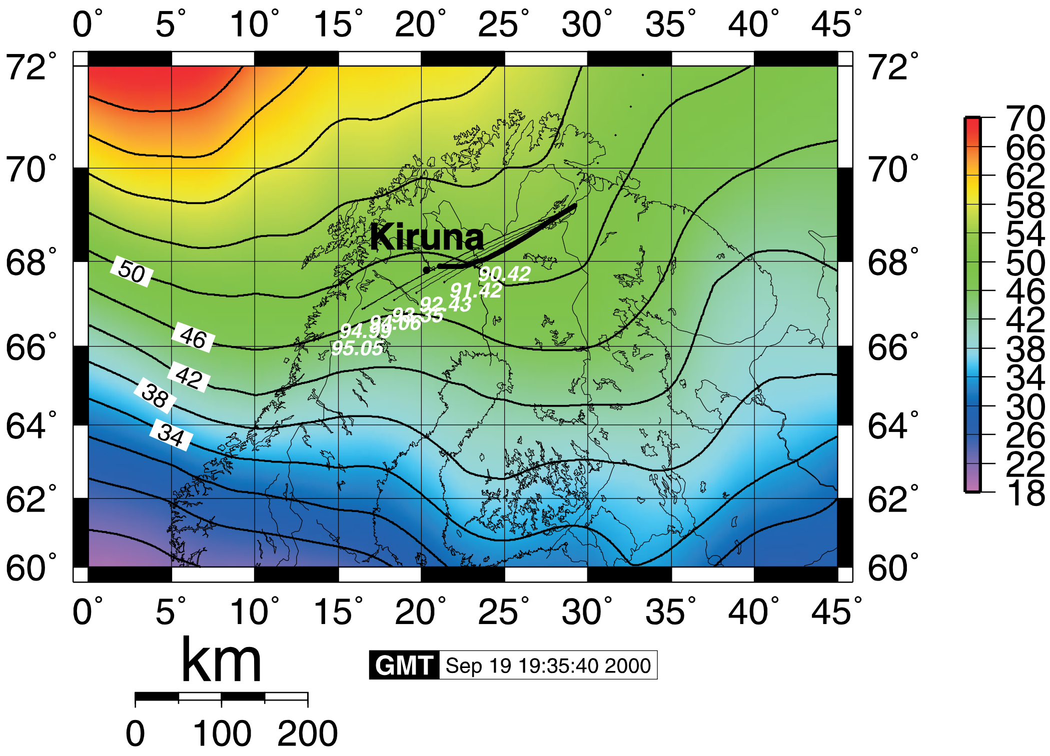

Figure 5.7: *Same as Figure 5.3, but for the balloon flight in Kiruna on Feb. 18, 2000.*

accompanied by an increase of the wind speeds and a decrease of the temperature [*Naujokat et al.* 1996].

The flight of the LPMA/DOAS gondola took place in León/northern Spain on November, 23, 1996. At 14:45 UT (SZA = 73°) the balloon was launched and the float altitude of 30.7 km was reached at 16:20 UT for a SZA of 86.4°. In accordance with the winterly flow pattern the balloon trajectory was pointing to the east and the line-of-sight of the measurements gathered light from the south/south-west direction. The beginning of the solar occultation was at 16:38 UT and ended early for a SZA of 92.8° at 16:53 UT, corresponding to a height of the tangent point of 19.9 km.

León, Mar. 19, 1998

The winter 1997/1998 was relatively warm and several minor warmings occurred, which significantly eroded the vortex, but it did not break up. That winter continued the series of winters without a major midwinter warming since 1990. The vortex itself formed much as usual at higher altitudes, but at lower altitudes it was much weaker than in most years, with noticeable slower winds. From the beginning of February, the vortex was warm and never well-established at altitudes below about 18 km. The final warming started in the middle of March [*EORCU* 1998; *Naujokat et al.* 1999].

The launch was carried out on March 19, 1998 from León at 16:05 UT (SZA = 65°). The polar vortex was located between Scandinavia and the Pole with León being clearly outside.

Similar to the previous flight at León, the gondola was moving to the east with a westerly line-of-sight direction. The float altitude of 38.0 km was reached at 18:08 UT (SZA = 87.2°). At 18:21 UT the solar occultation began and the last measurement was performed at 18:52 UT and a SZA of 96.5° (tangent height = 6 km).

Gap, Jun. 20, 1997

The predominant wind pattern in summer is a relatively undisturbed and strong zonal wind in westerly direction. The meridional transport is largely suppressed and the stratosphere comes close to radiative equilibrium (see chapter 3.9).

In contrast to the flights conducted in Kiruna and León, sunrise measurements were performed. The balloon gondola was launched on June 19, 1997 at 23:45 UT from Gap/southern France. On the next day, the float altitude of 39.8 km was reached. The sunrise measurements started at 3:24 UT for SZA = 95.5° (height of the tangent point = 12.9 km). While the gondola moved to the west, the light of the rising sun in north-easterly direction was measured. At 4:07 UT a SZA of 90° was reached. Afterwards measurements during the descent of the balloon were performed starting at 4:42 UT (SZA = 85.2°), but ending at a height of 33.8 km at 7:17 UT (SZA = 60.5°) already.

Gap, Jun. 25, 1999

The meteorological situation for this flight is similar to the previous flight performed in Gap. Again it was decided to conduct sunrise measurements. The balloon launch took place from Gap on Jun. 24, 1999 at 23:00 UT and the balloon reached the float altitude of 39.0 km at 3:00 UT on the next day. The gondola moved in westerly direction and the line of sight of the measurements pointed to the north-east. The sunrise measurements began for a SZA of 94.6° at 3:34 UT (tangent height = 18.1 km) and ended at 4:08 UT. At 4:34 UT (SZA = 86.3 °), the subsequent balloon descent started. Again, the descent measurement were stopped for a rather high balloon altitude of 20.8 km at 8:17 UT (SZA= 49.3°).

5.2 NO_2 and O_3 DOAS Evaluation

5.2.1 NO_2 Evaluation

The NO_2 evaluation was performed in the wavelength range from 425 nm to 465 nm. The used set of reference spectra contained a NO_2 reference spectrum for a temperature of $T = -70°C$ (for Arctic winter flights) or $T = -45°C$ (for all other flights) and two ozone spectra for $T = -40°C$ and $T = -60°C$, all of them recorded with the same instrument in the laboratory. The NO_2 spectra were calibrated (with respect to wavelength and the absolute value) with the NO_2 cross sections given by *Harder et al.* [1997]. For that purpose the high resolution cross section of *Harder et al.* [1997] was convoluted to our instrumental resolution using the standard convolution tool of *WinDOAS*. A I_0-corrected convolution was performed, too, and the differences between both calculated. This I_0-correction was then added to the measured, calibrated NO_2 reference spectra. Further, the O_4 spectrum of *Greenblatt et al.* [1990] and a H_2O spectrum for T = 213 K [*Rothman*

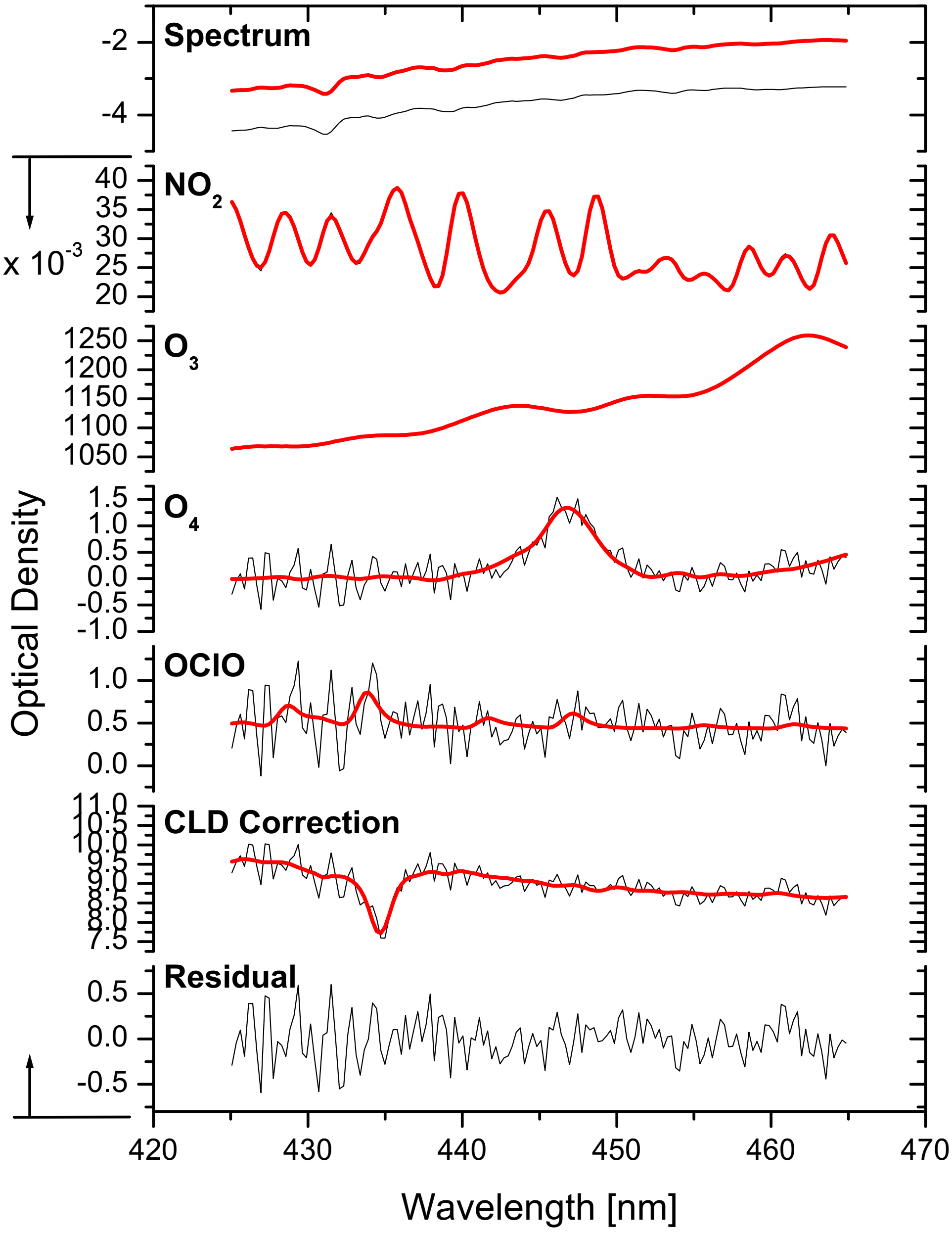

Figure 5.8: *Example of the NO_2 evaluation for a spectrum measured at Kiruna on Feb. 10, 1999 during solar occultation at 14:50 UT (SZA = 94.1°) . The upper panel shows the Fraunhofer spectrum (red line) and the measured spectrum (black line). In the panels below, the retrieved trace gas absorptions of NO_2 (T=-70°C), ozone (T=-60°C) (the ozone absorption for T=-40°C is not shown), O_4, OClO and the CLD corrections are shown. In the lowest panel the remaining residual of the fitting procedure is displayed. The red lines indicates the spectral absorption and the black line the sum of the spectral absorption and the residual.*

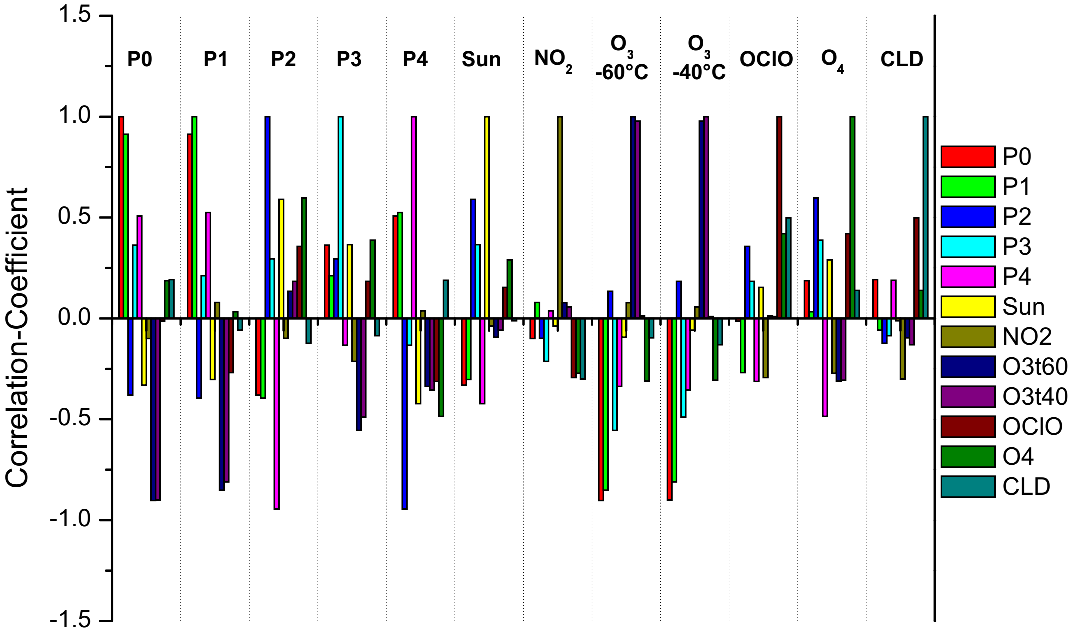

Figure 5.9: *Correlation-coefficients for the NO_2 evaluation. P0 - P4 denote the polynomial (of degree 0 to 4), Sun the Fraunhofer spectrum etc. A correlation-coefficient in the range of ± 1 indicates a large correlation, while a value around zero is an indication of a negligible correlation. The o3 reference spectra were not orthogolized here and a large correlation is obtained. However, this does not affect the result for NO_2.*

et al. 1996] was used[2]. For the Arctic winter flights a OClO spectrum recorded at T = 220 K with our instrument was included in the fitting procedure, too. As already discussed in section 4.1.4 a center to limb darkening correction (CLD correction) has to be applied to account for changes in the optical densities of the Fraunhofer lines during solar occultation. The consequences of this issue are discussed in more detail in chapter 7. As also shown in this chapter, a Ring spectrum has not to be included in the fitting procedure. A polynomial of degree 4 was used to approximate the broad-band components. An additional intensity offset (polynomial of degree 1) was included in the fit to account for the spectrometer stray light. The spectrum recorded immediately after the balloon float altitude was reached was used as Fraunhofer reference spectrum. The relative wavelength alignment of the O_3 and OClO reference spectra were obtained in a similar manner as for NO_2 (but without adding a I_0-correction), i.e. by fitting to convoluted cross sections taken from the literature (measured with Fourier Transform Interferometers). The whole package of trace gases was then aligned to the Fraunhofer spectrum. For that, a solar occultation spectrum was evaluated (with large NO_2 and O_3 absorption) with the set of reference spectra and the Fraunhofer spectrum allowed to shift and squeeze. The obtained coefficients for the shift and squeeze were then used for the evaluation of the whole flight where only the measured spectra

---

[2] Water vapor is in general not included in the fitting procedure as the H_2O absorption in the considered wavelength range is extremely weak, but it was used for sensitivity tests.

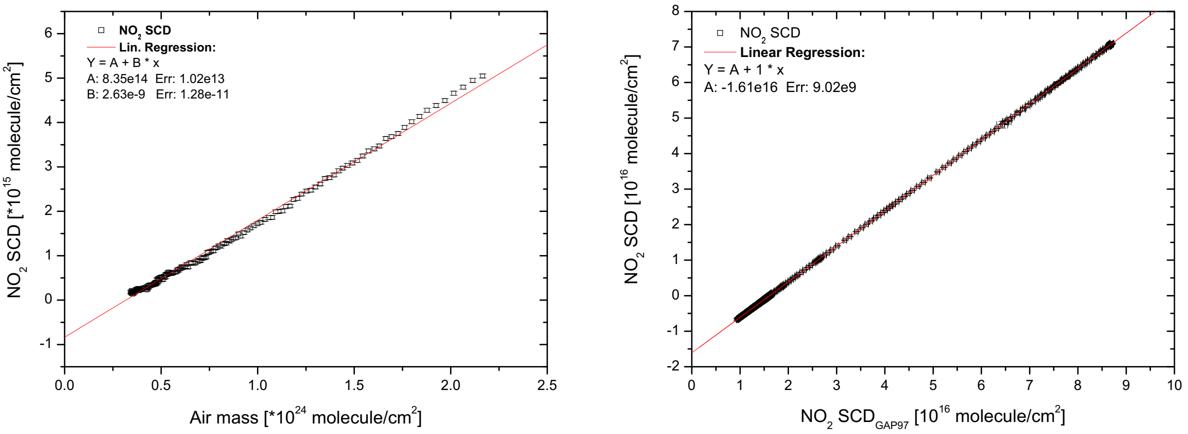

Figure 5.10: *The left panel shows the Langley-plot for NO_2 for the flight in Gap on June 20, 1997. The right panel shows an example of the determination of the absorber amount in the Fraunhofer spectrum for all other flights (here, for the flight in Kiruna, Feb. 14, 1997). The NO_2 evaluation is performed twice. Once with the Fraunhofer spectrum of the corresponding flight and once with the Fraunhofer spectrum of the Gap-flight in 1997. From the offset of the linear correlation and the known amount of NO_2 in the Gap 1997 Fraunhofer spectrum, the amount of NO_2 in the Fraunhofer spectrum of the flight itself can be obtained.*

were allowed to shift and squeeze. The correlation-coefficients for this set of reference spectra together with the polynomial is shown in Figure 5.9. Obviously, the correlations between the NO_2 reference spectrum and the polynomial or other reference spectra were negligible. Figure 5.8 shows an example for the spectral retrieval of NO_2 for a spectrum measured at 14:50 UT for $SZA = 94.1°$.

The total atmospheric SCD is given by the sum of the SCD retrieved by the fit and the amount of NO_2 in the Fraunhofer reference spectrum[3]. The absorber amount in the Fraunhofer reference spectrum is usually calculated with a so-called *Langley plot*. Assuming a constant mixing ratio VMR above balloon float altitude, the SCDs obtained for balloon float for $SZA <$ $90°$ can be written as[4]:

$$SCD = AMF \cdot VCD_{Air} \cdot VMR - SCD_{Fraunh} \tag{5.1}$$

with the air mass factor AMF, the vertical column density for air VCD_{Air} and the slant column density in the Fraunhofer spectrum SCD_{Fraunh}. The intercept with the SCD-axis of a linear fit to SCD plotted as a function of the slant column density of air $SCD_{Air} = AMF \cdot VCD_{Air}$ yields the amount of the absorber in the Fraunhofer reference spectrum SCD_{Fraunh}. However, the assumption of a constant NO_2 mixing ration is not fulfilled for typical balloon

---

[3] The Fraunhofer spectrum used for the spectral retrieval is recorded at balloon float height and hence includes some atmospheric absorptions.

[4] This is only valid for measurements of direct sunlight. For measurements of scattered light a different expression has to used [e.g., *Erle* 1999; *Frieß et al.* 2001].

Location and Date	NO_2: SCD_{Fraunh} [molec/cm^2]	O_3: SCD_{Fraunh} [molec/cm^2]
León, Nov. 23, 1996	$1.37 \cdot 10^{16} \pm 2.20 \cdot 10^{13}$	$1.91 \cdot 10^{19} \pm 1.20 \cdot 10^{16}$
Kiruna, Feb. 14, 1997	$1.69 \cdot 10^{16} \pm 1.02 \cdot 10^{13}$	$3.49 \cdot 10^{19} \pm 1.64 \cdot 10^{15}$
Gap, Jun. 20, 1997	$8.35 \cdot 10^{14} \pm 1.02 \cdot 10^{13}$	$1.45 \cdot 10^{18} \pm 1.64 \cdot 10^{15}$
León, Mar. 19, 1998	$7.69 \cdot 10^{15} \pm 1.02 \cdot 10^{13}$	$9.11 \cdot 10^{18} \pm 1.65 \cdot 10^{15}$
Kiruna, Aug. 19, 1998	$2.5 \cdot 10^{15} \pm 1.02 \cdot 10^{13}$	$5.79 \cdot 10^{18} \pm 1.71 \cdot 10^{15}$
Kiruna, Aug. 20, 1998	$2.82 \cdot 10^{16} \pm 1.10 \cdot 10^{13}$	$5.79 \cdot 10^{18} \pm 1.71 \cdot 10^{15}$
Kiruna, Feb. 10, 1999	$4.55 \cdot 10^{15} \pm 1.16 \cdot 10^{13}$	$1.24 \cdot 10^{19} \pm 2.66 \cdot 10^{15}$
Gap, Jun. 25, 1999	$1.39 \cdot 10^{15} \pm 1.02 \cdot 10^{13}$	$4.97 \cdot 10^{18} \pm 1.65 \cdot 10^{15}$
Kiruna, Feb. 18, 2000	$1.45 \cdot 10^{16} \pm 1.10 \cdot 10^{13}$	$2.70 \cdot 10^{19} \pm 1.73 \cdot 10^{15}$

Table 5.2: *Amount of NO_2 and O_3 in the Fraunhofer spectra. Please note, that for the O_3 retrieval of the Kiruna 1998 flight only one Fraunhofer spectrum was used for ascent/sunset and sunrise/descent. For each flight, the spectrum recorded immediately after the balloon float altitude was reached was used as Fraunhofer reference spectrum. For the corresponding balloon float altitudes and the SZAs see section 5.1.*

float altitudes ranging from 30 to 40 km and hence some uncertainties are indebted with this technique. Therefore, this Langley-plot technique was only used for the flight in Gap on June 20, 1997 (Figure 5.10, left panel). Inspecting this Langley-plot, a clear deviation from the assumed linear relationship can be observed for large air masses. This is certainly the result of the non-constant mixing ratios of NO_2 above balloon float, but probably photochemical changes of the NO_2 abundances contributed to this, too. For this flight, the Fraunhofer spectrum was taken at an altitude of 39 km and for a SZA of 76° resulting in a very small amount of NO_2 in the Fraunhofer spectrum. Therefore, the potential impact of the systematical error, introduced by the Langley-plot, on the total SCD is small. For all other flights, the NO_2 amount in the Fraunhofer spectrum was determined in the following way. First, a standard evaluation with the Fraunhofer spectrum of the flight was performed. Afterwards, the evaluation was performed again, but with the Fraunhofer spectrum of the Gap flight in 1997. The offset of the SCDs obtained from both evaluations can be easily derived by a linear fit with a fixed slope of one (Figure 5.10, right panel). The NO_2 amount in the corresponding Fraunhofer spectrum is then given by the sum of this offset and the amount of NO_2 in the Fraunhofer spectrum of the Gap 1997 flight. The NO_2 (and O_3) amounts in the Fraunhofer spectra for all flights are listed in Table 5.2 .

5.2.2 O_3 Evaluation

Ozone was evaluated in the temperature-independent wavelength range of the Chappuis band [*Burkholder and Talukdar* 1994] from 545 to 615 nm. The used O_3 absorption cross section was given by *Anderson and Mauersberger* [1992] for T=296 K. Two NO_2 reference spectrum

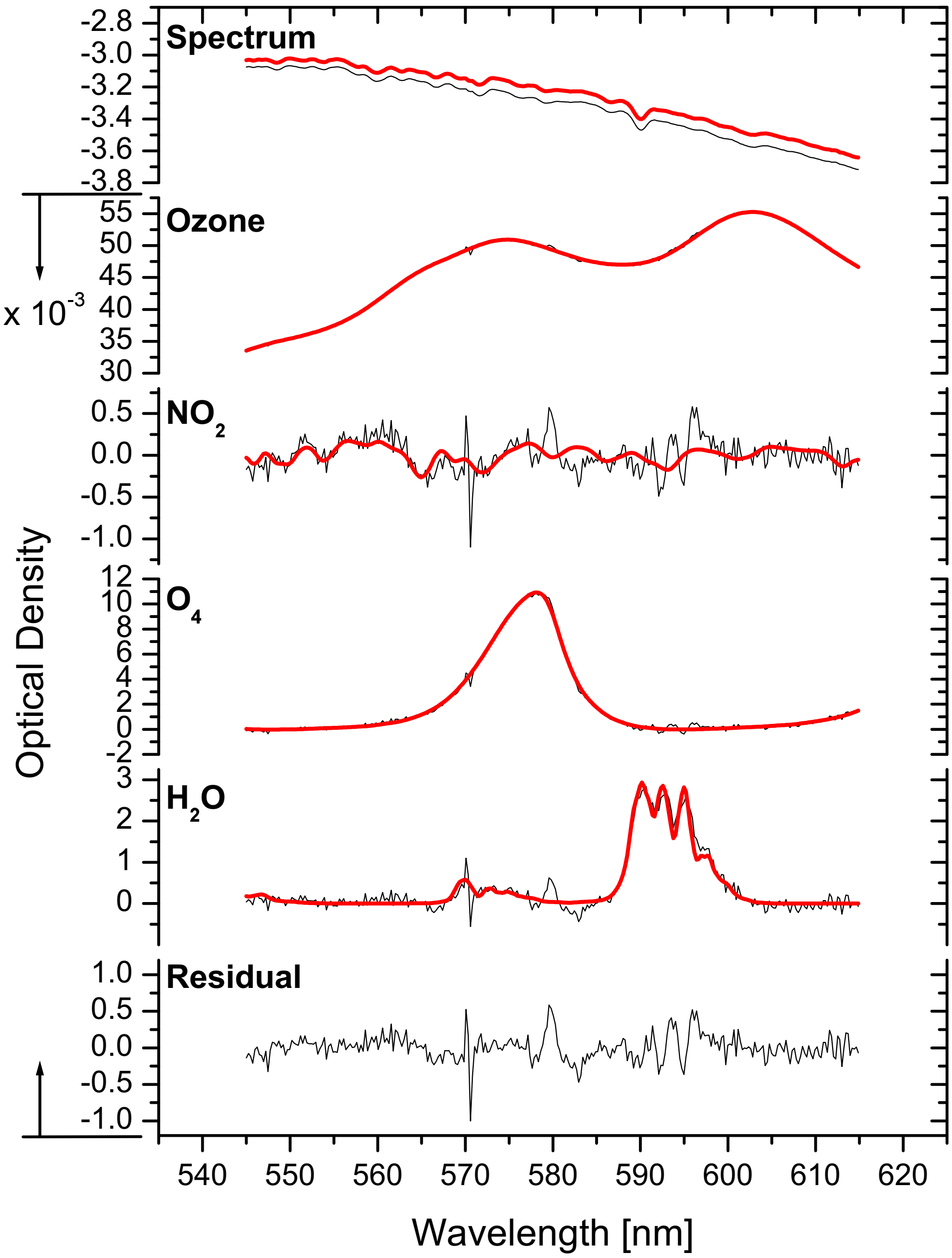

Figure 5.11: *Example of the O_3 evaluation for a spectrum measured in León on Nov. 23, 1996 during the balloon ascent at 15:02 UT (SZA = 74.6°) for a balloon altitude of 7.5 km. The upper panel shows the Fraunhofer spectrum (red line) and the measured spectrum (black line). In the panels below, the retrieved trace gas absorptions of O_3, NO_2 (T=-45°C) (the NO_2 absorption for T=-70°C is not shown), O_4, and H_2O are shown. The lowest panel displays the remaining residual of the fitting procedure. The red lines indicates the spectral absorption and the black line the sum of the spectral absorption and the residual.Besides other structures (mainly in the range of the H_2O absorption), a narrow structure occurs around 570 nm probably caused by the grating or the photodiode (see section 4.1.4). Obviouly. the impact on the ozone retrieval is small.*

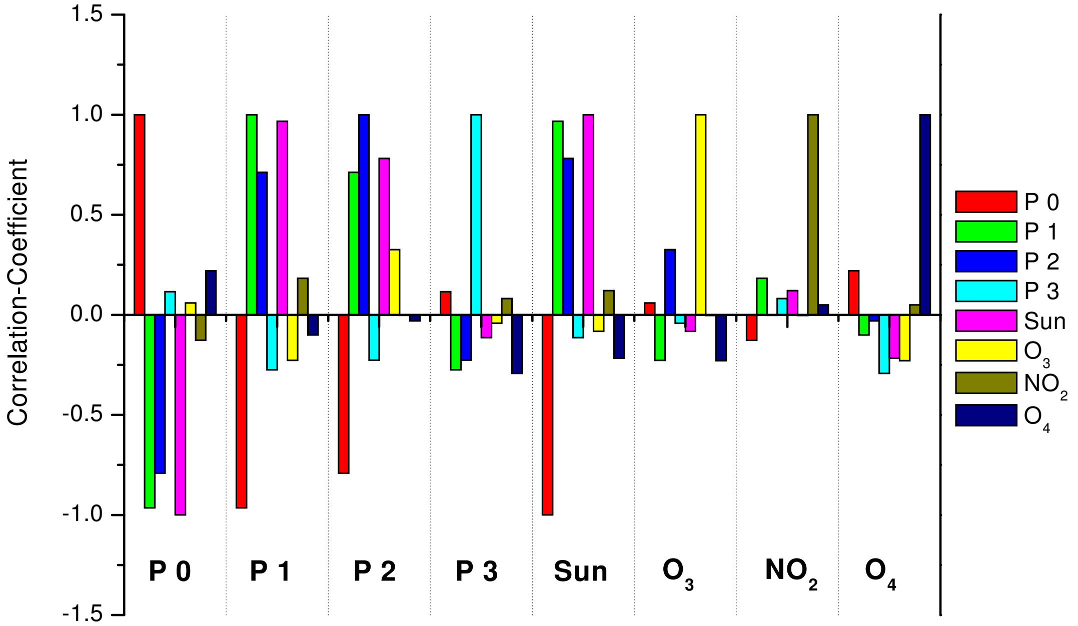

Figure 5.12: *Correlation-coefficients for the O_3 evaluation. P0 - P3 denote the polynomial (of degree 0 to 3), Sun the Fraunhofer spectrum etc. A correlation-coefficient in the range of ± 1 indicates a large correlation, while a value around zero is an indication of a negligible correlation.*

recorded in the laboratory for T=-70°C and T=-45°C, respectively (for the Arctic winter flight, only T=-70°C was used), the O_4 spectrum of *Greenblatt et al.* [1990] and a H_2O spectrum for T = 213 K [*Rothman et al.* 1996] were used in the fitting procedure. Neither a CLD correction nor a Ring spectrum were included, as both were found to be negligible in the considered wavelength range. To account for the broad-band extinction processes a polynomial of degree 3 was used. To reduce the degree of the polynomial to 3 is essential here, as a a larger degree of the polynomial results in strong correlations with the O_3 reference spectrum. The spectrometer stray light was approximated by an additional intensity offset (polynomial of degree one). The relative wavelength alignment was obtained in a similar way as already described in the previous section. During the fitting procedure, only the measured spectra were allowed to shift and squeeze. The same Fraunhofer reference spectra were used as for the NO_2 evaluation. The correlation-coefficients for the O_3 retrieval are shown in 5.12. No (or only small) correlations between the O_3 reference spectrum and the other reference spectra or the polynomial were found. A typical example for the O_3 retrieval is shown in Figure 5.11. The estimation of the amount of O_3 in the Fraunhofer reference spectra was performed with the same methods as described in the previous section. Figure 5.13 shows the Langley-plot for the Gap 1997 flight (left panel) and an example of the determination of the O_3 amount in the Fraunhofer spectrum for the other flights. The retrieved amounts of O_3 in the Fraunhofer spectra are given in Table 5.2.

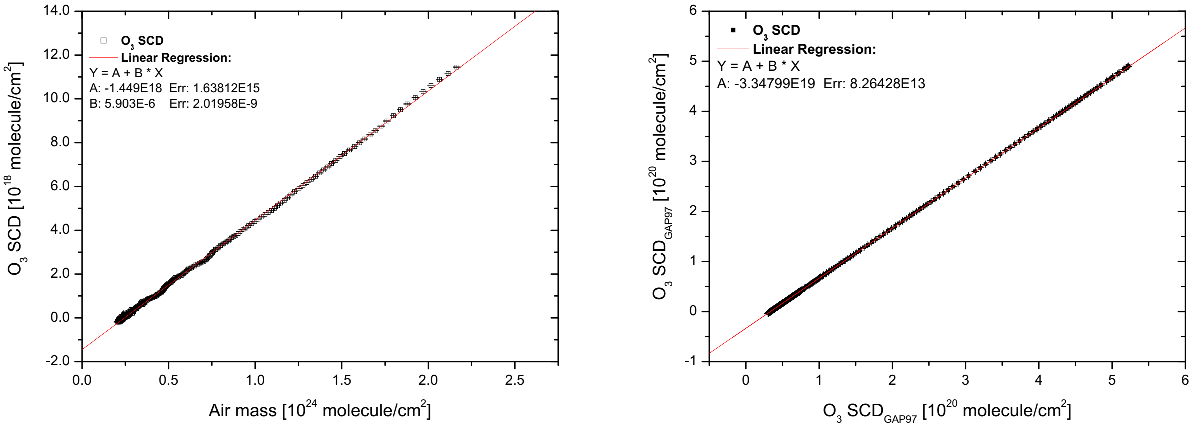

Figure 5.13: *The left panel shows the Langley-plot for O_3 for the flight in Gap on June 20, 1997. The right panel shows an example of the determination of the O_3 amount in the Fraunhofer spectrum for all other flights (here, for the flight in Kiruna, Feb. 14, 1997). For a more detailed explanation see Figure 5.10 and the text.*

5.2.3 Discussion of Errors

The accuracy of the slant column densities of NO_2 and O_3 is given by the precision of the fitting procedure and the systematical errors. The precision of the fit is calculated by the evaluation software as described in chapter 4.1.3. As stated there, this is based on the assumption, that the remaining residual consists of pure noise only. As can be seen from Figure 5.14 this assumption is not fulfilled. The figure shows the remaining residuals of the retrieval of NO_2 for spectra measured during the solar occultation in Kiruna on Feb. 14, 1997. In all residuals, the same structures can be found, but with different amplitude. This systematical structures are caused by the combination of the effects described in chapter 4.1.4. In consequence, the statistical error of the fit is largely overestimated, i.e. the statistical scatter of the SCDs is clearly smaller as the calculated 1-σ error. To make this visible, the NO_2 SCDs measured during the Kiruna 1997 flight were high-pass filtered with a 5-point running mean and plotted in combination with the calculated 1-σ error in Figure 5.15. It is evident, that in particular for the balloon ascent the scatter of the SCDs is only half as large as the given error bars. To a minor degree, the same is true for solar occultation. For the float phase, a large scatter of the SCDs is found, possibly an artefact of the filter. Thus, the error given by the fitting procedure is a combination of the true statistical error (due to the noise) and systematical components due deficits of the model function and instrumental shortcomings.

The total SCD_{total} is obtained by adding the SCD_{Fraunh} in the Fraunhofer spectrum to the SCD retrieved with the fitting procedure. Thus, the error of SCD_{total} is given by Gaussian error propagation of the individual errors of SCD_{Fraunh} and SCD.

There are several sources of systematic errors such as the temperature dependence of the cross sections, the error of the cross section itself and errors due to an improper wavelength alignment. Also the choice of the cross section is a source of a systematic error. Usually, the literature provides various cross sections for one species which can have a distinct bias. A detailed investigation of the propagation of these systematical uncertainties to the result of the fitting

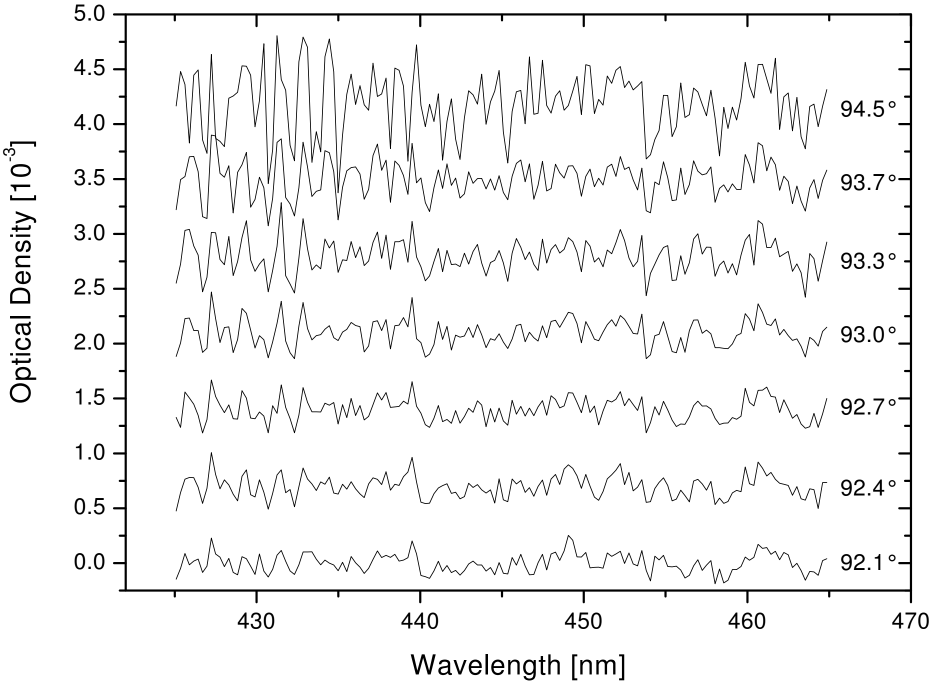

Figure 5.14: *Remaining residual structures of the retrieval of NO_2 for spectra measured during solar occultation at Kiruna, on Feb. 14, 1997. For clarification the different spectra are shifted by $7 \cdot 10^{-4}$. The numbers on the right side are the SZAs of the measurement.*

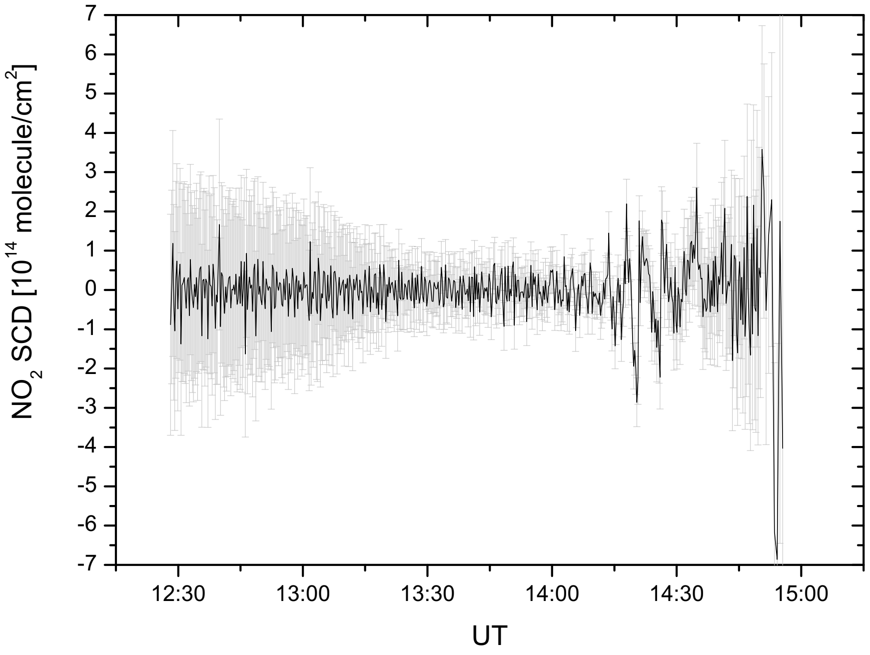

Figure 5.15: *High-pass filtered NO_2-SCDs measured during the Kiruna 1997 flight. For the filtering a 5-point running mean was used.*

procedure requires a large number of numerical tests. Thus, the various systematical errors will be estimated only.

The spectral retrieval of ozone is performed around the peak of the Chappuis band. In this range, the cross section is found to be almost independent of temperature with a variation below 1% [*Burkholder and Talukdar* 1994]. The accuracy of the used cross section of *Anderson and Mauersberger* [1992] is about 1%. The discrepancies between the various ozone cross sections in the Chappuis band given by different authors is relatively small, the different values agree within 3% [*Burrows et al.* 1999]. The error du to improper wavelength alignment was estimated to be around 0.5-1%.

In contrast to ozone, the cross section of NO_2 shows a strong temperature dependence. Figure 5.16 (upper panel) compares the differential cross sections of NO_2 measured at temperatures of 217 K, 230 K, and 294 K. The differential cross section largely increases when decreasing the temperature, whereas the changes of the shape are small. A change of the differential cross section of 10-15% is observed between 217 K and 230 K and even of 20-25% between 217 K and 294 K, respectively. Thus the uncertainty caused by temperature dependence is assumed to be 10%. The NO_2 cross sections used for the evaluation were measured with the instrument itself in the laboratory, however, to obtain proper values for the SCDs, they have to be calibrated with convoluted cross section given by the literature. This calibration was performed with the cross sections given by *Harder et al.* [1997]. Thus, the accuracy of this cross section of 4% and the error of the fit of 0.5% used for the calibration has to be taken into account. The error due to an improper wavelength alignment was estimated to be below 1%. The literature provides a large number of NO_2 cross section in the visible wavelength range. Figure 5.16 compares the differential cross section of NO_2 measured at room temperature by different authors. It is obvious, that they agree all within 5%. However, the recently measured cross section by *Voigt et al.* [2001] shows clearly smaller values. Thus, using this cross section instead of the cross section measured by *Harder et al.* [1997] would result in ~15% smaller SCDs.

5.3 Results and Discussion

For all eight flights of the LPMA/DOAS balloon gondola O_3 and NO_2 profiles were retrieved from the measured O_3 and NO_2-SCDs in the visible wavelength range during balloon ascent (or descent) and solar occultation. All profiles shown in this chapter were obtained with the inversion technique, for balloon ascent, the Onion Peeling technique (denoted OP) was used, additionally. For the Gap flight in 1997, a descent profile could not be measured due to technical problems. The error bars (of the DOAS measurements) given in this chapter correspond to the 1-σ error.

In the first section of this chapter, the j_{NO_2} measurements, performed during two flights, will be presented. A detailed discussion of the results of the O_3 and the NO_2 measurements is subject of sections 5.3.2 and 5.3.3. In the last section, the O_3 and NO_2 measurements will be compared with the model calculations of the CTMs SLIMCAT, KASIMA and REPROBUS.

5.3.1 j_{NO_2} Measurements

The photolysis of NO_2 is an important factor controlling the partitioning of stratospheric NO_x. It also indirectly affects the HNO_3 formation via the reaction NO_2+OH, since the NO_2 abundances

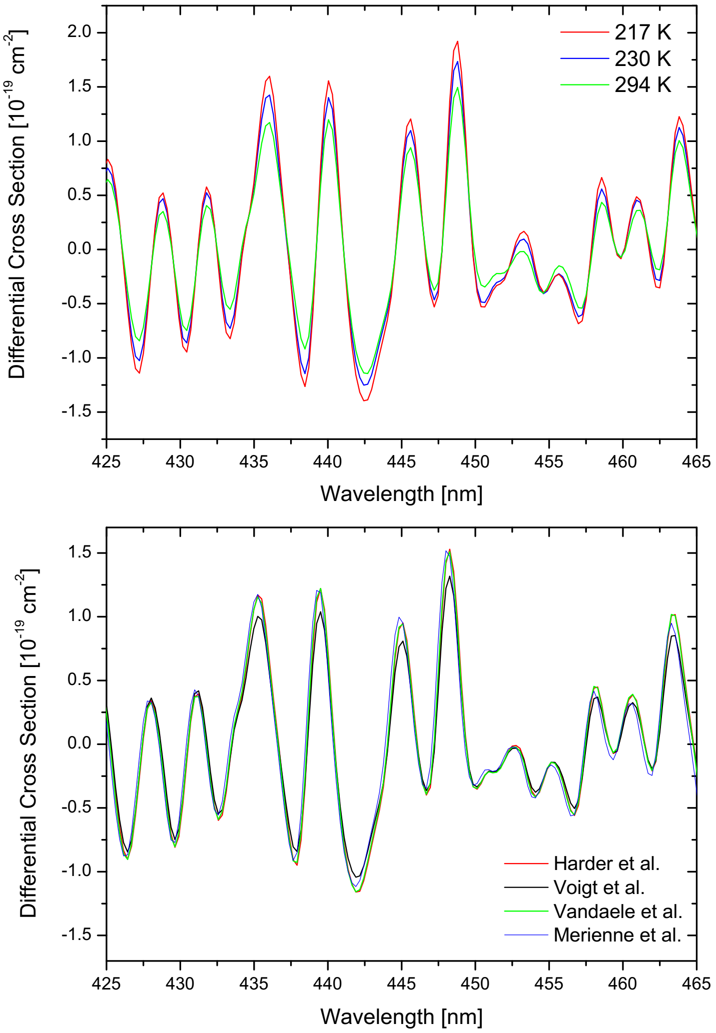

Figure 5.16: *Upper panel: Differential cross sections of NO_2 for the temperatures 217 K, 230 K and 294 K convoluted to the instrument resolution [Harder et al. 1997]. Lower panel: Comparison of the differential cross section of NO_2 at room temperature measured by Harder et al. [1997], Voigt et al. [2001], [Vandaele et al. 1996] and Merienne et al. [1995] convoluted to instrument resolution.*

are modulated by j_{NO_2}. The further investigations of the NO_x and NO_y chemistry (see the following sections and chapter 6) show some striking discrepancies between measurements and CTM modelling. In order to rule out uncertainties in the computed UV/vis actinic fluxes (and j-values) adopted in the photochemical models, measured proxy-j_{NO_2} values are compared with predictions based on radiative transfer (RT) calculations with two different models.

Stratospheric filter sensitivity weighted UV/vis actinic fluxes - approximating the NO_2 photolysis rate coefficients - were measured during the LPMA/DOAS balloon flights in León on Nov. 23, 1996 and Kiruna on Feb. 14, 1997 [*Bösch et al.* 2001]. Both flights were conducted under clear skies, but with a widely differing ground albedo (A). Since the actinometer's spectral sensitivity curve did not exactly match the actinic spectrum of NO_2 (see chapter 4.2.4) and the skylight's spectrum shape changes with atmospheric height and solar illumination, only proxies-j_{NO_2} rather than true j_{NO_2} values were monitored during balloon ascent (0-30 km) for 75^o < SZA < 86^o, and at balloon float altitude during solar occultation (86^o < SZA < 95^o). Knowing the spectrum's shape for each measurement, c.f., from radiative transfer modelling, and the sensor's calibration factors as well (see Figure 4.12 left y-axis), the measured proxy-j_{NO_2} (in units of mV as given in Figure 4.12) can be directly converted into j_{NO_2} values, 'a posteriori'.

Since the purpose of the present study was to test radiative transfer calculations rather than to infer j_{NO_2} values, the spectral sensitivity of each actinometer, rather than the actinic spectrum of NO_2 was used in the RT calculations standing as a surrogate for j_{NO_2} (i.e., the proxy-j_{NO_2}) values.

The photoelectrical response $\alpha_{\texttt{for}}$ and $\alpha_{\texttt{back}}$ of both sensors, one pointing to the sun ('for') and one pointing in the opposite direction ('back'), was obtained by an individually calibration. Assuming, that the diffuse contribution is the same on both the hemispheres, the measured signals $S_{\texttt{for}}$ and $S_{\texttt{back}}$ allow to infer proxy-$j_{\texttt{diff}} = \alpha_{\texttt{back}} \times S_{\texttt{back}}$, and proxy-$j_{\texttt{dir}} = \alpha_{\texttt{for}} \times S_{\texttt{for}} - \alpha_{\texttt{back}} \times S_{\texttt{back}}$. The above assumption appears to be justified because the diffuse actinic flux in the stratosphere is clearly dominated by the diffuse and almost isotropic back reflection from the earth's surface (or the cloud cover) and to a lesser extent by the more anisotropic Rayleigh- and Mie scattering of the clear sky atmosphere.

RT model 1 is based on the refined discrete ordinate algorithm (DISORT) [*Kylling and Stamnes* 1992]. The system of discrete ordinate equations has been modified to incorporate the effect of a spherical shell and refractive atmosphere necessary for the direct beam and primary scattered skylight [*Dahlback and Stamnes* 1991] since atmospheric refraction has shown to be very important for RT modelings for large SZA conditions [*Anderson et al.* 1986]. The spherical DISORT calculations (16 streams for 196 nm to 505 nm calculated in steps of 1 nm, 70 atmospheric layers of 1 km thickness) were based on the following parameters: the extraterrestrial solar flux from *Woods et al.* [1996] for 196 nm $\leq \lambda \leq$ 410 nm; the atmospheric pressure, temperature and O_3 profiles taken from nearby launched ECC sondes, and above 30 km from AFGL for mid-latitudes, and from *Anderson et al.* [1986] for the subarctic winter; the temperature-dependent O_3 absorption cross section taken from *Molina and Molina* [1986]; the Rayleigh scattering cross section from *Nicolet* [1984]; the wavelength dependent aerosol extinction profiles from SAGE II measurements (Michael Pitts, priv. comm.) for altitudes between 15 km and 30 km; a Henyey-Greenstein phase function and an asymmetry parameter taken from the MODTRAN optical data base as well as the standard aerosol profiles below 15 km, a standard aerosol profiles above 30 km from *Shettle* [1989]; the ground albedo (not measured directly) is assumed to be A=0.1 for the León flight (mixture of vegetation and pasture) and A=0.7 for Kiruna (snow covered ground).

The RT model 2 is contained in the SLIMCAT 3D photochemical model. The model calculates the actinic fluxes with a scheme based on *Lary and Pyle* [1991], which in turn was based on *Meier et al.* [1982] and *Nicolet et al.* [1982]. The scheme treats the attenuation of the direct solar beam using full spherical, and refractive geometry for solar zenith angles up to 96^o. Enhancement of the solar flux due to multiple scattering is included and is calculated using a plane-parallel atmosphere. In SLIMCAT actinic fluxes are precomputed in a four-dimensional look-up table which has coordinates of pressure altitude, temperature, O_3 column and zenith angles. These tabulated actinic fluxes are interpolated to a particular location in the atmosphere

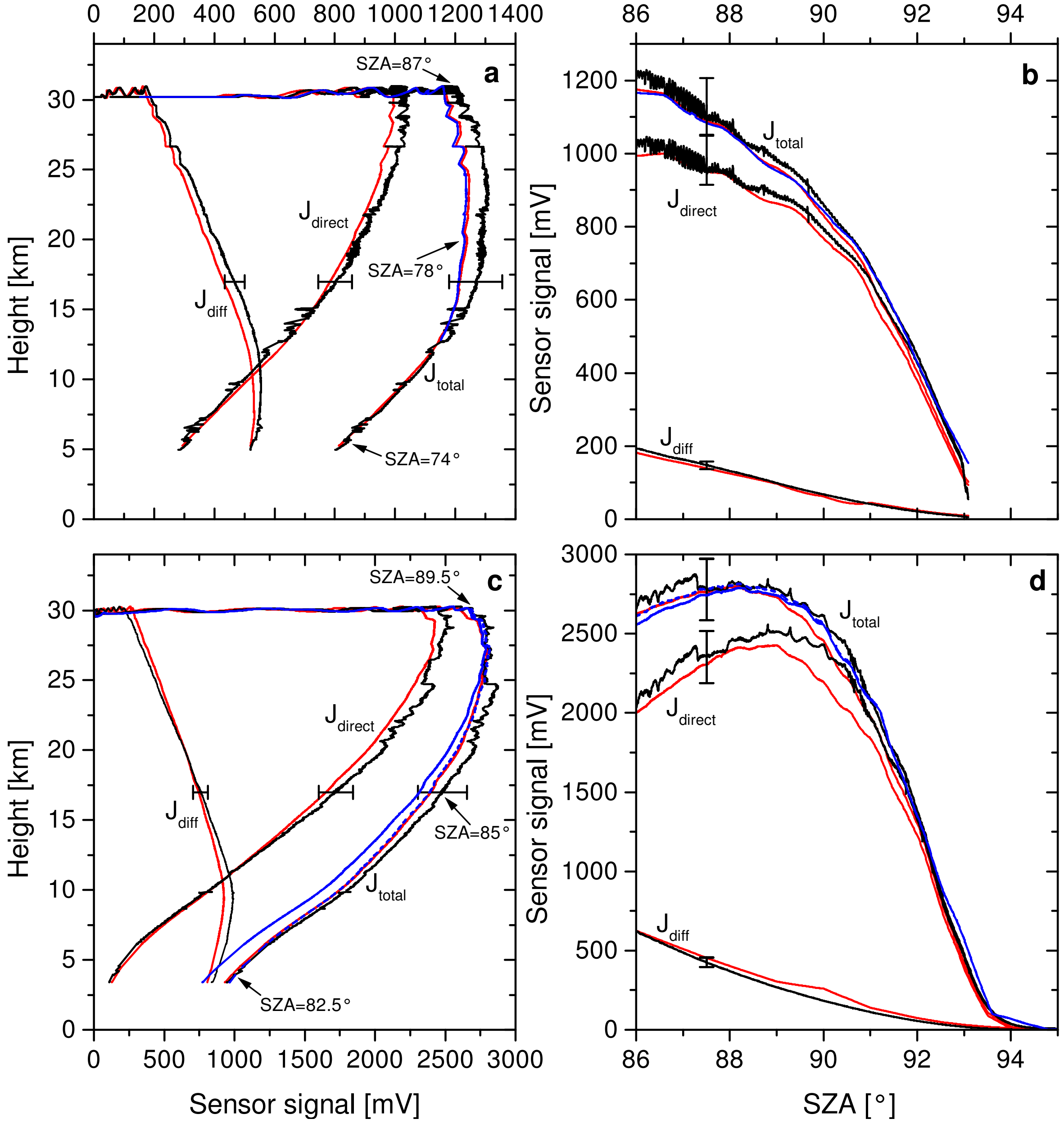

Figure 5.17: *Upper two panels: Comparison of measured (black line) and modelled diffuse, direct and proxy-*j_{NO_2} *values (DISORT: red line; LP-RT: blue line for A=0.3), for the Léon balloon flight on Nov. 23, 1996. Lower two panels: the same but for the Kiruna balloon flight on Feb. 14, 1997 (LP-RT: blue line for A=0.3 and dashed blue line for A=0.7) (left panel: balloon ascent; right panel: solar occultation). The increase of proxy-*j_{NO_2} *from SZA=86° to 89° is due to the increase in balloon flight altitude.*

and a particular time. In this study, local profiles of O_3 and temperature from the appropriate balloon flight up to 30 km and 3D model values for the atmosphere above were used. The photochemical data used to calculate the j-values were taken from *DeMore et al.* [1997] and the solar fluxes from [*WMO* 1996]. A fixed 'surface + cloud' A=0.3 was used. In order to account for the larger albedo of the snow covered ground at Kiruna, a model run with A=0.7 was performed in addition.

Figure 5.17 compares the measured and modelled proxy-j_{NO_2} values. Though the ground albedo was different during both flights, it is remarkable that, within the stated experimental errors, the measurements and both RT model calculations agree well for all modes of observation (balloon ascent and solar occultation). For the balloon ascent, however, the comparison indicates a small, but systematical underestimation of the measured proxy-j_{NO_2} values up to 10%, though this is still within the error bars. This agreement is perhaps less surprising for the DISORT calculations, since more parameters of the individual measurement (e.g., cloud cover, the meteorological parameters and aerosol content) were included than the assumptions (fixed surface and ground A of 0.3 and 0.7, respectively) made in the RT calculations of model 2. Obviously, for large ground or tropospheric clouds albedo the calculated stratospheric actinic fluxes at SZA $< 90°$ significantly increase, as demonstrated here (Figure 5.17, panel c), or by *Madronich* [1987] . The upwelling diffuse actinic flux reflected from clouds or the ground adds considerably to the downwelling direct solar actinic flux which usually dominates in the stratosphere (the enhancement being roughly $2\times A$ times the direct solar flux incident on the ground or on the cloud top [*Madronich* 1987]). Note that the SLIMCAT RT calculations show better agreement in the range of 5 - 25 km at high latitudes (Figure 5.17) when a more realistic A = 0.7 is assumed. For computational efficiency, the standard SLIMCAT model use a single value to set up the photolysis look-up table which, by default, is 0.3. Using a larger A at high latitudes would sightly improve the calculation of proxy-j_{NO_2}.

For SZA $> 90°$, however, a large ground or cloud albedo doesn't appear to be very influential on the actinic fluxes in the stratosphere, as the lower parts of the atmosphere and the ground reside in the shadow of the earth. In this case, the stratospheric photolysis is almost completely dominated by the direct solar beam, and the diffuse contribution becomes low (Figure 5.17, right row). Indeed, more detailed computations by *Swartz et al.* [1999] showed a 30% increase (at most) of the actinic fluxes at 20 km and a SZA=95° when the ground albedo is increased from 0 to 1. Tropospheric clouds, may also have a considerable influence on the actinic fluxes in the stratosphere for large SZA's, just by obscuring the direct solar beam as the sun sets.

Finally, it should be noted that the measured proxy-j_{NO_2} values can be directly related to j_{NO_2} using the following calibration factors: 7.4×10^{-4}/s/100 mV at SZA=75^o for the León flight, and 2.86×10^{-4}/s/100 mV at SZA=83^o for the Kiruna flight. Though the varying importance of Rayleigh scattering and the absorption of ozone may somewhat differently modify the relative contributions of the direct and diffuse actinic fluxes as well as the shape of the spectrum. In practice these calibration factors are accurate to within ± 15% for each of the balloon flights.

So as long as the RT code employs realistic parameters (e.g., albedo), errors of the RT models in calculating stratospheric UV/vis actinic fluxes can be ruled out as a considerable source of uncertainty in modelling correctly the stratospheric NO_x and NO_y partitioning (e.g. with the SLIMCAT model). It should be pointed out again, that the standard SLIMCAT model uses $A = 0.3$ for all locations and therefore j_{NO_2} is underestimated significantly for small SZAs and low altitudes during Arctic winter..

5.3.2 Ozone Comparison

In this section the O_3 profiles measured with the DOAS instrument during all eight balloon flights are presented and discussed in detail. The DOAS measurements are compared to measurements by the LPMA-FTIR (data available only for 5 flights) and by ozone sondes. The study is complemented by comparison to measurements of various satellite-borne instruments. Figures 5.18 and 5.19 show the O_3 profiles (concentrations and mixing ratios, respectively) obtained from balloon ascent as well as from solar occultation measurements in combination with O_3 profiles from the above mentioned sources.

A first look on both figures shows that there is a reasonable agreement for almost all flights between the various measurements, however some exceptions exist. It is obvious, that the O_3 measurements are strongly modulated by the seasonal and latitudinal trend. The main characteristics of this well-known trend is the large seasonal variation of the mean ozone concentration in high latitudes with high values in spring and small values in autumn. However, ozone is most abundant at higher latitudes during all seasons. Equatorwards this seasonal variation becomes smaller and is almost negligible in the tropics. This characteristic is a result of the mean circulation and turbulent diffusion, by which ozone rich air is transported to higher latitudes and lower altitudes [e.g., *Brasseur and Solomon* 1986].

Low and almost constant O_3 concentrations were found in the upper troposphere. Above the tropopause (8-9 km in polar regions during winter and approx. 10 km during summer, 11-12 km in mid-latitudes during all seasons) the O_3 concentrations strongly increase (overlaid are several small-scale structures). The maximum O_3 concentration of $4\text{-}5{\cdot}10^{12}$ molecule/cm^3 is reached at altitudes around 20-25 km at mid-latitudes. In polar regions the maximum is found for slightly lower altitudes, but with higher concentrations, being in the range of $6\text{-}7{\cdot}10^{12}$ molecule/cm^3 for winter as well as for summer. Above the maximum, the concentrations continuously decreases again. However, the measured O_3 profiles are not smoothly shaped, but small-scale variations and even some large dips (called *laminae*) are overlaid over the broad vertical distribution. This is mainly the result of the intrusion of air masses from different latitudes at this particular altitude.

Comparison of the different Flights

To compare our measurements with the mean seasonal characteristics, the ensemble of all O_3 mixing ratios for the polar and mid-latitudinal measurements, respectively, are shown in Figure 5.20. Each profile is shifted with respect to the tropopause height.

The profiles measured at mid-latitudes (left panel) do not reproduce the mean seasonal variation. The O_3 amounts measured in March are almost equal to those measured in summer. The O_3 profile measured in November even shows the highest values. However, the measurement in November took place close to the vortex boundary, which extended far to mid-latitudes during this period. Therefore, it can be speculated, that the probed air masses were rather quickly transported from high latitudes (with high O_3 concentrations), a matter affirmed by back-trajectory calculations based on the NASA GSFC model[5].

The O_3 profiles measured in the northern hemisphere winter clearly show higher values compared to the mid-latitudinal measurements (except for the flight in León 1996, where obtained values were almost as high as in polar regions) for the lower stratosphere. Further, the large

---

[5] available from Goddard Automailer

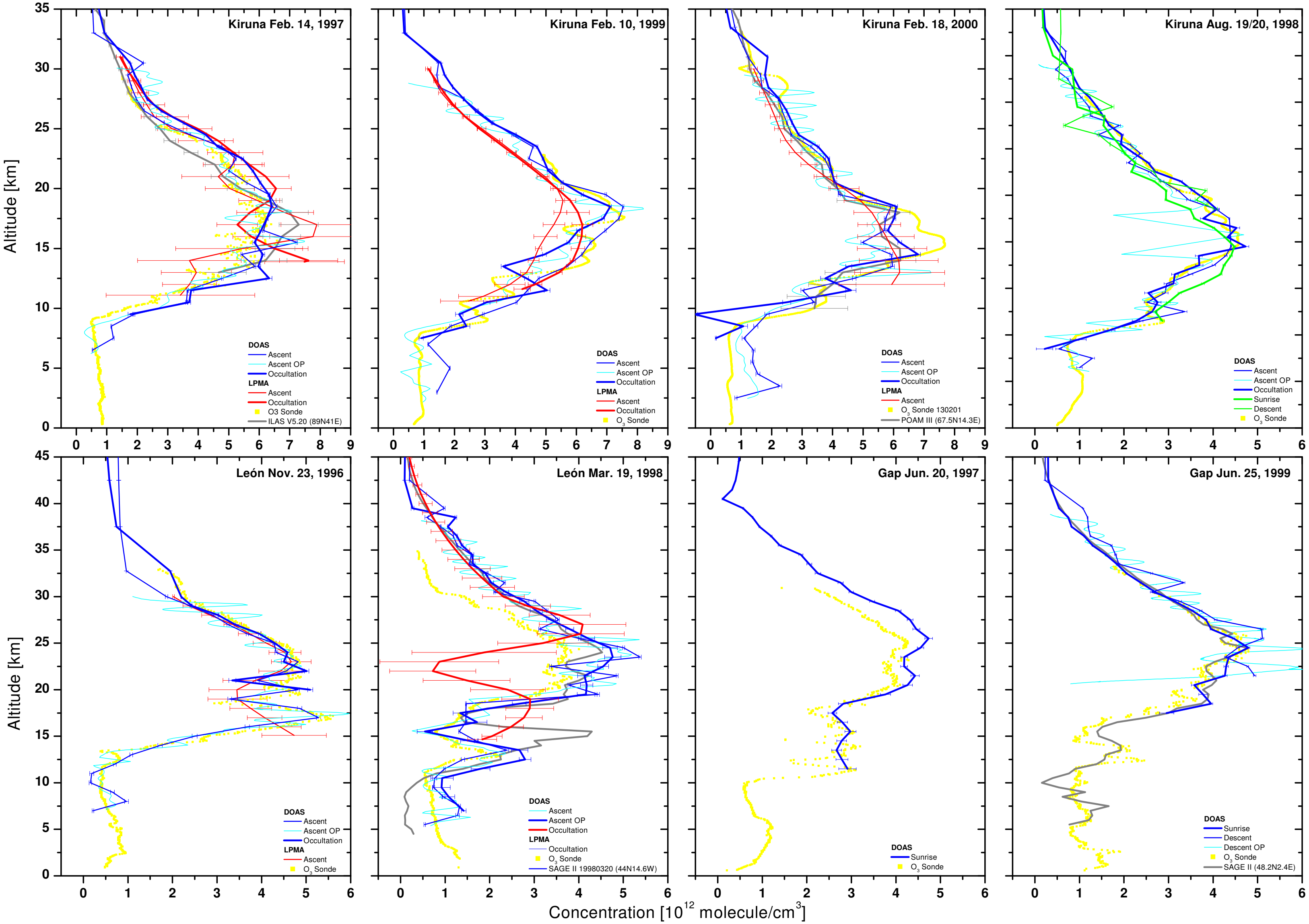

Figure 5.18: *Vertical profiles of the O_3 concentration for the LPMA/DOAS balloon flights. The upper row shows the measurements at high latitudes for winter (left three panels) and summer (right panel). The mid-latitudinal measurements are shown in the lower row for León (left) and Gap (right). Also shown are the O_3 sonde, LPMA and satellite measurements.*

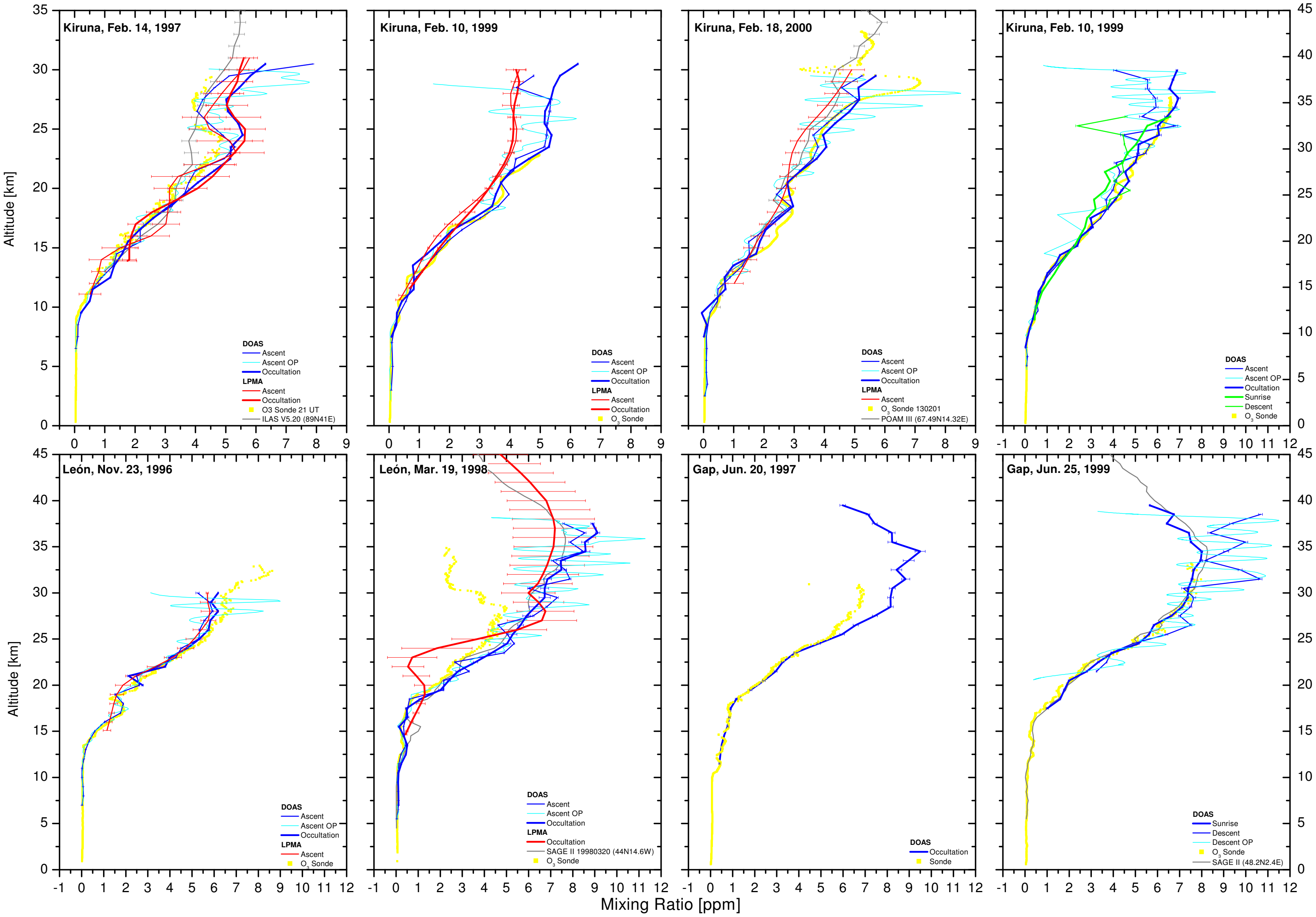

Figure 5.19: *Vertical profiles of the O$_3$ mixing ratio for the LPMA/DOAS balloon flights. The upper row shows the measurements at high latitudes for winter (left three panels) and summer (right panel). The mid-latitudinal measurements are shown in the lower row for León (left) and Gap (right). Also shown are the O$_3$ sonde, LPMA and satellite measurements.*

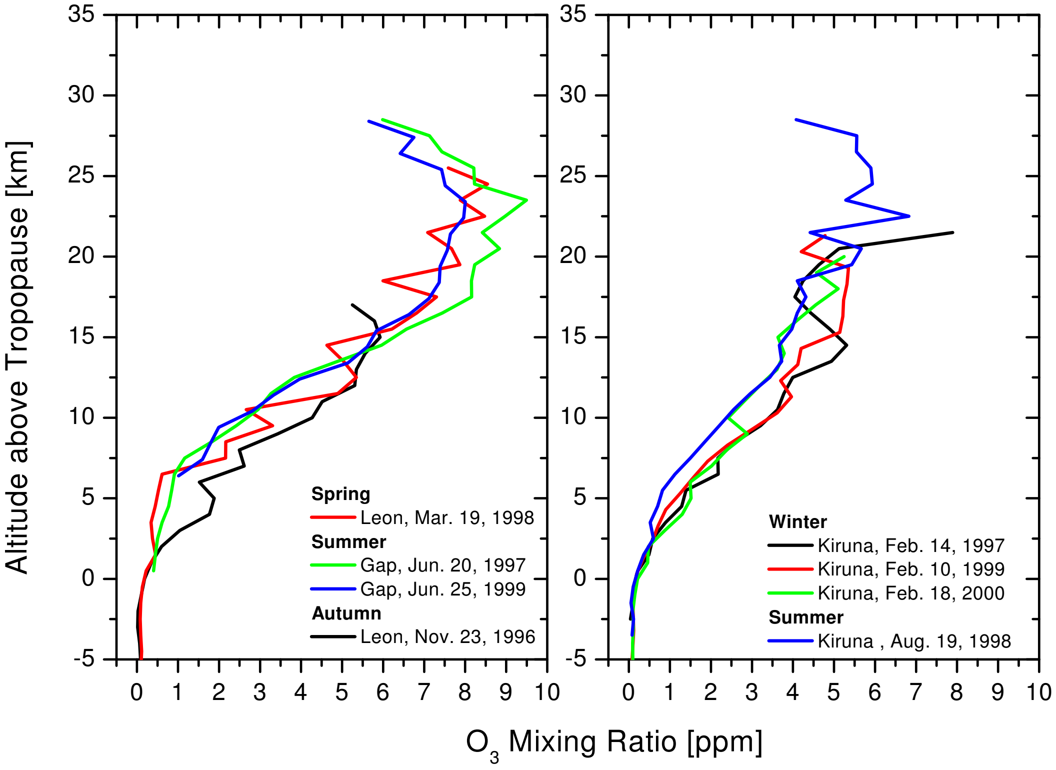

Figure 5.20: *Vertical distribution of the O_3 mixing ratio measured by the DOAS instrument. Left panel: Mid-latitudinal profiles. Right panel: High-latitudinal profiles.*

summer/winter variation for high latitudes is clearly visible. The profile measured in winter 2000 shows a systematic bias from 8 km above the tropopause on. This could be an indication of the larger ozone loss which occurred during this winter as compared to the previous winters. Nevertheless, this seems to be unlike, as the low O_3 values were found for relatively high altitudes only. Another possibility which could explain this feature will be discussed later in connection with the presentation of the NO_2 measurements (section 5.3.3).

Balloon Ascent/Descent and Solar Occultation Comparison

Ozone does not undergo fast photochemical variations, and hence, both measurements should end up in the same vertical distribution. It should be kept in mind, that during balloon ascent only air masses within a small area close to the balloon location are probed, while the distance between the balloon gondola and the tangent point increases up to several hundred kilometers for solar occultation. Accordingly, spatial inhomogeneities (e.g. near the boundary of the polar vortex) can lead to large differences between the ascent and the occultation profiles.

For mid-latitudinal measurements horizontal gradients of the ozone amount are usually small. Indeed, the ascent and the occultation profiles nicely agree for those flights (lower row in Figure 5.18 and Figure 5.19). Both profiles closely follow each other and even the small-scale structures can be found in both profiles (e.g. for both León measurements). However, for Gap 1999, the descent profiles shows slightly larger concentrations compared to the occultation profile. In addition, the Onion Peeling profile retrieved from the balloon ascent measurements is shown. The Onion Peeling profile nicely reproduces both profiles retrieved with the inversion technique, however large, disturbing high-frequent oscillations occur. Another shortcoming of this technique is, that it is only valid for SZAs being clearly smaller than 90°. Nevertheless this technique is a useful supplement as it is very simple and straight-forward (and can be used to check the inversion profile). Further, the Onion peeling works well for the beginning of the balloon ascent (small SZAs), where the inversion technique is less reliable.

For the high-latitude summer measurements, a good agreement between the solar occultation and the ascent measurement is found, too. The large scatter at 19 and 22 km of the Onion-Peeling profile is the result of small gaps in the measurements caused by a temporal malfunction of the suntracker. The subsequent sunrise measurement yields a slightly different O_3 profile, with higher O_3 amounts in the lower stratosphere and smaller values for high altitudes. The profile obtained during balloon descent rather well agrees with the ascent and occultation measurements. This is most likely due to the fact, that the descent measurement took place close to ascent (and occultation) measurements, while the sunrise measurements probed air masses more easterly[6].

The high-latitudinal winter measurements reveal relatively large differences between balloon ascent and solar occultation, an indication of inhomogeneities appearing inside and at the edge of the polar vortex. As shown in Figure 5.3 and 5.5, the air masses probed during balloon ascent and solar occultation differ with respect to the vortex boundary and hence different O_3 amount are likely to occur. For Kiruna 2000, both, the ascent and the occultation measurements were located clearly inside the polar vortex and even the similar with respect to the vortex edge (or with respect to PV). Indeed, a nice agreement between the ascent and the occultation profile is found, with rather small differences, only.

Comparison with Ozone Sondes

The comparison of the DOAS O_3 profiles with measurements of O_3 sondes launched the same day (or since 1998 on-board the gondola) shows a good agreement for most of the flights.

For the mid-latitudinal flights and the polar summer flight the agreement is excellent, however, with two striking exceptions. For the flight in León in 1998 and in Gap in 1997 large discrepancies were found. Below 20 km, the sonde measurements agree well with the DOAS observations, but above 20 km, the sonde measures systematically smaller values, though the small-scale structures were similar to those measured by the DOAS instruments. It can be speculated whether this is due to an improper correction of the height dependent pump efficiency of the O_3 sonde [*EN-SCI Corporation, Boulder, Colorado, USA* 1997]. Especially the sonde measurements for León 1998 are suspect, as they show unreasonable small values for high altitudes. For Gap 1997, the discrepancy can also be the result of inhomogeneities in the ozone pattern, as the air masses probed by the occultation measurement were located 100-500 km away from Gap.

The comparison with the DOAS measurements for high-latitude winter shows a reasonable agreement, although larger differences can be found mainly due to the same reasons discussed above for the DOAS ascent/occultation comparison. During the flight in Kiruna 2000, the on-

---

[6] An indication of a slight inhomogeneous ozone pattern is given by global ozone maps provided by various satellite instruments (e.g. GOME, TOMS)

board O_3 sonde did not work properly. Only data from O_3 sondes launched 5 days earlier and 9 days after the balloon flight is available making a tight comparison impossible.

In the upper troposphere and lower stratosphere the O_3 sonde measurements and the profile obtained with the Onion Peeling technique agree fairly well indicating that even for this altitude range the measurement technique is well suited. However, using the inversion technique lead quite often to a clear overestimates of the O_3 sonde data in combination with some scatter.

Comparison with LPMA Measurements

The comparison with the LPMA measurements yields a rather contradictory result. While for some flights there is good agreement, for others it is only fair or even bad. A relatively good agreement is obtained for the León 1996 and the Kiruna 1997 and 2000 flights. For Kiruna 1999 a large bias between the DOAS and the LPMA profile is found, with the smaller values measured by LPMA. A good agreement is obtained in León 1998 above 25 km, but large discrepancies occur below. Further, this comparison shows that the vertical resolution of the LPMA measurements is relatively low compared to the DOAS measurements indicated by the smooth shape of the profiles (clearly visible for e.g. the León 1996 flight).

Both instruments, the LPMA-FTIR and the DOAS instrument, uses the same beam of direct sunlight provided by the on-board suntracker. Consequently, both instruments probe the same air masses[7] and therefore the same ozone profiles. However, the retrieval techniques for UV/vis and IR measurements are completely different and hence there is a large number of sources of uncertainties. There could be a systematic bias between the UV/vis and the IR cross section. Further, the evaluation in the IR wavelength range is much more complex as in the UV/vis, since the knowledge of the line strengths, their temperature dependence and the pressure broadening of the lines is required. Another important question concerning the IR retrieval is, how independent is the retrieved profile from the first-guess profile. This might be important for flights with low balloon float altitudes in combination with absorbers with a concentration maximum located at high altitudes, as the whole profile is important to properly account for the strong temperature and pressure dependence of absorption lines. For the DOAS evaluation, the estimation of the absorber amount of the Fraunhofer spectrum is a significant source of uncertainties, but with the presented method this should be well treated (see section 5.2). The amount and distribution of O_3 above the balloon float altitude is a source of uncertainty, too, but to a much smaller degree compared to the IR. If the profile retrieval algorithm estimates a completely wrong amount and/or distribution of O_3 above the float altitude, then the values below will be distorted, too. As a result of the refraction, each measurement probe the height layers above the balloon float altitude slightly different. Thus, the measurements also include some information about the distribution above balloon float. However, small systematic errors in the measurements or a unreasonable reduction of the condition number during the inversion can distort the retrieval of the concentrations for large altitudes. To check this, the concentrations obtained for altitudes above balloon float are shown also in Figure 5.18. Even if the exact values should not be taken too serious, they seem to be reasonable range and decrease with increasing altitude. In conclusion, the reason for the discrepancies between the LPMA and DOAS measurements for some of the flights is unclear and needs to be further investigated, in particular since the situation is even

---

[7] Small differences of the refractive index of air for the UV/vis and IR wavelength range exist resulting in a slightly different line-of sight.

worse in the case of NO_2 as will be shown in section 5.3.3.

Comparison with Satellite Instruments

The flight in Kiruna 1997 was part of the ILAS validation campaign. ILAS is a solar occultation sensor which was brought on a sun-synchronous polar orbit on-board the ADEOS satellite. ILAS measures the wavelength range between 6.21 and 11.77 μm during sunrise or sunset on each of 14 orbits per day with a measurement region covering the high latitudes [*Sassano et al.* 1999]. The ILAS measurement located closest to the balloon measurements took place at 13:10 UT at 69°N41°E (for a tangent height of 20 km). Thus, the spatial coincidence is bad ($>$ 800 km difference) [*Sugita et al.* 2001]. The DOAS measurements were performed in proximity to the vortex edge, while ILAS probed air masses more from inside (see *Schneider* [1997]), making a comparison is difficult. Nevertheless, a reasonable agreement with the ILAS measurements[8] is found with the smaller values measured by ILAS.

On Feb. 18, 2000 a POAM III measurement took place at 67.5°N and 14.3°E, in reasonable coincidence with the DOAS measurements. POAM III is a nine channel photometer operated on board the SPOT 4 satellite on a sun synchronous orbit. POAM III makes 14 solar occultation measurements each day on each hemisphere which correspond to local sunset in the northern hemisphere [*Lucke* 1999]. As shown by [*Lumpe et al.* 2001] the DOAS and POAM III measurements both occurred inside the inner vortex and sampled nearly the same air masses except at the very bottom of the profile. A good agreement between the DOAS ascent and occultation profiles and the POAM III measurement is found, even the distinct notch around 15 km is well captured by both. The differences between the DOAS ascent and POAM III profile appear to be of zero mean with no significant bias however with a scatter that increases for lower altitudes. The occultation measurements show slightly larger values with a bias of around 5 %, possibly caused by a slightly different location of the measurement. Altogether this is a remarkable good comparison.

Finally, two DOAS flights were compared to measurements of the SAGE II instrument. SAGE II is a solar occultation instrument similar in concept to POAM III. SAGE II is installed on the ERBS satellite and performs primarily middle and low latitude measurements, reaching the polar regions only a few days per year [*Mauldin III et al.* 1985].

A measurement of SAGE II was carried out at 44°N14.6°W almost at the location of the occultation measurement of the León 1998 flight, but on the next day[9]. This measurements were carried out in the so-called surf-zone (see chapter 3.9), where large variabilities in the trace gas concentrations (e.g. for NO_2 see *Erle* [1999]) can occur. Fast changes in the amplitudes of the planetary waves can impact the stratospheric dynamics in the mid-latitudes and transport air parcels from mid-latitudes to high latitudes and vice versa. However, the SAGE II and the DOAS measurements show a nice agreement down to 17 km. Below 17 km, a notch appears for the DOAS measurement around 15 km followed by a maximum at 12 km. The same structure can be seen in the SAGE II measurement, but shifted upwards.

For the Gap 1999 flight a SAGE II measurement took place on the same day located at

---

[8] Version V5.2 ILAS data was used.

[9] During the solar occultation measurement the line of sight of the occultation measurements pointed towards the west with tangent points ranging approx. form 42.5°N5°W to 42.5°N10°W (see *Fitzenberger* [2000]).

48.2°N2.4°E which is in good coincidence with the DOAS measurements (however, the tangent point of the solar occultation measurements were shifted somewhat towards the north-east for very large SZAs). Accordingly, the comparison with the SAGE II measurements shows an excellent agreement for the whole altitude range covered by the DOAS occultation measurements. Astonishing is that the SAGE II measurements even follows the O_3 sonde measurements down to 5 km.

In summary, the comparison shown here impressively demonstrates the high quality of the DOAS O_3 measurements in combination with the profile retrieval technique. Several small scaled features were captured indicating a rather high vertical resolution. The reasons for the disagreement with some of the LPMA measurements however is still unclear and needs further investigation.

5.3.3 NO_2 Comparison

The NO_2 profiles measured with the DOAS instrument during balloon ascent (or descent) and solar occultation are compared with the LPMA (for 6 flights) and satellite measurements (for four flights). The NO_2 profiles (as concentrations and mixing ratios) obtained for all flights are shown in Figure 5.21 and 5.22

Compared to ozone, the situation is more complex for NO_2 as the concentrations show large diurnal variations (see chapter 3.2) and hence different measurements can only be compared for similar SZAs. Figure 5.21 and 5.22 clearly shows, that large differences between different measurement techniques occur for almost all flights and that, large variations of the NO_2 amounts between the different flights can be observed. The latter is certainly the result of the seasonal and latitudinal variation of the NO_2 concentrations and the differences between sunrise and sunset (see chapter 3.2). For balloon ascent, the diurnal variation of the NO_2 concentrations also contribute to this, since the measurements were performed at different SZAs. Increased NO_x amounts were usually found during high-latitude summer due to the mean atmospheric transport. Similar to ozone, NO_x is a long-lived tracer in the lower stratosphere whose source lies in the tropical regions. Downward, poleward transport by the mean meridional circulation leads to the increased NO_x. However, in the winter small NO_x amounts were found at high latitude as a result of the combined effects of dynamics and chemistry (denoxification)) [*Brasseur and Solomon* 1986].

The NO_2 profile found in mid-latitudes and during summer in high-latitudes shows a slow increase of the NO_2 concentration with increasing altitude from the tropopause (with vanishing NO_2 amounts) to $\sim$ 25 km. In the range of 25-30 km, the concentration maximum is obtained with values about $2{\cdot}10^9$ molecule/cm^3 for a SZA of $\sim 85°$, while above the NO_2 concentrations slowly decrease again. For high-latitude winter, a different profile shape is found. Very small and almost constant NO_2 concentration were found in the lower stratosphere ($<$ 20 km). Above, a strong increase is found with a peak values in the range of $0.5\text{-}1{\cdot}10^9$ molecule/cm^3 for a SZA of $\sim 85°$, but here a strong dependence on the history of the air masses is expected.

Comparison of the different Flights

A comparison of the DOAS NO_2 mixing ratio measurements for mid-latitudes and high latitudes is shown in Figure 5.23. Displayed are all NO_2 profiles obtained during solar occultation. Thus all profiles correspond to a SZA of 90°. Nevertheless, some photochemical variations will be

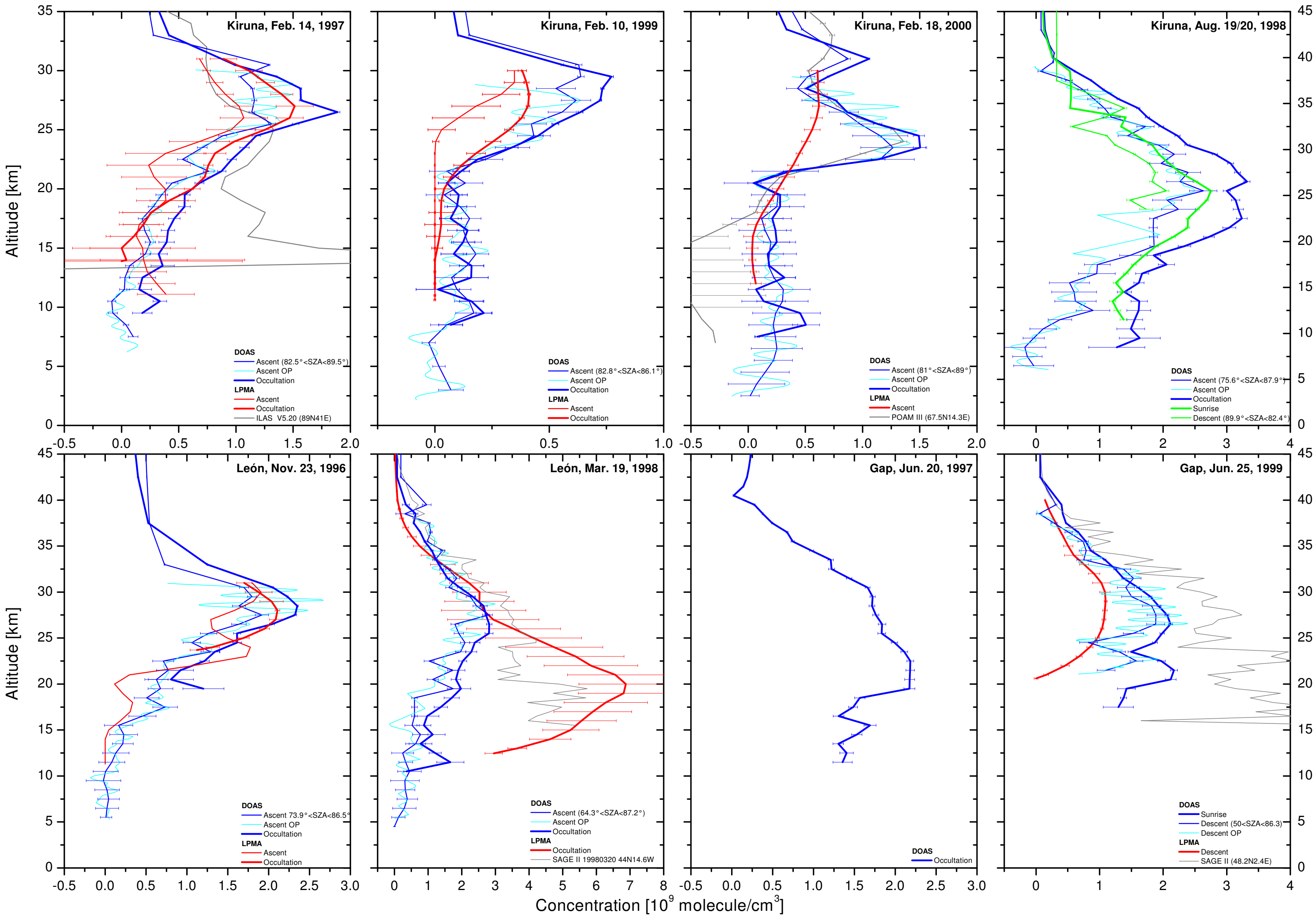

Figure 5.21: *Vertical profiles of the NO_2 concentration for the LPMA/DOAS balloon flights. The upper row shows the measurements at high latitudes for winter (left three panels) and summer (right panel). The mid-latitudinal measurements are shown in the lower row for León (left) and Gap (right). Also shown are the LPMA and satellite measurements.*

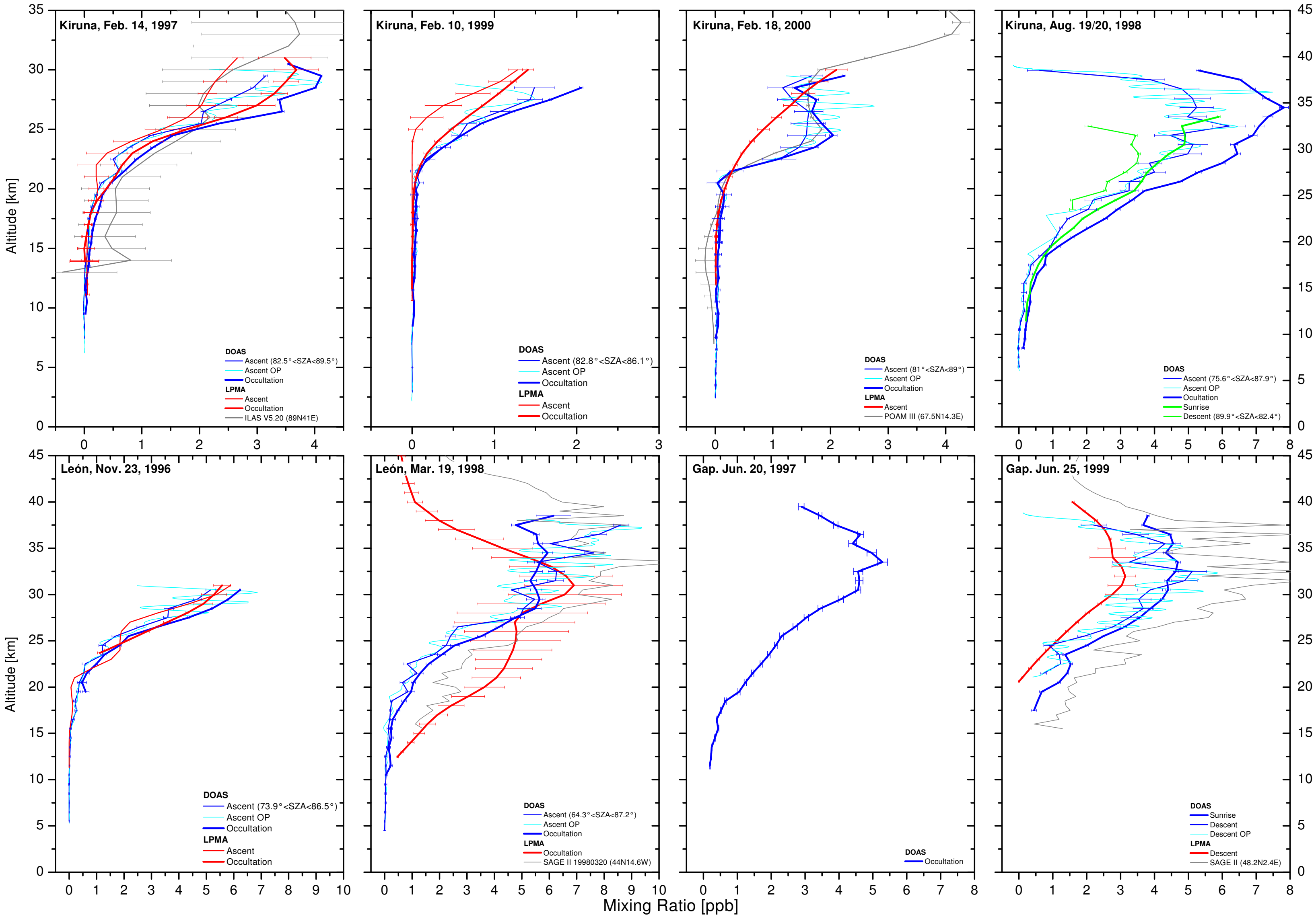

Figure 5.22: *Vertical profiles of the NO_2 mixing ratios for the LPMA/DOAS balloon flights. The upper row shows the measurements at high latitudes for winter (left three panels) and summer (right panel). The mid-latitudinal measurements are shown in the lower row for León (left) and Gap (right). Also shown are the LPMA and satellite measurements.*

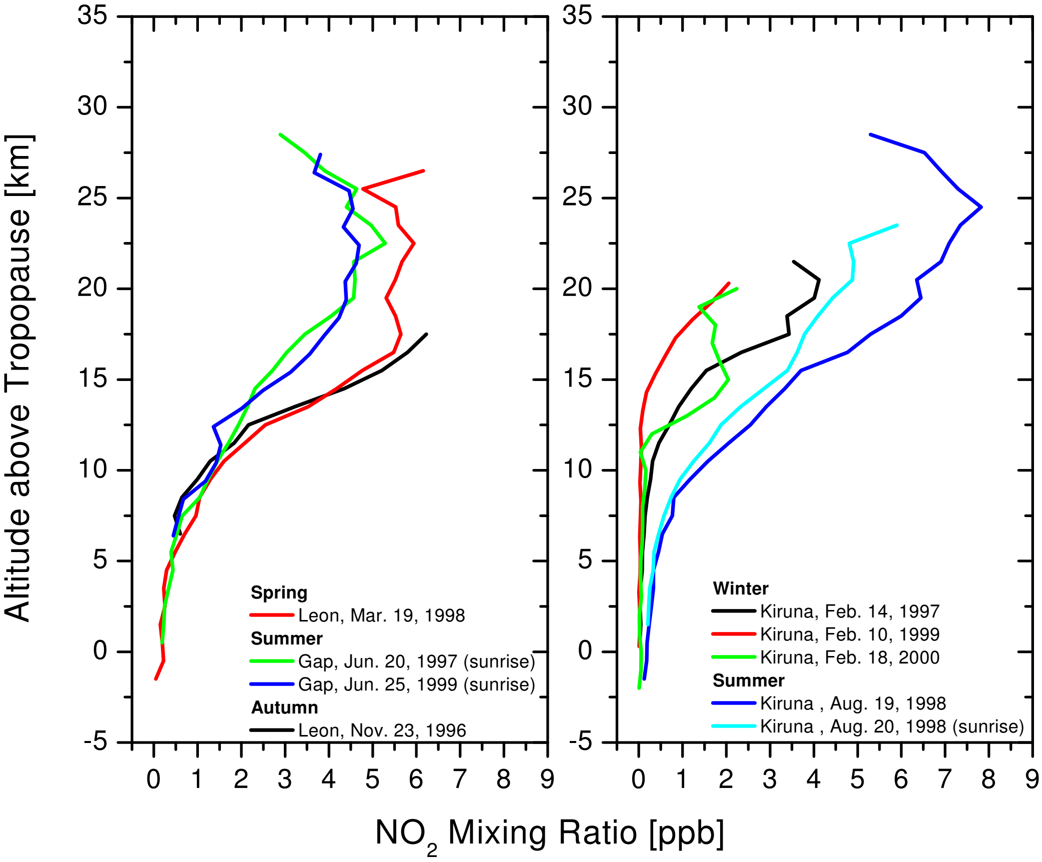

Figure 5.23: *Vertical distribution of the NO_2 mixing ratio measured with the DOAS instrument during solar occultation. Left panel: Mid-latitudinal profiles. Right panel: High-latitudinal profiles.*

included in the profiles. Most of the solar occultation measurements were performed during sunset, only for the two Gap flights sunrise measurements were conducted. The measurement on August 20, 1998 in Kiruna took also place during sunrise.

The comparison of the mid-latitude measurements is shown in the left panel of the Figure 5.23. A good agreement is found for both León and both Gap measurements, respectively. For the summer flights (Gap), this is not astonishing as both measurements were conducted in the same photochemical regime (almost the same day and same latitude/longitude) and as the stratospheric summer flow pattern is relatively homogenous. The measurements in León were performed in spring and autumn, both in the mid-latitudinal surf-zone, where large variations of the trace gas concentrations are likely to occur. Indeed, especially for lower altitudes, both profiles differ, with the lower amounts found during the flight in autumn 1996 (which is in accordance with the higher O_3 amounts found there). Both sunrise measurements (in Gap) clearly show smaller NO_2 mixing ratios compared to the sunset measurement (in León). This is mainly due to the diurnal variation of the NO_2 abundances. During the night, the reservoir species N_2O_5 is formed. After sunrise, N_2O_5 photodissociates and NO_2 is released back again.

Since the photolysis frequency of N_2O_5 is rather small, a sunrise/sunset asymmetry is observed.

The NO_2 profiles (shifted with respect to the tropopause height) measured at high-latitudes are presented in the right panel of Figure 5.23. In accordance to the mean seasonal variation of NO_2, the largest amounts were found during high-latitude summer. Again, the evening/morning asymmetry becomes obvious for the measurements performed on Aug. 19 and 20 in 1998. In contrast to the polar summer measurements, the NO_2 abundances measured during high-latitude winter are very small, particular below 20 km, where the stratosphere is strongly denoxified and NO_2 amounts close to zero were observed. However, the three winter flights show a large variability reflecting the large variability of the conditions during high-altitude winter. In addition, the location with respect to the vortex boundary was different for the three flights (as already discussed earlier), a matter that certainly impacts the NO_2 concentrations. Further, the observed NO_2 amount will depend strongly on the back-trajectory of the probed air parcel. In the winter polar stratosphere large amounts of HNO_3 are formed mainly through hydrolysis of N_2O_5. NO_2 (or NO_x) is only slowly released from HNO_3, strongly depending on the illumination of the air parcel. HNO_3 uptake by particles and the occurrence of denitrification also can significantly affect the NO_2 amounts.

The largest winterly NO_2 amounts were found in Kiruna 1997. During this flight, the measurement location was close to the vortex edge and even partly outside, hence, the air masses could be mixed with NO_x-rich mid-latitudinal air.

In contrast, the NO_2 amounts found for the Kiruna 1999 flight were the smallest measured for all flights, indicating a strong denoxification. Further, as the so-called renoxification starts in mid-February, it might be of importance that this measurement was conducted a few days earlier than the other winter measurements.

In Kiruna 2000, a unusual shaped NO_2 profile was measured. A maximum of the mixing ratio occurred already at an altitude of 23 km followed by a minimum at 28 km and an indication of again increasing values above. Comparing this with the ozone profile measured for the same flight (Figure 5.20) shows that this remarkable NO_2 maximum corresponds to an altitude range of reduced O_3 amount (probably through NO_x catalyzed ozone loss). This characteristics of the NO_2 profile cannot be easily explained. The NO_2 photochemistry will in general force the NO_2 mixing ratio profile to peak at an altitude of approx. 27-30 km, the altitude range where minimal mixing ratios were found here. The sedimentation of large HNO_3-containing particles to lower altitudes (denitrification) and a subsequent evaporation can re-distribute NO_y (and hence also NO_x). But this is only observed for the lower stratosphere and can therefore be excluded as a possible explanation. Also the intrusion of NO_x rich mid-latitude air at this particular altitude could serve as an explanation for the high NO_2 amount around 23 km, but as was pointed out in *EORCU* [2000] the polar vortex was isolated and stable until the end of February.

Inspecting the CH_4 and N_2O profiles measured by the LPMA instrument for the Kiruna 2000 flight (Figure 5.24), shows, it becomes evident that extremely low values were observed in the altitude range of the observed NO_2 peak, even a minimum is found here. For comparison, also the N_2O and CH_4 profiles measured during the Kiruna 1999 flight are shown. The low N_2O and CH_4 mixing ratios are a clear hint for a strong downward motion of the air masses inside the polar vortex. The CH_4 mixing ratios are clearly below 0.3-0.4 ppm, indicating air masses from above the stratopause (i.e. from the mesosphere) [*Siskind et al.* 2000]. In the absence of sunlight, NO produced in the mesosphere, can descend to lower altitudes, however, depending on descent rates and horizontal transport processes. As mentioned earlier, the polar vortex in the February 2000 fulfilled the prerequisites of a strong and stable vortex with low horizontal mixing and large

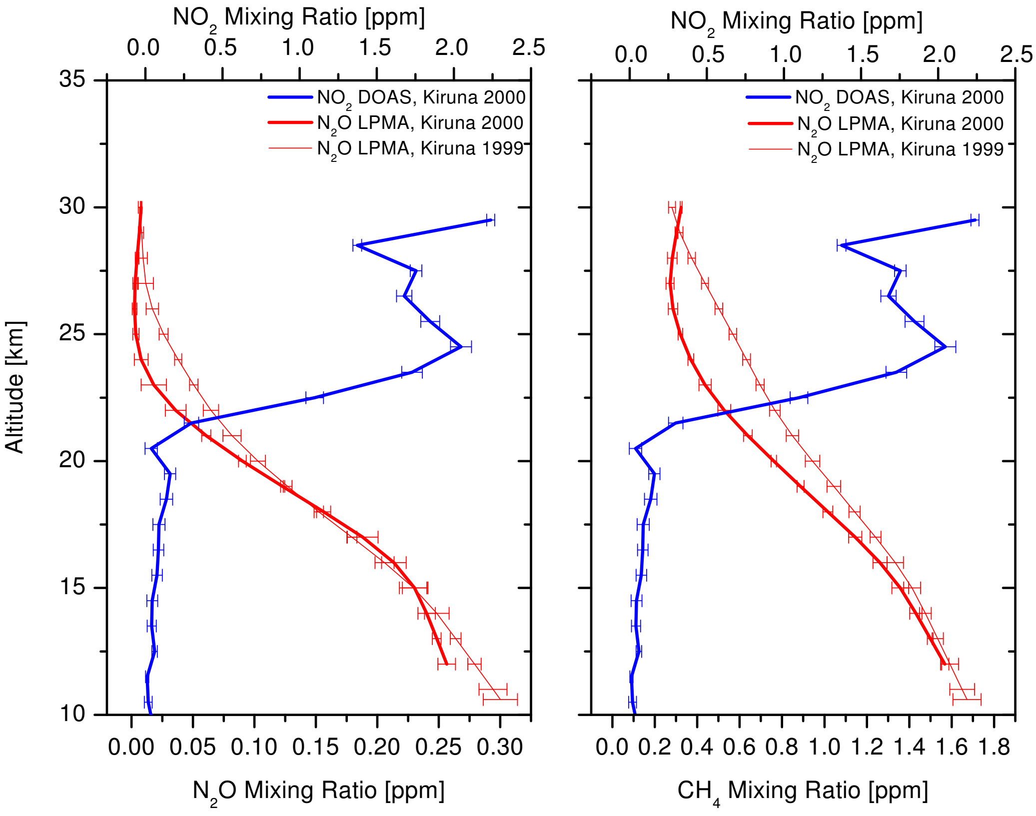

Figure 5.24: *Vertical profile of N_2O (left) and CH_4 (right) together with the NO_2 profile for the Kiruna 2000 flight. Also shown are the N_2O and CH_4 profiles measured in Kiruna 1999.*

descent rates. As the mesospheric NO_x levels are generally lower than those in the upper/middle stratosphere the descent of mesospheric air will result in smaller mixing ratios. However, the mesospheric NO production can be largely increased by particle-induced processes (see chapter 3.2). This enhanced NO_x levels can then be transported to lower altitudes inside the polar vortex. This phenomena is quite often observed at Antarctica, where very large enhancements were already measured (NO_2 mixing ratios up to 7-10 ppb on the 700 K level were observed e.g. after large solar proton events) [*Siskind et al.* 2000; *Randall et al.* 2001]. Following the arguments given by *Randall et al.* [1998], this results in a characteristic NO_2 profile with a distinct notch at approximately 800 K (depending on the degree of descent). Below, a peak is observed which is caused by the transport of the NO_x enhanced air from the mesosphere. The peak above the notch results from a combination of the normal seasonal increases as the sunlight returns to polar regions and possible mixing with extra-vortex air at high altitudes. This is exactly the characteristic of the observed NO_2 profile for the Kiruna 2000 flight. The lower peak, however, shows a rather small mixing ratio (1.5-2 ppb) compared to observations at Antarctica. Hence, the reported enhancement will only slightly contribute to the total ozone loss (however, relatively small O_3 amounts were observed at this altitude range). Nevertheless, this clearly shows, that the effect of NO_x enhancement is also likely to occur not only at Antarctica but also in the Arctic. The fact, that the enhancement was rather small is more related to the absence of

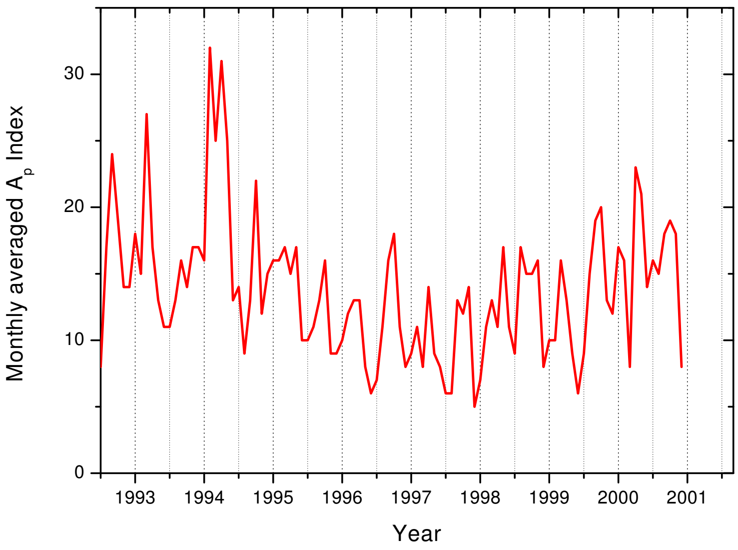

Figure 5.25: *Monthly averaged A_p index for the years 1993 to 2001.*

large particle events during this winter. The particle precipitation and thus the mesospheric NO_x source (one of several possible sources) is largely modulated by the solar-induced magnetic activity, measured by the A_p index. A close coincidence between NO_x enhancements and the A_p index is observed (for enhancements induced by particle precipitations). As shown in Figure 5.25, the A_p index slightly increases from the solar minimum in 1996 towards the year 2001, however, the values were still relatively low. This is consistent with the observed small, but significant NO_x enhancement.

Balloon Ascent/Descent and Solar Occultation Comparison

The comparison of the DOAS ascent/descent and the occultation measurements shows an increase of the NO_2 amounts between the ascent and the solar occultation measurements for all flights. This is simply the result of the decreasing NO_2 photolysis during sunset in combination with the fast $NO+O_3$ reaction. For most of the flights, both, the ascent and the occultation measurements show a similar shaped profile (e.g. for Kiruna 2000) indicating that (almost) the same air parcels were probed. For the Kiruna 1997 flight, this is probably not true as both measurements were differently located with respect to the vortex. Here, larger differences in the profile shape between both measurements can be observed and the occultation/ascent ratio is significantly larger than for the other winter flights.

A question of general interest is, to which degree the winterly lower stratosphere denoxifies. From Figure 5.21 it becomes clear, that it is difficult to answer this question as within the stated error bars the measured concentrations in the lower stratosphere (for Kiruna 1999 and Kiruna 2000) agree with zero or are only slightly above. For solar occultation, however, most of the lower stratospheric measurements disagrees with zero (note, that the error bars indicate only the 1-σ precision). A suspicious feature is that similar concentrations were found for the balloon ascent and the solar occultation, in contrast to the expected increase for larger SZAs.

The profiles obtained with the Onion Peeling technique nicely agree with those obtained with inversion technique, even for the lower stratosphere. As already mentioned earlier, the Onion Peeling profile tends to oscillate strongly.

Comparison with LPMA Measurements

The comparison with the LPMA measurements (possible for 6 flights) shows a bad agreement almost for all flights. Only for two flights (Kiruna 1997 and in León 1996) a rather good agreement is obtained. For all other flights, the NO_2 amounts measured by LPMA were significantly smaller than those measured by DOAS, except for the León 1998 flight were the LPMA NO_2 profile shows unreasonable large values in the lower stratosphere. As already discussed in connection with the ozone measurements, there are several possibilities that could serve as an explanation for these discrepancies, with the real reason still unknown.

Comparison with Satellite Instruments

The comparison of the DOAS NO_2 profile measured at Kiruna on Feb. 14, 1997 with the measurements of the ILAS instrument is shown in Figure 5.21. As already mentioned in section 5.3.2, the spatial coincidence between the ILAS and the DOAS measurements was bad. However, for NO_2 comparisons inside the polar vortex, a good coincidence is crucial Indeed, the agreement between both measurments[10] is relatively poor. Further, the quality of the ILAS NO_2 data for lower altitudes seems to be suspect as the NO_2 concentrations increases to unreasonable values up to $2 \cdot 10^9$ molecule/cm^3 at 15 km.

For the Kiruna 1999 flight, a POAM III measurement with a good spatial and temporal coincidence exists and hence both measurements can be nicely compared. Between 20 and 30 km there is an excellent agreement between the POAM III and the DOAS solar occultation measurement with differences less than 13 % [*Randall et al.* 2001]. Both measurements clearly show the unexpected NO_2 maximum around 23 km and, as already indicated by the DOAS measurements, POAM III measures a second maximum of the NO_2 concentration at higher altitudes. However, below 20 km, the data quality of the POAM III measurements becomes poor (indicated by negative values and very large error bars).

For two flights, the DOAS NO_2 measurements were compared to the measurements of the SAGE II instrument. A measurement of SAGE II took place at almost the same location as the measurements during the León flight in 1998, but on the next day. This will of course prevent a tight comparison of the NO_2 measurements. Nevertheless, above 25 km a reasonable agreement is found, but below 25 km the SAGE II measurements largely overestimate the NO_2 concentrations measured by DOAS. As the SAGE II profile shows no maximum of the NO_2 concentration around 25-30 km (as expected by the photochemistry), but further increases with decreasing altitude, it is unclear if the observed discrepancies to the DOAS measurements were caused by the time delay of one day or by problems concerning the SAGE II NO_2 evaluation for lower stratospheric measurements. The second flight took place in Gap in 1999. In this case, the SAGE II and DOAS measurement coincidenced well (in time and space). The comparison of the SAGE II and DOAS NO_2 profiles reveals the same characteristics as found for the León 1998 flight. This supports the suspicion, that the SAGE II NO_2 evaluation has some serious problems at least for the lower stratosphere.

Finally, the measured NO_2 profiles are be compared to the total vertical column densities VCDs measured by the GOME instrument. GOME is a nadir viewing UV/vis DOAS spectrometer installed on the ERS-2 satellite on a sun-synchronous polar orbit [*ESA Publication Division*

---

[10] ILAS, POAM and SAGE measure in occultation mode and hence these measurement must be compared with the DOAS occultation measurements.

1995]. The large field-of-view of the instrument with a corresponding ground pixel size of 320 x 40 km enables the GOME instrument to cover the whole earth within 3 days. To compare the DOAS profile to the GOME column measurements, first box-VCDs[11] were calculated from the measured NO_2 profile. The total VCD is then given by the sum of the box-VCDs (considering all levels up to 50 km altitude). The NO_2-VCDs obtained from the balloon profiles and the NO_2-VCDs measured by the GOME instrument ares given in Table 5.3[12]. However, the large ground pixel of the GOME instrument and the (mostly) different SZAs for the GOME and the balloon measurements make a reasonable comparison difficult. For both Gap flight, the differences of the SZAs are even as large as 60° and hence a comparison is not possible. In Arctic winter, the GOME and the DOAS measurements took place almost at the same SZAs, but of course the vicinity to the polar vortex results in some variation of the NO_2 concentration within the large GOME pixel. Nevertheless, both measurements show a fair agreement. For high-latitude summer, the NO_2-VCD measured with the balloon instrument is about 10% larger which is most likely due to the by ∼20° smaller SZA of the GOME measurement. In contrast, the GOME measurements for both León flights show higher NO_2 amounts, although the balloon measurements were performed at higher SZAs. This alleged discrepancy is probably the result of a tropospheric NO_2 background [*Wenig* 2001], which is only partly included in the balloon-borne measurements, as they are carried out for altitudes above ∼ 5 km, only.

The NO_2 comparison study presented in this section, clearly shows that there exist large discrepancies between the results obtained from different measurement techniques and further work has to be done to bring them into agreement. However, the results obtained for the different flights with the balloon-borne DOAS instrument show a high degree of consistency among each other, taking into account the diurnal as well as the seasonal and latitudinal variations of NO_2.

---

[11] Concentration times layer height

[12] The GOME data was provided by T. Wagner and S. Beirle.

Date	**Location**	**DOAS**		**GOME**		**Comments**
		SZA	VCD	SZA	VCD	
23/11/96	León	73.9-86.5	2.83 ± 0.07	65.4	3.16	
14/02/97	Kiruna	82.5-89.5	1.58 ± 0.02	81.7	1.43	GOME data for 13/02/97
20/06/97	Gap	90	4.4 ± 0.03	23.4	4.11	Pixel 10° west
19/03/98	León	73.9-86.5	4.1 ± 0.11	45.9	4.24	
19/08/98	Kiruna	75.-87.9	4.0 ± 0.12	55.6	3.68	
10/02/99	Kiruna	82.8-86.1	0.83 ± 0.03	82.1	1.14	Strong gradients
25/06/97	Gap	50-86	2.2 ± 0.05	24.3	4.68	DOAS data above 17 km
18/02/00	Kiruna	81.0-89.0	1.73 ± 0.11	80	2	Data from GOME map

Table 5.3: *Comparison of the NO_2-VCD measured by GOME and inferred from the DOAS profile measurement. The SZA is given in [°] and the VCD in [10^{15} molecule/cm^2].*

5.3.4 Comparison with Model Calculations

This section deals with the comparison of the O_3 and NO_2 profiles measured with the DOAS instrument and the model calculations of the 3-D CTMs SLIMCAT, KASIMA, and REPROBUS (for the flights were model data was available). Each measured profile is compared to the output for the model grid point located closest to the measurement The locations of the respective grid points are given in the legends of Figure 5.26 and 5.27. In the case of NO_2, the diurnal variation has to be taken into account, thus the model outputs for different SZAs are shown. If possible, the model outputs for the SZAs corresponding to the beginning and the end of the balloon ascent as well as the 90° SZA data (to be compared to the solar occultation measurement) are shown.

The SLIMCAT model data shown for the Kiruna and Gap flights is from a recently performed multiannual run (Version 194d, based on JPL-97 and JPL-2000). Model data from former annual runs is also available for the León 1996 flight, but not for Gap 1999 flight. This data is shown, too, although these model calculations were mostly based on JPL-97 only (if the update given by JPL-2000 was used, it is noted in the figure legend). Model calculations with the KASIMA model were performed for six flights with various model versions, however only the data from the recommended runs is shown. An additional multiannual run (Version 0008) was performed for the years 1999-2001. REPROBUS model data[13] is only available for the Kiruna flights in 1999 and 2000, and in the case of Kiruna 1999 only data for one single SZA is available. For the KASIMA and REPROBUS model calculations also the recent updates of the photochemical data given in JPL-2000 were used. This appears to be important as the given updates for the rate coefficients for the reactions 3.21, 3.34, and 3.42 (se chapter 3.2) increase the NO_x to NO_y ratio and hence also the NO_2 abundances [*Gao et al.* 1999].

It has to be mentioned here, that the models use a relatively low horizontal as well as vertical resolution. Accordingly, it cannot be expected, that the models capture small scale vertical structures. Further, the existence of large horizontal inhomogeneities (e.g. vortex boundary) can result in model/measurment discrepancies even for relatively small differences between the measurement location and the model grid point. In addition, there are several effects, that are significant on small horizontal scales, like polar filaments. These can largely affect the measurements probing air masses from a small area only[14], while this will not be treated by the model.

It should be emphasized, that the ensemble of flights presented here were conducted under largely different geophysical conditions with respect to chemistry and transport. Whereas the high-latitude winter/spring is characterized by low illumination, cold temperatures, downward motion and variable horizontal mixing processes, as well as by the occurrence of several heterogenous chemical reactions on cold surfaces, the mid- and high latitude summer is clearly dominated by gas-phase chemistry (though there also heterogenous reactions occurring in the lower stratosphere on cold background aerosol) and a rather homogenous transport pattern.

---

[13] The REPROBUS data shown is interpolated in space to the location of the ascent and occultation measurements, respectively

[14] For solar occultation, however, the probed area is increased

Model Comparison for Ozone

First, the comparison of the O_3 measurements with SLIMCAT calculations (with the results of the multiannual run, if not explicitly stated) will be discussed. For almost all flights a nice agrement is found (Figure 5.26), particulary for mid-latitudes. For both Gap flights and the León 1996 flight (annual run) the model is able to reproduce well the measured profile for all altitudes with some small fluctuations. For high-latitude winter the measured profile is qualitatively well reproduced, but up to 15-20 % larger modelled O_3 amount were found above 20 km for Kiruna 2000 and between 10-15 km for Kiruna 1999. It is obvious, that the results of the annual runs tend to agree better with the measurements. In Kiruna 1997, the measurement took place near/at the vortex boundary, where large spatial gradients occur, in particular during solar occultation air masses from the boundary or even from outside the vortex were probed. The SLIMCAT model grid point is located somewhat more inside vortex. As the vortex boundary is known as a region of strong descent [*Kreher et al.* 1999] resulting in large O_3 amount at lower altitudes (for chemical undisturbed conditions)[15], this might explain the observed larger discrepancies (especially to the occultation measurement). The largest discrepancies to the measurement were found for high latitude summer. Here, the model systematically overestimates the measured O_3 amounts by 15-25% for almost all altitudes up to 35 km. This finding is in accordance to previous studies comparing the SLIMCAT model output to ground-based and O_3 sonde measurements [*Chipperfield* 1999].

In contrast to SLIMCAT, the KASIMA model tends to overestimate the O_3 amounts at lower altitudes (below 20 km) up to 20 % during high-latitude winter (see Kiruna 1997 and Kiruna 1999). Above 20 km the measured and the modelled profiles agree with slightly smaller values calculated by the model. This overestimation by KASIMA was also observed in previous studies. There it was speculated if this might be caused by additional chlorine activation (and hence ozone depletion) by small-scale effect such as lee wave PSCs which are not resolved by the model [*Ruhnke et al.* 1999]. However, the opposite is found for the Kiruna 2000 flight. The measured O_3 concentrations are clearly underestimated by the model for low altitudes. The multiannual run (Version 0008), reveals very large shortcomings for the altitude range below 22 km, where unreasonable small O_3 concentrations were calculated. In the case of the annual run (Version 0003) this underestimation is restricted to the altitude range between 12 and 20 km. For the high latitude summer, the modelled profiles follows nicely the measurement for altitudes above 20 km, while the modelled O_3 amount strongly decreases with decreasing altitude below 20 km, resulting in an underestimation of the measurement of up to 50%. The comparison between the measurements of the Gap 1999 flight and the calculations of the multiannual run show a similar characteristic as found for the comparison for the Kiruna 2000 flight. A good agreement is found for altitudes above 25 km accompanied by a large underestimation of the measured O_3 abundances below. Probably most of the discrepancies found here (especially when using the multiannual data) can be attributed mainly to dynamical reasons, as, especially for high-latitudes, the ozone abundances are strongly transport-dependent.

The comparison of the measured O_3 profile with the REPROBUS calculations for the winter of 1999 and 2000 shows an excellent agreement. The REPROBUS model output was interpolated in space to the measurement location, therefore the model data for two locations (corresponding

---

[15] The downward motion transports air masses with a certain mixing ratio to lower altitudes and hence to high pressures, however depending on the photochemical lifetime and the transport time.

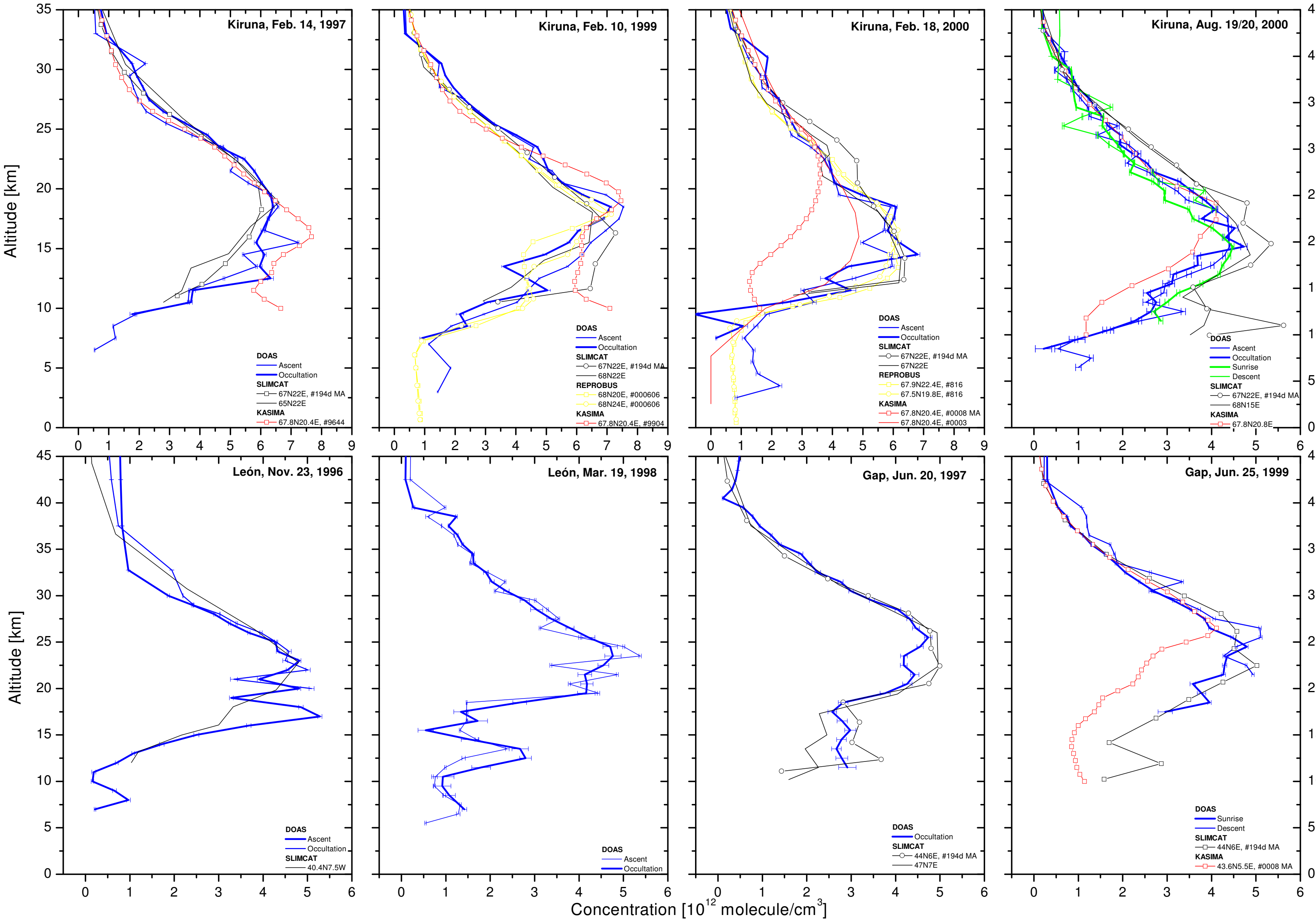

Figure 5.26: *Measured and modelled vertical profiles of the O_3 concentration. The upper row shows the measurements at high latitudes for winter (left three panels) and summer (right panel). The mid-latitudinal measurements are shown in the lower row for León (left) and Gap (right). Unfortunately there was no model data available for the flight in León 1998.*

to balloon ascent and solar occultation) is plotted. Especially in 2000, the model follows the measurement through the whole altitude range, with a slight underestimation above 25 km. For Kiruna 1999, the modelled O_3 concentrations are smaller by $\sim$10% for high altitudes. Below 20 km, the measured ascent profile shows up to 18-20% larger values compared to the corresponding REPROBUS grid point (68°N,24°E).

What we can learn from this section is, that in general the CTMs can reproduce fairly well the O_3 distribution, however, for high latitudes the ozone concentrations are mainly overestimated, an finding in agreement with several other studies [e.g., *Otten* 1997; *Chipperfield* 1999]. It is expected, that a more accurate representation of the model transport will significantly improve these long-term simulations [*Fahey and Ravishankara* 1999]. Also, it is discussed, if the discrepancies found for high-latitude winter might be caused by the finite resolution of the models [*Ruhnke et al.* 1999].

Model Comparison for NO_2

The comparison of the measured and modelled NO_2 profiles shows striking discrepancies for almost all flights and all models (Figure 5.27). Please note, that the solar occultation measurements have to be compared to the model output for SZA = 90°. For comparison with the balloon ascent/descent measurements, model data is shown for SZAs corresponding to the beginning and the end of the balloon ascent/descent. As the NO_2 concentrations undergo fast photochemical variations, especially during solar occultation, the profiles can be slightly distorted.

Going through the different winters, it becomes obvious, that the SLIMCAT model systematically underestimates the measured NO_2 amounts for each winter, but to different degrees. As the annual runs mostly do not include the important updates of the rate coefficients given by JPL-2000, the comparison with the multiannual run will be discussed mainly. For the winter 1997, the model calculations almost fairly agree with the measured ascent profile, however, for solar occultation, the model fails. As already discussed above, the grid point of the SLIMCAT model rather coincidence with the location of the ascent measurement and only to a smaller degree with the occultation measurement, giving a possible explanation for these discrepancies. For Kiruna 1999 a different situation is found. The measured NO_2 amounts during balloon ascent as well as for the solar occultation were underestimated up to 50-60% in the altitude range of maximum NO_2 concentrations. The modelled NO_2 concentrations in the lower stratosphere increases below a small strongly denoxified band between 17 and 20 km to concentrations similar to those measured. This observation is in clear contrast to the usually observed complete denoxification (with NO_2 concentrations close to zero) at low altitudes calculated by CTMs [e.g. *Payan et al.* 1999; *Denis et al.* 2000] Besides chemical reasons, also dynamical effects might have been contributed this feature as the vortex was relatively weak and unstable and the model may possibly assume large horizontal mixing with NO_x rich mid-latitudinal air. In contrast to the winter 1999, the SLIMCAT calculations for the winter 2000 show a complete denoxification for low altitudes. For altitudes above 20 km, a comparison with the model is difficult, as a rather unusually shaped NO_2 profile has been measured caused by downward transport of mesospheric air (see section 5.3.3). Indeed, the model cannot reproduce the measured NO_2 profile, it rather produces a conventionally shaped NO_2 profile, and hence not too much can be said about the comparison of the NO_2 amounts here. It is worth mentioning, that the annual run (already updated with JPL-2000) show NO_2 amounts approx. a factor of 3 larger between 22 and 30 km. Although the reason is unclear, the effect on ozone can nicely be studied. The ozone

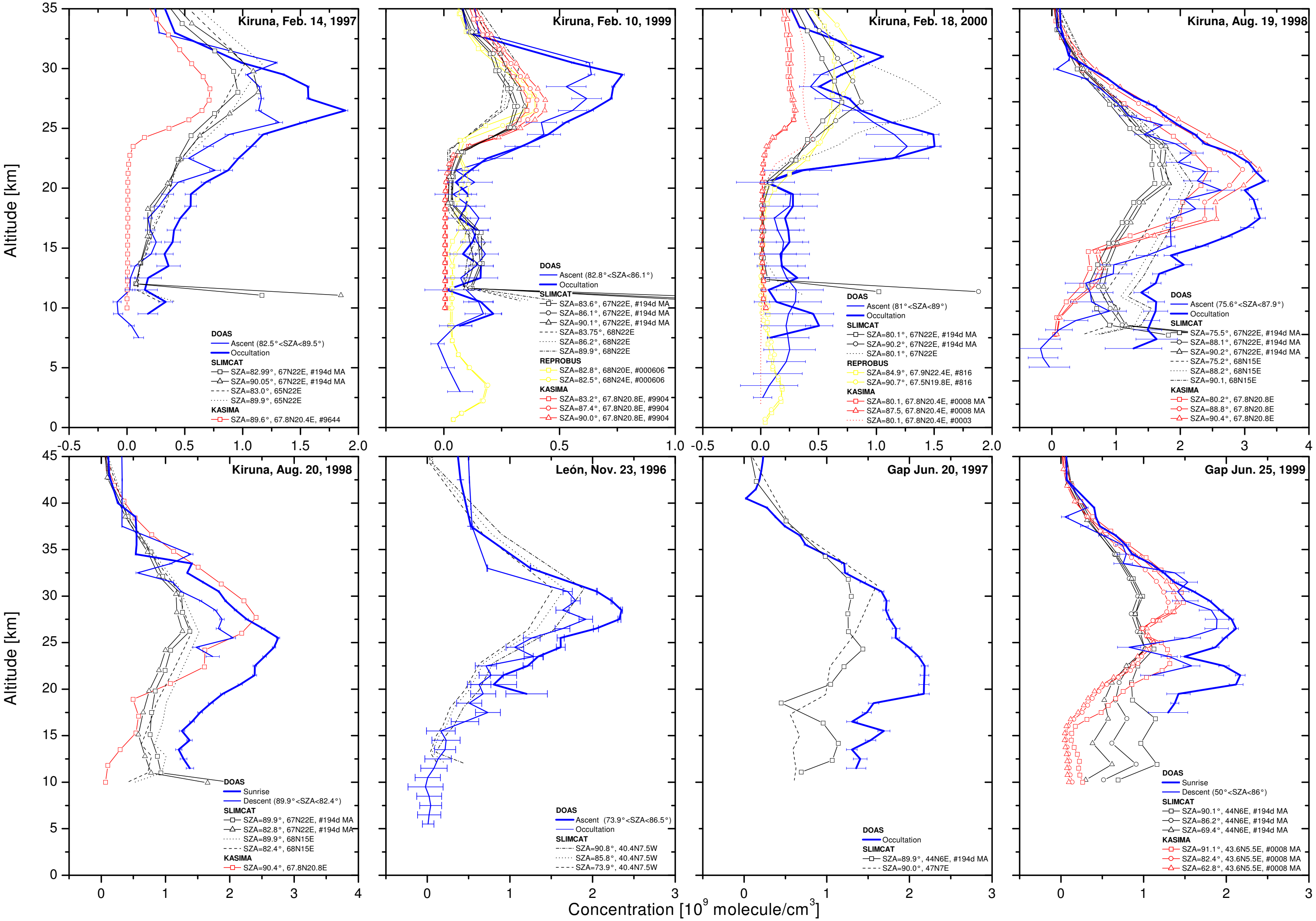

Figure 5.27: *Measured and modelled vertical profiles of the NO_2 concentration. The upper row shows the measurements at high latitudes for winter (left three panels) and summer during sunset(right panel). The high latitude sunrise measurement in summer is shown in the lower panel on the left hand side. On the right hand side, the mid-latitudinal measurements are shown. Please note, that the León 1998 flight has been removed here (no model data is available for this flight).*

amounts above 20 km were significantly decreased in the model output of the annual run. For high-latitude summer a relatively small underestimation for altitudes above 30 km is found for balloon ascent and some larger discrepancies for solar occultation ($< 30\%$). The gap between the modelled and measured NO_2 concentrations increases with decreasing altitude. At e.g. 22 km this deviation is about 40% for balloon ascent and about 60% for solar occultation. For very low altitudes, the agreement gets somewhat better. The data from the annual run provides larger values below 30 km resulting in a slightly better agreement with the measurements. The NO_2 measurements performed during sunrise and balloon descent on the following day compare in an almost identical way to the model calculations as for the day before. The NO_2 amounts measured during both Gap flights agree well with the modelled values for the upper part of the profile. For 1997 the model underestimates the measurement by 30-50% below 32 km. For 1999, a underestimation is obtained already for altitudes below 37 km with values being in the same range as for 1997. For León 1996, only model data from the annual run based on JPL-97 is available. A reasonable agreement is found with up to 20-25 % smaller amounts obtained by the model. However, using JPL-2000 would bring the model in better agreement with the measurement. All in all, it seems, that the results obtained with the annual runs agree better with the measurements as the results obtained from the multiannual runs.

The comparison with the KASIMA model for high-latitude winter shows qualitatively the same results as obtained from the SLIMCAT model. For all three winter flights, the measured NO_2 concentrations are largely underestimated. For Kiruna 1997, only the model calculation for SZA=90° is available. Since the model grid point is located inside the vortex, a reasonable comparison with the solar occultation profile (with tangent points located at the vortex boundary and slightly outside) is not possible. However, the ascent profile is already underestimated ($\sim$ 40% at 27 km), although it was located closer to the model grid point. The modelled profile for Kiruna 1999 is relatively similar to the SLIMCAT calculations, but with slightly larger NO_2 concentrations. The disagreement to the measurement in the altitude range of the concentration maximum is about 33% for ascent and 40% for solar occultation. For winter 2000, KASIMA calculates extremely low NO_2 concentrations, and hence a large disagreement to the measurement is found. However, as the KASIMA model extends to an altitude up to 120 km (but without treating the chemistry in the mesosphere), downward transport of mesospheric air masses is taken into account [*Ruhnke et al.* 1999]. Indeed, especially with the annual run (0003) a NO_2 profile is obtained similar in shape as the measured one, though the modelled values are clearly smaller. For all winters, the KASIMA model shows a strong denoxification in the lower stratosphere. In contrast to polar winter, a good agreement is found for high-latitude summer for altitudes above 25 km. The model even tends to overestimate the measured concentrations, clearly visible for the balloon ascent ($\sim$ 25-30%) and the sunset measurement on the following day ($\sim$ 15%). Below 25 km, the modelled NO_2 concentrations strongly decrease with decreasing altitude and a large underestimation of measured concentrations is found of up to 50% for ascent and sunrise and 60% for sunset, respectively[16]. For Gap 1999 a similar comparison is found with a slight overestimation in the upper part of the profile and an increasing underestimation of up to 60% for lower altitudes.

The NO_2 concentrations modelled with the REPROBUS model for the winter of 1999 and 2000 were almost identical to those calculated by SLIMCAT, both in shape and in absolute values. Even the relatively weak denoxification in the lower stratosphere is found in the REPROBUS

---

[16] No data is available for SZAs corresponding to the balloon descent.

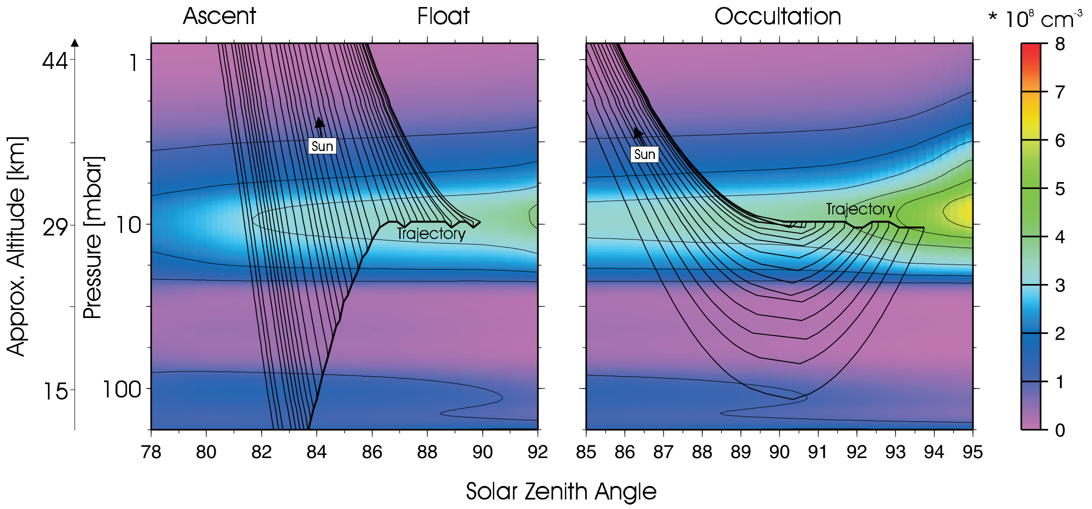

Figure 5.28: *SLIMCAT model simulation of stratospheric NO_2 as a function of solar zenith angle for sunset at Kiruna (67° N22° E) on Feb. 10, 1999. The isolines show NO_2 concentrations in units of 10^8 molecule/cm^3. Superimposed is the observation geometry of the balloon-borne DOAS measurements. In the left panel the balloon trajectory together with the line of sight for every tenth recorded spectrum is shown for balloon ascent and float. In the right panel the solar occultation measurements are shown similarly. The amount of absorbing NO_2 in each line of sight is the integral of the local concentration times the path length of a ray traversing an individual atmospheric layer.*

model calculations for winter 1999. Thus, the same as already discussed in connection with the SLIMCAT model is valid here, too.

As already discussed earlier, substantial photochemical changes of the NO_2 concentrations occur during the measurement period covering typically a SZA range from 80° to 95°. To take this into account, model-related integrated NO_2-SCDs were calculated and directly compared to the measured NO_2-SCDs. For that purpose, the geometry was simulated by which the solar zenith angle dependent photochemical field of NO_2 was observed (see Figure 5.28). This was obtained by interpolating between the given pressure levels and SZA intervals of the SLIMCAT model output (of the multiannual run). An integration of the local NO_2 concentration along the line of sight then yields the model-related integrated NO_2-SCD for each observation.

Figure 5.29 compares the modelled and measured NO_2-SCDs for high-latitude winter (upper panel), high latitude summer (middle panel) and mid-latitudes (lower panel). The comparison for polar winter draws a rather non-uniform picture. For Kiruna 1999 the measured SCDs are twice the modelled SCDs for almost all altitudes for balloon ascent and float as well as for solar occultation. For the Kiruna 1997 flight a small but constant underestimation by $\sim$ 20% was found for the balloon ascent, while for the float phase, the measured and modelled NO_2-SCDs almost agree, and for solar occultation the measurement is underestimated by 35%. The large variation of the discrepancies for different phases of balloon flight can probably be explained

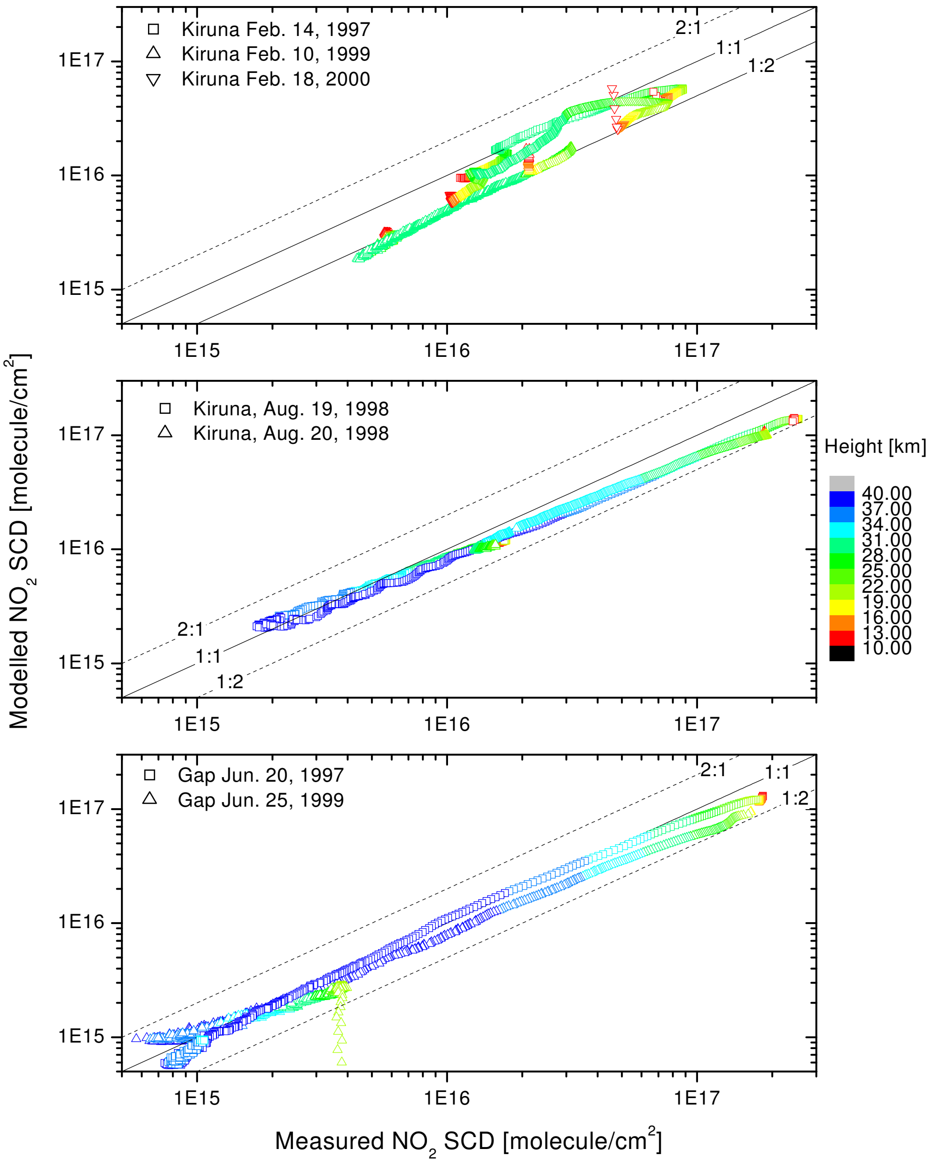

Figure 5.29: *Comparison of the measured and the along the line of sight integrated modelled SCDs of NO$_2$. The modelled NO$_2$-SCDs were calculated using the model output of the multiannual SLIMCAT run. The color code denotes the balloon height during the ascent/descent measurements, and the tangent height of the measurements for the solar occultation, respectively. The strong decrease in the lowest panel for the Gap 1999 flight is caused by the fact that SZAs beyond the range of the SLIMCAT data were reached.*

by changing measurement locations with respect to the vortex boundary (see discussion above). The Kiruna 2000 comparison shows a constant underestimation of 40% for altitudes below 20 km, both for ascent and solar occultation. Above 20 km, the comparison reflects the differences of the unusual shape of the measured profile to the conventional shaped model profile.

For high and mid-latitude summer, a rather similar comparison with the measurement is found. For high altitudes, the modelled and measured NO_2 amounts fairly agree, while with decreasing altitude, an increasing discrepancy occurs. For Kiruna 1998, almost the same correlation is obtained for sunset and sunrise with an underestimation of up to 40-45%. However, it is remarkable, that the underestimation appears to be smaller for ascent/descent compared to sunset/sunrise for comparable altitudes (the same feature is found for the Gap 1999 flight). The diurnal variation of NO_2 during daytime is largely controlled by the NO_2 photolysis and the reaction of $NO + O_3$. For sunrise the N_2O_5 photolysis has to be considered, too, however, as the sunset and sunrise correlations nicely agree, uncertainties concerning the N_2O_5 photolysis can be ruled out as explanation. Assuming constant O_3 concentrations during sunset/sunrise, this can only be explained by an underestimation/overestimation of the NO_2 photolysis in the lower stratosphere for small/large SZAs by the model. Inspecting again Figure 5.17 in section 5.3.1, it becomes clear, that, the model indeed tends to underestimate systematically the measured j_{NO_2} values during balloon ascent ($< 10\%$), even though within the rather large error bars both agree. In contrast, an excellent agrement is found for large SZAs, where the photolysis is dominated by the contribution of the direct sunlight.

The comparison for both Gap flights reveals a significant shift of the correlation-line between 1997 and 1999. For the 1997 flight, a nice agreement is found for altitudes above 30 km with an underestimation of up to 25% below, whereas for 1999 only at very high altitudes an agreement is found. For lower altitudes the modelled values are up to 40% smaller for occultation and up to 30% for descent. This difference between 1997 and 1999 is rather unexpected as both measurements were carried out in an identical photochemical regime. Also changes of the stratospheric aerosol content (an increase of the aerosol surface yield an increased importance of the hydrolysis reactions) can not explain these differences as measurements suggests that the stratosphere has already returned to background conditions since 1996[17] [e.g. *EC-Report* 2001].

The study above can be summarized as follows.

- For high-latitude winter, the models largely underestimate measured NO_2 concentrations at almost all altitudes, only above 30 km the agreement seems to be better. However, a detailed comparison is often difficult due to spatial inhomogeneities occurring at the vortex edge. The models tendency to denoxify completely in the lower stratosphere is only found in the winter 2000, whereas in winter 1999 the models show reasonable values (except KASIMA). Further, the modelled denoxification extend to higher altitudes compared to the measurement. The downward transport of mesospheric air can significantly change the measured NO_2 profile and should be taken into account by the models.

- For high latitude summer and mid-latitudes, a fair agreement is found for high altitudes (even a slight overestimation in some cases), but a large underestimation for low altitudes (up to 50%). This lower-stratospheric discrepancies were found to be slightly smaller for balloon ascent than for solar occultation, probably caused by the adopted j_{NO_2}-values in the model.

---

[17] In 1991, the eruption of the Mt. Pinatubo strongly pertubated the stratospheric aerosol level.

The above discussion, however, does not treat the denitrification effects inside the polar winter, which is obviously not easily accounted for by CTMs, but can significantly change the atmospheric NO_2 concentrations (through re-distribution of NO_y from altitudes around 20 km to rather low altitudes). It should be emphasized that denitrification can not explain the observed discrepancies, as it will result in smaller NO_2 concentrations around 20 km and higher, but probably not observable NO_2 amounts (as NO_y is mainly abundant as HNO_3) in the lower stratosphere, but exactly the opposite is observed in the model/measurement comparison. Nevertheless, the different winters will be briefly discussed with respect to denitrification. In 1997, denitrification was observed between February 11 and 20 for some air masses inside the vortex [*Kondo et al.* 2000], however, the LPMA/DOAS measurements took place at the vortex edge and hence it is unlikely that the observations were altered by denitrification. In 1999, the polar vortex was warm with temperatures being mostly above or only slightly below the PSC threshold [*Naujokat et al.* 1999] and denitrification was not observed. In February 2000, a stratospheric warming occurred and the temperatures were well above the PSC threshold during the time of the LPMA/DOAS balloon flight, but PSCs occurred until early February accompanied by extensive denitrification [e.g. *Popp et al.* 2001], which probably affected the NO_2 measurements on February, 18, for altitudes below 20-22 km.

In conclusion, it has been shown, that CTMs generally tend to underestimate the NO_2 concentrations both for high and mid-latitudes for winter as well as for summer. Similar observations have been made in previous studies, however the degree of the observed underestimation strongly varies [*Otten* 1997; *Chipperfield* 1999; *Erle* 1999; *Payan et al.* 1999]. Several explanations were proposed, like additional conversion of HNO_3 to NO_2 on soot aerosols [*Lary et al.* 1997], faster gas-phase reactions regulating the NO_2 to HNO_3 ratio (which was indeed confirmed by laboratory studies [*Brown et al.* 1999a; *Brown et al.* 1999b] and was already taken into account for the model calculations presented here), overestimation of the probability value for the heterogeneous conversion of N_2O_5 into HNO_3 under stratospheric conditions and for very low temperatures [*Zhang et al.* 1995] (the recommendation for the probability value changed from JPL-97 to JPL-2000) or a lacking additional pathway for the NO_2 re-formation in winter [*Payan et al.* 1999]. However, to rule out dynamical reasons, atmospheric tracers such as N_2O and CH_4 have to be included in the studies or trace gas ratios should be examined (this can be found in the more detailed investigation in chapter 6).

It is rather astonishing, that the models seem to properly model the O_3 abundances and at the same time largely fail to reproduce the NO_2 amounts. Qualitatively, this can be understood, besides the fact, that within an extremely complex chemical and dynamical system, various processes can compensate each other. At mid-latitudes and during high latitude summer, the O_3 loss is dominated by the NO_x catalyzed cycle, but this O_3 loss-cycle is effective mainly for altitudes above $\sim$25 km (and below $\sim$40 km). However, the very large disagreements with the NO_2 measurements were observed for altitudes below 25 km, while above a rather reasonable agreement is found. During high latitude winter, the O_3 abundance is mainly controlled by non-nitrogen processes as the winterly NO_x amounts were extremely low in the lower/middle stratosphere. Nevertheless, also small NO_x amounts indirectly modulate the O_3 depletion through the formation of chlorine and bromine reservoir species. Indeed, CTMs often fail to properly reproduce the observed ozone loss [e.g. *EORCU* 2000], but this can certainly not be directly attributed to the underestimation of NO_x.

Chapter 6

Investigation of the NO_y Partitioning and Budget using CTM and LPMA/DOAS Results

The model and measurement study of NO_2 and O_3, presented in chapter 5.3, revealed that CTMs largely fail to reproduce the measured NO_2 profiles. To distinguish between chemical and dynamical or model related reasons, it is helpful to consider the ratio of the NO_x species to the total reactive nitrogen NO_y or simply, the ratio of NO_2 to HNO_3. This ratio can be used to test the nitrogen chemistry adopted in the model, independent of (slow) transport processes and of the total amount of nitrogen assumed by the model. The measurements of HNO_3 by the LPMA-FTIR in combination with the DOAS NO_2 measurements, allow to compare the vertical distribution of this ratio with model calculations for different geophysical regimes. This comparison is presented in the first section of this chapter. The second section deals with an investigation of the NO_y budget. The total amount of inorganic nitrogen, and hence also the NO_2 abundance, strongly depends on atmospheric transport and mixing processes. Therefore, long-lived tracers such as N_2O measured with the LPMA-FTIR and calculated by the CTMs will be compared. During the Kiruna flight in 1999, an almost comprehensive set of NO_y species was measured allowing a detailed investigation of the individual compounds. In combination with the N_2O measurement, the important NO_y-N_2O correlation is studied for Arctic winter conditions and compared to the correlation obtained from the model calculations.

6.1 Partitioning of Reactive Nitrogen

NO_x directly catalyzes the stratospheric O_3-loss, but also affects the efficiency of the halogen and hydrogen O_3-destroying cycle. Thus a good understanding of the nitrogen chemistry is essential for treating the problem of stratospheric ozone loss. Previous studies examining the NO_x/NO_y or NO_2/HNO_3 ratio suggested an incomplete understanding of the mechanisms regulating the partitioning of the NO_y species [e.g. *Lary et al.* 1997; *Sen et al.* 1998; *Ostermann et al.* 1999]. The agreement with models could be significantly improved if the newly measured rate constants for the $OH+HNO_3$ and $OH+NO_2$ reactions were used [*Brown et al.* 1999a; *Brown et al.* 1999b], e.g. the study of *Gao et al.* [1999] based on ER-2 measurements during Arctic summer showed that the slope of the linear fit to the model/data regression increased from 0.62 to 0.84 when using the new rate constants. Other Arctic summer studies report an excellent agreement if the reaction rate of the NO_2+OH reaction was reduced by 35% [*Ostermann et al.* 1999], which is significantly more as proposed by *Brown et al.* [1999a]. A remaining difference of up to 20% is obtained by *Randeniya et al.* [1999] for mid- to high latitude summer at altitudes above 27 km. During high-latitude winter the NO_y partitioning is mainly controlled by heterogenous chemistry and, hence, the new rate constants only slightly changed the modelled NO_x/NO_y ratio. The spares measurements inside the polar vortex [*Payan et al.* 1999; *Stowasser et al.* 2000; *Wetzel et al.* 2000] reveal an underestimation of the NO_x/NO_y ratio by the models, but the large meteorological variability and the highly variable radiation field that control the photodissociation make it rather difficult to draw a conclusive picture.

The NO_2/HNO_3 ratio calculated from the NO_2-DOAS measurement and HNO_3 measured by the LPMA-FTIR for the three Arctic winter, the Arctic summer and the mid-altitude autumn flights is shown in Figure 6.1. For each flight, the measured NO_2/HNO_3 ratio is shown for balloon ascent and solar occultation. The calculations of the models SLIMCAT, KASIMA and REPROBUS are displayed for the same SZAs as in chapter 5.3.4. For clarity, the results of the 'old' annual runs of the SLIMCAT model are not shown for Arctic winter.

In winter 1997, the LPMA/DOAS measurements were performed near the vortex edge, thus a comparison with models is difficult. In contrast to the inner-vortex flights in 1999 and 2000, the measurements in 1997 show no distinct denoxified lower stratosphere, instead a steady increase of the NO_2/HNO_3 ratio is found. Large discrepancies between the measurement and the KASIMA model calculations occur, probably the caused by the different locations of the model grid point and the measurements. The KASIMA model result shows a strong denoxification up to about 20 km, a clear indication for air masses more from the inner-vortex. The SLIMCAT model calculations agree well with the measurement for altitudes below 22 km, even the measurements show some oscillations. This is consistent with the fact, that the SLIMCAT grid point is located relatively close to the measurement location. Above 22 km, a clear underestimation is found with a maximum of 55% for ascent and 65% occultation at about 25 km. However, the measured N_2O profile (Figure 6.2), shows significantly increased mixing ratios above 21 km being a hint that possibly the probed air masses were mixed with mid-latitudinal air.

In winter 1999, the measurements were carried out inside the polar vortex. Below 21 km, a strong denoxification is observed with a NO_2/HNO_3 ratio being in the range of 0.01 and slightly decreasing with increasing altitude. Above 21 km, the NO_2/HNO_3 ratio strongly increases up to a value of one at 30 km. Surprisingly, the SLIMCAT as well as the REPROBUS model manage to reproduce the degree of denoxification excellently, only the KASIMA model overestimates the observed denoxification by almost a factor of ten. Nevertheless, discrepancies exist concerning the height of this denoxified layer. While SLIMCAT tends to denoxify only up to an altitudes of 18 km, REPROBUS denoxifies almost up to 22 km. Between 21-22 km and 32 km, similar values for the NO_2/HNO_3 ratio are obtained with all models, whereas the measured values are significantly larger. Here, an underestimation is observed ranging from almost zero at 25 km to 40% at 23 km and 30 km

The Kiruna 2000 measurement shows a similar situation for the lower stratosphere as the year before. The NO_2/HNO_3 ratio is almost constant with values around 0.01-0.02 up to altitudes of 21 km. Above, the measured NO_2/HNO_3 profile shows a large dip at 23-24 km followed

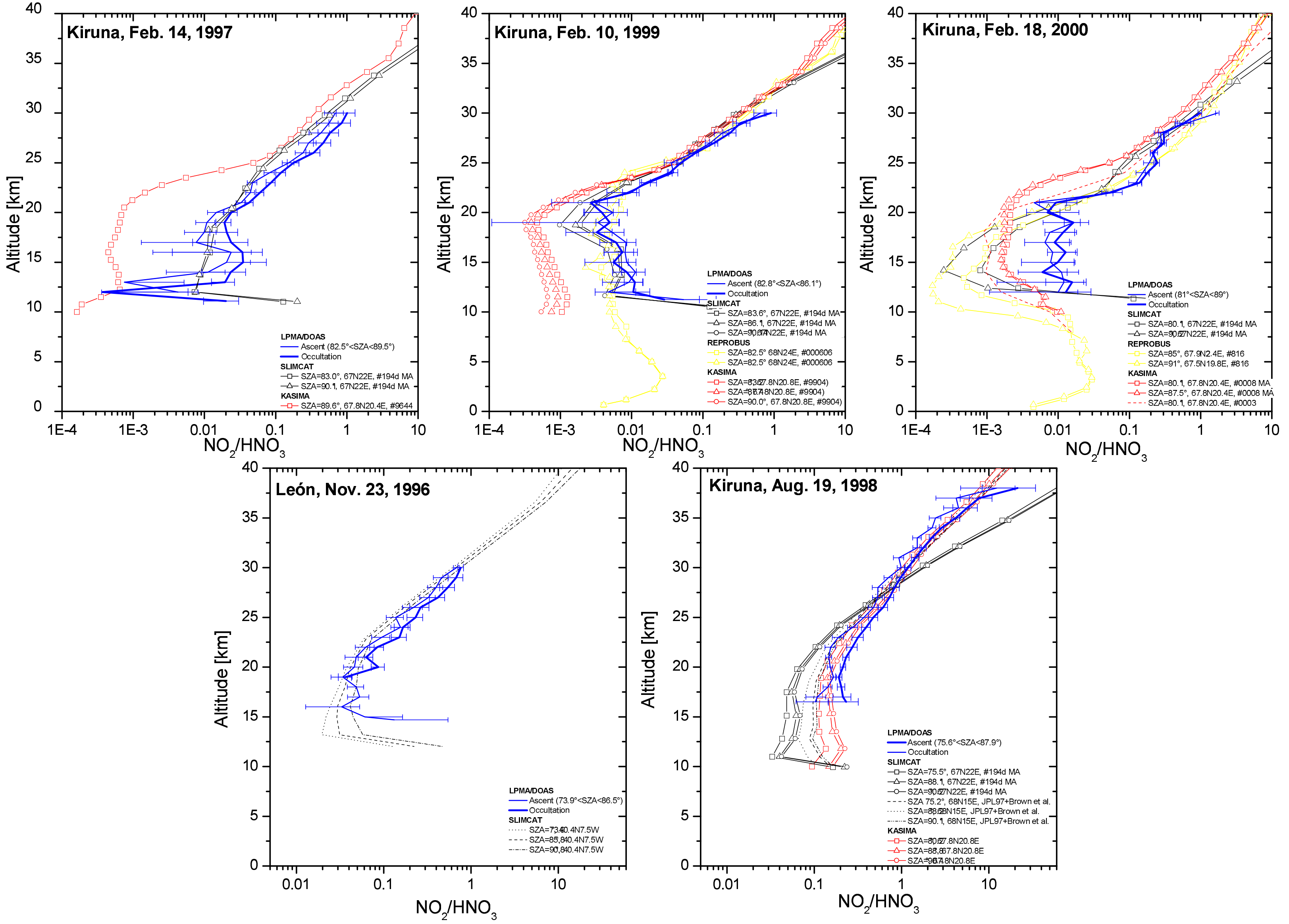

Figure 6.1: *Measured and modelled NO$_2$/HNO$_3$ ratios for the Arctic winter (upper panel), Arctic summer (lower panel, left) and mid-latitude autumn (lower panel, right).*

by a distinct notch. This is certainly the result of the impact of the descended mesospheric air (see chapter 5.3.3). The large change of the NO_2/HNO_3 ratio, however, implies that the photochemical equilibrium is not reached yet. In contrast to the previous winter, the models fail to properly model the NO_2/HNO_3 ratio in the lower stratosphere. The measured NO_2/HNO_3 ratio is underestimated by a factor of 10-30. Due to the distorted NO_2 profile and hence NO_2/HNO_2 ratio above 20 km, no reasonable comparison is possible there.

For the León 1996 flight, only SLIMCAT data from an 'old' run based on JPL-97 is available. The comparison shows a moderate disagreement, particular for altitudes between 20 km and 28-30 km, where the measured NO_2/HNO_3 ratios are underestimated by 25-40%. This observation is in accordance to previous studies using JPL-97 [e.g. *Sen et al.* 1998; *Ostermann et al.* 1999]. The modelled NO_2/HNO_3 ratio would be significantly increased using JPL-2000, bringing the measurement and the model in better agreement.

The measurement during high latitude summer shows a steady increase of the NO_2/HNO_3 ratio from values around 0.1-0.2 at 17 km to about 12 and 20 at 38 km for balloon ascent and solar occultation, respectively. The measured NO_2/HNO_3 ratio is qualitatively well reproduced by KASIMA as well as by SLIMCAT. However, this is not true for the multiannual SLIMCAT run, which is inconsistent to the measurements and all other model calculations. The reason for that is unclear yet and the discussion will be restricted to the results of KASIMA and of the annual run of SLIMCAT (based on JPL-2000). A nice agreement between the models and the measurements is found for solar occultation, while both models clearly overestimate the NO_2/HNO_3 ratio above 25 km measured during balloon ascent. This dependence of the model/measurment agreement on SZA was already observed for the NO_2 model/measurment comparison in chapter 5.3.4. There it was speculated whether this is caused by a slight underestimation of the NO_2 photolysis frequencies for small SZAs. Thus we will focus on the comparison for solar occultation. Both models show an excellent agreement with the measurement above 28 km, while an increasing underestimation with decreasing altitude is found below. This discrepancies gets as large as 25% and 40% at the lowest altitudes using the KASIMA and the SLIMCAT model results, respectively.

The study presented in this section can be summarized a follows:

- Arctic winter: SLIMCAT and REPROBUS can reproduce the measured NO_2/HNO_3 ratio in the lower stratosphere for conditions with moderate temperatures (Kiruna 1999). The underestimation of the NO_2/HNO_3 ratio by the models reported by other studies is only confirmed for conditions with very low temperatures and extensive PSC formation. This indicates, that the reaction probability for the N_2O_5 hydrolysis for very low temperatures and stratospheric HNO_3 concentrations adopted by the models may still be too large, although the value given in the new release of the kinetic and photochemical database of JPL has experienced an update [*Sander et al.* 2000]. However, it can not be excluded that the extensive occurrence of PSCs in the winter 2000 possibly (even if the reaction probability for the N_2O_5 hydrolysis on PSCs is relatively small) influenced the results of the measurements and/or the models. A significant underestimation of the NO_2/HNO_3 ratio by the models is found in the upper stratosphere, a finding confirmed by the studies of *Jucks et al.* [1999] and *Wetzel et al.* [2000], but in contradiction to *Payan et al.* [1999]. However, studies performed inside the polar vortex are spares and due to the large variability of the different Arctic winters and the large dependence on the transport history of the air parcels (and hence illumination) a tight comparison is difficult.

- High latitude summer: Above 28-30 km a good model/measurement agreement is found. Therefore, increasing the HNO_3 photolysis rate as proposed by *Jucks et al.* [1999] could bring the modelled NO_2/HNO_3 ratio in better agreement in the upper stratosphere for the Arctic winter, but at the same time will worsen the agreement for summer. The underestimation of the NO_2/HNO_3 ratio below 28 km, and hence within the stratospheric aerosol layer, suggests the existence of further heterogenous HNO_3-loss reactions. Several heterogenous mechanisms were proposed like the reduction of HNO_3 on carbon aerosols [*Lary et al.* 1997]. However, very little is known about the reaction probabilities of these mechanisms. A crucial parameter for modelling the NO_2/HNO_3 ratio is the aerosol surface [*Kondo et al.* 2000]. Large uncertainties, however, exist for the measurements of the number density of small particles [*Hervig and Deshler* 2001]. As a smaller amount of small aerosols would significantly decrease the total aerosol surface available for heterogenous reactions such as the N_2O_5 hydrolysis, a larger NO_2/HNO_3 ratio would be calculated by the models. A better agreement with the measurement could also be achieved by further reducing the rate coefficient for the pressure dependent NO_2+OH reaction [*Ostermann et al.* 1999], since this will mainly impact the results for the lower stratospheric during summer.

In conclusion, it could be shown, that a complete understanding of the stratospheric nitrogen chemistry has not yet been achieved, although a large degree of agreement between models and measurements is found. A single source of error cannot be identified which can account for the remaining discrepancies between the measured and modelled NO_2/HNO_3 ratios and future investigations are needed. Finally it should be pointed out, that the observed underestimation of the NO_2/HNO_3 ratio by the models can only partly account for the large underestimation of the NO_2 concentrations, particular for high-latitude winter.

6.2 The NO_y Budget

6.2.1 N_2O as a Proxy for the Tracer Transport

As already discussed in chapter 3.2, NO_y and its source gas N_2O are strongly anti-correlated, i.e. while N_2O decreases with altitude, the opposite is found for NO_y. In the lower stratosphere both have a very long lifetime. At higher altitudes, however, the lifetime of NO_y dramatically decreases caused by the rapid loss of NO_y through the reaction NO+O. Therefore, the typical vertical distribution of NO_y shows an increase in the lower stratosphere, a maximum in the middle stratosphere and a subsequent decrease. It is evident, that transport processes such as diabatic descent (or ascent) can significantly change the NO_y abundance at a certain altitude. Thus, reliable calculations of the tracer transport within the models are essential for the simulation of nitrogen species (and others). Large uncertainties, however, exist, when calculating the descent rates within the winter polar vortex or the mixing of polar with mid-latitudinal air during high-latitude winter. To a smaller extend, the same is true for high latitude summer. A simple way to test the tracer transport is to compare the measured and modelled N_2O profiles. This comparison doesn't allow to distinguish between decent and mixing processes, but especially for polar winter conditions (for a moderate stable vortex) the N_2O distribution is mainly the result of the subsidence inside the polar vortex with smaller contributions from horizontal mixing processes.

The comparison of the measured and modelled N_2O profiles (Figure 6.2) confirms the existence of large uncertainties for the treatment of the tracer transport. For high-latitude winter (upper panel) large differences between the N_2O profiles calculated by the different models can be observed. While the REPROBUS model reproduces the measured N_2O profiles fairly well, KASIMA tends to underestimate the subsidence of air, whereas the opposite is found for SLIMCAT. This is certainly a result of the different meteorological analysis, of the different techniques to calculate the descent rates, and of the different horizontal and vertical resolution used in the models.

The N_2O measurements confirm that during the flights in winter of 1999 and 2000, air masses inside the polar vortex were probed. In contrast to winter 1999 and 2000, the measurement in winter 1997 took place near the vortex edge. Indeed, the measured N_2O profiles (for ascent and solar occultation) show higher N_2O values above 21 km indicating mid-latitudinal or a mixture of polar and mid-latitudinal air.

As expected, high N_2O mixing ratios were observed during high-latitude summer and at mid-latitudes. The N_2O profile measured at high latitude summer is nicely reproduced by the KASIMA model, while the SLIMCAT model largely overestimates the summerly descent rates. This is consistent with the observed larger underestimation of the measured NO_2 concentrations by the SLIMCAT model compared to KASIMA. For the measurement in León 1996, a reasonable agreement with the SLIMCAT model (annual run) is found.

Thus, the observed discrepancies between the measured and modelled NO_2 profiles (see chapter 5.3.4) can be explained partly by the improper treatment of the transport processes by the models. However, it should be emphasized that all models underestimate the NO_2 abundances (especially during high-latitude winter), while the N_2O mixing ratios are under- and overestimated depending on the model used.

6.2.2 NO$_y$ budget and Partitioning for Feb. 10, 1999

During the LPMA/DOAS balloon flight in Kiruna on Feb. 10, 1999, the NO_y species NO, NO_2, HNO_3, and $ClONO_2$ were simultaneously measured within the polar vortex. However, the used configuration of the LPMA-FTIR does not allow to detect N_2O_5. Thus, to complete the NO_y budget, the N_2O_5 abundance will be estimated[1]. Based on steady-state assumptions the diurnal average N_2O_5 concentration can be calculated [*Brasseur and Solomon* 1986]:

$$\frac{[N_2O_5]_{avg}}{[NO_2]_{day}} = \frac{k_{3.28}[O_3]\left(1+\frac{j_{NO_2}+k_{3.22}[O]}{k_{3.21}[O_3]}\right)F_d}{j_{N_2O_5}\cdot F_s} \tag{6.1}$$

where F_s and F_d represent the fraction of the day being sunlit and dark, respectively. Ignoring further the NO_2+O reaction (reaction 3.22), N_2O_5 can easily be derived from the measured NO_2 and O_3 concentrations in combination with calculations of j_{NO_2} and $j_{N_2O_5}$[2]. To scale this

---

[1] A truly complete NO_y budget has to consider additionally HO_2NO_2, $BrONO_2$ as well as aerosol nitrate, but as their abundances are extremely small they can be neglected here.

[2] For the calculation of j_{NO_2}, the actinic flux modelled with DISORT for Kiruna 1997 (see chapter 5.3.1), the quantum yields from [*Roehl et al.* 1994] and the cross section from *Davidson et al.* [1988] was used. $j_{N_2O_5}$ is taken from the look-up table used within the SLIMCAT model.

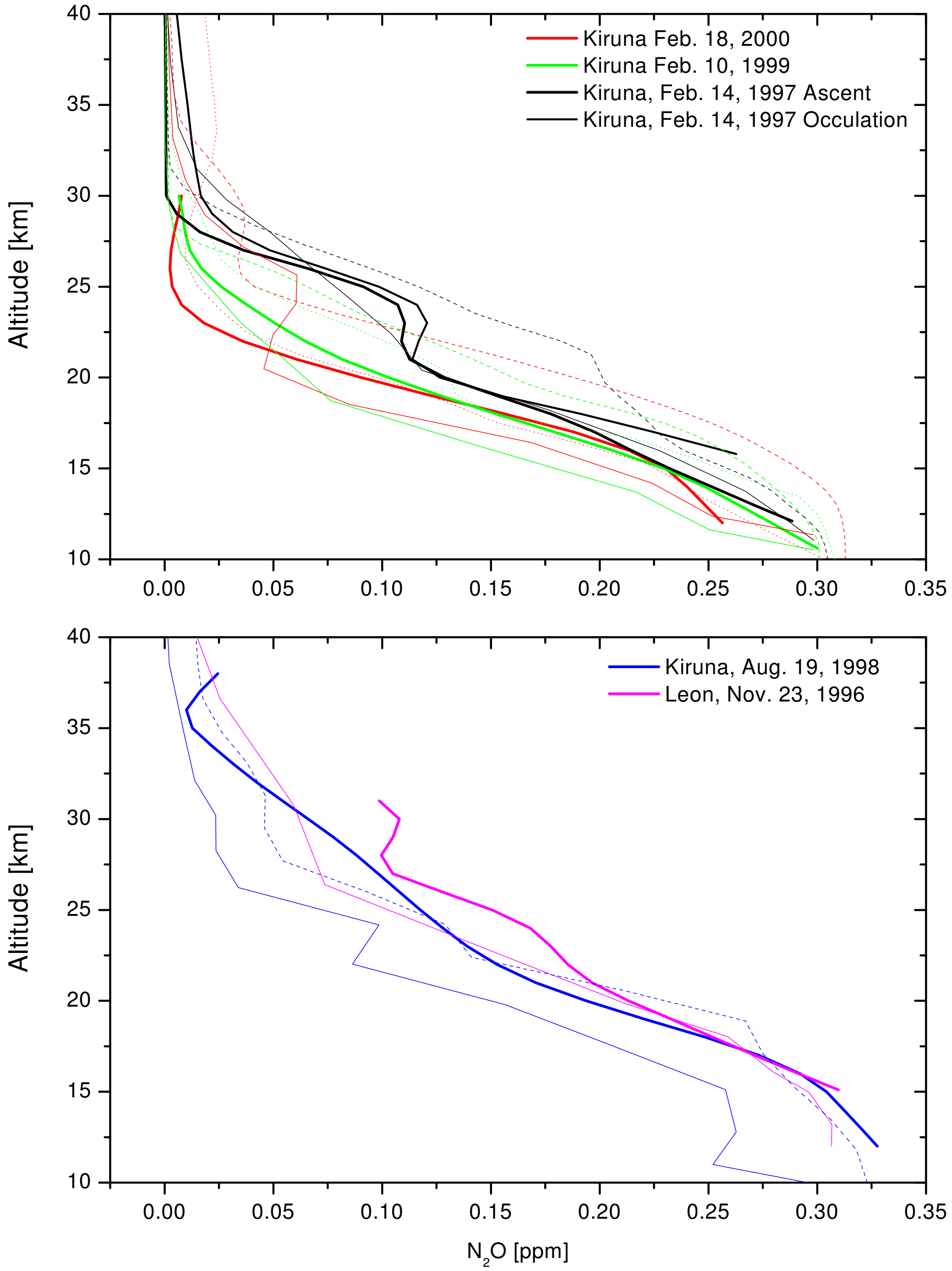

Figure 6.2: *Measured and modelled N_2O profiles for high latitude summer and mid-latitude autumn (upper panel) and for high-latitude winter (lower panel) by LMPA/DOAS (thick solid lines), by SLIMCAT (thin solid lines), by KASIMA (dashed lines), and by REPROBUS (dotted lines), respectively.*

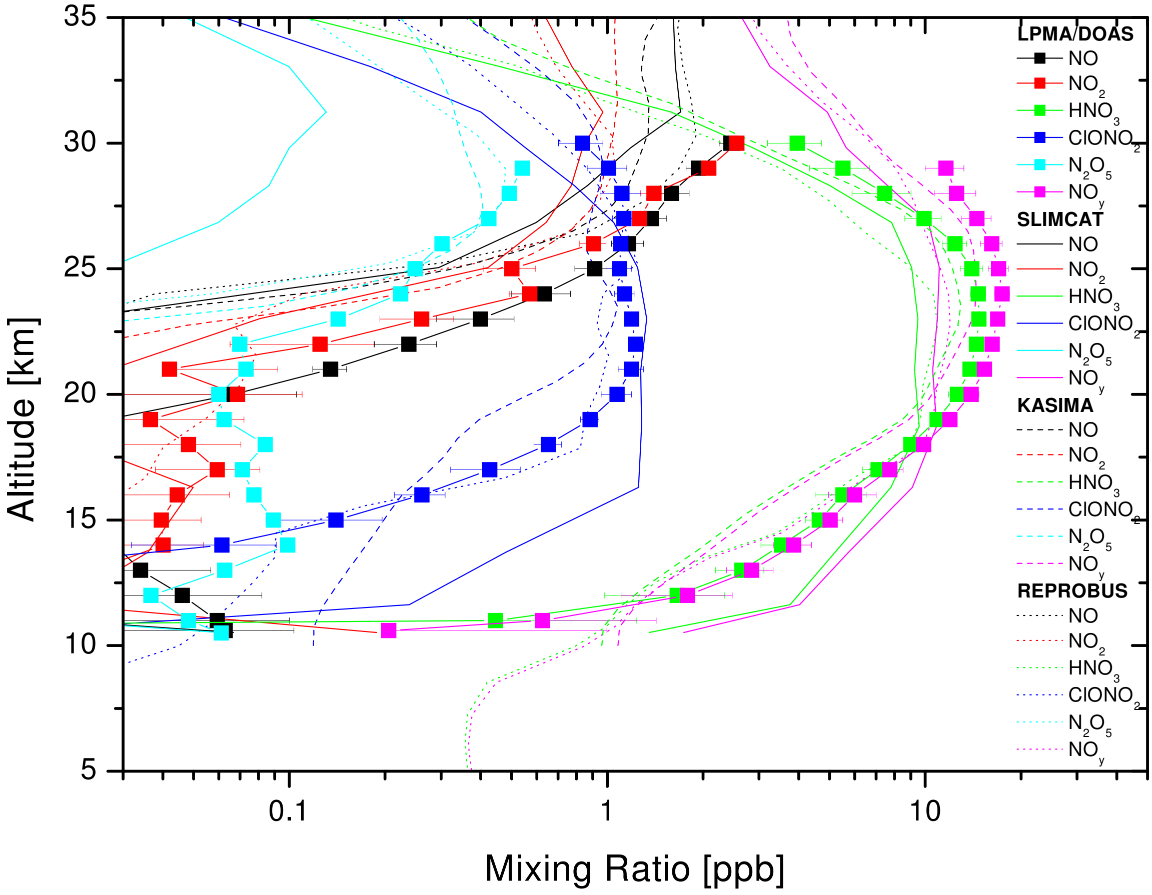

Figure 6.3: *NO_y budget observed during balloon ascent on Feb. 10, 1999 within the polar vortex. The model calculations of SLIMCAT, KASIMA and REPROBUS are also shown.*

average value to the measurement conditions (SZA ≈ 86°), the SLIMCAT model calculations of the relative diurnal variation of N_2O_5 was used. It should be pointed out, that this is a very crude estimation neglecting all heterogenous processes. Also, the steady-state assumption is rather suspicious as for high-latitude winter the illumination of an air parcel may strongly vary.

Figure 6.3 shows the measured ascent profiles of the individual NO_y species and the estimated N_2O_5 as well as the total NO_y[3] profile. The error of the mixing ratios of total NO_y are obtained by Gaussian error propagation of the given errors of the individual species. For N_2O_5, an error of 100% was assumed. The comparison with model outputs of SLIMCAT, KASIMA and REPROBUS reveals a relatively poor agreement with the measurements for almost all species. Further, a large variability between the different model calculations can be observed. However, the shape of the measured profiles is reasonably reproduced in most cases. As discussed above, the models tend to over/underpredict the subsidence inside the polar vortex and therefore the

---

[3] here, NO_y=NO+NO_2+$ClONO_2$+HNO_3+2·N_2O_5

profiles of long-lived species are down- or upward shifted.

During polar winter/spring, almost all inorganic nitrogen is abundant as HNO_3 in the lower stratosphere (below 30 km), formed through the N_2O_5 hydrolysis in the absence of sunlight. The HNO_3 profile measured by the LPMA-FTIR shows a relatively broad profile shape with a maximum of the mixing ratio around 24 km. As HNO_3 has a long photochemical lifetime in the lower stratosphere, the modelled profiles (in the lower stratosphere) seem to be shifted according to the corresponding N_2O profiles. For higher altitudes, the lifetime decreases and the mixing ratio is no longer dominated by transport effects, only. Therefore, an overestimation of the descent rate results in a broader profile and vice versa. Besides the effect of the different descent rates, it is obvious that the measured HNO_3 abundances are systematically underestimated by all models. Below 17 km, SLIMCAT calculates larger HNO_3 amounts, which is certainly the result of the overestimation of the subsidence. A rather fair agreement is found with the REPROBUS model below 17 km and with KASIMA above 22 km.

Below 25 km, $ClONO_2$ is the second most abundant NO_y species, however, with by a factor of 10 smaller mixing ratio compared to HNO_3. The measured $ClONO_2$ shows a broad and smooth profile with a maximum mixing ratio of 1 ppb. The smooth profile shape (in combination with the HCl measurements, which are not shown here) is an indication that no chlorine activation has occurred [*Payan et al.* 2000]. Similar to HNO_3, the modelled $ClONO_2$ profiles are shifted corresponding to the over/underestmiation of the descent rates. In contrast to HNO_3, a nice agreement between the modelled and measured $ClONO_2$ mixing ratio is found. Small notches can be observed in the $ClONO_2$ profiles modelled by KASIMA and REPROBUS, indicating that some chlorine activation was assumed by these models. This can be explained probably by a small, cold bias of the used ECMWF analysis.

For NO and NO_2, almost identical profiles are found above 20 km, in agreement with an expected NO/NO_2 ratio in the range of one [e.g. *Schneider* 1997]. Both, NO and NO_2 are clearly underestimated by all models. The NO_x amount at the altitude range of the maximum depends on the total amount of NO_y and therefore is sensitive to the different modelled descent rates. However, a clear trend cannot be observed here.

The N_2O_5 profile estimated from the NO_2 and O_3 measurements (equation 6.1) shows small, almost constant values around 0.1 ppb up to 22 km and a sharp increase above. At 29 km the estimated mixing ratio is in the range of 0.5 ppb. These values can be compared to N_2O_5 measurements, that were carried out with the MIPAS instrument on Jan. 27, 1999 inside the polar vortex [*Stowasser et al.* 2000]. They found N_2O_5 mixing ratios around 2 ppb at an altitude of 30 km during the night. Taking into account the diurnal variation of the N_2O_5 abundances and the increasing illumination between January 27 and February 10, the estimated N_2O_5 mixing ratios seem to be reasonable.

The NO_y profile obtained by summation of the mixing ratios of the individual species closely follows the HNO_3 profile in the lower stratosphere. Above 26 km, a substantial part of NO_y is abundant as NO_x and the HNO_3 and NO_y profiles show an increasing disagreement with increasing altitude. The same as mentioned for HNO_3, holds true for NO_y. Total NO_y is clearly underestimated by all models. Further, the modelled profiles are shifted (in the lower stratosphere) corresponding to the different descent rates assumed by the models.

In conclusion, the observations carried out on Feb. 10, 1999 showed, that the models largely underestimate the NO_x and the HNO_3 abundances, whereas $ClONO_2$ is reasonably reproduced. These findings agree with previous studies of *Payan et al.* [1998] and *Stowasser et al.* [2000]. The tracer transport calculated by the models has a large impact on the NO_y budget if not properly accounted for. However, the observed differences can only partly be attribute to transport processes. The disagreement of the modelled and measured $ClONO_2/HNO_3$ ratios is a clear hint to uncertainties in modelling the nitrogen/chlorine interaction. This confirms the studies of *Rivière et al.* [2000] who could not bring modelled NO_2 and OClO profiles in agreement with measurements at the same time.

6.2.3 The NO_y-N_2O Correlation

The measurement of NO_y in combination with N_2O allows to investigate the NO_y-N_2O correlation. As discussed in chapter 3.2, a compact correlation between both is established in the stratosphere. In the lower stratosphere, this correlation is almost linear, while it becomes overwhelmingly non-linear for higher altitudes. Since this relationship is the result of the combined effects of transport and photochemistry, it depends on latitude and season [*Michelson et al.* 1998]. Such NO_y-N_2O correlations are commonly used to initialize the NO_y amounts for chemical model calculations. Departures from this compact relation can be used to identify and quantify horizontal mixing of distinct air masses and denitrification processes inside the polar vortex. To distinguish between both effects, further correlations such as the CH_4-N_2O correlation have to be used. However, there are some serious concerns about the reliability of this technique [*Plumb et al.* 2000].

The comparison of the measured NO_y-N_2O correlation with the model calculations is shown in Figure 6.4. In addition, the correlations obtained from ATLAS measurements during the AASE and AASE II campaigns during polar winter [*Loewenstein et al.* 1993] and from the ATMOS measurements during the ATLAS II campaign during Arctic winter (outside the polar vortex) [*Rinsland et al.* 1999] and during ATLAS III during northern mid-latitude winter [*Sugita et al.* 1998] are displayed. The underestimation of the total amount of NO_y by the models, already indicated in Figure 6.3, becomes dramatically obvious in this figure. While the measurement show a maximum value of NO_y around 17 ppb, the modelled peak value is only 10-12 ppb and 14 ppb for SLIMCAT/REPROBUS and KASIMA, respectively, i.e. the NO_y amount is underestimated up to 40% on the 50 ppb N_2O level.

Below N_2O mixing ratios of 100 ppm, the observed NO_y-N_2O correlation agrees well with the ATMOS/ATLAS III measurements, while above 100 ppm the (negative) slope of the NO_y-N_2O correlation decreases and both correlations deviate. Above 200 ppm a reasonable agreement between the measured and the modelled correlations is found. The agreement with the ATMOS/ATLAS III measurements is rather unexpected, as these measurements were conducted at mid-latitudes. The correlation obtained with the same instrument during high-latitude winter (but outside the vortex) show somewhat smaller mixing ratios of NO_y than observed here. However, measurements during high-latitude winter, for undisturbed conditions, are rare and there is some discussion about the proper correlation. The study of *Rex et al.* [1999] make use of a NO_y-N_2O correlation obtained from MkIV measurements to represent the conditions in the polar vortex before denitrification, descent, and isentropic mixing which is very similar to the correlation presented here. It is evident, that the correlation observed for N_2O mixing ratios below 100 ppm implies that the probed air masses did not undergo these processes, i.e. denitrification, horizontal mixing with mid-latitudinal air or large descent[4]. This is consistent with the

---

[4] It should be pointed out, that horizontal mixing across the vortex can only change the NO_y-N_2O correlation, if the air masses inside the vortex substantially descended.

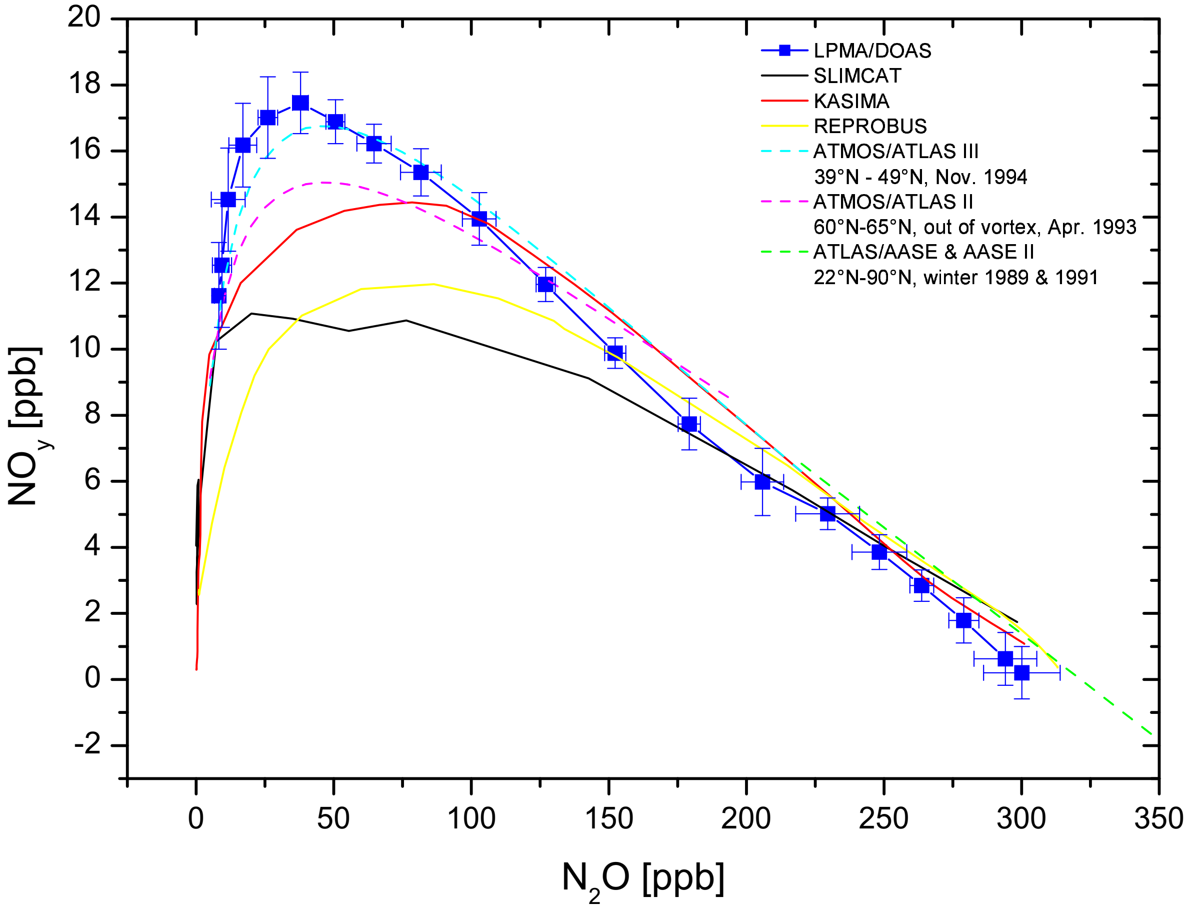

Figure 6.4: *NO_y as a function of N_2O derived from LPMA/DOAS measurements at Kiruna on Feb. 10, 1999. For comparison, the model results of SLIMCAT, KASIMA, and REPROBUS as well as correlations from various data sources are shown.*

observations of *Müller et al.* [2000]. They compared the N_2O profile measured on Feb. 6, 1999 with a balloon-borne cryogenic whole air sampler to a mean arctic, inner vortex N_2O profile and found that above the isentropic level of 500 K ($\simeq$ 21 km) the N_2O values are higher than the mean while the opposite occurs below, i.e. the descent seems to be intensive at low altitudes and weak at high altitudes. The notch in the correlation for N_2O mixing ratio below 100 ppb is possibly due to some mixing effects of the descended air masses with air masses from outside the vortex. It should be stated, that the NO_y-N_2O correlation measured in the winter 1998/1999 is certainly not representative for other winters and is the result of rather unusual meteorological conditions.

The above study raises the question, why the modelled NO_y-N_2O correlations largely deviate from the observation? Obviously this is not only true for winter 1998/1999, as the underestimation of the NO_2 abundances is a commonly observed feature (see chapter 5.3.4). CTMs are usually initialized with the measured mid-latitudinal NO_y-N_2O correlations before the vortex is formed, therefore a mechanism must exist that excessively flattens the modelled NO_y-N_2O

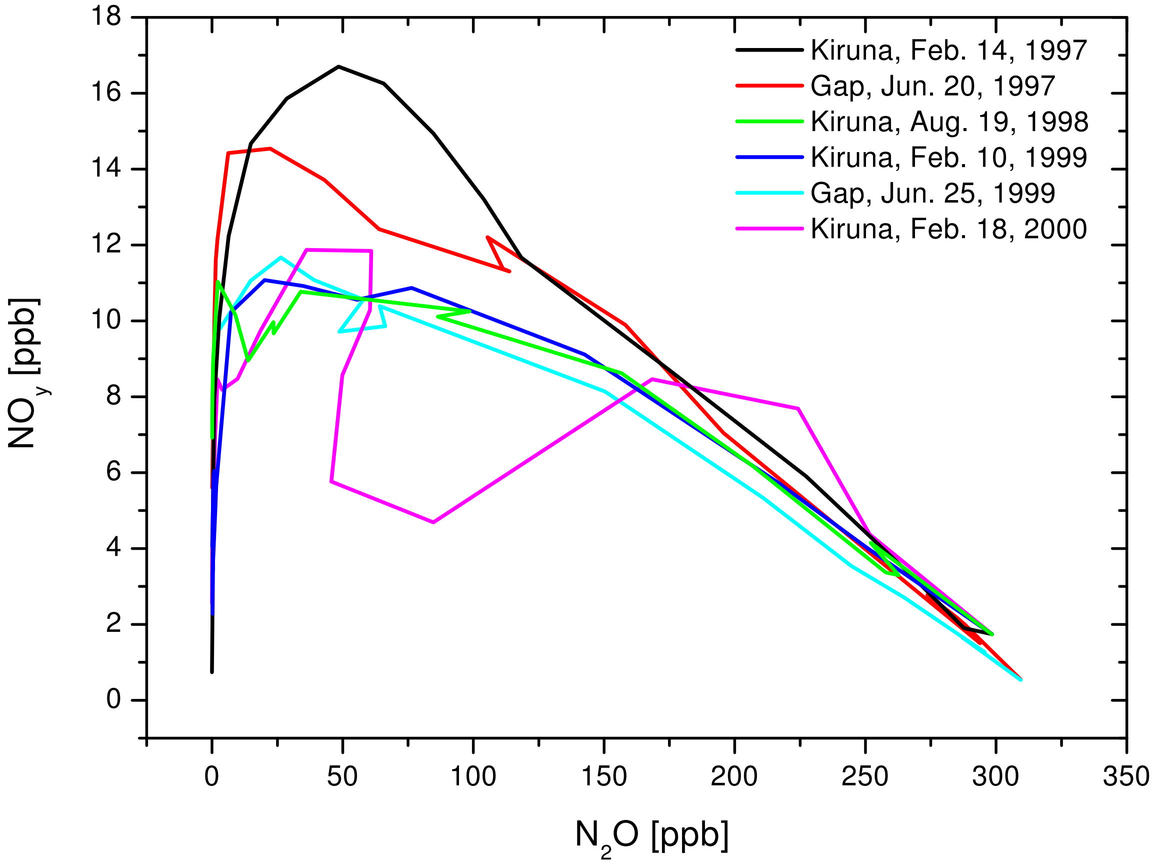

Figure 6.5: *N_2O-NO_y correlations calculated by the SLIMCAT multiannual model for the LPMA/DOAS balloon flights in Kiruna and Gap.*

correlation. Denitrification and the mixing of two distinct air parcels from outside and inside the vortex (through e.g. filaments) can be excluded, as these processes lead to anomalies in the relationship and distort the compactness. *Plumb et al.* [2000], however, showed, that continuous mixing across the vortex edge produces entirely changed relations inside the vortex and that separate, compact relationship can develop. CTMs usually use a grid size of several degrees in latitude and longitude and hence only large scale transport processes are catched. The transport processes on the sub-grid scale are considered with a numerical diffusion model. Measurements of *Balluch and Haynes* [1997] indicated, that the numerical diffusion is largely overestimated by the models. Therefore, the presence of horizontal transport barriers, will lead to a degraded, but still compact correlations through the mechanisms described by *Plumb et al.* [2000].

This effect can nicely be studied with the results of the SLIMCAT multiannual run (Figure 6.5). After the initialization in 1996, the NO_y-N_2O correlation is degrading to smaller values of NO_y. After 1998, the same, strongly distorted correlation can be found at all latitudes and seasons. In conclusion, the overestimation of the sub-grid diffusion seems to be a dominating shortcoming of CTMs and changes the NO_y-N_2O correlation even on a global scale. The unusually shaped NO_y-N_2O correlation obtained for the winter 2000 is the product of the small dip in the modelled N_2O profile at 25 km, re-distribution of NO_y through denitrification assumed by the model, and possibly the removal of HNO_3 from the gas-phase through the presence of particles. The observed better agreement of the measured and modelled NO_2 concentrations for the flights in Kiruna 1997 and in Gap 1997 compared to the following flights can certainly be attributed to this effect for the most part.

The major results of the study of the nitrogen partitioning and budget presented in this chapter showed that

- there still exist substantial problems to properly model the partitioning of the nitrogen species for polar winter as well as for summer conditions
- the calculation of the diabatic descent rates within the models show significant shortcomings expressed by the large variability found between the different models
- the numerical diffusion adopted in the CTMs is overestimated resulting in a essential distortion of the NO_y-N_2O correlation and hence the NO_y budget.

Chapter 7

Stratospheric Iodine

The importance of iodine for atmospheric photochemistry has been subject of several studies. As a result of the high ozone depletion efficiency, already a small amount of iodine, injected into the stratosphere, would be detrimental for the ozone levels, particularly in the lower part of the stratosphere. Thus, an accurate knowledge of the stratospheric iodine abundances is necessary to obtain a quantitative understanding of the ozone depletion in the lowermost stratosphere. However only few, contradictory measurements of stratospheric IO are available so far. The balloon-borne DOAS measurements presented in chapter 5.1 offers the possibility to sensitively detect stratospheric IO, and for the first time, also OIO. The molecule OIO is included in the presented study, as new results are available that suggest that OIO might be photolytically stable. Hence OIO possibly forms a major iodine daytime species in the lower stratosphere.

This chapter is organized as follows. First, the DOAS evaluation of IO and OIO will be described. Several spectral retrieval tests were performed, which showed that an additional correction has to be included in the spectral retrieval, the so-called center to limb darkening correction (see section 4.1.4). However, significant amounts of stratospheric IO and OIO are not detected. The inferred upper limits of IO and OIO are given in section 7.3. In combination with photochemical model calculations, an upper limit for the total amount of inorganic stratospheric iodine is derived (section 7.4). Finally the implications for stratospheric ozone will be discussed.

7.1 IO Evaluation

The standard IO spectral retrieval was conducted in the wavelength interval 425 nm to 465 nm, where 5 strong of the 'cold' (4-0, 3-0, 2-0, 1-0, 0-0) and two weaker of the 'hot' (3-1, 2-1) vibrational absorption bands of the IO $A^2\Pi_i \leftarrow X^2\Pi_i$ electronic transitions are located. The used IO differential cross section was from *Hönninger* [1999] scaled to the IO cross section of *Cox et al.* [1999]. The following set of trace gases was used: two numerically orthogonal ozone reference spectra for T = 213 K and T = 233 K, two numerically orthogonal NO_2 spectra for T = 228 K and T = 203 K, for the arctic winter flights an OClO spectrum recorded at T = 220 K in all measured with the present instrument in the laboratory, an O_4 spectrum [*Greenblatt et al.* 1990], and a H_2O spectrum generated by convoluting from the HITRAN96 spectroscopic database for T = 213 K [*Rothman et al.* 1996] (since the H_2O absorption in the considered wavelength interval

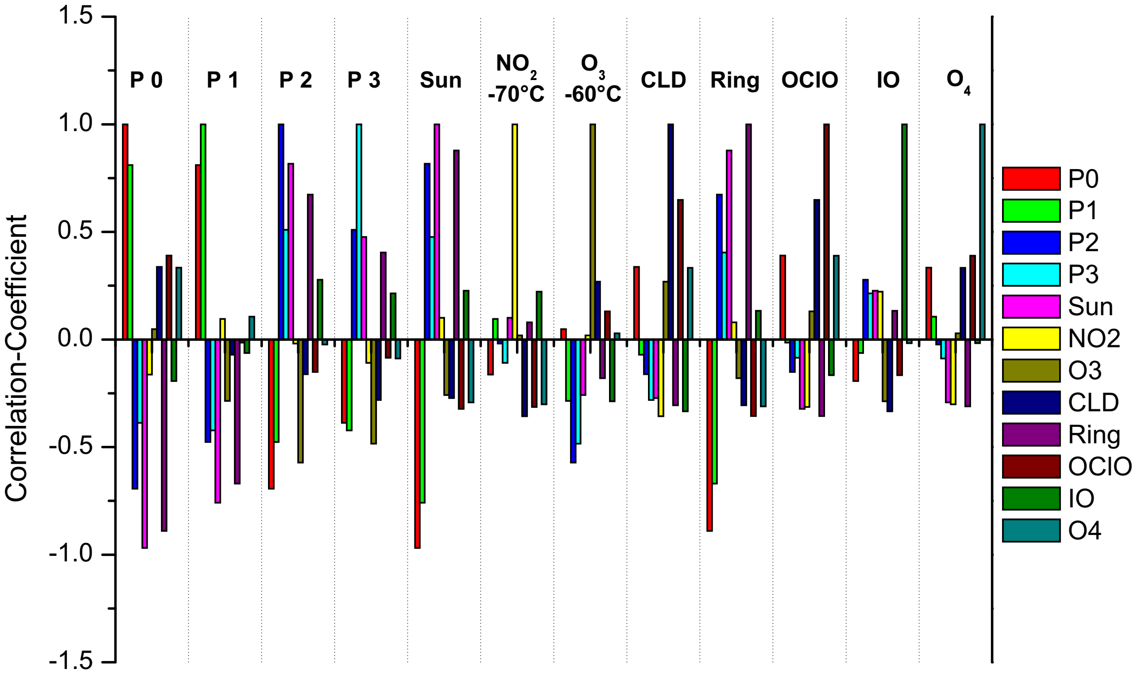

Figure 7.1: *Correlation-coefficients for the IO evaluation. P0 - P3 denote the polynomial (for degree 0 to 3), sun the Fraunhofer spectrum etc. A correlation-coefficient in the range of* ± *1 indicates a large correlation, while a value near zero is an indication of a vanishing correlation. Here, only one ozone and one* NO_2 *reference spectrum is taken into account.*

is very weak and is in general not found by the fitting procedure and to reduce the number of cross sections used, H_2O was only used for sensitivity runs). A calculated Ring spectrum[1] was also included into the fitting procedure as at very low sun, i.e. at large air masses, some solar photons were likely to be Raman scattered into the instrument's line-of-sight. In addition, our spectral retrieval exercises showed that a center to limb darkening (CLD) correction had to be included into the spectral retrieval. As already discussed in section 5.2 a synthetic I_0 correction was applied to the NO_2 cross sections[2]. A polynomial of degree 3 is used to compensate the broad band components. As shown in Figure 7.1 only small correlations occur between the IO cross section and other cross sections or the polynomial. For other reference spectra, however, larger correlations are found, but this should not affect the evaluation of IO.

The wavelength alignment of the reference spectra recorded with the field instrument in the laboratory is obtained with reference spectra taken from the literature. The relative wavelength alignment to the Fraunhofer reference spectrum of the two packages was determined once per flight for measured spectra with a clear NO_2 and O_3 absorption. In the standard fitting procedure, the whole package of reference spectra and the Fraunhofer reference spectrum are held

---

[1] calculated with *MFC*

[2] therefore the measured NO_2 absorption spectrum was normalized and wavelength calibrated with the cross section given by *Harder et al.* [1997]

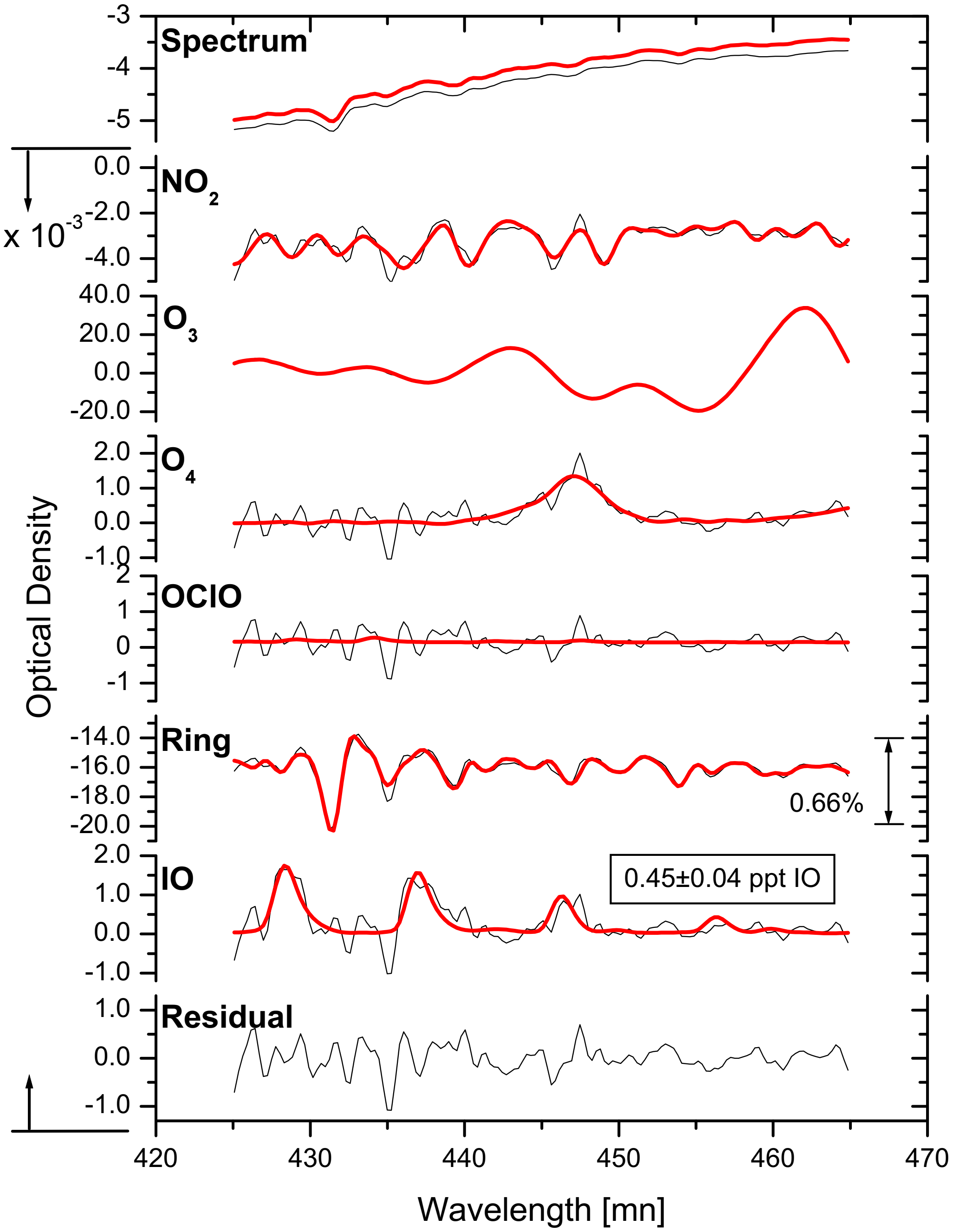

Figure 7.2: *Example of an IO evaluation for a spectrum measured at Kiruna on Feb. 10, 1999 for SZA=94.5° (tangent height=12.5 km), not including the CLD correction. The upper panel shows the Fraunhofer spectrum (red line) and the measured spectrum (black line). In the panels below, the retrieved trace gas absorptions of* NO_2 *(T=-70° C), ozone (T=-60° C) (the ozone absorption for T=-40° C is not shown),* O_4*, OClO, Ring, and IO are shown. In the lowest panel the remaining residual of the fitting procedure is displayed. The red lines indicate the spectral absorption and the black line the sum of the spectral absorption and the residual.*

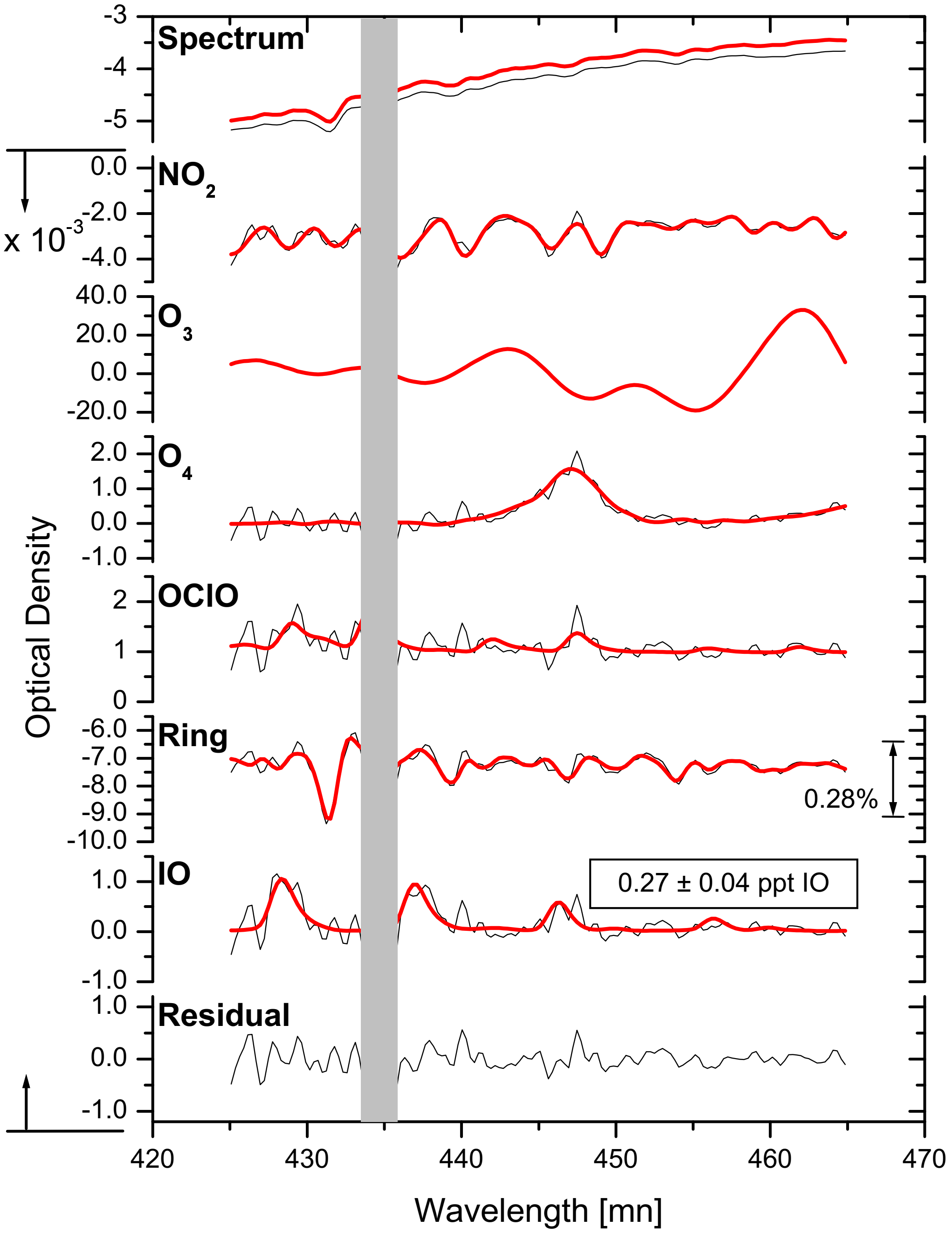

Figure 7.3: *Same as Figure 7.2, but excluding the wavelength interval 433.5 nm - 435.5 nm (grey shaded area) in the spectral fitting procedure.*

fix with respect to their wavelength alignment, only the measured spectrum is allowed to shift and squeeze. To account for the spectrometer stray light, an additional intensity offset is used (a polynomial of degree one).

Figure 7.2 shows the inferred spectroscopic features in the considered wavelength interval of all absorbing gases, the inferred Ring spectrum, and the unexplained residual for a SZA =94.6° observation (tangent height = 11.5 km) from the balloon flight over Northern Scandinavia on February 10, 1999. Some IO absorption was found by the fitting procedure, but a disturbing large residual remained around 434 nm. Obviously, the unexplained residual was partly compensated for by the calculated Ring spectra, having an unreasonably large amplitude.

The same spectral retrieval is shown in Figure 7.3 but here the wavelength interval 433.5 to 435.5 nm (the grey shaded bar in the Figure) centered around the dominant residual structure was numerically excluded from the fitting procedure. The Ring absorption decreased by 2/3 while the inferred IO absorption decreased by approximately 40%. This findings indicate a cross correlation/interference of the unexplained residual structure and some major absorbing trace gases with the Ring and the IO spectra.

Further investigating the causes for that dominant residual structure at 434 nm by performing a set of spectral retrieval sensitivity and stability studies has made it clear that neither the inclusion or exclusion of reference spectra nor inclusion or exclusion of solar I_0-corrected reference spectra, nor allowing for spectral shifts and squeezes of the reference spectra with respect to each other, nor varying the wavelength interval for the spectral retrieval could improve the results significantly. These findings suggest that the physical model used to describe the solar occultation observation is incorrect at this stage. A closer inspection of Figure 7.2 and 7.3 provides a hint on the physical model's deficit i.e., the location of large residual close to the solar H_γ line (at 434 nm). Furthermore, the observed residual structure increases with SZA. Thus, it can be speculated whether the residual was due to effects arising from the observation geometry during solar occultation.

It is evident, that this residual structure may be the result of the solar center to limb darkening (see chapter 4.1.4), which is not accounted for in these spectral retrievals. As discussed in chapter 4.1.4, the optical densities of the solar Fraunhofer lines undergo changes in the course of the solar occultation measurements. This can be explained by the fact, that optical densities of the solar Fraunhofer lines change across the solar disk and the atmospheric transmission with respect to Rayleigh scattering is a function of the location (on the solar disk). This effect is particularly strong for the strong hydrogen lines. In chapter 4.1.4 a correction is deduced, called center to limb (CLD) darkening correction, which has to be included in the fitting procedure.

Clearly, the spectral retrieval was dramatically improved including a CLD correction in the fitting routine (Figure 7.4). In this case, a lower and more reasonable amplitude of the Ring spectrum, a lower spectral residual structure and much lower IO absorption (mainly below the detection limit) was obtained. Obviously, the deficits of the model function (without CLD correction) lead to mis-interpretations (especially for weak absorbers) and large systematical uncertainties (apparent by the large residual structure). This impressively demonstratie the shortcomings of the least-square fit. If not all important processes are properly accounted for in the model function, the fitting result can be strongly biased even in the presence of rather small correlation. Hence, care has to be taken, when interpreting DOAS results for weak absorbers if the residual contains systematical structures. The improvement of the fitting process also becomes obvious through the form and size of the residual structure and the magnitude of the root-mean square *rms* of the residual almost approaching the theoretical limit given by the

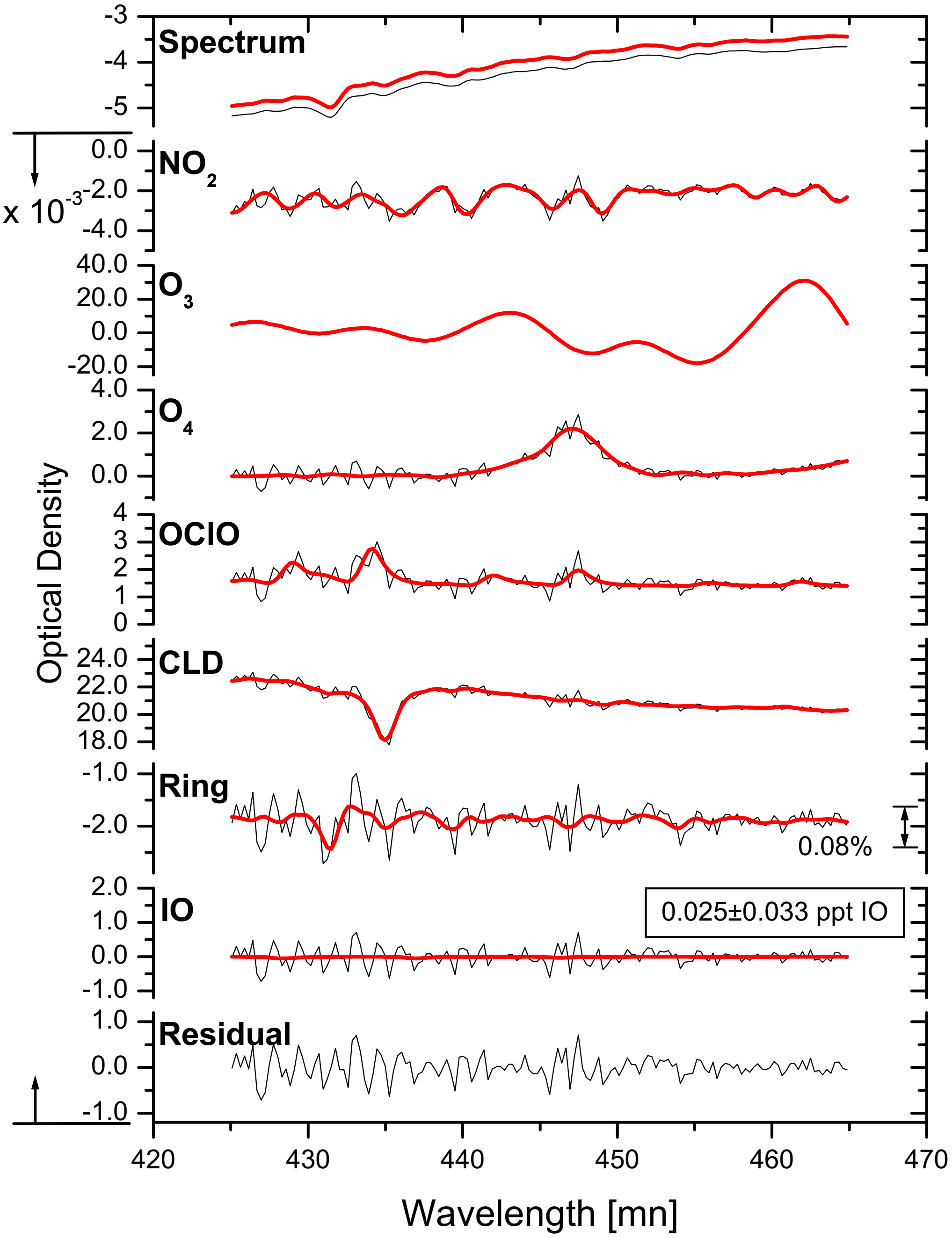

Figure 7.4: *Same as Figure 7.2, but including the CLD correction in the spectral fitting procedure.*

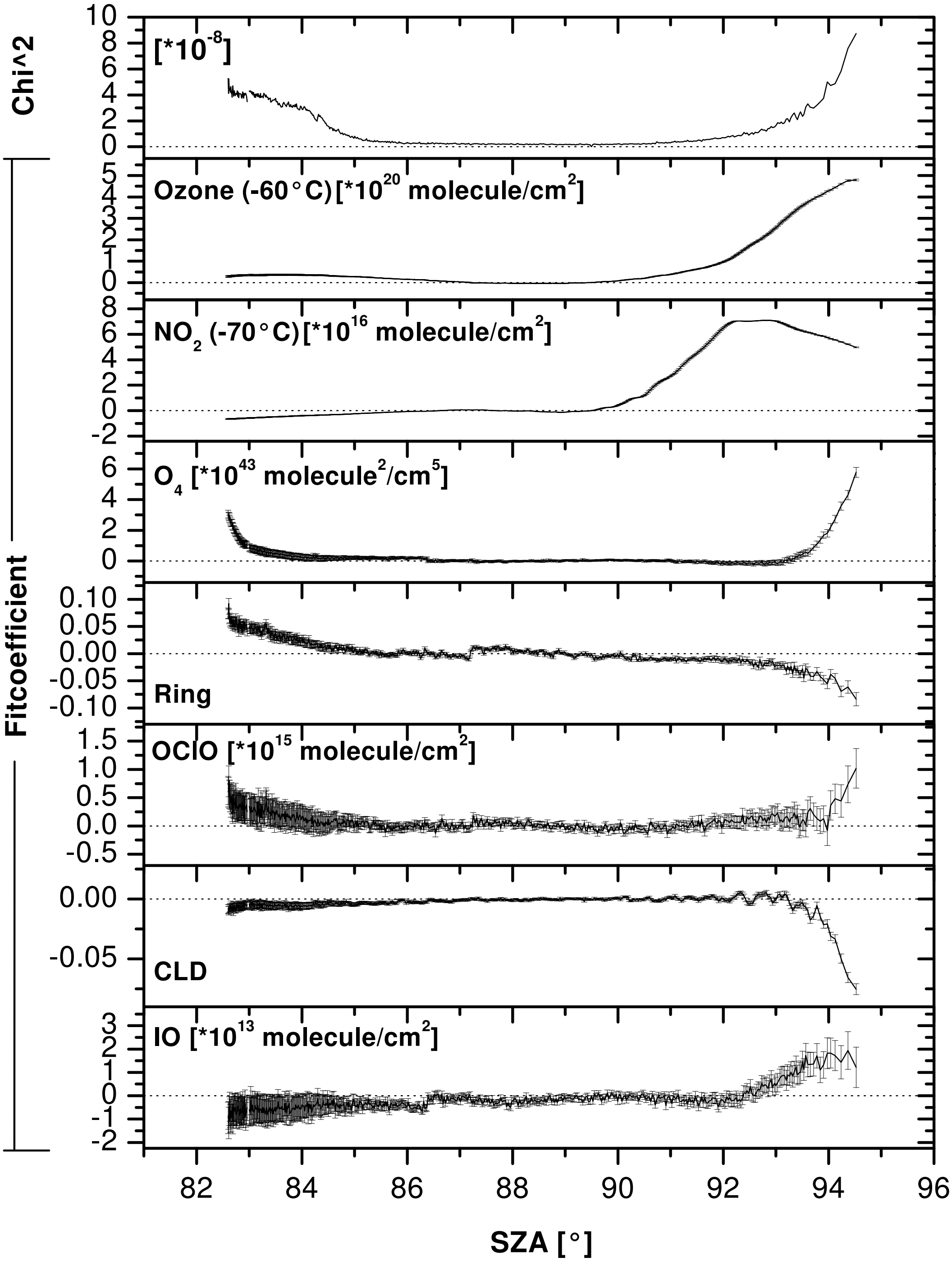

Figure 7.5: *Result of an IO evaluation for the flight in Kiruna on Feb. 14, 1997. The upper panel shows the* χ^2 *of the residual. The panels below shows the fit coefficient of ozone,* NO_2, O_4, *Ring, OClO, CLD, and IO. The error bars given indicate the* 1σ *fit error. At the end of the solar occultation measurements, the fit-coefficients for IO increase, but are still smaller than the detection limit given by two times the error.*

photoelectron shot noise (e.g. for the evaluation shown in Figure 7.4 the *rms* is $2.5 \cdot 10^{-4}$, while the theoretical limit is in the range of $1.5 \cdot 10^{-4}$)

Figure 7.5 shows the results of the IO evaluation for the Kiruna 1997 flight. Large residual structures (large χ^2) were found at the beginning of the balloon ascent and at the end of the solar occultation (as a result of the smaller signal to noise ratio and large absorptions of NO_2 and O_3). The trend shown by fit coefficients for NO_2 and ozone are typical for stratospheric absorbers with a concentration maximum in the middle stratosphere. The O_4 abundances are strongly decreasing with altitude and, hence, the largest fit coefficients are found at the beginning and the end of the measurements. The fit-coefficients obtained for the Ring-spectrum are all relatively small. The positive values found for the balloon ascent are probably the result of the correlation with the Fraunhofer spectrum and the polynomial. The fit-coefficients for OClO show the expected trend and reproduces reasonably the values gained by the UV-evaluation [*Fitzenberger* 2000]. The fit coefficient of the CLD correction is close to zero for SZAs < 90°. For large SZAs, a strong negative increase of the fit-coefficient is obtained. This corresponds nicely to the expected behavior (see chapter 4.1.4). However, further test are performed to verify if the applied correction works well, which will be subject of the the next sections. The IO fit coefficients clearly agree with zero (within the error bars). For SZAs > 92.5° the fit-coefficients slightly increase, but are still below the detection limit given by two times the fit-error (see chapter 4.1.3). For large SZAs the optical densities of NO_2 and O_3 become exceptionally large, thus, small systematic uncertainties can occur. Considering all flights, the IO fit coefficients for large SZAs show a large scatter around zero with positive and negative values, but all below or at least very close to the detection limit[3].

CLD Model

In this section, the amplitude of the CLD correction given by the fitting procedure will be compared to the calculations of a simple model. For that purpose, it is assumed that, the intensity at the center of the H_γ line is independent of the distance from the center of the solar disk. An assumption justified by the large saturation of the H_γ line. Further, the following relation is assumed for the intensity outside the absorption line [*Unsöld and Baschek* 1999]:

$$I_\lambda(\theta)/I_\lambda(0) = 0.85 \cdot \cos\theta + 0.15 \tag{7.1}$$

For a description of the notation see section 4.1.1. Further, the solar disk is horizontally subdivided and the transmission dependent contributions with respect to Rayleigh scattering are calculated for each disk slice[4] In combination with the above assumptions, the mean intensity inside (in arbitrary units) and outside the absorption line can be calculated. To obtain absolute values, the calculated intensities inside and outside the H_γ-line are calibrated with the disk-averaged spectrum given by *Brault and Neckel* [1987]. The optical density of the H_γ-line is then given by the negative logarithm of the ratio of both intensities. Accordingly, the change of the optical density of the H_γ line during the course of the solar occultation measurements can be

---

[3] It should be pointed out, that given definition of the detection limit is accurate only if the remaining residual consists of pure noise. Usually, the obtained residual is somewhat larger and thus the true detection limit is larger.

[4] The air masses for the light beams leaving the solar disk from different locations can be calculated with the ray tracing program *DAMF*.

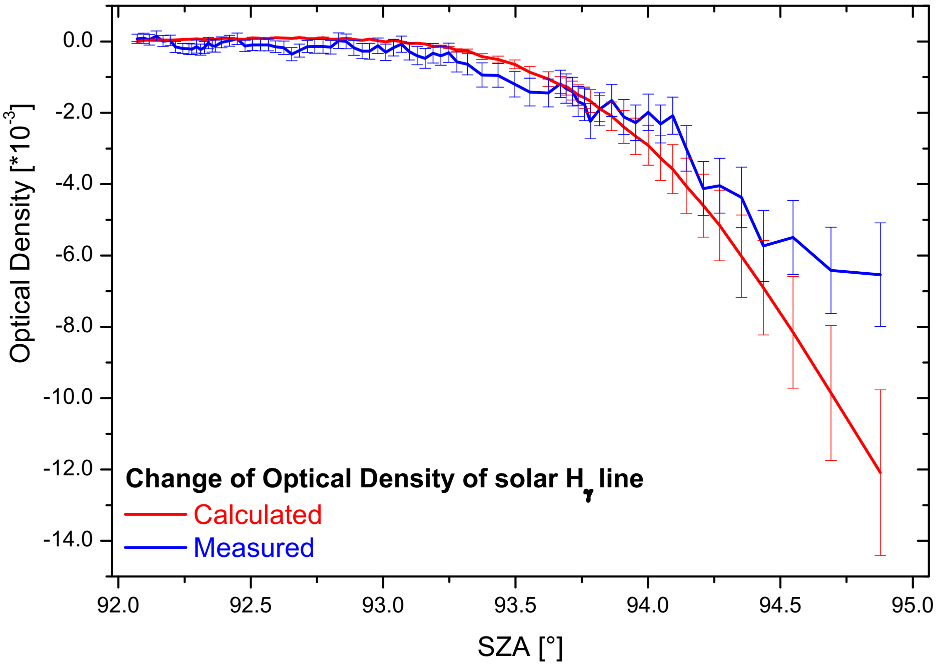

Figure 7.6: *Comparison of the inferred and the calculated change of the optical density of the solar H_γ line.*

calculated. However, to be able to compare this calculation with the measurements performed with a certain instrumental resolution a calibration factor of 4.8 is estimated. Figure 7.6 shows the comparison of the inferred change of optical density of the H_γ line with the modelled expectation for the flight conducted at Kiruna on Feb. 10, 1999. The error bars for the modelled values denote the uncertainties associated with the calibration of the relative intensities. Both curves closely follow each other for a reasonable wide range of SZA values, and they start to diverge only as the light from the sun's lower edge traverses through the lower stratosphere and upper troposphere. Probably, this divergence is due to additional contributions from Mie scattering in the lower stratosphere/upper troposphere, a process which eventually moves the apparent brightness center slightly back towards the solar disk's center as the sun dives into the atmospheric horizon.

Solar Eclipse Measurements

This section presents the results of a second test, performed to verify the CLD correction. A similar spectral retrieval as used in Figure 7.2, or alternatively in Figure 7.4 is applied to direct sun spectra taken with the same instrument during the solar eclipse that occurred over South

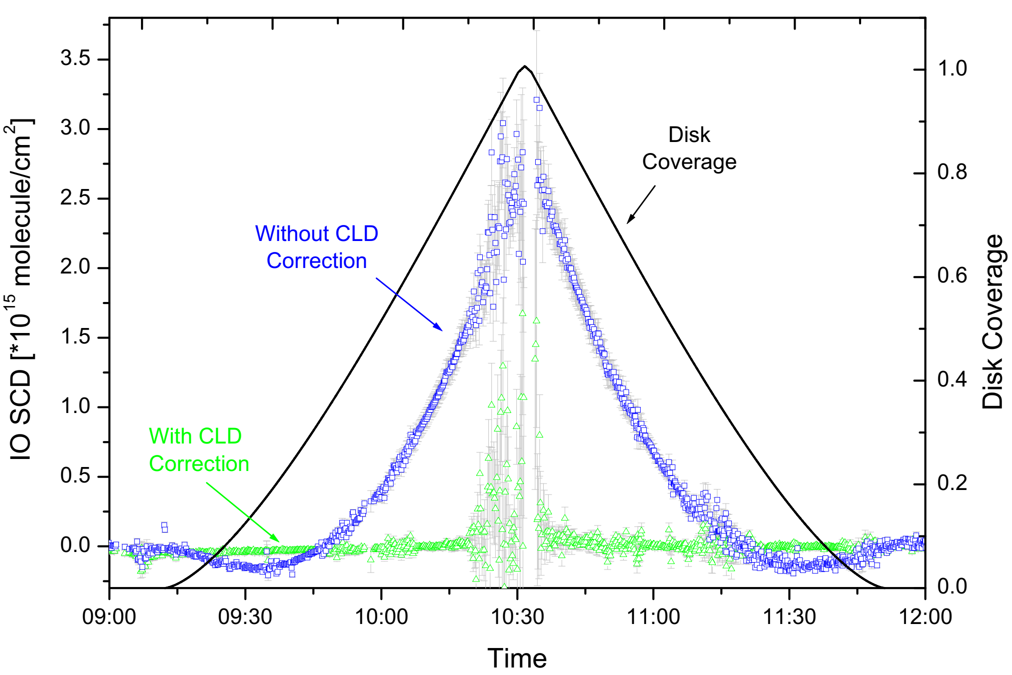

Figure 7.7: *Inferred IO absorption for the solar eclipse measurements on August, 11, 1999 in Karlsruhe (blue squares: excluding a CLD correction; green triangles: including a CLD correction). The full line indicates the coverage of the solar disk.*

Germany on August 11, 1999[5]. It is well known, that large variations of the optical densities of the solar Fraunhofer line occur during solar eclipses [*Gill et al.* 2000]. This can be explained easily, following the arguments given in chapter 4.1.1 and 4.1.4. large changes of the optical densities of the Fraunhofer lines. Likewise, this study indicates that by not including a CLD correction in the fitting routine, fake amounts of IO are inferred for increasing disk coverage[6] while no IO is detected including the CLD correction (see Figure 7.7). The large scatter at 10:30 UT is due to the strongly decreasing intensity (and hence signal to noise ratio) as the sun becomes completely covered. In conclusion, this test shows, that by including the CLD correction, the obtained result are reasonable, even for very large changes of the optical densities of the Fraunhofer lines and that the CLD correction do not overcompensate the fake IO absorptions (this would turn out as negative IO-SCDs here).

---

[5] The measurements were performed by R. Fitzenberger and R. Huppert from the roof of the Forschungszentrum Karlsruhe

[6] The data for the disk coverage was provided by Christoph von Friedeburg

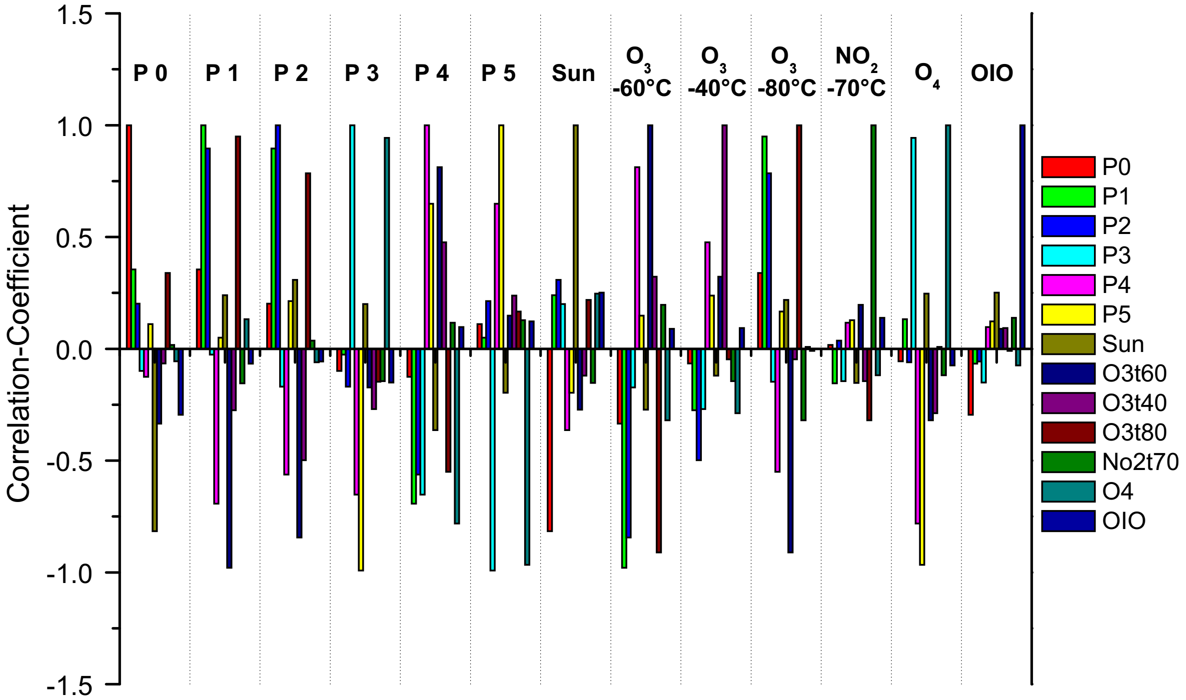

Figure 7.8: *Correlation-coefficients for the OIO evaluation. P0 - P5 denote the polynomial (for degree 0 to 5), sun the Fraunhofer spectrum etc. A correlation-coefficient in the range of ± 1 indicates a large correlation, while a value near zero is an indication of a negligible correlation. Only one NO_2 reference spectrum was considered here.*

7.2 OIO Evaluation

The OIO evaluation was performed in the wavelength range between 530 - 570 nm, where a set vibrational transitions of the $\tilde{A} \longrightarrow \tilde{X}$ transition occur [*Himmelmann et al.* 1996]. For the evaluation, three numerical orthogonal ozone reference spectra for T = 193 K, T = 213 K , and T = 233 K and two numerical orthogonal NO_2 spectra for T = 203 K and T = 228 K (for the Arctic winter flights only T = 203 K was used) were used, all recorded with the same instrument in the laboratory. In addition an O_4 spectrum [*Greenblatt et al.* 1990] and if necessary a H_2O spectrum generated by convoluting from the HITRAN96 spectroscopic database for T = 213 K [*Rothman et al.* 1996] was included in the fitting procedure. For OIO, the relative wavelength alignment and cross section of *Rowley et al.* [2001] was used. If instead, the OIO cross section of *Ingham et al.* [2000] would have been used, then accordingly the results would be smaller i.e., by as much as a factor of 6.9 assuming for reaction 13 a (see Table in Appendix A) branching ratio of 0.3. The relative wavelength alignment of the reference spectra was fixed in a similar manner as for the IO evaluation. The correlations between the polynomial and the OIO reference spectra were found to be small (see Figure 7.8), hence, a polynomial of degree 5 was used to approximate the broadband components. Strong correlations, however, occur between the polynomial and the ozone reference spectra or O_4. As these correlations were already found for polynomials of degree

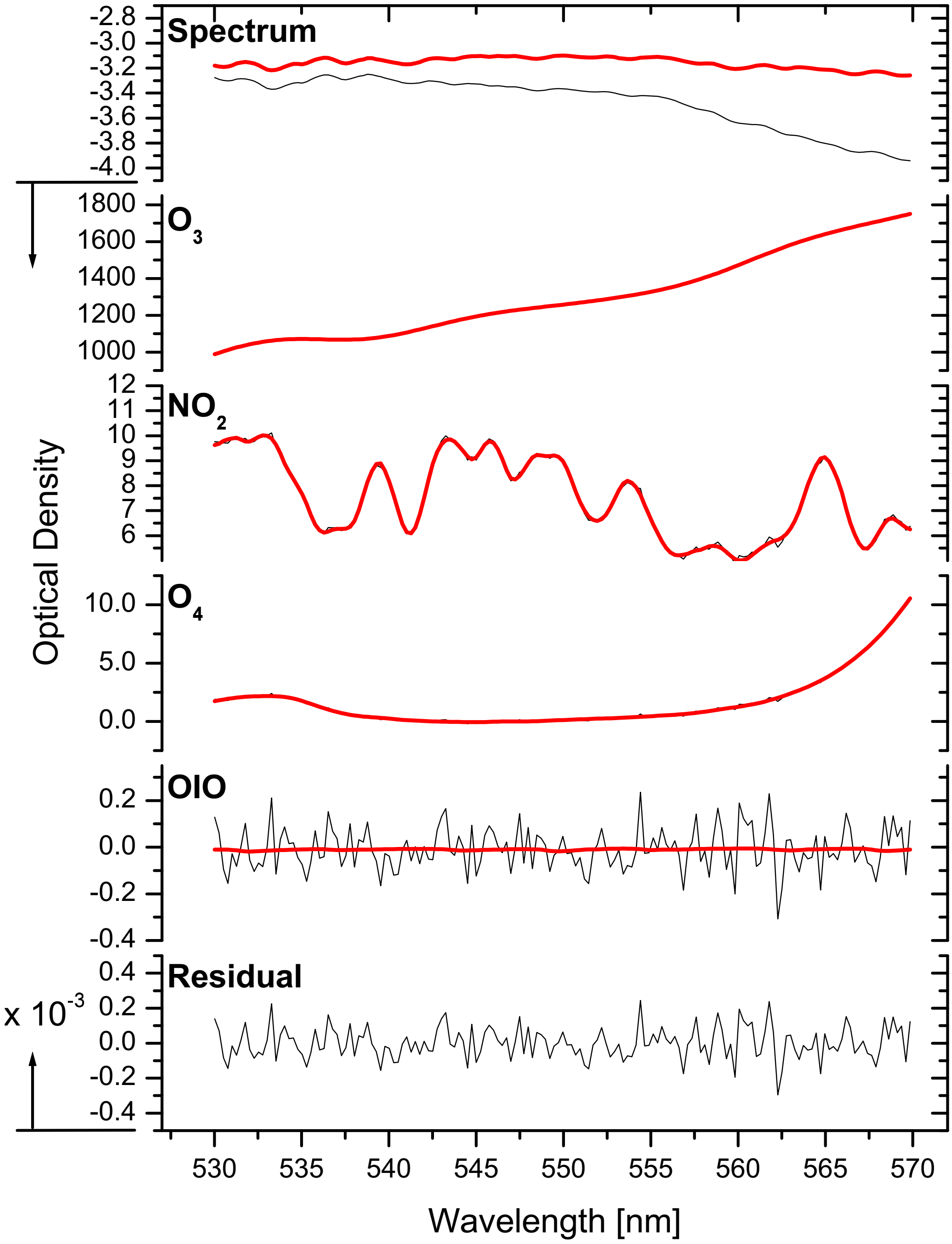

Figure 7.9: *Example of the spectral retrieval of OIO evaluation for for the Kiruna flight on Feb. 14, 1997 for SZA=92.4°. The upper panel shows the Fraunhofer spectrum (red line) and the measured spectrum (black line). In the panels below, the retrieved trace gas absorptions of* NO_2 *(T=-70°C), ozone (T=-60°C) (the ozone absorption for T=-40°C and T=-80°C are not shown),* O_4*, and OIO are shown. In the lowest panel the remaining residual of the fitting procedure is displayed. The red lines indicates the spectral absorption and the black line the sum of the spectral absorption and the residual.*

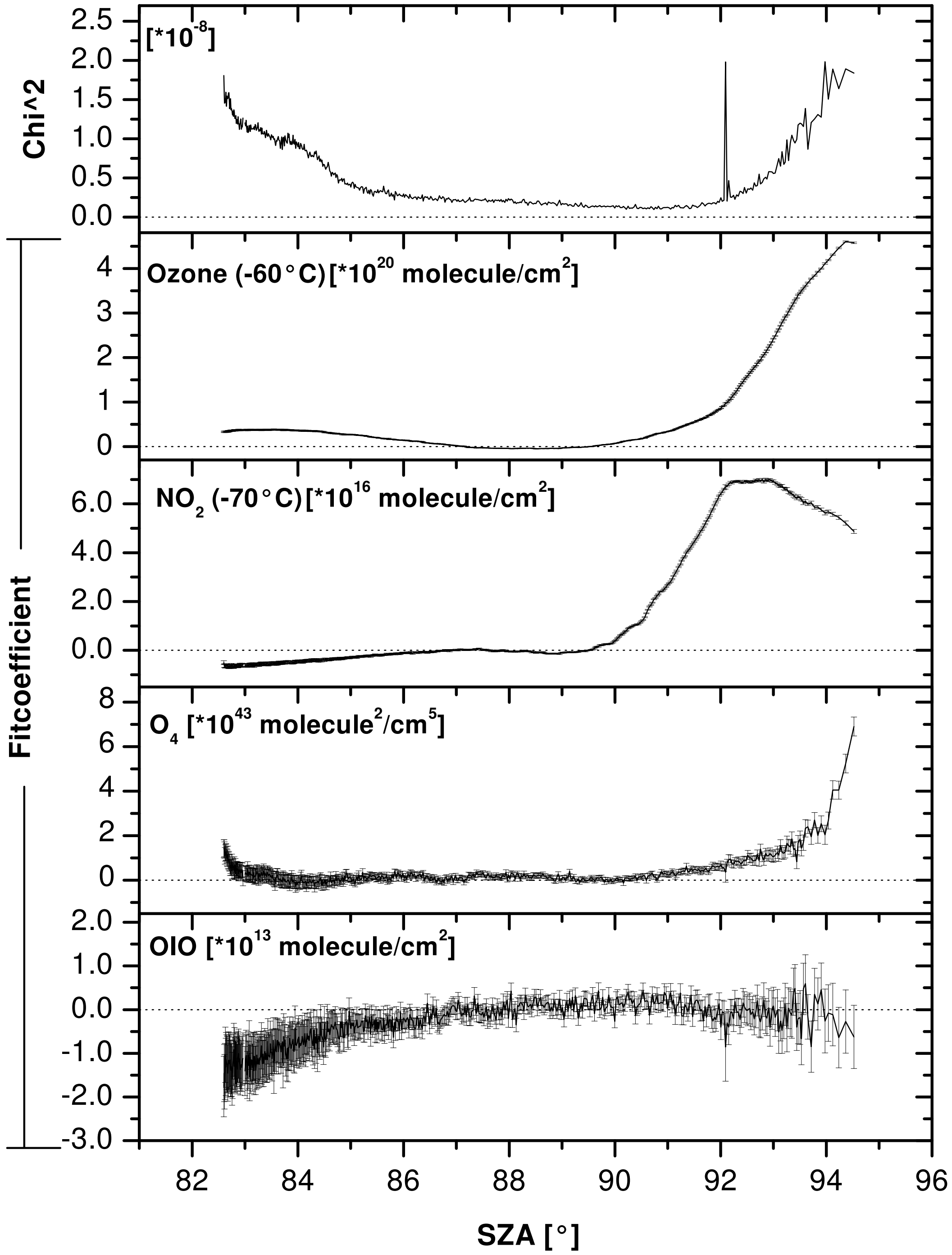

Figure 7.10: *Result of an OIO evaluation for the flight in Kiruna on Feb. 14, 1997. The upper panel shows the* χ^2 *of the residual. The panels below shows the fit coefficient of ozone,* NO_2*,* O_4*, and OIO. The error bars given indicate the* 1σ *fit error.*

three and smaller, a reasonable reduction of degree of the polynomial gives no improvements. In addition an intensity offset was used (polynomial of degree 2) to correct the spectrometer stray light. In the retrieval procedure only the measured spectra were allowed to shift and squeeze with respect to the set of reference spectra and the Fraunhofer reference spectrum.

An example for the spectral retrieval is shown in Figure 7.9 for a spectrum recorded in Kiruna on Feb. 14, 1997 for a SZA of 92.4°. The inferred trace gas absorptions of ozone, NO_2, O_4, OIO and the remaining residual structure is displayed. This example shows clearly, that OIO could not be detected. In contrast to the IO evaluation (without CLD correction), no significant systematical structures are found in the remaining residual and the *rms* is close to the theoretical limit (the *rms* for the evaluation shown in Figure 7.9 is $9 \cdot 10^{-5}$, while the theoretical limit is given by $5.5 \cdot 10^{-5}$).

Figure 7.10 shows the results of the OIO evaluation for the Kiruna 1997 flight. The dependence on SZA of the fit-coefficients for O_3, NO_2 and O_4 are already discussed in more detail in section 7.1. Only for the first part of the balloon ascent, small but non-zero OIO absorptions were found, however, they were still below the detection limit, given by two times the fit-error. Similar results were obtained for all flights, i.e. OIO absorptions exceeding the detection limit with the above given set of parameters could not be detected.

Further sensitivity tests included changes in the values of the polynomial, relaxing subsequently from fixed relative wavelength alignment of the reference spectra, adding a Ring spectrum or the CLD correction[7] (both are not found by the spectral retrieval procedure), exchanging individual reference spectra with those from other sources, and finally changing the considered wavelength interval within a reasonable range (i.e., up to ±10 nm at the short and long wavelength side of the interval), showed like before no OIO absorption larger than the detection limit in either of the tests.

7.3 IO and OIO Upper Limits

From the previous sections it becomes clear, that neither the detection of IO nor OIO was possible for either of the flights, but the upper limits were derived for the absorption of both molecules. Applying the inversion technique (see chapter 4.3) it is possible to obtain the vertical distribution of these upper limits for the combined balloon ascent and solar occultation measurements, respectively. Figure 7.11 and Figure 7.12 show the vertical distribution of the upper limits (given as mixing ratio) of IO and OIO inferred all eight balloon flights measured during balloon ascent (thin line) and during solar occultation (thick line). The upper limits derived for solar occultation are by a factor of 5-10 smaller as for balloon ascent. This is due to the long atmospheric light pathes (and hence large air masses) obtained for the solar occultation measurements. For the same reasons, the lowest upper limits occur for the lower stratosphere. Here, the upper limits scatter around values of 0.05 ppt for IO as well as for OIO. With increasing altitude, the upper limits increase to values up to 0.5 ppt or even more.

For each of the flights, a mean upper limit for the lower stratosphere (as iodine chemistry potentially contributes to ozone loss there) was calculated by averaging all values below 20 km. These mean lower stratospheric upper limits together with the standard deviations are shown

---

[7] The spectral range used for the OIO evaluation does not include solar hydrogen lines, and, hence, the CLD correction shows no narrow structures here.

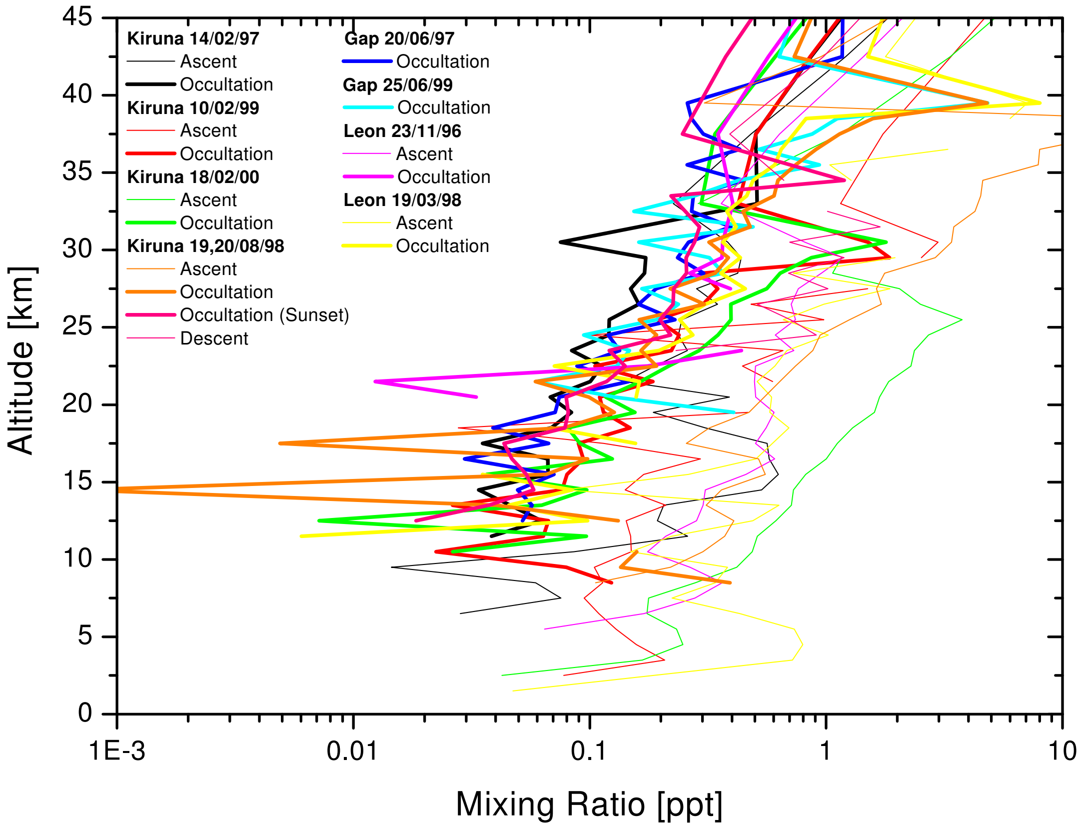

Figure 7.11: *Vertical distribution of the upper limits of IO. The thick lines refer to solar occultation and the thin lines to balloon ascent measurements.*

in Figure 7.13. Unfortunately, for the flights conducted in León in 1996 and in Gap in 1999, the lowest tangent heights of the occultation measurements are only slightly below 20 km and thus a reasonable averaging is not possible. For all other flights, lower stratospheric upper limits of IO and OIO in the range of 0.03 - 0.1 ppt are found. The combination of all flights yield for the lower stratosphere, an error weighted mean upper limit of (0.055 ± 0.004) ppt for IO and of (0.056 ± 0.003) ppt for OIO.

This study largely confirms the results of previous studies [*Wennberg et al.* 1997; *Pundt et al.* 1998], but the up to a factor 5 lower upper limit for IO and the for the first time measured upper limit for OIO puts an even tighter constraint on total iodine I_y in the lower stratosphere. Like the other two studies, however, it is in disagreement with the findings of *Wittrock et al.* [2000] claiming up to $(0.65 - 0.8 \pm 0.2)$ ppt of stratospheric iodine above Spitsbergen. Here, it can only be speculated about the possible reasons for that discrepancy. First, *Wittrock et al.* [2000] reported IO differential slant column amounts larger than the detection limit for SZAs $>89^o$, only. Evidently, one may assume that a CLD correction not included in the spectral retrieval of their study was probably important for skylight IO measurements at large SZAs, as demonstrated above for the direct sun measurements. When inspecting the observation geometry for zenith scattered sunlight measurements in detail [e.g., *Solomon et al.* 1987; *Frießet al.* 1999], however, it is hard to imagine that CLD effects could have played a significant role in the *Wittrock*

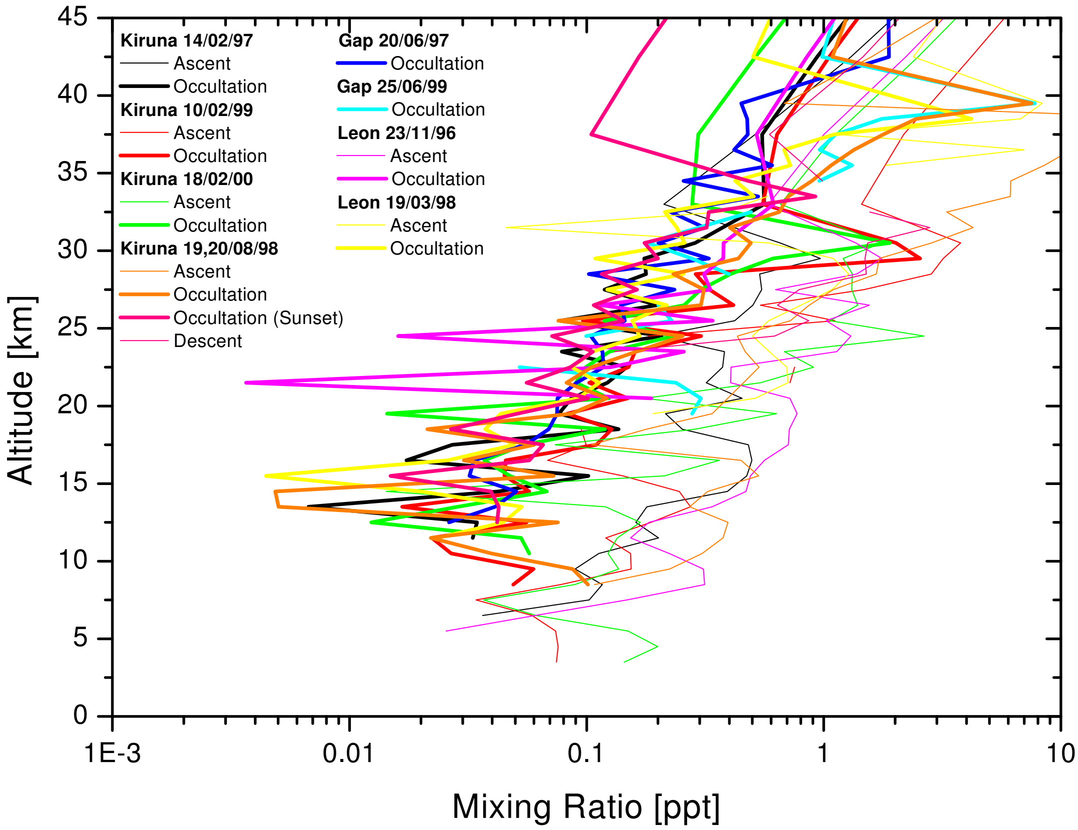

Figure 7.12: *Vertical distribution of the upper limits of OIO. The thick lines refer to solar occultation and the thin lines to balloon ascent measurements.*

et al. [2000] observations. In order to exclude that possibility totally, it warrants further detailed investigation. Second, the IO detected by *Wittrock et al.* [2000] constituted a total atmospheric rather than a stratospheric column. In order to be able to attribute the increase in measured IO differential slant column amounts with SZA as a sign for stratospheric IO, the authors included some photochemical modelling (on top of radiative transfer modelling to account for observation geometrical effects) into their study. Their photochemical modelling did not include, however, new information on the atmospheric iodine chemistry that became available only recently (e.g., the potential role of OIO in photochemistry, or updates of the reaction rate coefficient for reaction 8 (table in Appendix A) et cetera. If this new information had been included then stratospheric IO would have reacted more rapidly into the nighttime reservoir gases i.e., $IONO_2$, OIO, and HOI at low sun. Therefore by including these IO-depleting reactions, a match of observed and modelled IO slant column amounts would require an even larger stratospheric I_y than reported. Third, one may argue, that iodine was inhomogeneously distributed in the lower stratosphere leading to more I_y in high than at lower latitudes. This hypothesis could then possibly explain the discrepancy between the high latitude *Wittrock et al.* [2000] observations and the mid-latitude measurements of *Wennberg et al.* [1997], *Pundt et al.* [1998], and of the present study. Still, the mixing hypothesis would not allow to bring the *Wittrock et al.* [2000] and our high latitude measurements into agreement. Also, significant inhomogeneities are not being observed for all other major trace elements in the stratosphere. Therefore, that possibility is also rather unlikely, and we conclude that probably unknown reasons exist for the, in the present context, outstanding observations of *Wittrock et al.* [2000].

7.4 Total Iodine

Since both measured iodine species, IO and OIO are potentially subject to a photochemical concentration change as the sun sets or rises, the partitioning of the stratospheric I_y species during solar occultation has been modelled. For that purpose, the photochemistry of stratospheric iodine as detailed in section 3.3.3 and in the table in Appendix A was adopted in the 1D photochemical box model *LABMOS* [*Erle* 1999; *Fitzenberger* 2000]. The *LABMOS* model uses a photochemical scheme based on the JPL-97 kinetic data [*DeMore et al.* 1997] with the recent update as given by *Sander et al.* [2000]. Beside the additional added iodine chemistry, the model includes full O_x, NO_x, HO_x, ClO_x and BrO_x chemistry with a total of 68 gas phase reactions, 29 photolytical reactions and 7 heterogeneous reactions on the liquid background aerosols. The photolysis rates were adopted from the pre-computed look-up table of the SLIMCAT model. The iodine chemistry scheme itself includes only 6 species (I, IO, OIO, HI, HOI and $IONO_2$) with 17 gas phase reactions and 6 photolytical reactions. The photolysis rates of these iodine species were calculated with the cross-sections and quantum yields as given in the table in Appendix A (see Figure 7.14) and the actinic fluxes, which were calculated with the scheme of *Lary and Pyle* [1991] for the Kiruna 1997 and the León 1996 flights (see chapter 5.3.1 or *Bösch et al.* [2001]). For the model calculations of the Arctic winter flights, the photolysis frequencies as calculated for Kiruna 1997 are used. For all other flights the calculations for the León 1996 are adopted. Other iodine compounds like INO, INO_2, ICl, IBr or I_2 were not considered since no large built-up in

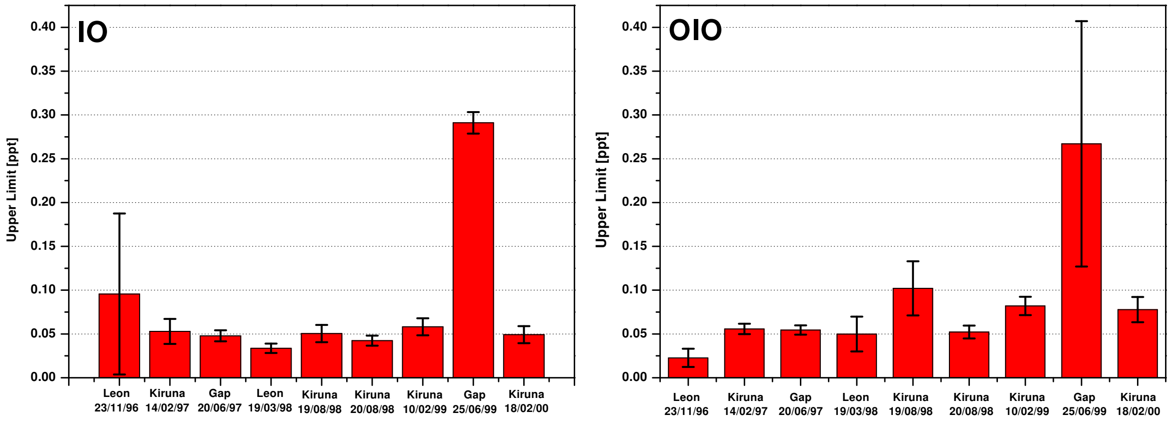

Figure 7.13: *Mean upper limit for IO (left) and OIO (right) inferred for the lower stratosphere (<20 km). Please note, that for the flights in León 1996 and in Gap 1999 the tangent heights of the occultation measurements only slightly fall below 20 km and thus averaging over several measurements was not possible.*

the stratosphere is expected mainly due to their rapid photolysis in combination with their slow formation. For the dimer I_2O_2 and the higher oxides I_xO_y no kinetic and thermochemically data were available so far which could serve as input in the model and hence they were not taken into account even if they possibly have some relevance. Further, heterogeneous iodine chemistry is neglected in the scheme, because there is no new information available that would provide new arguments for statements going beyond what was already discussed by *Solomon et al.* [1994]. As outlined there, heterogeneous processes are not likely to represent a net sink for stratospheric iodine, and the net photochemical impact of heterogeneous chemistry on stratospheric iodine is likely to be negligible, conclusions primarily drawn from analogies to reactive chlorine, and

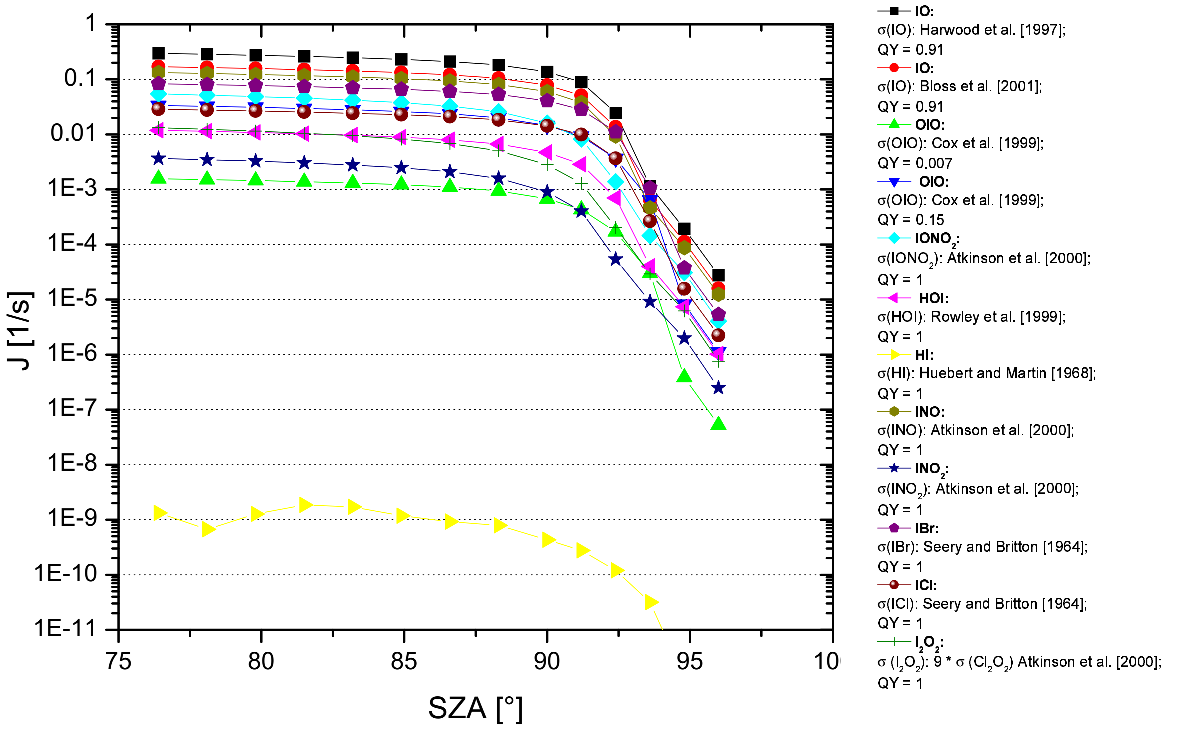

Figure 7.14: *Photolysis frequencies of the most important iodine species as a function on SZA for an altitude of 20 km calculated for the flight in Kiruna on Feb. 14, 1997 for a ground albedo of 0.7 and cloud free conditions. The absorptions cross-section (σ) and quantum yields (QY) used for the calculation were given in the legend of the graph. Please note, that the species INO, INO_2, IBr, ICl, and I_2O_2 are not included in the photochemical model. The photolysis frequency of IO used for the model was calculated with the cross section of [Harwood et al. 1997], using instead the more recently measured cross section of Bloss et al. [2001] results in smaller j-values.*

bromine. The box model calculations were initialized with the 12:00 UT (of the day of the corresponding balloon flight) model output of the 3D SLIMCAT model and was run on the levels as given by the SLIMCAT model[8]. In the model runs I_y was constrained to 0.11 pptv at all levels. The integration of the system of differential equations of the chemical scheme is performed with the FACSIMILE package for the solar zenith angles and the meteorological parameters (temperature, pressure) for days and the locations of respective balloon flights. To bring the chemical scheme to equilibrium the cycles were performed (for the same day). An schematic overview of the model can be found in Figure 7.15.

For each flight, two model runs were performed for which the OIO photolysis frequency was either set to zero (quantum yield $\chi_{OIO} = 0$) or calculated with the quantum yields $\chi^{IO}_{OIO} = 0.007$ and $\chi^{I}_{OIO} = 0.15$ The model calculations then provide the mixing ratios of the various (iodine) species for different altitudes as a function of SZA including and excluding OIO photolysis. The obtained diurnal variation of the iodine amount for both cases for the León flight in 1996 (high NO_x and low ClO_x, representative for mid-latitudes in all seasons and high latitude summer) and the Kiruna flight in 1997 (low NO_x and high ClO_x, representative for high latitude winter) is shown in Figure 7.16. Clearly as anticipated from the adopted iodine chemistry, OIO is getting most abundant in the lowermost stratosphere, when its formation reactions 12a and 13a (see table in Appendix A) are most efficient, and its losses are low i.e., when NO_x is low and OIO photolysis is omitted (χ_{OIO} =0). Conversely, OIO is less abundant when its formation reactions 12a and 13a are less efficient, and its losses are large i.e., at high NO_x and allowing OIO photolysis. In the sunlit lower stratosphere, OIO thus occurs in ant-phase with IO. As the sun sets IO disappears into its major nighttime reservoir species (mostly $IONO_2$, OIO, and HOI). In the middle and upper stratosphere, IO increases at the expense of I atoms owing to their fast

---

[8] SLIMCAT uses 12 (old version) or 18 (new version) levels

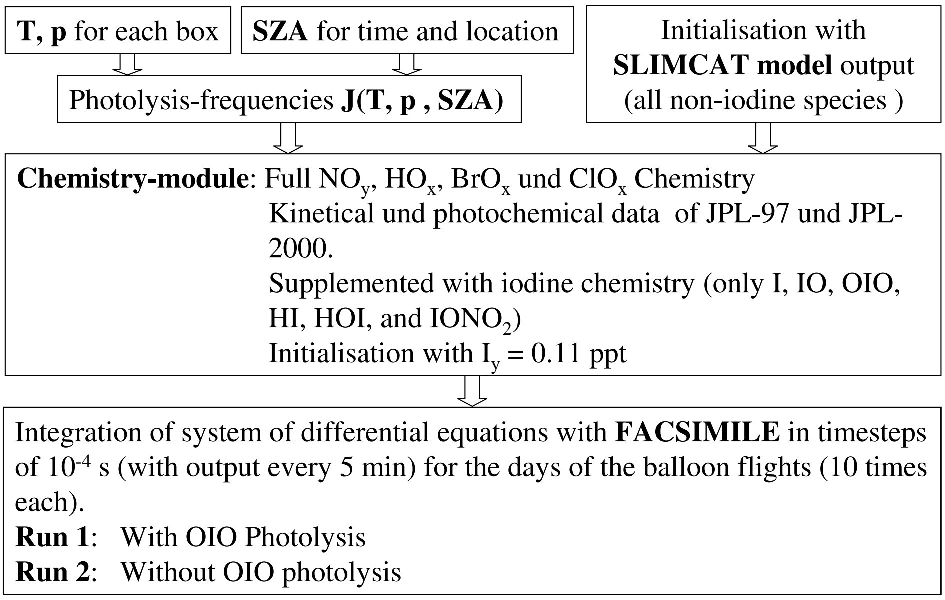

Figure 7.15: *Schematic overview of the photochemical model.*

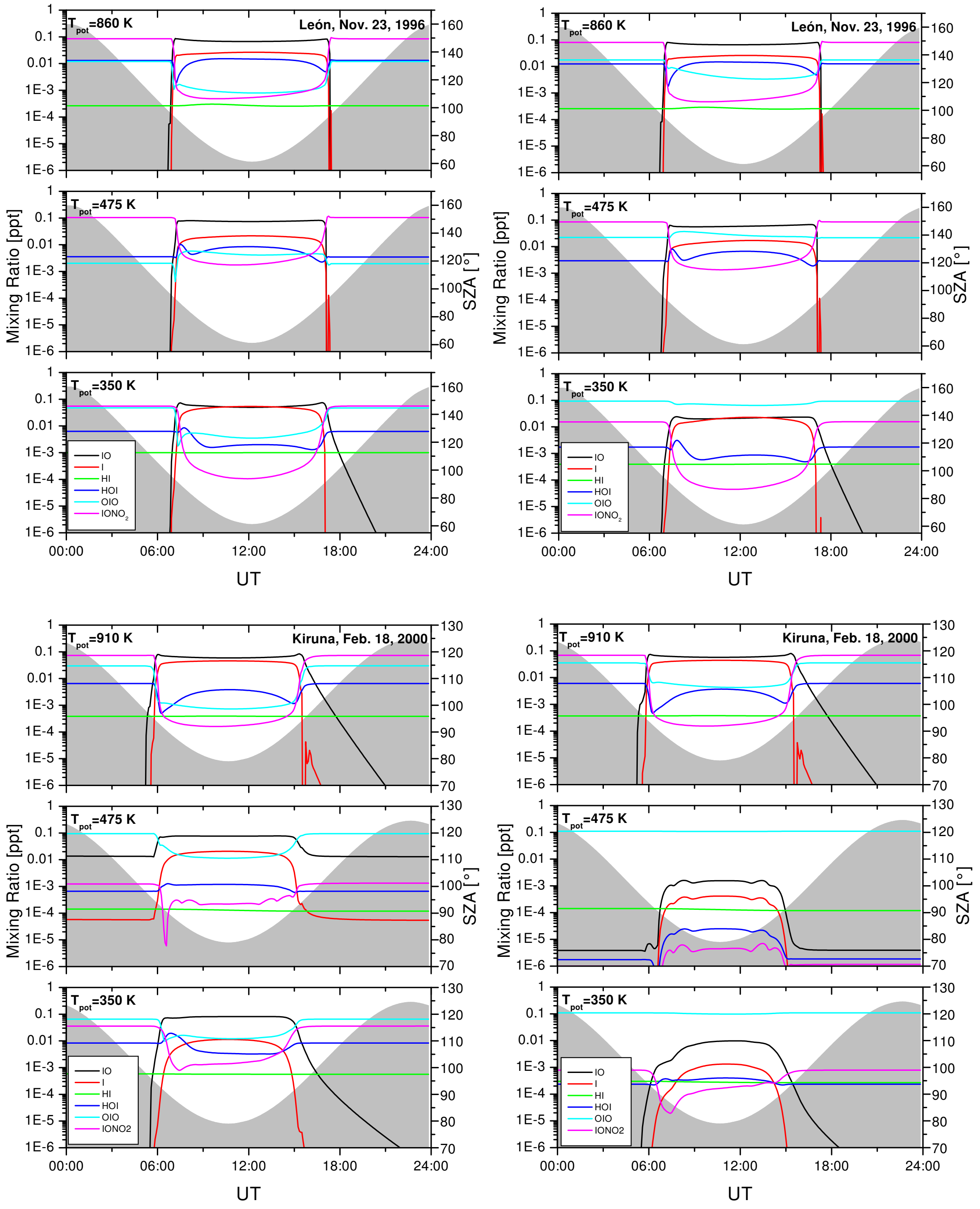

Figure 7.16: *Modelled diurnal variation of the iodine species including (left column) or excluding OIO photolysis (right column) for the León flight in 1996 (high* NO_x *and low* ClO_x *conditions) and the Kiruna flight in 2000 (low* NO_x *and high* ClO_x *conditions). The SZA is indicated by the gray shaded area.*

reaction with O_3, and the successively decreasing IO photolysis as the sun sets.

Like in chapter 5.3.4, rather than comparing instantaneous profiles, the geometry was simulated by which the SZA dependent stratospheric fields of IO and OIO is observed. These simulated photochemical fields (x-axis SZA, y-axis pressure/height) for the species IO and OIO are shown in Figure 7.17 and Figure 7.18 for León flight in 1996 and the Kiruna flight in 1997, respectively. Overlaid is the balloon trajectory and the line of sight of the measurements. These two figure clearly show the above discussed dependence of the IO and OIO mixing ratios on the OIO photolysis and the NO_x amounts. Figure 7.17 and Figure 7.18 also indicates that the line of sight mostly crosses through the layers where either IO or OIO (or both) is predicted to occur maximal - except for OIO during the León flight on Nov. 23, 1996 when the flight had to be terminated due to logistic problems before complete sun set. Thus, it is demonstrated that even though IO and OIO are occurring in anti-phase, the simultaneous observation of IO and OIO largely constrains the total amount of lower stratospheric I_y, irrespective what is assumed for OIO photolysis.

The photochemical fields of IO and OIO were interpolated between the outputs for each SZA interval (the output timestep of 5 minutes provided a SZA binning of 0.8°) and the modelled pressure levels. Therefore the modelled IO and OIO concentrations were then linearly interpolated on the grid of the logarithmic pressures and SZAs. An integration of the IO and OIO concentrations along the line sight of then yields the model-related integrated IO-SCD and OIO-SCD values for each observation, which can be directly compared to the measurements.

Figure 7.19 compares the inferred upper limits of IO and OIO with the line of sight integrated slant column amounts of IO and OIO (denoted IO-SCD, and OIO-SCD), respectively of model based predictions (upper two panel allowing for OIO photolysis, and lower two panels omitting OIO photolysis). Since the limits for IO and OIO detection (the y-axis in Figures 7.19) decrease with decreasing tangent heights (see the color code), the individual groups of upper limit data representing different flights group along different descending lines. The x-axis of both figures show for each line of sight (each IO or OIO upper limit measurement) the expected SCD when integrating the predicted IO or OIO concentrations along the line of sight. Clearly the prediction change by turning on (upper panels) or off (lower panels) the photolysis of OIO, resulting in different branches of the data for altitudes (mostly of the lowermost stratosphere) where OIO significantly contributes to total I_y. Moreover, the predicted IO-SCD and OIO-SCD also change with the amount of I_y put into the model, but for the assumed small total I_y amounts the predicted SCD linearly reacts with I_y (indicated by the black diagonal lines in Figures 7.19). Therefore, the crossing points of the data with the diagonals indicate the upper limit of I_y compatible with the measured upper limits of IO and OIO, and the adopted iodine photochemistry. In particular, this statement still holds true if either all IO or OIO upper limit data from all individual flights are combined, or if all the IO and OIO data is combined. The resulting I_y upper limit line of the combined data is indicated by the black curved lines in Figure 7.19. It connects the lowest upper limits inferred from the combined data. In order to further illustrate the result, the solar occultation measurements of OIO upper limits constrain I_y only when it is predicted to be present or better maximized, i.e., in the low NO_x lowermost stratosphere when OIO photolysis is omitted (Figure 7.18, lower panel). In all other cases the measured OIO upper limits are not constraining I_y, but instead the IO measurements because IO is then predicted to be the most abundant iodine species. Accordingly, the black lines connecting the lowest values of upper limits have then to be regarded as the height dependent upper limits for stratospheric I_y that we can infer from our measurements.

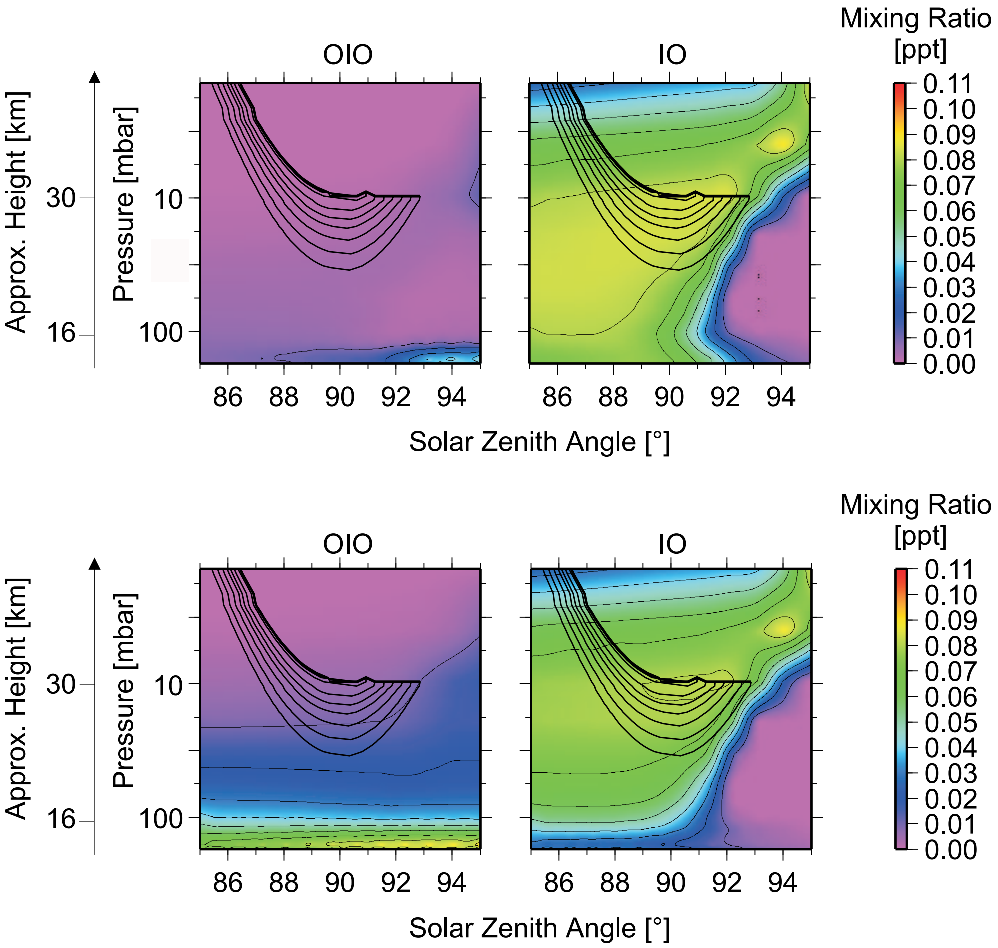

Figure 7.17: *Simulated stratospheric photochemistry of OIO (left column of panels) and IO (right column of panels) for the León flight on Nov. 23, 1996. For all simulations total iodine was set to* I_y*=0.11 ppt. In the upper row of panels, OIO photolysis was included while in the lower row of panel, it was set to zero. Overlaid over all panels are the line of sight of the measurements through which the chemical fields were probed by the solar occultation measurements (black lines).*

As the presented method to infer an upper limit for stratospheric I_y involves photochemical modelling, uncertainties associated with modelling the IO/I_y and OIO/I_y ratios have to be addressed. First, one may question whether the adopted photochemical scheme for iodine is correct at all. As it is discussed in chapter 3.3.3, there are good arguments for it, i.e., analogies with the stratospheric photochemistry of the other halogens (F, Cl, and Br), and the already existing photochemical and kinetic data even though not being complete. Second, major uncertainties in estimating the IO/I_y ratio are probably due to uncertainties in the photochemical data. Inspecting the photochemistry more closely, here most important are uncertainties in (a) the IO

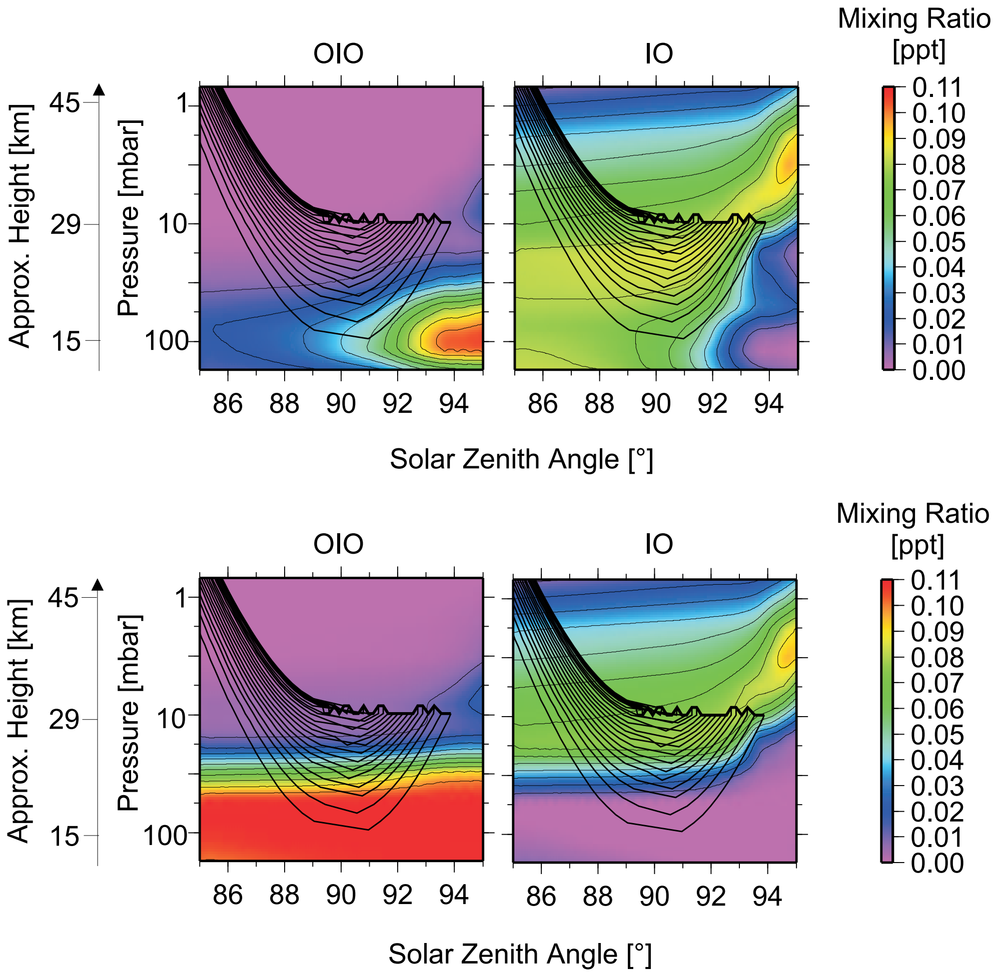

Figure 7.18: *Same as Figure 7.17 but for the Kiruna flight on Feb. 18, 2000.*

photolysis rates due to uncertainties in the IO cross section, (b) the reaction rate coefficient for reaction 10 (IO+NO_2) and $IONO_2$ photolysis, (c) the reaction rate coefficient for reaction 6 (I+O_3), (d) the reaction rate coefficients for the interhalogen reactions 11, 12, and 13, and (e) the photolysis of OIO.

(a) According to the information provided in the comments 11 and 12 in the table in Appendix A, the strength of the IO continuum absorption between ~340 nm and ~440 nm is somewhat controversially discussed in the literature (e.g., *Laszlo et al.* [1995] versus *Harwood et al.* [1997] versus *Bloss et al.* [2001]). Using the cross section of *Bloss et al.* [2001] instead of *Harwood et al.* [1997] for the calculation of the IO photolysis frequencies results in up to 40% smaller values. In effect, a slower IO photolysis would lead to larger predicted IO mixing ratios, and hence to lower upper limits of the inferred I_y. (b) At stratospheric temperatures, the rate coefficient for reaction 10 is uncertain by a factor of 2, i.e., for p = 100 bar, and T = 220 K, the error limits given in *DeMore et al.* [1997] suggest a rate coefficient in the range of 2.3 to $8.5 \cdot 10^{-12}$ cm^3/s with a recommended value $4.6 \cdot 10^{-12}$ cm^3/s). Here the recently measured

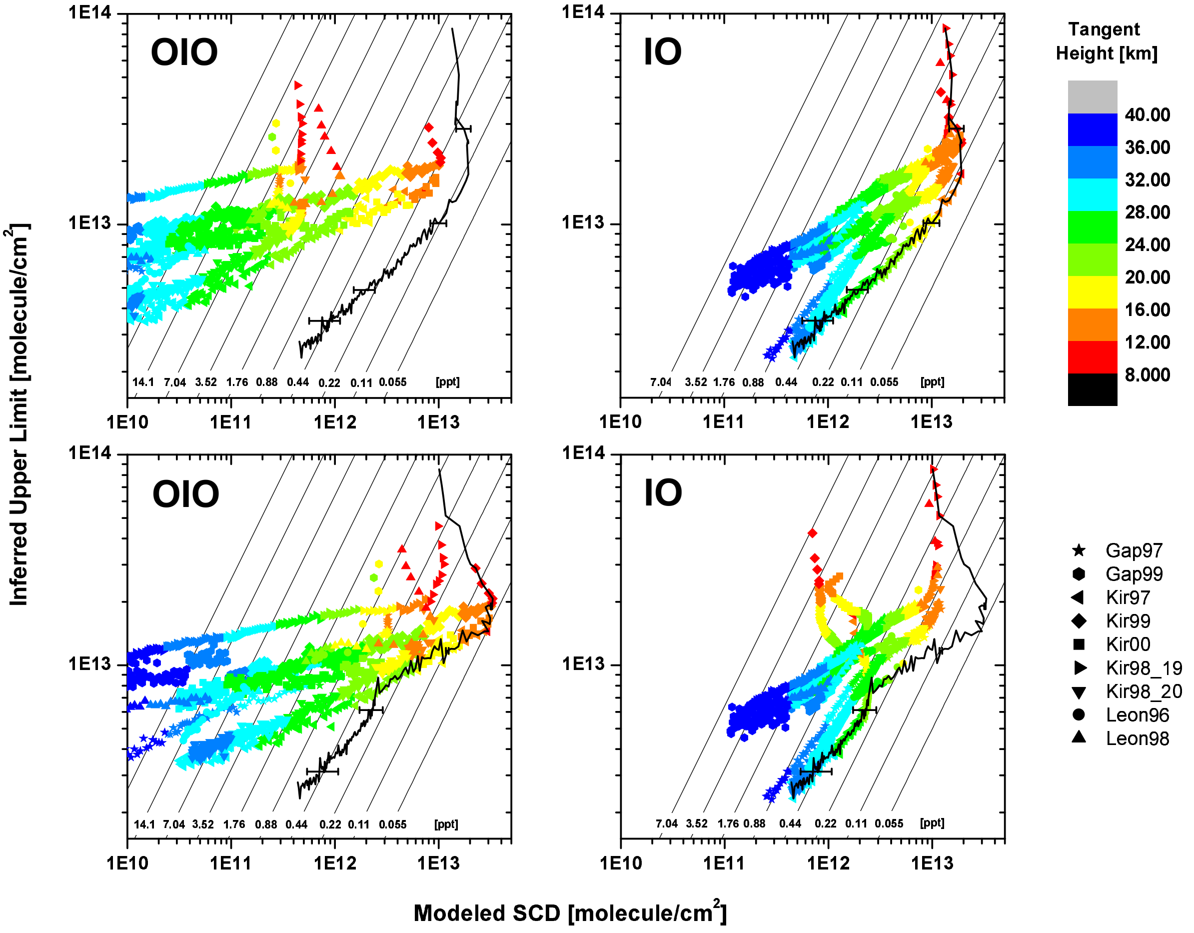

Figure 7.19: *Inferred upper limits of* I_y *in the coordinates of measured IO-SCDs, and OIO-SCDs upper limits (y-axis in the figures, respectively) and as a function of along the line of sights integrated modelled IO-SCDs and OIO SCDs. Upper two panels including OIO photolysis, and lower two panels omitting OIO photolysis, respectively. In the model calculations* I_y*=0.11 ppt is assumed. The diagonal lines indicate the model predictions for IO-SCD and OIO-SCD if* I_y *ratios as given by the mixing ratios indicated at the bottom of the Figures were assumed in the model. The grey line in all panels indicates the combined total iodine upper limits inferred for the case including OIO photolysis (upper two panels) and omitting OIO photolysis (lower two panels), respectively.*

$IONO_2$ spectrum from Mössinger et al. [distributed through *Atkinson et al.* 2000 is taken,. The uncertainty of the cross section is taken into account by shifting the cross section by ± 50 nm. Evidently, the combined uncertainties of the formation reaction 10 and photolysis will determine the $IONO_2$/IO ratio with the lower photolysis rate and the upper limit of reaction 10 will contribute to uncertainty of the inferred I_y upper limits. (c) According to the literature, the uncertainty of reaction 6 is about a factor of 3 at T = 220 K, i.e., $4.4(+7.5/-2.8)\cdot 10^{-11}$ cm^3/sec with the smaller limit constraining the inferred I_y upper limit. (d) Here, most important are reaction 11 (IO+ClO) and 12 (IO+BrO) with the channels leading directly or via unstable intermediate species to I atoms. Since for reaction 11 the channels leading to I atoms are already maximized (sum of ϵ=1), most important is the uncertainty associated with the reaction rate coefficient ($k_{11} = 1.8(+1.8/-0.9)\cdot 10^{-11}$ cm^3/sec at T = 220 K), however, only for the high ClO_x cases, because for all other conditions reaction 12 (IO+BrO) is more rapid. The recent studies of *Bloss et al.* [2001] and *Rowley et al.* [2001] have largely reduced the uncertainties associated with the channels of reaction 12, in particular those leading directly or indirectly to I atoms (the other reaction product OIO is not important here as we probed the stratosphere for it). In effect, since the remaining uncertainties in the (IO+OIO)/I_y ratio due to reaction 12 are much smaller than that of the reaction I + O_3 being the bottleneck in recycling iodine back into its observable forms (IO and OIO), they are not likely to contribute much to the uncertainty of the inferred upper limit. (e) As already discussed above, the OIO photolysis is a major uncertainty in the adopted photochemistry and as the existing discrepancies in the contradictory information presently available cannot be solved here (*Cox et al.* [1999] versus *Ingham et al.* [2000] and *Allan et al.* [2001]), model runs were performed reflecting both cases.

To estimate the uncertainties of the inferred I_y upper limits associated with the adopted photochemistry additional model were performed where the IO/I_y and OIO/I_y ratio were minimized/maximized (by tuning the reaction rate coefficients and photolysis rates (a to e) according to the limits given by their error bars). The inferred uncertainties of I_y were indicated by the error bars given in Figure 7.19.

Including all the information gained from the inferred upper limits of IO and OIO including the photochemical modelling with its uncertainty, total lower stratospheric I_y (<20 km) is assessed to 0.1±0.05 ppt, and 0.065±0.01 ppt for the OIO photolysis or no OIO photolysis cases, respectively. Accordingly, for the middle stratosphere (< 35 km), the inferred total I_y is larger due to smaller detection sensitivity there. Note, however, that the upper limits are only valid if the adopted iodine photochemistry is correct. If this is not the case, then this constrains only upper limits of stratospheric IO and OIO as given in section 7.3. Moreover, it should be pointed out that the inferred I_y must not stringently agree with total stratospheric iodine, as possibly some stratospheric iodine can be is tied to or taken up by other yet unknown species.

7.5 Implications for Ozone

In this section, the implication of iodine on the stratospheric ozone will be explored even for the low upper limits for total gaseous stratospheric iodine give in the previous section. For this purpose, photochemical box-model calculations[9] were performed, where the iodine chemistry was switched on and off. Two case studies were shown, representative for two different photochemical

---

[9] A model description can be found in section 7.4

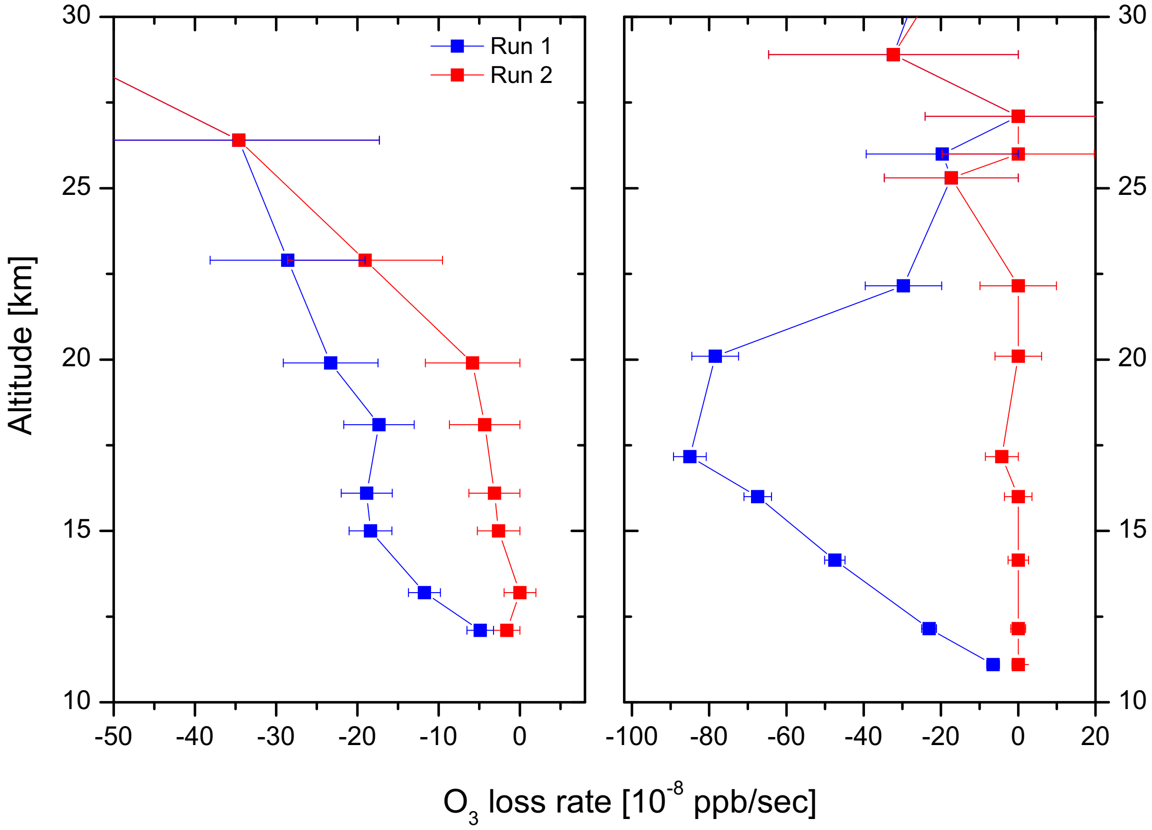

Figure 7.20: *Inferred vertical distribution of stratospheric ozone loss rates due to iodine chemistry for Léon in 1996 (left panel) and for Kiruna 2000 (right panel). The ozone loss rates were inferred with the model described in section 7.4 assuming I_y=0.11 ppt. The result for two model runs were performed, allowing (Run 1) or omitting (Run 2) OIO photolysis. The given error bars indicate the accuracy of the model output.*

regimes: León on November 23, 1996 was used as a representative for mid-latitudinal conditions (with high NO_x and low ClO_x) and Kiruna on February 18, 2000 for Arctic winter conditions (with low NO_x and high ClO_x).

As already discussed in chapter 3.3.3, the key reaction for ozone depletion involving iodine chemistry are the interhalogen reactions, the IO+HO_2 reaction and the IO+NO_2 reaction. Evidently, the relevance of the different cycles depends strongly on the photochemical conditions. During summer, the IO+HO_2 will dominate the iodine induce ozone loss in the lower stratosphere, while for higher altitudes ozone loss is due to the ClO+IO cycle with lesser contributions from the IO+BrO cycle. For winter condition, in particular at high-latitudes, the ClO concentrations can be significantly increased (depending on the degree of chlorine activation) in the lower stratosphere, and hence the ozone loss through the IO+ClO cycle intensifies in the lower stratosphere. However, the IO+HO_2 and IO+NO_2 cycles will be less efficient. The rate-limiting step of these cycles is the photolysis of HOI and $IONO_2$, which is significantly reduced in winter.

The possible role of iodine for stratospheric ozone depends greatly on the OIO photolysis. Assuming a rapid photodissociation of OIO into the products I and O_2 then yields an additional, efficient ozone loss mechanism. OIO is mainly formed through the reaction of IO with BrO with a yield of 0.65-1, which themselves are formed via the reaction with ozone. The subsequent OIO dissociation recycles the I atom and two ozone molecules were destroyed within one cycle.

Figure 7.20 shows the inferred ozone loss rates for a iodine content of 0.11 ppt for Léon in November 1996 (left panel) and for Kiruna in February 2000 (right panel) assuming or omitting OIO photolysis (denoted as run 1 and run 2). In both panels, the large impact of the OIO photolysis is clearly visible. Assuming a moderately fast OIO photolysis (see Figure 7.14) increases the O_3 depletion potential of iodine by a factor of 5-10 for León 1996 and of $\sim$50 for Kiruna. For high-latitude winter, almost vanishing ozone loss rates were obtained with the model run 2. However, allowing for OIO photolysis (run 1), the BrO+IO reaction causes a large increase of the loss rates below 25 km with a maximum loss rate of $-8 \cdot 10^{-7}$ ppb/sec at 17 km.

For León, the ozone loss rates inferred with run 2 show very low values at the lower stratosphere with a slight increase towards higher altitudes. Above 20 km, a strong increase of the loss rate is found, but the uncertainty due to the limited accuracy of the model output increases strongly too. This may be the result of the IO+ClO cycle. Between 15 and 20 km, larger ozone loss rates are observed as for high-latitude winter most likely caused by the IO+NO_2 reaction, which is completely suppressed in polar winter. Below 12 km a small increase is visible indicating the contribution of the IO+HO_2 cycle. However, this cycle seem to be less important for November, where the photolysis is already less efficient and the HO_2 concentrations are likely to be small. The O_3 loss rates are clearly increased using the model run 1, but still with smaller values compared to high-latitude winter. The combination of the considerable smaller BrO concentrations and the fast OIO+NO reaction (reduces the ozone depletion through the recycling of IO) for the large NO concentrations to be found in Leon results in a significantly smaller ozone depletion potential of iodine. The maximum value of the ozone loss rate in the lower stratosphere obtained from run 1 for León is in the range $-2 \cdot 10^{-7}$ ppb/sec.

It is self-evident, that this two case studies does not allow to draw conclusions about the potential role of iodine chemistry for the global stratospheric ozone content, but the inferred ozone loss rates can be put into context to typical ozone loss rates ozone induced by HO_x, NO_x, BrO_x or ClO_x chemistry. During high-latitude winter, usually a massive ozone depletion is observed caused by catalytic cycles involving chlorine and bromine. The loss can easily exceed 40 ppb per day ($\simeq 4 \cdot 10^{-4}$ ppb/sec), which is several orders of magnitude larger than the loss rates inferred for iodine. However, a large variability during the winter itself as well as between different winters is observed. Therefore, a typical mean value will be clearly smaller than 40 ppb/day, but still the iodine induced loss seem to be negligible. The mid-latitudinal ozone loss rates calculated by *Garcia and Solomon* [1994] for 39°N in March shows values in the range of 10^{-6} ppb/sec for altitudes below 15 km. Above 15 km the ozone loss is more intensive with values about 10^{-5} ppb/sec at 20 km and about 10^{-2} ppb/sec at 30 km. Comparing this to the inferred potential ozone loss rates (for run 1), it is obvious that iodine chemistry could contribute substantially (by approximately 10 %) to the ozone loss in the lower stratosphere at mid-latitudes and at high-latitudes during summer. In conclusion, even with the stated upper limits for total gaseous iodine, it still has a potential impact on the lower stratospheric ozone abundances and thus may also contribute to the not yet understood mid-latitudinal trend in ozone [*WMO* 1998].

7.6 Discussion

The reported upper limits of stratospheric IO (0.055±0.004) ppt and OIO (0.056±0.003) ppt (the former detected with an unprecedented high sensitivity, and the latter for the first time) monitored at mid- and high latitudes during all seasons allowed in combination with photochemical model calculations to reveal a lower stratospheric I_y ($<$ 20 km) of 0.1±0.05 ppt, and 0.065±0.01 ppt allowing for, or omitting OIO photolysis, respectively. For the middle stratosphere ($<$ 35 km), the inferred total iodine is larger due to smaller detection sensitivity there. Combining this study with findings of previous studies (except of *Wittrock et al.* [2000] which cannot be reconciled with the findings reported in the studies of *Wennberg et al.* [1997] and *Pundt et al.* [1998] and this studies) then provokes the following questions on the stratospheric iodine budget and chemistry:

- Does less iodine enter the stratosphere than be expected from the iodine bearing source gas concentrations measured at entry level ?
- Is I_y very inhomogeneously mixed in the stratosphere and the presented measurements fortuitously missed to probe I_y rich air masses
- Is I_y predominantly present in other chemical forms than IO and OIO at daytime ?

At this point nothing can be said about the first question that goes beyond what was already said in the chapter 3.3.3. There are some reasons to expect total stratospheric iodine in the range of 0.1 to 1 ppt. The second possibility is also very unlikely primarily due to fact, that large inhomogeneities are usually not observed for other species (at least outside the polar vortex). Since the balloon flights covered a wide range of stratospheric conditions including flights at mid-, and high northern latitudes in all seasons, some IO and/or OIO should have been present, at least occasionally, if I_y is generally more abundant than stated here. In consequence, possibility (3) is favored, i.e., that the stratospheric chemistry of iodine is still not completely understood. Inspecting again Figure 3.8 reveals that in analogy to the other halogens (F, Cl, and Br) - even though some discrepancies exist - major reaction pathways connecting the gaseous iodine species to the other known stratospheric trace gas families (odd oxygen, nitrogen, and hydrogen and the halogens) are already well represented by the available kinetic and thermochemical data. Therefore, major uncertainties in the stratospheric partitioning of I_y are not very likely.

Major uncertainty, however, still exists in the uptake efficiency of inorganic iodine bearing molecules on the stratospheric sulfuric acid aerosol. Likewise, the kinetics and thermochemistry of higher iodine oxides (I_xO_y) - frequently observed in laboratory studies conducted at atmospheric pressures and larger iodine concentrations than those expected for the stratosphere [e.g. *Hönninger* 1999] - at low pressures, temperatures and iodine concentrations are not known. Due to the lack in these kinetic and thermochemical data, it can only be speculated here where or in what species the missing iodine resides in the lower stratosphere. Conversely, if iodine is taken up on aerosols or present as higher oxides in the lower stratosphere then one can expect that these constituents eventually release the iodine back into the gas phase either where the aerosol evaporates due to increasing temperatures, or where the actinic fluxes (mainly in the UV) for the I_xO_y photolysis getting much larger than those experienced the lower stratosphere i.e., in the middle and upper stratosphere. The latter possibility, however, affects the inferred lower stratospheric I_y and accordingly its impact on ozone at daytime, since the typical timescales involved in the formation of I_xO_y (Reaction 13c in table in Appendix A) are reasonably rapid to allow for a diurnal cycle of I_y, which we then would miss to detect.

Finally, it should be emphasized that even within the inferred low upper limits of total gaseous stratospheric iodine, its potential impact on the ozone loss is not negligible. In the lower stratosphere at mid-latitudes iodine still has a the potential to reduces the ozone level by 10%.

Chapter 8

Summary and Outlook

The subject of this thesis is to study the stratospheric chemistry of nitrogen and iodine compounds. For this purpose, a DOAS instrument, designed for airborne applications, was deployed on the LPMA/DOAS balloon gondola. Applying the DOAS technique to the measured direct sunlight spectra allows a sensitive analysis of the absorption signatures of NO_2, O_3, IO and OIO. These measurements are combined with the results obtained from an IR Fourier Transform Interferometer (LPMA-FTIR) mounted on the same gondola.

- Within the scope of this Ph. D. thesis, a new and important effect which impact the spectral retrieval of direct sun measurements is identified. It is well known, that the optical densities of the solar Fraunhofer lines change across the solar disk. Since the propagation of a solar light beam is a function of the solar disk's location, the combination of both effects generates an apparent change of the Fraunhofer lines during the course of the solar occultation measurements. A constant solar spectrum, however, is an important prerequisite for the DOAS technique and, hence, spectral artifacts occur which might be mis-interpretated as atmospheric absorptions. A proper correction can be achieved with a new method presented in this thesis, referred to as solar center to limb darkening correction. It has to be emphasized, that this effect does not only impact the measurements presented in this thesis, but also the observations of several other instruments, in particular satellite borne sensors, operated in the solar occultation mode. Still unclear is the importance of this effect for measurements of scattered sun light at large solar zenith angles. Although it is believed to be small, it requires further investigation.

- The NO_2 and O_3 measurements performed during a series of eight balloon flights showed a seasonal and latitudinal behavior being in agreement with the present understanding of the stratospheric photochemistry. The obtained profiles are extensively compared to the measurements by O_3 sondes, various satellite instruments and the LPMA-FTIR. The comparison with the results of the LPMA-FTIR revealed large discrepancies, in particular in the case of NO_2. This can be attributed probably to the complicated spectral retrieval for the IR measurements, but a cross-validation of the UV, visible and IR cross sections is required, too. The diurnal variation of NO_2 usually prevents a tight comparison of balloon-borne and satellite measurements. As good temporal and spatial coincidence is necessary, the observed discrepancies are not surprising. However, different measurements can be linked through photochemical model calculations if similar air masses have been probed. Therefore, future satellite validation activities, like the upcoming SCIAMACHY validation activity, will include meteorological forecasts of the trajectories[1] to ensure that the same air parcels are probed by the satellite and the DOAS instrument.

- In February 2000, a clear enhancement of the stratospheric NO_2 concentrations inside the polar vortex was found. In combination with tracer measurements, it was shown that this observation can be explained by descent of NO_x-rich mesospheric air. This is a commonly observed feature during the Antarctic winter, but not yet observed in the Arctic. The NO_x cycle is the main loss mechanism of ozone in the middle stratosphere, thus such enhancements are directly linked to an increasing ozone depletion. The global effect, however, of these enhancement is unclear, but near the maximum of the solar cycle or during strong particle events (such as solar proton events) the stratospheric ozone levels can be significantly distorted. To account for the potential consequences on stratospheric ozone, this polar mesospheric source of nitrogen has to be included in chemical models. Therefore, the magnitude of this mesospheric source of nitrogen oxide has to be quantification by satellite measurements.

- The current understanding of the stratospheric photochemistry can be tested by comparing measurements with simulations by 3-D Chemical Transport Models (CTMs).The comparison of the NO_2 and O_3 profiles revealed a large underestimation of the NO_2 concentrations by the models while the measured and modelled O_3 concentrations agree fairly well. This is a commonly observed feature of CTMs, although the recently measured rate constants of the reactions linking NO_2 and HNO_3 [*Brown et al.* 1999a; *Brown et al.* 1999b] lead to a significant increase of the modelled NO_2 amounts, in particular during summer. A tight investigation, however, of observed discrepancies based on NO_2 and O_3 measurements alone is not possible. Therefore, the DOAS measurements were combined with the the LPMA-FTIR measurements allowing to distinguish between chemical, dynamical and model-related reasons. Thereby, the partitioning of the nitrogen species, the tracer transport and the budget of the individual nitrogen species as well as total NO_y were studied in more detail. The main results can be summarized as follows:
  - The NO_2/HNO_3 ratio in the high-latitudinal lower stratosphere is strongly underestimated during cold winters, while a good agreement is found during warm winters.
  - In the middle stratosphere, the NO_2/HNO_3 ratio is underestimated during winter.
  - During high-latitude summer, the models reproduce the NO_2/HNO_3 ratio fairly well in the middle stratosphere, while they underestimate the ratio in the lower stratosphere.
  - Large model deficits are observed for the calculation of the descent rates during high-latitude winter as well as during high-latitude summer.
  - HNO_3, NO and NO_2 are largely underestimated by the models, while $ClONO_2$ is reproduced well .
  - The total amount of NO_y is largely underestimated by the models, very likely as a result of an overestimation of the numerical diffusion on small scales.

---

[1] provided by the FU Berlin

It is evident, that the main contributions to the discrepancies between the measurements and the model calculations of the NO_2 (and NO_y) are rather due to model-specific and dynamical reasons than to the adopted chemistry. Nevertheless the investigation of the partitioning reveals a still uncomplete understanding of the stratospheric nitrogen chemistry. The identification of a single source of error, that can account for all observed discrepancies is not possible, however some points should be emphasized:

  - *Zhang et al.* [1995] proposed, that the N_2O_5 hydrolysis for very low temperatures and stratospheric HNO_3 concentrations may be slower as usually assumed. A hypothesis strongly supported by the presented lower stratospheric observations during polar winter.
  - The model's underestimation of the NO_2/HNO_3 ratio within the aerosol layer during summer points to a possible lacking heterogenous reaction pathway on background aerosol or to a possible overestimation of the available aerosol surface [*Kondo et al.* 2000].
  - The observations in the middle stratosphere in winter and summer cannot come into agreement with models by changing a single parameter only, e.g. the HNO_3 photolysis rate as proposed by *Jucks et al.* [1999].
  - The model/measurement agreement for $ClONO_2$ is remarkable and indicates uncertainties in the modelling of the chlorine/nitrogen interaction.

- Stratospheric IO and OIO could not be detected, even undertaken with an unprecedented high sensitivity. The inferred upper limits are of (0.055 ± 0.004) ppt for IO and of (0.056 ± 0.003) ppt for OIO for lower stratosphere. The combination with photochemical model calculations revealed an upper limit of total iodine of (0.1 ± 0.05) ppt and (0.065 ± 0.01) ppt, allowing for or omitting OIO photolysis, respectively. This gives rise to the question, whether less iodine enters the stratosphere than expected from the (sparse) measurements in the upper tropical tropopause, or whether the adopted chemistry is still incomplete, e.g. is iodine permanently uptaken by aerosols or does it reside in higher oxides. It is noteworthy that even within the stated small upper limits of total iodine, its potential impact on the ozone levels in the lower stratosphere may be as large as 10%, assuming that OIO rapidly photodissociates. Hence, iodine chemistry has the potential to substantially contribute to the observed mid-latitudinal ozone loss. Further studies such as laboratory studies of iodine reactions at stratospheric conditions and more sensitive measurements of total iodine at the stratospheric entry level are required.

Appendix A

Adopted Iodine Chemistry

No	Reaction			Rate Parameter	Remark
1	O + I_2	$\longrightarrow$	IO + I	$1.4 \cdot 10^{-10} \cdot \exp((-0 \pm 250)/T)$	(1)
2	O + IO	$\longrightarrow$	O_2 + I	$1.2 \cdot 10^{-10}$ at 298 K	(1)
3	OH + I_2	$\longrightarrow$	HOI + I	$1.8 \cdot 10^{-10}$ at 298 K	(1)
4	OH + HI	$\longrightarrow$	H_2O + I	$3.0 \cdot 10^{-11}$ at 298 K	(1)
5	HO_2 + I	$\longrightarrow$	HI + O_2	$1.5 \cdot 10^{-11} \cdot \exp((-1090 \pm 500)/T)$	(1)
6	I + O_3	$\longrightarrow$	IO + O_2	$2.3 \cdot 10^{-11} \cdot \exp((-870 \pm 200)/T)$	(1)
7	I + BrO	$\longrightarrow$	IO + Br	$1.2 \cdot 10^{-11}$	(1)
8	IO + HO_2	$\longrightarrow$	HOI + O_2	$(2.2 \pm 0.6) \cdot 10^{-11} \cdot \exp(400 \pm 80/T)$	(16)
9	IO + NO	$\longrightarrow$	I +NO_2	$(8.3 \pm 2.3) \cdot 10^{-12} \cdot \exp((269 \pm 85)/T)$	(15)
10	IO + NO_2 + M	$\longrightarrow$	$IONO_2$ + M	see Table 2 in DeMore et al. [1997]	(1)
11a	IO + ClO	$\longrightarrow$	I + OClO	$\epsilon=0.55 \pm 0.03$	
11b		$\longrightarrow$	I + ClO_2	$\epsilon=0.0$	
11c		$\longrightarrow$	ICl + O_2	$\epsilon=0.2 \pm 0.02$	
11d		$\longrightarrow$	I + Cl + O_2	$\epsilon=0.25 \pm 0.02$	
11e		$\longrightarrow$	OIO + Cl	$\epsilon=0.0$	
11f		$\longrightarrow$	IO_2 + Cl	$\epsilon=0.0$	
11g		$\xrightarrow{M}$	IO_2Cl	$\epsilon=0.0$	
				$k_{11} = 5.1 \cdot 10^{-12} \cdot \exp((280 \pm 150)/T)$	(3)

No	Reaction			Rate Parameter	Remark
12a	IO + BrO	$\longrightarrow$	OIO + Br	ϵ=0.65...1.0	
12b		$\longrightarrow$	I + Br + O_2	$\epsilon <0.3$	
12c		$\longrightarrow$	IBr + O_2	$\epsilon <0.05$	
12d		$\longrightarrow$	OBrO + I	ϵ=0 (assumed)	
12e		$\longrightarrow$	$IBrO_2$	ϵ=0 (assumed)	
				$k_{12}=6.7(\pm 0.8) \cdot 10^{-12} \cdot \exp((760\pm30)/T)$	(4)
13a	IO + IO	$\longrightarrow$	I + OIO	ϵ=0.3...0.46	
13b		$\longrightarrow$	$I_2 + O_2$	$\epsilon <0.05$	
13c		$\xrightarrow{M}$	I_2O_2	ϵ=0.42...0.55 at 295 K	
13d		$\longrightarrow$	2I + O_2	ϵ=0.07...0.15	(14)
				$k_{13}=4.1(\pm 3.4) \cdot 10^{-11} \cdot \exp((220\pm230)/T)$	(14)
14	IO + HO	$\longrightarrow$	I + HO_2	$1.0 \cdot 10^{-10}$	(18)
15	OIO + NO	$\longrightarrow$	IO + NO_2	$(6.34\pm1.08)\cdot10^{-12}$ at 300 K	(5)
16	OIO + OH	$\longrightarrow$	HOI + O_2	$4.5\cdot10^{-13}\cdot\exp(-(120\pm50)/T)$	(13)
17a	OIO + h·ν	$\longrightarrow$	IO + O	$\chi_{OIO}^{IO} < 0.007$	
17b		$\longrightarrow$	O_2 + I	$\chi_{OIO}^{I} < 0.15$	(6)
18a	$IONO_2$ + h·ν	$\longrightarrow$	IO + NO_2	ϵ=0.5 (assumed)	
18b		$\longrightarrow$	I + NO_3	ϵ=0.5 (assumed)	(7, 8)
19a	HOI + h·ν	$\longrightarrow$	OH + I		(9)
19b		$\longrightarrow$	H + IO		(10)
20	IO + h·ν	$\longrightarrow$	I + O		(11, 12)
21	HI + h·ν	$\longrightarrow$	I + H		(17)

Comments:
Units: unimolecular reactions, (1/s); bimolecular reactions, (cm^3/(molecule·s)); termolecular reactions (cm^6/($molecule^2$·s)); ϵ is the reaction efficiency;
(1) see *DeMore et al.* [1997];
(2) see *McFiggins et al.* [2000];
(3) For the rate reaction coefficient see *Turnipseed et al.* [1995a]. Based on results of *Turnipseed et al.* [1995b], the product yield for the channels yielding I atoms is 0.8±0.2. Conversely, the branching ratio for all channels not producing I atoms is determined to (0.14±0.04) at 298 K [*Turnipseed et al.* 1997]. This in reasonable agreement with the branching ratios (0.55±0.03) (11a), (0.20±0.02) (11c), and (0.25±0.02) (11d) reported by *Bedjanian et al.* [1997]; Combining both information then leads to branching ratios for 11b and for the sum of 11e to 11g being close to 0;
(4) According to *Gilles et al.* [1997] the reaction rate coefficient for non I atom producing channels (12a, 12c, and 12e) is $2.5(\pm 1.0) \cdot 10^{-11} \cdot \exp((260 \pm 100)/T) \cdot cm^3/sec$, and the branching ratio for the I atom producing channels are < 35% (at 298 K). They reported the following branching ratios: for 12a (0.65 to 1.0), for 12b (< 0.3), and for 12c (< 0.05), the latter being in

agreement with recent reports of *Rowley et al.* [2001] ($k_{12c}/k_{12} < 0.2$). The product channel I + OBrO (12d) is endothermic by (5.5±8.6) kcal/mol and indeed *Rowley et al.* [2001] found $k_{12d}/k_{12} < 0.15$; *Rowley et al.* [2001] found no evidence for reaction 12e. They also reported an overall reaction rate coefficient k_{12}=6.7(± 0.8) $\cdot 10^{-12}$·exp((760 ± 30)/T)·cm^3/sec in agreement with $k_{12a+12b+12c}$=8.5(±1.5)·10^{-11}·cm^3/sec) reported by *Bedjanian et al.* [1998] at 298 K;
(5) The reaction is exothermic by ΔH = (- 17.28±20) kcal/mole [*Ingham et al.* 2000]. The reaction rate coefficient is from *Allan et al.* [2001].
(6) The recently reported constrained value of the OIO cross section ($1.29\pm0.22 \geq \sigma_{OIO}\cdot 10^{17} \geq 0.87\pm0.15$) for the (5,1,0) transition at 549 nm (T=295 K, p=760 Torr) has been taken for the present study [*Rowley et al.* 2001]. *Ingham et al.* [2000] reported a minimum σ_{OIO} cross section of 2.7·$10^{-17}$$\text{cm}^2$ at 549 nm assuming that 13a has a branching ratio of 1. If the branching ratio for 13a is taken from *Bloss et al.* [2001] ($0.30 \leq k_{13a}/k_{13} \leq 0.46$), then σ_{OIO} could be as large as 9·$10^{-17}$$\text{cm}^2$ using *Ingham et al.* [2000] OIO cross section. For the quantum yield of 17a, an upper limit of 0.007 was assumed according to recent measurements at 532 nm [*Ingham et al.* 2000]. For the quantum yield of reaction 17b, an upper limit of 0.15 at 532 nm was assumed;
(7) for the yield see *Davis et al.* [1996];
(8) the recently measured $IONO_2$ cross section from the University of Cambridge/UK is used [Juliane Mössinger and Anthony Cox, private communication 2000]. For the data see *Atkinson et al.* [2000];
(9) absorption cross cross section after *Rowley et al.* [1999];
(10) private communication with A. R. Ravishankara;
(11) the strength of the IO continuum absorption between 340 nm and 440 nm and the T-dependence of the IO cross section is somewhat controversial [e.g., *Sander* 1986; *Laszlo et al.* 1995; *Harwood et al.* 1997; *Hoelscher and Zellner* 2000; *Bloss et al.* 2001]. Here, for the photochemical modelling we used the IO cross section of *Harwood et al.* [1997], when not stated otherwise;
(12) according to *Ingham et al.* [2000], the lower limit for the quantum yield is (0.91+0.19/-0.26);
(13) the reaction is exothermic by ΔH = -(43±3.79) kcal/mole [*Ingham et al.* 2000]. The same reaction rate coefficient as for OClO + OH [e.g., *DeMore et al.* 1997] is assumed;
(14) The overall rate coefficient and the branching ratios for reaction 13 are from *Bloss et al.* [2001]
(15) Following a private communication with John Crowley [2000], the recent measured rate reaction coefficient by *Knight and Crowley* [2000] has been taken, which is in agreement with the value of [*Cronhite et al.* 1999] (9.3·$10^{-12}$$\text{cm}^3$/s) measured at 298 K, and of *Canosa-Mas et al.* [1999] (7.1±1.6)·$10^{-12}$$\text{cm}^3$/s) measured at 296 K. Within the stated error, all these rate reaction coefficients are in agreement with a recent result ((6.1±1.6)·10^{-12} exp((325±72)/T) cm^3/s) of *Hoelscher and Zellner* [2000];
(16) see *Knight and Crowley* [2000];
(17) for the absorption cross section of HI see *Huebert and Martin* [1968];
(18) the reaction enthalpies for the (HI + O_2)/(H + I + O_2) channels are -33.5 kcal/mole/37.4 kcal/mole, respectively. By analogy with the ClO + OH (1.7·10^{-11} cm^3/s) and BrO + OH (7.5·10^{-11} cm^3/s) reactions, a reaction rate coefficient of 1.0·10^{-10} cm^3/s is assumed;

References

Albritton, D. L., A. L. Schmeltkopf, and R. Zare (1976). An introduction to the least-square fitting of spectroscopic data. In R. Narahari and M. W. Weldon (Eds.), *Molecular Spectroscopy: Modern Research.* Academic, Orlando, Florida.

Alicke, B., K. Hebestreit, J. Stutz, and U. Platt (1999). Iodide oxide in the marine boundary layer. *Nature,* Vol. 397, 572–573.

Allan, B. J., S. Ashworth, and J. M. C. Plane (2001). The diurnal behaviour of the OIO radical: photolysis and reaction with NO. *Geophys. Res. Lett.,* Vol. in press.

Allan, B. J., G. McFiggans, and J. M. C. Plane (2000). Observation of iodine monoxide in the remote marine boundary layer. *J. Geophys. Res.,* Vol. 105, 14363–14369.

Allan, B. J., G. McFiggans, and J. M. C. Plane (2001). Observation of OIO in the remote marine boundary layer. *Geophys. Res. Lett.,* Vol. 28, 1945–1948.

Amoruso, A., L. Crescentini, G. Fiocco, and M. Volpe (1993). New measurements of the NO_2 absorption cross section in the 440-460 nm region and estimates of the NO_2-N_2O_4 equilibrium constant. *J. Geophys. Res.,* Vol. 98, No. D9, 16857–16863.

Anderson, G., S. A. Clough, F. X. Kneizys, J. H. Chetwynd, and E. P. Shettle (1986). AFGL Atmospheric constituent profiles (0-120 km). *AFGL (OPI), Hanscom AFB, MA 01736,* Vol. AFGL-TR-86-0110.

Anderson, S. and K. Mauersberger (1992). Laser measurements of ozone absorption cross sections in the Chappuis band. *Geophys. Res. Lett.,* Vol. 19, No. 9, 933–936.

Andreae, M. O., E. Atlas, C. W. Harris, G. Helas, A. de Kock, R. Koppmann, W. Maenhaut, S. Manö, W. H. Pollock, J. Rudolph, D. Scharfe, G. Schebske, and M. Welling (1996). Methyl halide emissions from savanna fires in southern Africa. *Geophys. Res. Lett.,* Vol. 101, 23603–23614.

Andrews, D. G., J. R. Holton, and C. B. Leovy (1987). Middle atmoshere dynamics. *Academic Press, Orlando,*.

Atkinson, R., D. L. Baulch, R. A. Cox, R. F. Hampson, J. A. Kerr, M. J. Rossi, and J. Troe (2000). Evaluated kinetic and photochemical data for atmospheric chemistry: supplement III, halogen species. *J. Phys. Chem. Ref. Data,* Vol. 29, 167 – 266.

Balluch, M. and P. Haynes (1997). Quantification of lower stratsospheric intrusion. *J. Geophys. Res.,* Vol. 102, 23487–23504.

Bates, D. R. and M. Nicolet (1950). Atmospheric hydrogen. *Pup. Astron. Soc. Pacific,* Vol. 62.

Bauer, N. (1997). Charakterisierung des DOAS-Ballon-Spektrographen zur Bestimmung stratosphaerischer Spurenstoffe. *Master thesis, Institut für Umweltphysik, Universität Heidelberg,.*

Bedjanian, Y., G. Le Bras, and G. Poulet (1997). Kinetics and mechanism of the IO + ClO reaction. *J. Phys. Chem. A,* Vol. 101, 4088–4096.

Bedjanian, Y., G. LeBras, and G. Poulet (1998). Kinetics and mechanism of the IO + BrO reaction. *J. Phys. Chem. A,* Vol. 102, 10510–10511.

Blake, N. J., D. R. Blake, T. Y. Chen, J. E. Collins Jr, G. W. Sachse, B. E. Anderson, and F. S. Rowland (1997). Distribution and seasonality of selected halocarbons over the Western Pacific basin during PEM-West A and PEM-West B. *J. Geophys. Res.,* Vol. 102, 28315–28351.

Bloss, W., D. M. Rowley, R. A. Cox, and R. L. Jones (2001). Kinetics and products of the IO self reaction. *J. Phys. Chem. A.,* Vol. 105, 7840–7854.

Bösch, H., C. Camy-Peyret, M. Chipperfield, R. Fitzenberger, H. Harder, C. Schiller, M. Schneider, T. Trautmann, and K. Pfeilsticker (2001). Comparison of measured and modeled startospheric UV/visible actinic fluxes at large solar zenith angles. *Geophys. Res. Lett.,* Vol. 28, No. 7, 1179–1182.

Brasseur, G. and S. Solomon (1986). *Aeronomy of the middle atmosphere.* Dordrecht, Boston, Lancaster, Tokyo: D. Reidel Publ.

Brault, J. and H. Neckel (1987). Solar spectra. Provided by Hamburger Sternwarte distibuted through http://www.hs.uni-hamburg.de/german/forsch_int/sonnenspec.html.

Brewer, A. W. (1949). Evidence for a world circulation provided by the measurement of helium and water vapor distibution in the stratosphere. *Q. J. R. Meteorol. Soc.,* Vol. 75, 351–363.

Browell, E. V., C. F. Butler, S. Ismail, P. A. Robinette, A. F. Carter, N. S. Higdon, O. B. Toon, M. R. Schoeberl, and A. F. Tuck (1990). Airborne lidar observations in the wintertime arctic stratsophere: Polar stratospheric clouds. *Geophys. Res. Lett.,* Vol. 17, 385–388.

Brown, S. S., R. K. Talukdar, and A. R. Ravishankara (1999a). Rate constant for the reaction $OH + NO_2 + M \rightarrow HNO_3 + M$ under atmpsheric conditions. *Chem. Phys. Lett.,* Vol. 299, 277–284.

Brown, S. S., R. K. Talukdar, and A. R. Ravishankara (1999b). Reconsideration of the rate constants for the reaction of the hydroxyl radicals with nitric acid vapor. *J. Phys. Chem.,* Vol. 103, 3031–3037.

Burkholder, J. B. and R. K. Talukdar (1994). Temperature dependence of the ozone absorption spectrum over the wavelength range 410 too 760 nm. *Geophys. Res. Lett.,* Vol. 21, No. 7, 581–584.

Burrows, J. P., A. Dehn, B. Deters, S. Himmelmann, A. Richter, S. Voigt, and J. Orphal (1999). Atmospheric remote-sensing reference data from GOME: temperature-dependent absortpion cross section of ozone in the 231- 794 nm range. *J. Quant. Spectroscopy and Rad. Transfer,* Vol. 61, 509–517.

Bussemer, M. (1993). Der Ring-Effekt: Ursachen und Einfluß auf die spektroskopische Messung stratosphärischer Spurenstoffe. *Master thesis, Institut für Umweltphysik, Universität Heidelberg,.*

Callis, L. B. (2001). Stratsopheric studies consider crucial question of particle precipations. *EOS,* Vol. 82, No. 27.

Camy-Peyret, C., P. Jeseck, T. Hawat, G. Durry, G. Berubeé, L. Rochette, and D. Huguenin (1995). The LPMA balloon borne FTIR spectrometer for remote sensing of the atmospheric constituents. In *12th ESA Symposium on Rocket and Balloon Programmes and Related Research.*

Camy-Peyret, C., P. Jeseck, S. Payan, T. Hawat, G. Durry, and J.-M. Flaud (1995). Comparison of CH_4 and N_2O profiles at high and mid-latitudes using the LPMA balloon borne Fourier Tranform instrument. In *Air Pollution Research Report, Polar Stratospheric Ozone Symposium, Schliersee.*

Camy-Peyret, C. Payan, S., P. Jeseck, Y. Té, T. Hawat, K. Pfeilsticker, H. Harder, R. Fitzenberger, and H. Bösch (1999). Recent results obtained with the LPMA and DOAS balloon-borne instruments during the ILAS, SABINE and THESEO campaigns. In *14th ESA Symposium on Rocket and Balloon Programmes and Related Research.*

Canosa-Mas, C. E., M. L. Flugge, A. Shah, D. andVipond, and R. P. Wayne (1999). Kinetics of the reaction of IO with HO_2 and $O(^3P)$. *J. Atmos. Chem.,* Vol. 34, 134–162.

Carlotti, M. (1988). Global fit approach to the analysis of limb-scanning atmospheric measurements. *Appl. Opt.,* Vol. 27, 3250–3254.

Carpenter, L., W. Sturges, S. A. Penkett, P. Liss, B. Alicke, K. Hebestreit, and U. Platt (1999). Short-lived alkyl iodides and bromides at Mace Head, Ireland: links to biogenic sources and halogen oxide production. *J. Geophys. Res.,* Vol. 104, 1679–1689.

Carslaw, K. S., J. T. Peter, T. Bacmeister, and S. D. Eckermann (1999). Widespread solid particle formation by mountain waves in the Arctic stratosphere. *J. Geophys. Res.,* Vol. 104, 1827–1836.

Carslaw, K. S., M. Wirth, A. Tsias, B. P. Luo, A. Dörnbrack, M. Leutbecher, H. Volkert, W. Renger, J. T. Bacmeister, E. Reimer, and T. Peter (1998). Increased stratospheric ozone depletion due to mountain-induced atmospheric waves. *Nature,* Vol. 391, 675–678.

Chapman, S. (1930). On ozone and atomic oxygen in the upper atmosphere. *Phil. Mag.,* Vol. 10.

Chipperfield, M. P. (1999). Multiannual simulations with a three-dimensional chemical transport model. *J. Geophys. Res.,* Vol. 104, No. D1, 1781–1805.

Chipperfield, M. P. and J. A. Pyle (1998). Model sensitivity studies of arctic ozone depletion. *J. Geophys. Res.,* Vol. 103, No. D21, 28389–28403.

Coffey, M. T., W. G. Mankin, and A. Goldman (1981). Simultaneous spectroscopic determination of the latitudinal, seasonal and diurnal variability of stratopsheric N_2O, NO, NO_2 and HNO_3. *J. Geophys. Res.,* Vol. 86, 7331–7341.

Cordero, E. C. and S. R. Kawa (2001). Ozone and tracer transport variations in the summer northern hemisphere stratosphere. *J. Geophys. Res.,* Vol. 106, No. D11, 12227–12239.

Cornu, A. (1879). Observation de la limit ultraviolett du spectre solaire a diverse altitudes. *C. R. Acad. Sci.,* Vol. 89, No. 808.

Cox, R. A., W. J. Bloss, and R. L. Jones (1999). OIO and the atmospheric cycle of iodine. *Geophys. Res. Lett.,* Vol. 26, No. 13, 1857–1860.

Coy, L., E. R. Nash, and P. A. Newman (1997). Meteorology of the polar vortex: spirng 1997. *Geophys. Res. Lett.,* Vol. 24, No. 22, 2693–2697.

Cronhite, J., R. Stickel, J. M. Nicovich, and P. H. Wine (1999). Laser flash photolysis studies of radical-radical reaction kinetics: HO_2 + IO reaction. *J. Phys. Chem.,* Vol. 103, 3228–3236.

Crutzen, P. J. (1970). The influence of nitrogen oxides on the atmospheric ozone content. *Quart. J. Met. Soc.,* Vol. 96.

Crutzen, P. J. and F. Arnold (1986). Nitric acid cloud formation in the cold Antarctic stratosphere: a major cause for the springtime ozone hole. *Nature,* Vol. 324, 651–655.

Dahlback, A. and K. Stamnes (1991). A new spherical model for computing the radiation field available for photolysis and heating at twilight. *Planet. Space Sci.,* Vol. 39, 671–683.

David, C., S. Bekki, S. Godin, G. Mégie, and M. P. Chipperfield (1998). Polar stratospheric clouds climatology over Dumont d'Urville between 1989 and 1993 and the influence of volcanic aerosols on their formation. *J. Geophys. Res.,* Vol. 103, 22163–22180.

Davidson, J. A., C. A. Cantrell, A. H. McDaniel, R. E. Shetter, S. Madronich, and J. G. Calvert (1988). Visible-ultraviolet absorption cross section for NO_2 as a function of temperature. *J. Geophys. Res.,* Vol. 93, No. D6, 7105–7112.

Davis, D., J. Crawford, S. Liu, S. McKeen, A. Bandy, D. Thornton, F. Rowland, and D. Blake (1996). Potential impact of iodine on tropospheric levels of ozone and other critical oxidants. *J. Geophys. Res.,* Vol. 101, 2135–2147.

Delbrück, M. (1992). Berechnung von stratosphärischen Spurenstoffprofilen aus der Spektroskopie von im Zenit gestreuten Sonnenlicht. *Master thesis, Institut für Umweltphysik, Universität Heidelberg,.*

DeMore, W. B., S. P. Sander, D. M. Golden, R. F. Hampson, M. J. Kurylo, C. J. Howard, A. R. Ravishankara, C. E. Kolb, and M. J. Molina (1997). Chemical kinetics and photochemical data for use in statospheric modeling. *Technical Report, NASA/JPL Publication,* , No. 97-4.

Denis, L., J. P. Pommereau, F. Lefè're, F. Goutail, B. Knudsen, and G. Letrenne (2000). Ozone loss and NO_2 recovery in the Arctic winter and spring of 1997 as observed from long duration balloon flights in the vortex. In *Stratospheric Ozone, Proceedings of the fifth European Symposium, St. Jean de Luz, France.*

Dobson, G. M. B. (1956). Origin and distribution of the polyatomic molecules in the atmosphere. *Proc. R. Soc. London A,* Vol. 236, 187–193.

Dvortsov, V., M. A. Geller, S. Solomon, S. M. Schauffler, E. L. Atlas, and D. R. Blake (1999). Rethinking reactive halogen budget in the midlatitude stratosphere. *Geophys. Res. Lett.,* Vol. 26, No. 12, 1699–1702.

EC-Report (2001). European Research in the stratsosphere 1996-2000. Scientific Assessment of the European Commission.

EN-SCI Corporation, Boulder, Colorado, USA (1997). *EN-SCI Corporation Model 4Z ECC-O_3-sondes.* EN-SCI Corporation, Boulder, Colorado, USA. Instruction Manual.

Engel, A., U. Schmitt, W. B. Sturges, S. Penkett, K. Pfeilsticker, U. Platt, F. Stroh, C. Schiller, R. Müller, D. McKenna, J. Ovarlez, C. Camy.Peyret, M. Pirre, and J. B. Renard (2000). Final Report: HALOMAX-Mid and high latitude stratospheric distribution of long and short lived halogen species during the maximum of the chlorine loading. *CEC-Contract,* Vol. ENV4-CT97-0524.

EORCU (1998). The northern hemisphere stratosphere in the winter 1997/1998. *Preliminary report,.*

EORCU (1999). The northern hemisphere stratosphere in the winter of 1998/1999. *Preliminary report,.*

EORCU (2000). The northern hemisphere stratosphere in the winter and spring of 1999/2000. *Preliminary report,.*

Erle, F. (1999). Untersuchungen zur Halogenaktivierung der winterlichen Stratospäre anhand flugzeuggestützter spektroskopischer Messungen. *Ph. D. thesis, Institut für Umweltphysik, Universität Heidelberg,.*

Erle, F., A. Grendel, D. Perner, U. Platt, and K. Pfeilsticker (1998). Evidence of heterogenous bromine chemistry on cold stratospheric sulphate aerosols. *Geophys. Res. Lett.,* Vol. 25, 4329–4332.

ESA Publication Division (1995). *GOME User Manual.* ESTEC, Noordwijk, The Netherlands: ESA Publication Division. SP-1182.

Fahey, D. W., R. S. Gao, K. S. Carslaw, J. Kettleborough, P. J. Popp, M. J. Northway, J. C. Holece, S. C. Ciciora, R. J. McLaughlin, T. L. Thompson, R. H. Winkler, D. G. Baumgardner, B. Gandrun, P. O. Wennberg, S. Dhaniyala, K. McKinney, T. Peter, R. J. Salawitch, T. P. Bui, J. W. Elkins, C. R. Webster, E. L. Atlas, H. Jost, J. C. Wilson, R. L. Herman, A. Kleinböhl, and M. von König (2000). The detection of large HNO_3-containing particles in the winter Arctic stratosphere. *Science,* Vol. 291.

Fahey, D. W., K. K. Kelly, S. R. Kawa, A. F. Tuck, M. Loewenstein, K. R. Chen, and L. E. Heidt (1990). Observations of denitrification and dehydration in in the winter polar stratosphere. *Nature,* Vol. 344, 321–324.

Fahey, D. W. and A. R. Ravishankara (1999). Summer in the stratosphere. *Science,* Vol. 285, 208–210.

Farman, J. C., B. G. Gardiner, and J. D. Shanklin (1985). Large losses of total ozone in Antarctica reveal seasonal ClO_x/NO_x interaction. *Nature,* Vol. 315, 207–210.

Ferlemann, F. (1998). Ballongestützte Messung stratosphärischer Spurenstoffe mit differentieller optischer Absorptionsspektroskopie. *Ph. D. thesis, Institut für Umweltphysik, Universität Heidelberg,.*

Ferlemann, F., N. Bauer, R. Fitzenberger, H. Harder, H. Osterkamp, D. Perner, U. Platt, M. Scheider, P. Vradelis, and K. Pfeilsticker (2000). A new DOAS-instrument for stratospheric balloon-borne trace gas studies. *Appl. Opt.,* Vol. 39, 2377–2386.

Ferlemann, F., C. Camy-Peyret, R. Fitzenberger, H. Harder, T. Hawat, H. Osterkamp, M. Schneider, D. Perner, U. Platt, P. Vradelis, and K. Pfeilsticker (1998). Stratospheric BrO profiles measured at different latitudes and seasons: Instrument description, spectral analysis and profile retrieval. *Geophys. Res. Lett.,* Vol. 25, No. 20, 3847–3850.

Feynman, R. B., R. B. Leighton, and M. Sand (1965). *The Feynamn lectures on physics.* Reading, Palo Alto, London: Addison-Wesley Publishing Company Inc.

Fish, D. J. and R. L. Jones (1995). Rotational Raman scattering and the Ring effect in zenith-sky spectra. *Geophys. Res. Lett.,* Vol. 22, No. 7, 811–814.

Fitzenberger, R. (2000). Investigation of the stratospheric inorganic bromine budget for 1996-2000: Ballon-borne measurements and model comparison. *Ph. D. thesis, Institut für Umweltphysik, Universität Heidelberg,.*

Fitzenberger, R., H. Bösch, C. Camy-Peyret, M. Chpperfield, H. Harder, U. Platt, J. Pyle, T. Wagner, and K. Pfeilsticker (2000). First profile measurement of troposheric BrO. *Geophys. Res. Lett.,* Vol. 27, 2921–2924.

Fraser, P. J., D. E. Oram, C. E. Reeves, and S. A. Penkett (1999). Southern hemisphere halon trends (1987-1998) and global halon emissions. *J. Geophys. Res.,.*

Frieß, U. (2000). Spectroscopic measurements of atmospheric trace gases at Neumayer-Station, Antarctica. *Ph. D. thesis, Institut für Umweltphysik, Universität Heidelberg,.*

Frieß, U., C. M. Chipperfield, C. Otten, U. Platt, J. Pyle, T. Wagner, and K. Pfeilsticker (1999). Intercomparison of measured and modelled BrO slant column amounts for the Arctic winter and spring 1994/95. *Geophys. Res. Lett.,* Vol. 26, 1861–1864.

Frieß, U., T. Wagner, I. Pundt, K. Pfeilsticker, and U. Platt (2001). Spectroscopic measurement of tropospheric iodine oxide at Neumayer Station, Antarctica. *Geophys. Res. Lett.,* Vol. 28, 1941–1944.

Funk, O. (2000). Photon pathlengths distributions for cloudy skies - Oxygen A-band measurements and radiative transfer model calculations. *Ph. D. thesis, Institut für Umweltphysik, Universität Heidelberg,.*

Gao, R. S., D. W. Fahey, L. A. Del Negro, S. G. Donnelly, E. R. Keim, L. Teveroski, P. O. wennberg, T. F. Hanisco, M. H. Proffitt, J. J. Margitan, J. C. Wilson, J. W. Elkins, R. M. Stimpfle, R. C. Cohen, C. T. McElroy, T. P. Bui, R. J. Salawitch, S. S. Brown, A. R. Ravishankara, R. W. Portmannn, M. K. W. Ko, D. K. Weisenstein, and P. A. Newman (1999). A comparison of observations and model simulations of NO_x/NO_y in the lower statosphre. *Geophys. Res. Lett.,* Vol. 26, 1153–1156.

Garcia, R. R. and S. Solomon (1994). A new numerical model of the middle stratosphere: 2. ozone and related species. *J. Geophys. Res.,* Vol. 99, No. D6, 12937–12951.

Gill, M., O. Puentedura, M. Yela, and E. Cuevas (2000). Behaviour of NO_2 and O_3 columns during the eclipse of February 26, 1998, as measured by visible spectroscopy. *J. Geophys. Res.,* Vol. 105, No. D3, 3583–3593.

Gilles, M. K., A. A. Turnipseed, J. B. Burkholder, A. R. Ravishankara, and S. Solomon (1997). Kinetics of the IO radical. 2. reaction of IO with BrO. *J. Phys. Chem. A,* Vol. 101, 5526–5534.

Gomer, T., F. Brauers, F. Heintz, J. Stutz, and U. Platt (1995). MFC, User Manual, Version 1.98. *Institut für Umweltphysik, Universität Heidelberg,.*

Goutail, F., J. P. Pommereau, and F. Lefèvre (2000). Winter ozone loss in the Arctic and at mid-latitudes in 1998 and 1999 from the SAOZ ground-based network and balloon measurements. In *Stratsopheric ozone 1999. Proceedings of the fifth Eurpoean symposium. Air pollution research report 73*, pp. 433–436.

Grainger, J. F. and J. Ring (1962). Anomalous Fraunhofer line profiles. *Nature,* Vol. 193, No. 762.

Greenblatt, G. D., J. J. Orlando, J. B. Burkholder, and A. R. Ravishankara (1990). Absorption measurements of oxygen between 330 and 1140 nm. *J. Geophys. Res.,* Vol. 95, No. D11, 18577–18582.

Hansen, D. R. and K. Mauersberger (1988). The vapour pressur of HNO_3-H_2O solutions. *J. Phys. Chem.,* Vol. 92, 6167–6170.

Harder, H. (1999). Messung und Modellierung stratosphärischer Spurenstoffprofile zur Abschätzung des anorgansichen Gesamt-Brom-Budgets. *Ph. D. thesis, Institut für Umweltphysik, Universität Heidelberg,*.

Harder, H., H. Bösch, C. Camy-Peyret, M. Chpperfield, R. Fitzenberger, S. Payan, D. Perner, U. Platt, B.-M. Sinnhuber, and K. Pfeilsticker (2000). Comparison of measured and modeled Stratospheric BrO: implications for the total amount of stratospheric bromine. *Geophys. Res. Lett.,* Vol. 27, No. 22, 3695–3698.

Harder, H., C. Camy-Peyret, F. Ferlemann, R. Fitzenberger, T. Hawat, H. Osterkamp, M. Schneider, D. Perner, U. Platt, P. Vradelis, and K. Pfeilsticker (1998). Stratospheric BrO profiles measured at different latitudes and seasons: atmospheric observations. *Geophys. Res. Lett.,* Vol. 25, No. 20, 3843–3846.

Harder, J. W., J. W. Brault, P. V. Johnston, and G. H. Mount (1997). Temperature dependent NO_2 cross sections at high spectral resolution. *J. Geophys. Res.,* Vol. 102, No. D3, 3861–3879.

Hartley, W. N. (1880). On the probable absorption of solar radiation by atmospheric ozone. *Chem. News,* Vol. 42, No. 268.

Harwood, M. H., J. B. Burkholder, M. Hunter, R. W. Fox, and A. R. Ravishankara (1997). Absorption cross sections and self-reaction kinetics of the IO radical. *J. Phys. Chem. A,* Vol. 101, 853–863.

Harwood, M. H. and R. Jones (1994). Temperature dependent ultraviolet-visible absorption cross sections of NO_2 and N_2O_4: low temperature measurements of the equilibrium constant for $2\ NO_2 \longleftrightarrow N_2O_4$. *J. Geophys. Res.,* Vol. 99, No. D11, 22955–22964.

Haug, H. (1996). Raman-Streuung von Sonnenlicht in der Erdatmosphäre. *Master thesis, Institut für Umweltphysik, Universität Heidelberg,*.

Hausmann, M., U. Brandenburger, T. Brauers, and H. P. Dorn (1997). Detection of tropospheric OH radicals by long-path differential-optical-absorption sepctroscopy: experimental setup, accuracy and precision. *J. Geophys. Res.,* Vol. 102, No. D13, 16011–16022.

Hausmann, M., U. Brandenburger, T. Brauers, and H. P. Dorn (1999). Simple Monte Carlo methods to estimate the spectral evaluation error in differential-optical-absortion-spectroscopy. *Appl. Opt.,* Vol. 38, No. 3, 462–475.

Hawat, T., C. Camy-Peyret, P. Jeseck, and R. Torguet (1995). Desciption and performance of a balloon-borne heliostat for solar absorption measurements. In *12th ESA Symposium on Rocket and Balloon Programmes and Related Research.*

Hebestreit, K. (2001). Halogen oxides in the mid-latitude planetary boundary layer. *Ph. D. thesis, Institut für Umweltphysik, Universität Heidelberg,.*

Hervig, M. and T. Deshler (2001). Evaluation of aerosol measurements from SAGE II, HALOE, and balloonborne optical particle counters. *J. Geophys. Res.,*, in press.

Himmelmann, S., J. Orphal, H. Bovensmann, A. Richter, A. Ladstätter-Weissenmayer, and J. P. Borrows (1996). First observation of the OIO molecule by time-resolved flash photolysis absorption spectroscopy. *Chem. Phys. Lett.,* Vol. 251, 330–334.

Hoelscher, D. and R. Zellner (2000). Absorption cross section of the IO radical and kinectics of the IO + IO and IO + NO reactions. In *Stratospheric Ozone, Proceedings of the fifth European Symposium, St. Jean de Luz, France.*

Hoffmann, D. J., S. J. Oltmans, J. M. Harris, B. J. Johnson, and J. A. Lathrop (1997). Ten years of ozonesonde measurements at the south pole: implications for recovery of springtime Antarctic ozone. *J. Geophys. Res.,* Vol. 102, 8931–8943.

Hoffmann, T., C. D. O'Dowd, and J. H. Seinfeld (2001). Iodine oxides homogeneous nucleation: an explanation for coastal new particle production. *Geophys. Res. Lett.,* Vol. 28, No. 10, 1949–1952.

Hönninger, G. (1999). Referenzspektren reaktiver Halogenverbindungen für DOAS Messungen. *Master thesis, Institut für Umweltphysik, Universität Heidelberg,.*

Huebert, B. and R. M. Martin (1968). Gas-phase far UV absorption spectrum of HBr and HI. *J. Phys. Chem.,* Vol. 72, 3046–3048.

Huppert, R. (2000). Theoretische und experimentelle Untersuchungen zum solaren I_0-Effekt. *Master thesis, Institut für Umweltphysik, Universität Heidelberg,.*

Ingham, T., M. Cameron, and J. N. Crowley (2000). Photodissociation of IO (355 nm) and OIO (532 nm): Quantum yields for $O(^3P)$ and $I(^3P)$ production. *J. Phys. Chem. A,* Vol. 104, 8001–8010.

Jackman, C. H., E. L. Fleming, and F. M. Vitt (2000). Influence of extremely large solar proton events in a changing stratosphere. *J. Geophys. Res.,* Vol. 105, No. D9, 11659–11670.

Jackman, C. H., R. D. McPeters, G. J. Labow, E. L. Fleming, C. J. Praderas, and J. M. Russell (2001). Northern hemisphere atmospheric effects due to the July 2000 solar proton event. *Geophys. Res. Lett.,* Vol. 28, No. 15, 2883–2886.

Johnston, H. S. (1971). Reduction of stratosperic ozone by nitrogen oxide catalysts from supersonic transport exhaust. *Science,* Vol. 173.

Johnston, P. V. (1997). Making UV/vis cross sections, reference Fraunhofer and synthetic spectra. unpuplished.

Jucks, K. W., D. G. Johnson, K. V. Chance, W. A. Traub, and R. Salawitch (1999). Nitric acid in the middle stratosphere as a function of altitude an aerosol loading. *J. Geophys. Res.,* Vol. 104, No. D21, 26715–26723.

Junge, C. E. (1961). Vertical profiles of condensation nuclei in the stratosphere. *J. Meterol,* Vol. 18, 501–509.

Junkermann, W., U. Platt, and A. Volz-Thomas (1989). A photoelectric detector for the measurement of the photolysis frequencies of ozone and other molecules. *J. Atmos. Chem.,* Vol. 8, 203–227.

Keim, E. R., M. Loewenstein, J. R. Podolske, D. W. Fahey, R. S. Gao, E. L. Woodbridge, R. C. Wamsley, S. G. Donnelly, L. A. DelNegro, C. D. Nevison, S. Solomon, K. H. Rosenlof, C. J. Scott, M. K. W. Ko, D. Weisenstein, and K. R. Chan (1997). Measurements of the NO_y - N_2O correlation in the lower stratosphere: latitudinal and seasonal canges and model comparison. *J. Geophys. Res.,* Vol. 102, No. D11, 13193–13212.

Kirmse, B., A. Delon, and R. Jost (1997). NO_2 absorption cross section and its temperature dependence. *J. Geophys. Res.,* Vol. 102, No. D13, 16089–16098.

Knight, G. P. and J. N. Crowley (2000). The reactions of IO with HO_2, NO, and CH_3SCH_3. *J. Phys. Chem.,* Vol. submitted.

Ko, M., N. Sze, C. Scott, and D. Weissenstein (1997). On the relation between chlorine/bromine loading and short-lived tropospheric source gases. *J. Geophys. Res.,*.

Komminga, H. S., S. Voigt, J. Orphal, and J. P. Burrows (1999). UV-visible FT spectra of OClO at atmospheric temperatures. In *Proceedings of the 1st European Symposium on atmospheric measurements from space, ESA special puplication.*

Kondo, Y., H. Irie, M. Koike, and G. E. Bodeker (2000). Denitrification and nitrification in the Arctic stratosphere during the winter of 1996/1997. *Geophys. Res. Lett.,* Vol. 27, No. 3, 337–340.

Kondo, Y., M. Koike, A. Engel, U. Schmidt, M. Mueller, T. Sugita, H. Kanzawa, T. Nakazawa, S. Aoki, N. Irie, H. Toriyama, T. Suzuki, and Y. Sasano (1999). NO_y-N_2O correlation observed inside the Arctic vortex in February 1997: dynamical and chemical effects. *J. Geophys. Res.,* Vol. 104, No. D7, 8215–8224.

Kondo, Y., U. Schmidt, T. Sugita, P. Aimedieu, M. Koike, H. Ziereis, and Y. Iwasaka (1994). Total reactive nitrogen, N_2O, and ozone in the winter Arctic stratosphere. *Geophys. Res. Lett.,* Vol. 21, No. 13, 1247–1250.

Kondo, Y., U. Schmidt, T. Sugita, A. Engel, M. Koike, P. Aimedieu, M. R. Gunson, and J. Rodriguez (1996). NO_y correlation with N_2O and CH_4 in the midlatitude stratosphere. *Geophys. Res. Lett.,* Vol. 23, No. 17, 2369–2372.

Kondo, Y., T. Sugita, M. Koike, S. R. Kawa, M. Y. Danilin, J. M. Rodriguez, S. Spreng, K. Golinger, and F. Arnold (2000). Partitioning o freactive nitrogen in the midlatitude lower stratosphere. *J. Geophys. Res.,* Vol. 105, No. D1, 1417–1424.

Kouker, W. (1995). The Karlsruhe simulation of the middle atmosphere (KASIMA). *Wiss. Ber., Forschungszentrum Karlsruhe,* Vol. 5653.

Kreher, K., G. E. Bodeker, H. Kanzawa, H. Nakane, and Y. Sasano (1999). Ozone and temperature profiles measured above Kiruna inside, at the edge of, and outside the Arctic polar vortex in February and March 1997. *J. Geophys. Res.,* Vol. 26, No. 6, 715–718.

Kubo, Y. (1980). *Rep. of Hydrographic Res.,* Vol. 15.

Kurucz, R. L., I. Furenlid, J. Brault, and L. Testerman (1984). Solar flux atlas from 296 to 1300 nm. National Solar Observatory, Sunspot, New Mexico, U.S.A.

Kylling, A. and K. Stamnes (1992). Efficient yet accurate solution of the linear transport equation in the presence of internal sources: the exponential-linear approximation. *J. Comp. Phys.,* Vol. 102, 265–276.

Labitzke, K. (1999). Die Stratosphäre. *Springer-Verlag, Berlin, Heidelberg, Tokyo,.*

Lary, D. J., A. M. Lee, R. Toumi, M. J. Newchurch, M. Pierre, and J. B. Renard (1997). Carbon aerosols and atmospheric chemistry. *J. Geophys. Res.,* Vol. 102, 3671–3682.

Lary, D. J. and J. A. Pyle (1991). Diffuse radiation, twilight and photochemistry. *J. Atmos. Chem.,*, 373–392.

Laszlo, B., J. Kurylo, and R. E. Huie (1995). Absorption cross sections, kinetics of formation and self-reaction of the IO radical produced via the laser photolysis of $N_2O/I_2/N_2$ mixtures. *J. Phys. Chem.,* Vol. 99, 11701–11707.

Lefèvre, F., G. P. Brasseur, I. Folkins, A. K. Smith, and P. Simon (1994). Chemistry of the 1991-1992 stratospheric winter: Three-dimensional model simulations. *J. Geophys. Res.,* Vol. 99, No. D4, 8183–8195.

Lefèvre, F., F. Figarol, K. S. Carslaw, and T. Peter (1998). The 1997 Arctic ozone depletion quantified from three-dimensional model simulations. *Geophys. Res. Lett.,* Vol. 23, No. 13, 2425–2428.

Loewenstein, M., J. R. Podolske, D. W. Fahey, E. L. Woodbridge, P. Tin, A. Weaver, P. A. Newman, S. E. Strahan, S. R. Kawa, M. R. Schoeberl, and L. R. Lait (1993). New observations of the NO_y/N_2O correlation in the lower stratosphere. *Science,* Vol. 283.

Lucke, R. L. (1999). The Polar Ozone and Aerosol Measurement (POAM) instrument and early validation results. *J. Geophys. Res.,* Vol. 104, 18785–18799.

Luderer, G. (2001). Simulated annealing zur Berechnung von Spurenstoffprofilen aus Direktlichtmessungen. *Internal paper, Institut für Umweltphysik, Universität Heidelberg,.*

Lumpe, J. D., M. Fromm, K. Hopperl, R. M. Bevilacqua, C. E. Randall, E. V. Browell, W. B. Grant, T. McGee, J. Burris, L. Twigg, E. C. Richard, G. C. Toon, J. J. Margitan, B. Sen, H. Boesch, R. Fitzenberger, K. Pfeilsticker, F. Goutail, and J.-P. Pommereau (2001). Comparison of POAM III ozone measurements with correlative aircraft and balloon data during SOLVE. *J. Geophys. Res.,* Vol. submitted.

Madronich, S. (1987). Photodissociation in the atmosphere, 1. Actinic flux and the effect of ground reflections and clouds. *J. Geophys. Res.,* Vol. 92, 9740–9752.

Manney, G. L., L. Froidevaux, M. L. Santee, R. W. Zurek, and J. W. Waters (1997). MLS observations of Arctic ozone loss in 1996-1997. *Geophys. Res. Lett.,* Vol. 24, No. 22, 2697–2700.

Mauldin III, L. E., N. H. Zaun, M. P. McCormick, J. H. Guy, and W. R. Vaughn (1985). Stratospheric Aerosol and Gas Experiment instrument: a functional description. *Opt. Eng.,* Vol. 24, 307–312.

McCormick, M. P., H. M. Steele, P. Hamill, W. P. Chu, and T. J. Swissler (1982). Polar stratospheric cloud sightings by SAM II. *J. Atmos. Sci.,* Vol. 39, 1387–1397.

McElroy, M. B., R. J. Salawitch, S. C. Wofsy, and J. A. Logan (1986). Reductions of Antarctic ozone due to synergetic interactions of chlorine and bromine. *Nature,* Vol. 321, 759–762.

McFiggins, G., J. M. Plane, B. J. Allan, and L. J. Carpenter (2000). A modeling study of iodine chemistry in the marine boundary layer. *J. Geophys. Res.,* Vol. 105, No. D11, 14371–14385.

Meier, R., D. Anderson, and M. Nicolet (1982). Radiation field in the troposphere and stratosphere from 240 nm - 1000 nm, General Analysis. *Planet. Space Sci.,* Vol. 30, No. 9, 923–933.

Merienne, M. F., A. Janouvrier, and B. Coquart (1995). The NO_2 absorption spectrum, 1. Absorption cross section at ambient temperature in the 300-500 nm region. *J. Atmos. Chem.,* Vol. 20.

Michelson, H. A., G. L. Manney, M. R. Gunson, and R. Zander (1998). Correlations of stratospheric abundances of NO_y, O_3, N_2O and CH_4 derived from ATMOS measurements. *J. Geophys. Res.,* Vol. 103, No. D21, 28347–28359.

Milankovitch, M. (1920). Théorie mathématique des phénomènes thermique prodult par la radiation solaire. *Gauthier-Villars, Paris,*.

Misra, A. and P. Marshall (1998). Computational investigation of iodine oxides. *J. Phys. Chem. A,* Vol. 102, 9056–9060.

Molina, L. T. and M. J. Molina (1986). Absolute absorption cross sections of ozone in the 185 to 350 nm wavelength range. *J. Geophys. Res.,* Vol. 91, 14501–14508.

Molina, L. T. and M. J. Molina (1987). Production of Cl_2O_2 from the self-reaction of the ClO radical. *J. Phys. Chem.,* Vol. 91, 433–436.

Molina, M. J. and F. S. Rowland (1974). Stratospheric sink for chlororflourmethanes: chlorine atom-catalysed destruction of ozone. *Nature,* Vol. 249, 810–812.

Mueller, R. Crutzen, P. J., J.-U. Grooß, C. Brühl, J. M. Russel III, and A. F. Tuck (1996). Chlorine activation and ozone depletion in the Arctic vortex: observations by the Halogen Occultation Experiment in the Upper Atmosphere Research Satellite. *J. Geophys. Res.,* Vol. 101, 12531–12554.

Müller, M., A. Engel, and U. Schmidt (2000). Structure of vertical profiles of long-lived trace gases: a basis for the analysis of stratsopheric dynamics. In *Stratospheric Ozone, Proceedings of the fifth European Symposium, St. Jean de Luz, France.*

Murphy, D. M. and D. S. Thompson (2000). Halogen ions and NO^+ in the mass spectra of aerosols in the upper troposphere and lower stratosphere. *Geophys. Res. Lett.,* Vol. 27, 3217–3220.

Murphy, D. M., D. S. Thompson, and M. J. Mahoney (1998). In situ measurements of organics, meteoric material, mercury and other elements in aerosol at 5 to 19 kilometers. *Science,* Vol. 282, 1664–1669.

Murphy, D. M., D. S. Thompson, and A. Middlebrock (1997). Bromine, iodine, and chlorine in single aerosol particles at Cap Grim. *Geophys. Res. Lett.,* Vol. 24, 3197–3200.

Nash, E. R., P. A. Newman, J. E. Rosenfield, and M. R. Schoeberl (1996). An objective determination of the polar vortex using Ertel's potential vorticity. *J. Geophys. Res.,* Vol. 101, No. D5, 9471–9478.

Naujokat, B., R. Alfier, P. Braesicke, T. Kubitz, R. Lenschow, M. Prechtl, B. Rajewski, E. Reimer, and R.-C. Wohlfart (1996). Meteorologische Daten für CHORUS-Ballon, León/Spain. *Institut für Meteorologie, Freie Universität Berlin,*.

Naujokat, B., K. Labitzke, R. Lenschow, B. Rajewski, and R.-C. Wohlfart (1999). The stratospheric winter 1998/1999. *Beilage zur Berliner Wetterkarte,.*

Naujokat, B., K. Labitzke, R. Lenschow, and R.-C. Wohlfart (1999). The stratospheric winter 1999/2000. *Beilage zur Berliner Wetterkarte,.*

Naujokat, B., K. Petzold, K. Labitzke, R. Lenschow, B. Rajewski, M. Wiesner, and R.-C. Wohlfart (1999). The stratospheric winter 1996/1997. *Beilage zur Berliner Wetterkarte,.*

Naujokat, B., K. Petzold, K. Labitzke, R. Lenschow, B. Rajewski, and R.-C. Wohlfart (1999). The stratospheric winter 1997/1998. *Beilage zur Berliner Wetterkarte,.*

Newman, P., J. G. Gleason, R. D. McPeters, and R. S. Solarski (1997). Anomalously low ozone over the Arctic. *Geophys. Res. Lett.,* Vol. 24, 2689–2692.

Nicolet, M. (1975). On the production of nitric oxide by cosmic rays in the mesosphere and stratosphere. *Planet. Space Sci.,* Vol. 23, 637–649.

Nicolet, M. (1984). On the molecular scattering in the terrestrial atmosphere: An empirical formula for its calculation in the homosphere. *Planet. Space Sci.,* Vol. 32, 1467–1486.

Nicolet, M., R. Meier, and D. E. Anderson (1982). Radiation field in the troposphere and stratosphere from 240 nm - 1000 nm, numerical analysis. *Planet. Space Sci.,* Vol. 30, No. 9, 935–941.

NOAA-S/T76-1562 (1976). *US Standard Atmosphere.* NOAA-S/T76-1562. Supplement Document, US Printing Documents, Washington DC.

Noxon, J. F. (1979). Stratospheric NO_2: global behaviour. *J. Geophys. Res.,* Vol. 84.

Osterkamp, H. (1997). Messung von atmophärischen O_4-Profilen. *Master thesis, Institut für Umweltphysik, Universität Heidelberg,.*

Ostermann, G. B., G. C. Sen, R. J. Salawitch, J. J. Margitan, J.-F. Blavier, D. W. Fahey, and R. S. Gao (1999). Partitioning of NO_y species in the summer Arctic stratosphere. *Geophys. Res. Lett.,* Vol. 26, No. 8, 1157–1160.

Otten, C. (1997). Messung stratosphärischer Spurenstoffe in den Wintern 1992/93 bis 1994/95 über Kiruna in Nordschweden. *Ph. D. thesis, Institut für Umweltphysik, Universität Heidelberg,.*

Palmer, A. S., T. D. van Ommen, M. A. J. Curran, and V. Morgan (2001). Ice-core evidence for a small solar-source of atmospheric nitrate. *Geophys. Res. Lett.,* Vol. 28, No. 10, 1953–1956.

Pawson, S. and B. Naujokat (1999). The cold winters of the middle 1990s in the northern lower stratosphere. *J. Geophys. Res.,* Vol. 104, No. D12, 14209–14222.

Payan, S., C. Camy-Peyret, P. Jeseck, T. Hawat, G. Durry, and F. Lefèvre (1998). First direct simultaneous HCl and $CLONO_2$ profile measurements in the artic vortex. *Geophys. Res. Lett.,* Vol. 25, No. 14, 2663–2666.

Payan, S., C. Camy-Peyret, P. Jeseck, T. Hawat, M. Pirre, J.-B. Renard, C. Robert, F. Lefèvre, H. Kanzawa, and Y. Sasano (1999). Diurnal and nocturnal distribution of stratospheric NO_2 from solar and stellar occultation measurements in the arctic vortex: comparison with models and ILAS satellite measurements. *J. Geophys. Res.,* Vol. 104, No. D17, 21585–21593.

Payan, S., C. Camy-Peyret, P. Jeseck, Y. Té, M. Pirre, J. B. Renard, F. Lefèvre, F. Stroh, T. Woyke, B. Vogel, K. Pfeilsticker, R. Fitzenberger, H. Bösch, and F. Goffinont-Taupin (2000). HALOMAX results on reservoir and acitve chlorine species: balloon measurements and comparison with 3-D chemical transport model. In *Stratospheric Ozone, Proceedings of the fifth European Symposium, St. Jean de Luz, France.*

Penndorf, R. (1957). Tables of the refractive index for standard air and the Rayleigh scattering coefficient for the spectral region between 0.2 and 200 μ and their application to atmospheric optics. *J.Opt. Soc. Am.,* Vol. 47, No. 2, 176–182.

Perlinski, L. M. and S. Solomon (1993). On the evaluation of air mass factors for atmospheric near-ultraviolett and visible absorption spectroscopy. *J. Geophys. Res.,* Vol. 98, No. D6, 10363–10374.

Pfeilsticker, K., H. Bösch, C. Camy-Peyret, R. Fitzenberger, H. Harder, and H. Osterkamp (2000). First atmospheric profile measurements of the atmospheric UV/vis O_4 absorption bands strength: Implications for the spectroscopy and the formation enthalpy of the O_2–O_2 dimer. *Geophys. Res. Lett.,* Vol. submitted.

Pfeilsticker, K., F. Erle, and U. Platt (1999). Observation of the stratospheric NO_2 latitudinal distribution in the northern winter hemisphere. *J. Atmos. Chem.,* Vol. 32, 101–120.

Pfeilsticker, K., W. T. Sturges, H. Bösch, C. Camy-Peyret, M. P. Chipperfield, A. Engel, R. Fitzenberger, M. Müller, S. Payan, and B.-M. Sinnhuber (2000). Lower stratospheric organic and inorganic bromine budget for the Artic winter 1998/99. *Geophys. Res. Lett.,* Vol. 27, No. 20, 3305–3308.

Platt, U. (1994). Differential optical absorption spectroscopy (DOAS). In M. Sigrist, W. (Ed.), *Air Monitoring by Spectroscopic Techniques*, Volume 127, pp. 27–84. John Wiley & Sons, Inc.

Platt, U., D. Perner, and H. Pätz (1979). Simultaneous measurement of atmospheric CH_2O, O_3 and NO_2 by differential optical absorption. *J. Geophys. Res.,* Vol. 84, 6329–6335.

Plumb, R. A. and M. K. W. Ko (1992). Interrelationsship between mixing ratios of long-lived stratospheric constituents. *J. Geophys. Res.,* Vol. 97, No. 10, 10145–10165.

Plumb, R. A., D. W. Waugh, and M. P. Chipperfield (2000). The effect of mixing on tracer realtionsships in the polar vortices. *J. Geophys. Res.,* Vol. 105, No. D8, 10047–10062.

Popp, P. J., M. J. Northway, J. C. Holecek, R. S. Gao, D. W. Fahey, J. W. Elkins, D. F. Hurst, P. A. Romashkin, G. C. Toon, B. Sen, S. M. Schauffler, R. J. Salawitch, C. R. Webster, R. L. Herman, H. Jost, T. P. Bui, P. A. Newman, and L. R. Lait (2001). Severe and extensive denitrification in the 1999-2000 Arctic winter stratosphere. *Geophys. Res. Lett.,* Vol. 28, No. 15, 2875–2878.

Portmann, R. W., S. S. Brown, T. Gierczak, R. K. Talukdar, J. B. Burkholder, and A. R. Ravishankara (1999). Role of nitrogen oxides in the stratsophere: a reevaluation based on laboratory studies. *Geophys. Res. Lett.,* Vol. 26, No. 15, 2387–2390.

Press, W. H., B. P. Flannery, S. A. Teukolsky, and W. T. Vetterling (1986). Numerical recipes: the art of scientific computing. *Cambridge, University Press,.*

Proffitt, M. H., J. Margitan, K. Kelly, M. Loewenstein, J. Podolske, and K. Chan (1990). Ozone loss in the Arctic polar vortex inferred from high altitude aircraft measurements. *Nature,* Vol. 342, 31–36.

Pundt, I., J. Pommereau, C. Phillips, and E. Lateltin (1998). Upper limit of iodine oxide in the lower stratosphere. *J. Atmos. Chem.,* Vol. 30, 173–185.

Pyle, J. A., J. Austin, M. P. Chipperfield, R. A. Cox, J. C. Farman, L. J. Gray, N. R. P. Harris, R. L. Jones, A. McCulloch, S. A. Penkett, C. E. Reeves, H. K. Roscoe, K. P. Shine, R. Toumi, and A. R. Webb (1999). Stratospheric ozone 1999. A report from the stratospheric ozone review group. *Goodfellow & Egan Publishing Managment, Cambridge,* Vol. 99EP0458.

Randall, C. E., J. D. Lumpe, R. M. Bevilacqua, K. W. Hoppel, E. P. Shettle, D. W. Rusch, L. . L. Gordley, K. Kreher, K. Pfeilsticker, H. Boesch, G. C. Toon, F. Goutail, and J.-P. Pommereau (2001). Validation of POAM III NO_2 measurements. *J. Geophys. Res.,* Vol. submitted.

Randall, C. E., D. W. Rusch, R. M. Bevilacqua, K. W. Hoppel, and J. D. Lumpe (1998). Polar ozone and Aerosol Measurement (POAM) II stratospheric NO_2, 1993-196. *J. Geophys. Res.,* Vol. 103, No. D21, 28361–28371.

Randall, C. E., D. E. Siskind, and R. M. Bevilacqua (2001). Stratospheric NO_x enhancements in the southern hemisphere vortex in winter/spring 2000. *Geophys. Res. Lett.,* Vol. 28, No. 12, 2385–2388.

Randeniya, L. K., I. C. Plump, and K. R. Ryan (1999). NO_y and Cl_y partitioning in the middle stratosphere: A box model investigation using HALOE data. *J. Geophys. Res.,* Vol. 104, No. D21, 26667–26686.

Rex, M., R. J. Salawitch, G. C. Toon, B. Sen, J. J. Margitan, G. B. Osterman, J.-F. Blavier, R. S. Gao, S. Donelly, E. Keim, J. Neuman, D. W. Fahey, C. R. Webster, D. C. Scott, R. L. Herman, R. D. May, E. J. Moyer, M. R. Gunson, F. W. Irion, A. Y. Chang, C. P. Rinland, and T. P. Bui (1999). Subsidence, mixing, and denitification of Arctic polar vortex air measured during POLARIS. *J. Geophys. Res.,* Vol. 104, No. D21, 26611–26623.

Rinsland, C. P., R. J. Salawitch, M. R. Gunsoon, S. Solomon, R. Zander, E. Mathieu, A. Goldman, M. J. Newchurch, F. W. Irion, and A. Y. Chang (1999). Polar stratospheric descent of NO_y and CO and Arctic denitrification during winter 1992-1993. *J. Geophys. Res.,* Vol. 104, No. D1, 1847–1861.

Rivière, E. D., N. Huret, F. G. Taupin, J.-B. Renard, M. Pirre, S. D. Eckermann, N. Larsen, T. Deshler, F. Lefèvre, S. Payan, and C. Camy-Peyret (2000). Role of lee waves in the formation of solid polar stratospheric clouds: case studies from February 1997. *J. Geophys. Res.,* Vol. 105, No. D5, 6845–6853.

Rodgers, C. W. (1976). Retrieval of atmospheric temperature and composition from remote measurements of thermal radiation. *Rev. of Geophys. and Space Phys.,* Vol. 14, No. 4, 609–623.

Roedel, W. (2000). Physik unserer Umwelt: Die Atmoshäre. *Springer-Verlag, Berlin, Heidelberg, Tokyo,.*

Roehl, C. M., J. J. Orlando, G. S. Tyndall, R. E. Shetter, G. J. Vazquez, C. A. Cantrell, and J. G. Calvert (1994). Temperature dependence of the quantum yields for the photolysis of NO_2 near the dissociation limit. *J. Phys. Chem.,* Vol. 98, 7837–7843.

Roscoe, H. K., D. J. Fish, and R. L. Jones (1996). Interpolation errors in the UV-visible spectroscopy for stratospheric sensing: implications for sensitivity, spectral resolution, and spectral range. *Appl. Opt.,* Vol. 35, 427–432.

Rosenlof, K. H. (1999). Estimates of the seasonal cycle of mass transport and ozone transport at high northern latitudes. *J. Geophys. Res.,* Vol. 104, No. D21, 26511–26523.

Röth, E.-P. (1992). A fast algortihm to calculate the photonflux in optically dense media for use in photochemical models. *Ber. Bunsen- Ges. Phys. Chem.,* Vol. 96, 417–420.

Rothman, L. S., C. P. Rinsland, A. Goldman, S. T. Massie, D. P. Edwards, J.-M. Flaud, A. Perrin, C. Camy-Peyret, V. Dana, J.-Y. Mandin, J. Schroeder, A. McCann, R. R. Gamache, R. B. Wattson, K. Yoshino, K. V. Chance, K. W. Jucks, L. R. Brown, V. Nemtchinov, and P. Varanasi (1996). The HITRAN molecular spectroscopic data database and HAWKS (HITRAN atmospheric workstation): 1996 edition. *J. Quant. Spectroscopy and Rad. Transfer,* Vol. 60, 665–710.

Rowley, D., J. C. Mossinger, R. A. Cox, and R. L. Jones (1999). The UV-visible cross section and atmospheric photolysis rate of HOI. *J. Atmos. Chem.,* Vol. 34, 137–151.

Rowley, D. M., W. J. Bloss, R. A. Cox, and R. L. Jones (2001). Kinetics of the IO + BrO reaction. *J. Phys. Chem. A,* Vol. 105, 7855–7864.

Ruhnke, R., W. Kouker, and T. Reddmann (1999). The influence of the $OH + NO_2 + M$ reaction on the NO_y partitioning in the late winter 1992/1993 as studied with KASIMA. *J. Geophys. Res.,* Vol. 104, No. D3, 3755–3772.

Sander, S., R. R. Friedl, W. B. DeMore, D. M. Golden, R. F. Hampson, M. J. Kurylo, R. Hampson, R. E. Huie, A. R. Ravishankara, C. E. Kolb, M. J. Molina, and G. K. Moortgart (2000). Chemical kinetics and photochemical data for use in statospheric modeling: supplement to evaluation 12: update of key reactions. *Technical Report, NASA/JPL Publication,* , No. 00-3.

Sander, S. P. (1986). Temperature dependence of the NO_3 absorption spectrum. *J. Phys. Chem.,* Vol. 90, 4135–4142.

Sanders, R. (1996). Improved analysis of atmospheric spectra by including the temperature dependence of NO_2. *J. Geophys. Res.,* Vol. 101, No. D15, 20945–20952.

Santee, M. L., G. L. Manney, N. J. Livesey, and J. W. Waters (2000). UARS microwave limb sounder observations of denitrification and ozone loss in the 2000 Arctic late winter. *Geophys. Res. Lett.,* Vol. 27, No. 19, 3213–3216.

Sassano, Y., M. Suzuki, T. Yokota, and H. Kanzawa (1999). Improved limb atmospheric spectrometer (ILAS) for stratospheric ozone layer measurements by solar occultation technique. *Geophys. Res. Lett.,* Vol. 26, 197–200.

Schall, C. and K. G. Heumann (1993). GC determination of volatile organoiodine and organobromine compounds in Arctic seawater and air samples. *Fres. J. Anal. Chem.,* Vol. 346, 717–722.

Scheffler, H. and H. Elsässer (1974). Physik der Sterne und der Sonne. *B.I.-Wissenschaftsverlag, Mannheim, Wien, Zürich,.*

Schiller, C., A. Hofzumahaus, M. Müller, E. Klein, E.-P. Röth, and S. U. (1994). Ultraviolett actinic flux in the stratosphere: an overview of balloon-borne measurements during the EASOE, 1991/92. *Geophyis. Res. Lett.,* Vol. 21, 1239–1242.

Schneider, M. (1997). Gleichzeitige, ballongestützte Messungen von O_3, NO_2 und der Photolysefrequenz von NO_2 in der Stratosphäre. *Master thesis, Institut für Umweltphysik, Universität Heidelberg,.*

Schreiner, J., C. Voigt, A. Kohlmann, F. Arnold, K. Mauersberger, and M. Larsen (1999). Chemical analysis of polar stratospheric cloud particles. *Science,* Vol. 283, 968–970.

Schulte, M. (1996). DAMF V1.22 direct light airmass factors. *Internal paper, Institut für Umweltphysik, Universität Heidelberg,.*

Schulz, A., M. Rex, N. R. P. Harris, G. O. Braathen, E. Reimer, R. Alfier, I. Kilbane-Dawe, S. Eckermann, M. Allaart, M. Alpers, B. Bojkov, J. Cisneros, H. Claude, E. Cuevas, J. Davis, H. De Backer, H. Dier, V. Dorokhov, H. Fast, S. Godin, B. Johnson, B. Kois, Y. Kondo, E. Kosmidis, E. Kyrö, Z. Litnyska, I. S. Mikkelsen, M. J. Molyneux, G. Murphy, T. Nakai, H. Nakane, F. O'Connor, C. Parrondo, F. J. Schmidlin, P. Skrivankova, C. Varotsos, C. Vialle, P. Viatte, V. Yuskov, C. Zerefos, and P. van der Gathen (2001). Arctic ozone loss in threshold conditions: Match observations in 1997/1998 and 1998/1999. *J. Geophys. Res.,* Vol. 106, No. D7, 7495–7503.

Schulz, A., M. Rex, J. Steger, N. R. P. Harris, G. O. Braathen, E. Reimer, R. Alfier, A. Beck, M. Alpers, J. Cisneros, H. Claude, H. De Backer, H. Dier, V. Dorokhov, H. Fast, S. Godin, G. Hansen, H. Kanzwaw, B. Kois, Y. Kondo, E. Kosmidis, E. Kyrö, Z. Litynska, M. J. Molyneux, G. Murphy, H. Nakane, C. Parrondo, F. Ravegnani, C. Varotsos, C. Vialle, P. Viatte, V. Yuskov, C. Zerefos, and P. van der Gathen (2000). Match observations in the Arctic winter 1996/1997: High stratospheric ozone loss rates correlate with low termperatures deep inside the polar vortex. *Geophys. Res. Lett.,* Vol. 27, No. 2, 205–208.

Schwabl, F. (1993). *Quantenmechanik.* Berlin, Heidelberg, New York: Springer-Verlag.

Seery, D. and D. Britton (1964). The continous absorption spectra of chlorine, bromine, bromine chloride, iodine chloride, and iodine bromide. *J. Phys. Chem.,* Vol. 68, 2264–2266.

Sen, G. C., G. C. Toon, G. B. Ostermann, J.-F. Blavier, J. J. Margitan, R. J. Salawitch, and G. K. Yue (1998). Measurement of reactive nitrogen in the stratosphere. *J. Geophys. Res.,* Vol. 103, No. D3, 3571–3585.

Shettle, E. P. (1989). Models of aerosols, clouds and precipitation for atmospheric propagation studies. Paper presented at Conference on Atmospheric Propagation in the UV, Visible, IR and MM-Region and Related Aspects. *NATO Adv. Group for Aerosp. Res. and Dev. Copenhagen, Denmark, 9 - 13 October, 1989,.*

Shindell, D. T., D. Rind, and P. Lonergan (1998). Increased polar stratospheric ozone losses and delayed eventuel recovery owing to increasing greenhouse-gas concentrations. *Geophys. Res. Lett.,* Vol. 18, 763–766.

Shine, K. (1987). The middle atmosphere in the absence of dynamical heat fluxes. *Q. J. R. Meteorol. Soc.,* Vol. 113, 603–633.

Sinnhuber, B.-M., M. P. Chipperfield, S. Davis, J. P. Burrows, K.-U. Eichmann, M. Weber, P. von der Gathen, M. Guirlet, G. A. Cahill, A. M. Lee, and J. A. Pyle (2000). Large loss of total ozone during the Arctic winter of 1999/2000. *Geophys. Res. Lett.,* Vol. 27, No. 21, 3473–3476.

Siskind, D. E., J. T. Bacmeister, M. E. Summers, and J. M. Russell III (1997). Two-dimensional model calculation of nitric oxide transport in the middle atmosphere and comparison with Halogen Occultation Experiment data. *J. Geophys. Res.,* Vol. 102, No. D3, 3527–3545.

Siskind, D. E., G. E. Nedoluha, C. E. Randall, M. Fromm, and J. M. Russell III (2000). An assessment of southern hemisphere stratospheric NO_x enhancements due to the transport from the upper atmosphere. *Geophys. Res. Lett.,* Vol. 27, No. 3, 329–332.

Solomon, S. (1999). Stratospheric ozone depletion: a review of concepts and history. *Rev. Geophys.,* Vol. 37, 275–316.

Solomon, S., R. R. Garcia, and A. R. Ravishankara (1994). On the role of iodine in ozone depletion. *J. Geophys. Res.,* Vol. 99, No. D10, 20491–20499.

Solomon, S., R. R. Garcia, F. S. Rowland, and D. J. Wuebbles (1986). On the depletion of Antartic ozone. *Nature,* Vol. 321, 755–758.

Solomon, S., G. H. Mount, R. W. Sander, and A. L. Schmeltkopf (1987). Visible spectroscopy at McMurdo station, Antartica, 2, Observation of OClO. *J. Geophys. Res.,* Vol. 92, 8329–8338.

Solomon, S., R. W. Portman, R. R. Garcia, W. Randel, F. Wu, R. Nagatani, J. Gleason, L. Thomason, L. R. Poole, and M. P. McCormick (1998). Ozone depletion at midlatitudes: coupling of volcanic aerosols and temperature variability to anthropogenic chlorine. *Geophys. Res. Lett.,* Vol. 25, 1871–1874.

Solomon, S., A. L. Schmeltkopf, and R. W. Sanders (1987). On the interpretation of zenith sky absorption measurements. *J. Geophys. Res.,* Vol. 92, No. D7, 8311–8319.

Steinegger, M. (1999). Die Sonne als veränderlicher Stern. Vorlesungsskript 98/99, Institut für Geophysik, Astrophysik und Meteorologie, Universität Graz.

Stowasser, M., H. Oelhaf, G. Wetzel, H. Fischer, F. Friedl-Vallon, A. Kleinert, A. Lengel, G. Mauchert, N. Nordmeyer, O. Trieschmann, and M. P. Chipperfield (2000). Nitrogen partitioning in 1999 winter Arctic vortex, measured by MIPAS-B. In *Stratospheric Ozone, Proceedings of the fifth European Symposium, St. Jean de Luz, France.*

Sturges, W. T., H. P. McIntire, S. A. Penkett, J. Chappellaz, J.-M. Barnolo, R. Mulvaney, E. Atlas, and V. Stroud (2001). Methyl bromide, other brominated methanes and methyl iodide in polar firn air. *J. Geophys. Res.,* Vol. 106, No. D2, 1595–1606.

Stutz, J. (1996). Messung der Konzentration troposhärischer Spurenstoffe mittels Differentieller- Optischer-Absorptionsspektroskopie: Eine neue Generation von Geräten und Algorithmen. *Ph. D. thesis, Institut für Umweltphysik, Universität Heidelberg,.*

Stutz, J. and U. Platt (1996). Numerical analysis and error estimation of Differential Optical Absorption Spectroscopy measurements with least square fits. *Appl. Opt.,* Vol. 30, No. 30, 6041–6053.

Sugita, T., Y. Kondo, H. Nakaijma, U. Schmidt, A. Engel, H. Oelhaf, G. Wetzel, M. Koike, and P. A. Newman (1998). Denitrification observed inside the Arctic vortex in february 1995. *J. Geophys. Res.,* Vol. 103, No. D13, 16221–16233.

Sugita, T., H. Nakajima, H. Kanzawa, T. Yokata, Y. Sasano, T. Deshler, K. Shibasaki, Y. Kondo, V. Yushkov, H. Gernandt, F. Goutail, S. Godin, J.-P. Pommereau, H. Schlager, H. Boesch, , K. Pfeilsticker, C. Camy-Peyret, J.-B. Renard, M. von Koenig, H. Bremer, H. Kuellmann, I. Murata, H. Fukunishi, J. J. Margitan, B. Stachnik, J. Toon, K. Jucks, and W. Traub (2001). Validation of ozone measurements from the Improved Limb Atmospheric Spectrometer (ILAS). *J. Geophys. Res.,* Vol. submitted.

Swartz, W. H., S. A. Lloyd, T. L. Kusterer, D. E. Anderson, and C. T. McElroy (1999). A sensitivity study of photolysis rate coefficients during POLARIS. *J. Geophys. Res.,*, 26725–26735.

Toon, O. B., P. Hamill, R. P. Turco, and J. Pinto (1986). Condensation of HNO_3 and HCl in the winter polar stratosphere. *Geophys. Res. Lett.,* Vol. 13, 1284–1287.

Toumi, R., S. Bekki, and R. Cox (1993). A model study of ATMOS observations and the heterogenous loss of N_2O_5 by the sulphate aerosol layer. *J. Atmos. Chem.,* Vol. 16, 135–144.

Tsias, A. Wirth, M., K. S. Carslaw, J. Biele, H. Mehrtens, J. Reichelt, C. Wedekind, V. Weiss, W. Renger, R. Neuber, U. von Zahn, B. Stein, and T. Peter (1999). Aircraft lidar observations of enhanced type 1a polar stratospheric clouds during APE-POLECAT. *J. Geophys. Res.,*.

Turnipseed, A., M. K. Gilles, J. B. Burkholder, and A. R. Ravishankara (1995b). Iodine chemistry in the stratosphere: kinetics of the IO + ClO and IO + BrO reactions. *EOS, Trans. Amer. Geophys. U., supplement,* Vol. 76, No. F116.

Turnipseed, A., M. K. Gilles, J. B. Burkholder, and A. R. Ravishankara (1995a). LIF detection of IO and the rate coefficient for I + O_3 and IO + NO reactions. *Chem. Phys. Lett.,* Vol. 242, 427–434.

Turnipseed, A. A., M. K. Gilles, J. B. Burkholder, and A. R. Ravishankara (1997). Kinetics of the IO radical. 1. reaction of IO with ClO. *J. Phys. Chem. A,* Vol. 101, 5517–55525.

Unsöld, A. and B. Baschek (1999). Der neue Kosmos. *Springer-Verlag, Berlin, Heidelberg, Tokyo,*.

Van De Hulst, H. C. (1957). Light scattering by small particles. *Dover Publ., New York,*.

Van Roozendael, M. and C. Fayt (2000). WinDOAS 2.1. Software user manual. *Belgium Institute for Space Aeronomie (BIRA/IASB),*.

Vandaele, A., C. Hermans, P. Simon, M. Van Roozendael, J. Guilmot, M. Carleer, and R. Colin (1996). Fourier Transform Measurements of NO_2 absortpion cross-section in the visible range at room temperature. *J. Atmos. Chem.,* Vol. 25, 289–305.

Vitt, F. M. and C. H. Jackman (1996). A comparison of sources of odd nitrogen production from 1974 through 1993 in the Earth's middle atmosphere as calculated using a two-dimensional model. *J. Geophys. Res.,* Vol. 101, No. D3, 6729–6739.

Vogt, S., R. Sander, R. von Glasow, and P. J. Crutzen (1999). Iodine chemistry and its role in halogen activation and ozone loss in the marine boundary layer: a model study. *J. Atmos. Chem.,* Vol. 32, 375–395.

Voigt, C., J. Schreiner, A. Kohlmann, P. Zink, K. Mauersberger, N. Larsen, T. Deshler, C. Kröger, J. Rosen, A. Adriani, F. Ciaro, G. Di Donfrancesco, M. Viterbini, J. Ovarlez, H. Ovarlez, D. C., and A. Dörnbrack (2000). Nitric Acid Trihydrate (NAT) in polar stratospheric clouds. *Science,* Vol. 290, 1756–1758.

Voigt, S., J. Orphal, K. Bogumil, and J. P. Burrows (2001). The temperature dependence (203-293 K) of the absorption cross section of O_3 in the 230-850 nm region measured by Fourier-transform spectroscopy. *J. Photochem. Photobiol. A,* Vol. 143, 1–9.

Vradelis, P. (1998). Verbesserung der Ballon-DOAS-Messungen durch Streulichtunterdrückung und numerische Untersuchung des Auswerteprozesses. *Master thesis, Institut für Umweltphysik, Universität Heidelberg,.*

Wagner, T., C. Leue, K. Pfeilticker, and U. Platt (2001). Monitoring of the stratospheric chlorine activation by Global Ozone Monitoring Experiment (GOME) OClO measurements ni the austral and boreal winters 1995 through 1999. *J. Geophys. Res.,* Vol. 106, No. D5, 4971–4989.

Wahner, A., G. S. Tyndall, and A. R. Ravishankara (1987). Absorption cross section for OClO as a function of temperature in the wavelength range from 240 - 480 nm. *J. Phys. Chem.,* Vol. 91, 2734–3738.

Waibel, A. E., T. Peter, K. S. Carslaw, H. Oelhaf, G. Etzel, P. J. Crutzen, U. Pöschl, A. Tsias, E. Reimer, and H. Fischer (1999). Arctic ozone loss due to denitrification. *Science,* Vol. 238, 2064–2068.

Wamsley, P. R., J. W. Elkins, D. W. Fahey, G. S. Dutton, R. C. Volk, C. M. Myers, S. A. Montzka, J. H. Butler, A. D. Clarke, P. J. Fraser, L. P. Steele, M. P. Lucarelli, E. L. Atlas, S. M. Schauffler, D. R. Blake, F. S. Rowland, W. T. Sturges, J. M. Lee, S. A. PEnkett, A. Engel, R. M. Stimpfle, K. R. Chan, D. K. Weisenstein, M. K. W. Ko, and R. J. Salawitch (1998). Distribution of halon-1211 in the upper troposphere and lower stratosphere and the 1994 total bromine budget. *J. Geophys. Res,* Vol. 103, No. D1, 1513–1526.

Waugh, D. W., R. A. Plimb, J. W. Elkins, D. W. Fahey, K. A. Boering, G. S. Dutton, E. Volk, C. M. Keim, B. C. Gao, B. C. Daube, S. C. Wofsy, M. Loewenstein, J. R. Podolske, K. R. Chan, K. K. Proffitt, M. H. Kelly, P. A. Newman, and L. R. Lait (1997). Mixing of polar vortex air into middle latitudes as revealed by tracer-tracer scatterplots. *J. Geophys. Res.,* Vol. 102, No. D11, 13119–13134.

Webster, C. R., R. D. May, H. A. Michelson, D. C. Scott, J. C. Wilson, H. H. Jonason, C. A. Brock, J. E. Dye, D. Baumgardner, R. M. Stimpfle, J. P. Koplow, J. J. Margitan, M. J. Profitt, L. Jaeglé, R. L. Herman, H. Hu, G. J. Flesch, and M. Loewenstein (1998). Evolution of HCl in the lower stratosphere from 1991 to 1996 following the eruption of Mt. Pinatubo. *Geophys. Res. Lett.,* Vol. 25, 995–998.

Wenig, M. (2001). Satellite measurement of long-term global tropospheric trace distributions and source strength - Algorithm development and data analysis. *Ph. D. thesis, , Universität of Heidelberg,.*

Wennberg, P. O., J. W. Brault, T. F. Hanisco, R. J. Salawitch, and G. H. Mount (1997). The atmospheric column abundance of IO: Implications for stratospheric ozone. *J. Geophys. Res.,* Vol. 102, No. D7, 8887–8898.

Wetzel, G., T. von Clarmann, H. Oelhaf, and H. Fischer (1995). Vertical profiles of N_2O_5 along with CH_4, N_2O, and H_2O in the late Arctic winter retrieved from MIPAS-B infrared limb emission measurements. *J. Geophys. Res.,* Vol. 100, No. D11, 23173–23181.

Wetzel, G. H., H. Oelhaf, W. Ruhnke, R. Kouker, F. Friedl-Vallon, A. Kleinert, G. Mauchert, M. Seefeldner, M. Stowasser, O. Trieschmann, T. von Clarmann, and H. Fischer (2000). Nitrogen partitioning in summer mid-latitudes and the late-winter Arctic vortex, measured by MIPAS-B. In *Stratospheric Ozone, Proceedings of the fifth European Symposium, St. Jean de Luz, France.*

Wittrock, F., R. Müller, A. Richter, H. Bovensmann, and J. P. Burrows (2000). Measurement of iodine oxide (IO) above Spitsbergen. *Geophys. Res. Lett.,* Vol. 27, No. 10, 1471–1474.

WMO (1996). Atmospheric Ozone 1985. *World Meteorological Organisation (WMO), Geneve, Switzerland, Report No. 16,* Vol. 1.

WMO (1998). Scientific assesment of ozone depletion: 1998. *World Meteorological Organisation (WMO), Geneve, Switzerland,.*

Wofsy, S. C., M. B. McElroy, and Y. L. Yung (1975). The chemistry of atmosheric bromine. *Geophys. Res. Lett.,* Vol. 2, 215–218.

Woods, T. N., D. K. Prinz, G. J. Rottman, J. London, P. C. Crane, R. P. Cebula, E. Hilsenrath, G. E. Brueckner, M. D. Andrews, O. R. White, M. E. VanHoosier, L. E. Floyd, L. C. Herring, B. G. Knapp, C. K. Pankratz, and P. A. Reiser (1996). Validation of the UARS solar ultraviolet irradiances: Comparison with the Atlas 1 and 2 measurements. *J. Geophys. Res.,* Vol. 101, 9541–9569.

Yokouchi, Y., L. A. Barrie, D. Toon, and H. Akimoto (1996). The seasonal variation of selected natural and anthropogen halocarbons in the Arctic troposphere. *Atmos. Environ.,* Vol. 30, 1723–1727.

Yokouchi, Y., H. Mukai, H. Yamamoto, A. Otsuki, C. Saitoh, and Y. Nojiri (1997). Distribution of methyl iodide, ethyl iodide, bromoform, and dibromomethane over the ocean (east and southeast Asian seas and the western Pacific). *J. Geophys. Res.,* Vol. 102, 8805–8809.

Zhang, R., M.-T. Leu, and L. F. Keyser (1995). Hydrolysis of N_2O_5 and $ClONO_2$ on the $H_2SO_4/HNO_3/H_2O$ ternary solutions under stratospheric conditions. *Geophys. Res. Lett.,* Vol. 22, 289–292.

Acknowledgements

Zum Abschluß möchte ich mich noch bei all denjenigen Bedanken die zum erfolgreichen Gelingen dieser Arbeit beigetragen haben.

An erster Stelle möchte hier Herrn Prof. Dr. Ulrich Platt nennen, unter dessen wissenschaftlicher Leitung diese Arbeit durchgeführt wurde.

Herrn Prof. Dr. Konrad Mauersberger danke ich für die freundliche Übernahme der Begutachtung dieser Arbeit.

Ganz herzlich bedanken möchte ich mich auch bei Klaus Pfeilsticker, der diese Arbeit stets gefördert hat und mit Rat und Tat zur Seite stand.

Desweiteren möchte ich mich bei meinen Mitstreitern Martin, Frank und Marcel, sowie den Ehemaligen Frieder, Hartwig, Hartmut, Matthias, Paul, Richard und Rüdiger bedanken. Frank und Marcel gebührt dabei besonderer Dank für das unermüdliche Korrekturlesen.

Der gesamten Arbeitsgruppe danke ich für die stets gute Atmosphäre und die vielen Kaffeepausen-Diskussionen. Hervorheben möchte ich dabei diejenige die einen kleinen oder auch grösseren Beitrag zu dieser Arbeit beigetragen haben, allen voran Christoph, Gerd, Hans, Irene, Kai-Uwe, Nicole, Thomas (Wat), Thomas (Scholl) und Udo.

Besonders bedanken möchte ich mich bei Frank Erle und Oliver Funk von denen ich viel gelernt habe während meiner Zeit am Institut für Umweltphysik und mit denen mich auch heute noch sehr viel verbindet.

Vielen Dank auch an Claude Camy-Peyret, Pascal Jeseck, Yao Té, Isabelle Pepin sowie Sebastien Payan vom LPMA-Team für die hervorragende Zusammenarbeit auf den gemeinsamen Meßkampagnen und bei der wissenschaftlichen Interpretation.

Für die bereitgestellten Modelldaten möchte ich mich herzlich bei Martyn Chipperfield und Björn-Martin Sinnhuber (SLIMCAT), Roland Ruhnke (KASIMA) und Frank Lefèvre (REPROBUS) bedanken.

Bedanken möchte ich mich auch bei Caroline Fayt und Michel van Roozendael, die das Programm *WinDOAS* bereitgestellt haben und die stets offen für Fragen und Anregungen waren.

Bei Cora Randall und Jerry Lumpe bedanke ich mich für die gute Zusammenarbeit bei den Vergleichen mit POAM III.

Zum Schluß möchte ich mich bei meinen Eltern und Geschwistern für die fortwährende Unterstützung während meines Studiums und meiner Doktorarbeit bedanken. Ganz spezieller Dank gebührt natürlich meiner Freundin Corinna und meiner Tochter Svea, denen ich nun hoffentlich mehr Zeit widmen kann.